Cranial Suture Three-Dimensional Analysis: An Image Processing, Morphometry, and Finite Element Study

by

Ross Louis Jordan Remesz

A thesis submitted in partial fulfillment of the requirements for the degree of

Master of Science

Department of Mechanical Engineering

University of Alberta

Abstract

Cranial sutures are a network of vasculature, extracellular matrix, and fibers that join the bones in the skull of most vertebrates. Not only do sutures play an important mechanical role in the skull, but they are also vital for growth and development. Sutures respond to mechanical stimuli, reorganizing and transforming on a cellular level, which in turn shapes the bulk morphometric form of the suture. Sutures exhibit non-linear viscoelastic material properties that cause them to behave differently in tension and compression. Morphometry of sutures ranges from a straight butt-ended form to a highly interdigitated tortuous form; both of which may even be found within a single suture structure in different regions.

Due to the enclosed location in the skull, suture structures are typically viewed in a cross-sectional planar form. This cross-sectional view of the suture is often taken to represent the complexity of the entire structure, despite the fact that sutures can be highly spatially variable in three dimensions (3D). Previous works have typically noted morphometric and cellular variability within sutures qualitatively or analyzed the planar morphometry quantitatively. However, little attention has been given to quantifying 3D suture morphometry. The extent that a sutures' form changes through the skull thickness, or how through-thickness variability could affect mechanical behaviour represents a gap in literature.

The first objective of this work was to develop methods that quantify bulk suture complexity through the skull thickness by processing and segmenting X-ray

computed tomography images to a binary form where morphometric properties could be quantified by an automated method. Second, the potential implications of treating sutures as 2D structures in mechanical simulations as opposed to using the true 3D geometry was studied using finite element analysis. Third, an age-based 3D morphometric analysis that focused on through thickness interdigitation and width variability, using the methods developed within this thesis was considered.

The results of this thesis showed morphometric variability within a given suture and between sutures in a rat model. The geometric models generated using swine X-ray computed tomography datasets assumed cross-sectional as well as 3D suture representations. The geometric models were exposed to tensile loading by finite element methods, where it was found that 2D models can approximately represent the bulk average mechanics of the 3D model in certain instances. However, the 2D representations were typically found to have more uniformly distributed mechanical parameters and are unable to provide comparable resolution along the suture-bone interface to the 3D model. The age-based 3D morphometry analysis showed interdigitation and width variability of more than two times within a single suture, which highlights the necessity to treat highly interdigitated sutures as 3D structures. With one exception, there was no statistical significance found in mean suture interdigitation between age groups, and none found in mean suture width between age groups.

The methods and general ideas presented in this thesis focus on treating suture complexity as a 3D problem, this has potential applications in studies that are

interested in suture morphometry, development, mechanics, or simulations. The advancement of these fields could improve and optimize treatments and instruments related to orthodontics and pathological conditions involving sutures.

Preface

This thesis is original work completed by Ross Remesz. The contents of this thesis have not been previously published. However, Chapter 3 of this thesis has been submitted to Biomechanics and Modeling in Mechanobiology for review. The author of this thesis was responsible for data collection, data preparation, data analysis, and the writing of the document.

Acknowledgements

Throughout my research and the writing of this thesis I have been fortunate to receive an abundance of support and assistance.

I would like to first thank my advisor, Dr. Dan Romanyk, for his expertise, patience, and continued guidance. I am extremely grateful for the time and efforts you have invested in me and this research. Thank you for the knowledge you have shared with me and your efforts to help me grow professionally and academically. I would also like to commend you for maintaining an interactive lab group that supported and provided feedback to each member's research despite the pandemic, it helped maintain some level of normalcy over the past couple years.

I would like to acknowledge and thank my colleagues from the Romanyk Lab group for their continued feedback as well as the undergraduate students involved in this research. I would like to extend a special thanks to Tomo Khurelbaatar for the collaboration and countless hours spent in online meetings working through problems, working with you was truly a pleasure.

I also would like to extend thanks to Dr. Mike Doschak, for providing immense knowledge of μCT scanning to this research. Without your collaboration and generosity of resources and time, this research would not have been possible.

To my former professors and colleagues for their help in growing my fundamental knowledge of engineering, professionalism, confidence, and passion for growth.

Lastly, I would like the acknowledge and thank my family and friends. Your endless support has been invaluable, I could not have completed this work without you. Thank you, mom, dad, Trevor, sisters, and grandparents, for continually exemplifying the importance of learning, self-improvement, and for inspiring my career as an engineer.

Table of Contents

List of Tables

List of Figures

List of Nomenclature and Acronyms

A	Amplitude
AL LHS	Left-hand-side anterior lambdoid suture
AL RHS	Right-hand-side anterior lambdoid suture
BMI	Brain machine interface
C LHS	Left-hand-side coronal suture
C RHS	Right-hand-side coronal suture
FE	Finite element
l	Length
LHS	Left hand side
LII	Linear interdigitation index
ME	Maxillary expansion
PL	Posterior lambdoid suture
RHS	Right hand side
ROI	Region of interest
S	Sagittal suture
2D	Two-dimensional
2DV	Two-dimensionally-variable
3D	Three-dimensional
3DV	Three-dimensionally-variable
μCT	Micro computed tomography
λ	Wavelength

Chapter 1: Introduction

This chapter discusses the importance of studying cranial suture morphometry and mechanics in three-dimensions and provides a brief introduction to methods of defining suture complexity. This chapter will also outline thesis objectives, organization, and contributions.

1.1 Thesis Motivation

Cranial sutures are a crucial component of the skull that facilitate growth, join adjacent bones, and absorb mechanical loading[1]. Cranial sutures are primarily composed of collagen fibers, extracellular matrix, and vasculature[1,2]. Suture geometry, material composition, and the mechanical loading conditions are spatially and temporally variable[3–5]. Sutures create a network of soft tissue that connects skull bones, as shown in Figure 1.

When considering mechanical modelling of sutures, their inhomogeneous structure and rate-dependent behaviour makes generating generic, consistent, and reliable models representing their true material response challenging. Therefore, simplifying assumptions must be made to allow for practical modelling approaches. A common simplification that is made to reduce the complexity of cranial suture geometry is to determine the linear interdigitation index (LII). LII is the suture path length between two reference points on a single plane divided by the linear length between the points, shown in equation (1) and highlighted in Figure 2.

$$LII = \frac{l_{suture}}{l_{linear}} \qquad (1)$$

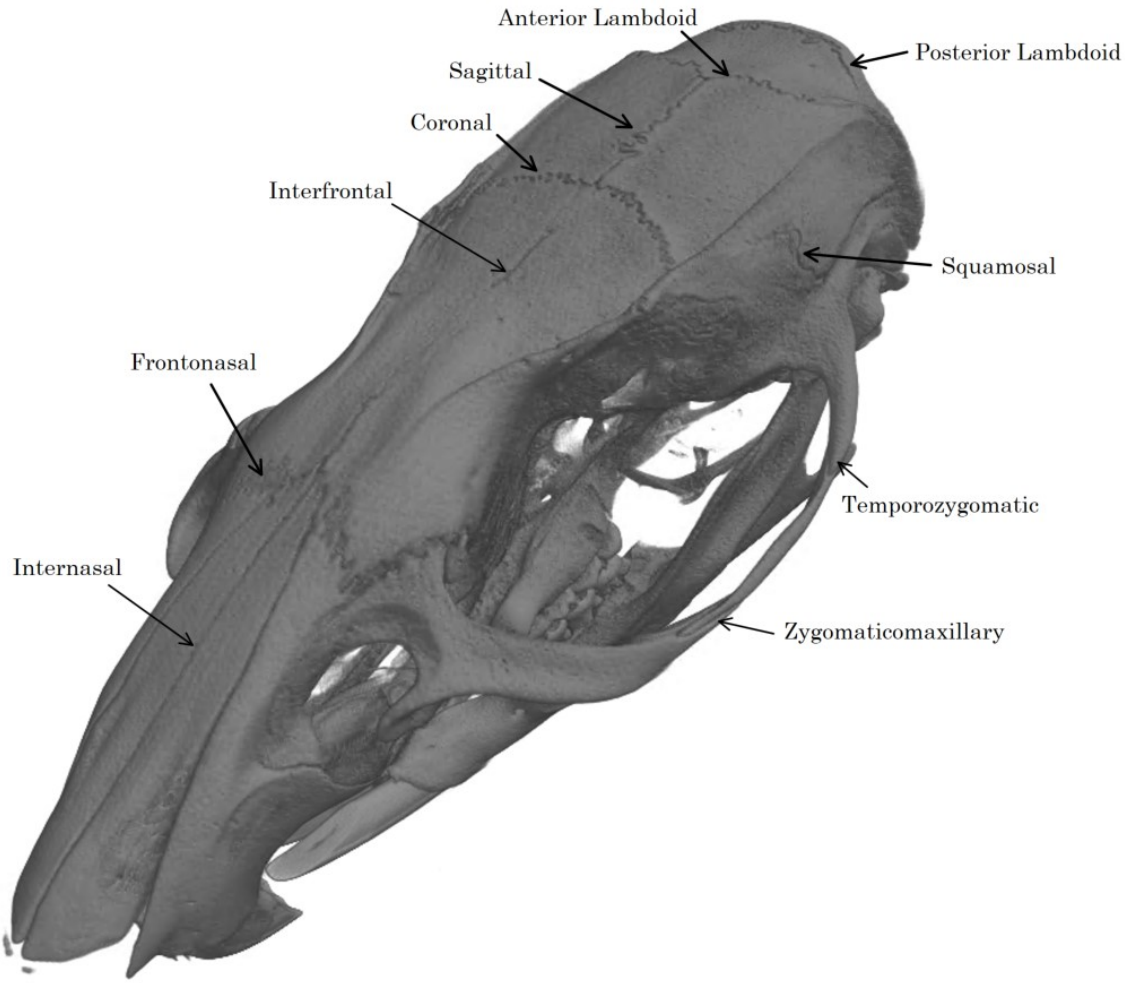

Figure 1 *μCT reconstruction of full rat skull with craniofacial sutures marked*

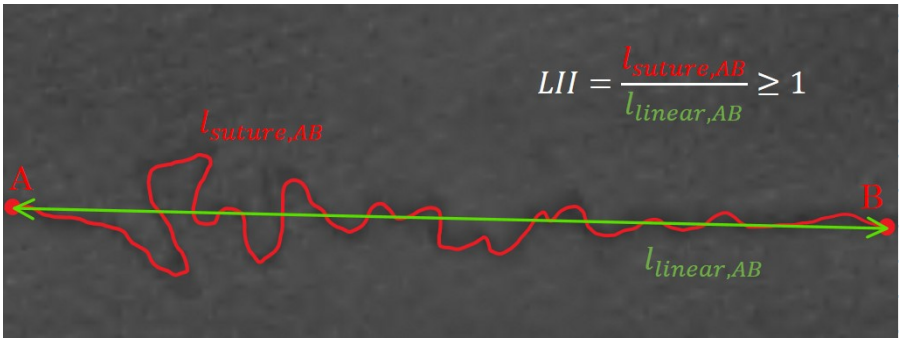

Figure 2 *Method for determining LII. The suture path length is denoted by* $l_{suture,AB}$ *and* $l_{linear,AB}$ *shows the linear length between the ends of the suture being analyzed. Ectocranial view of rat sagittal suture shown*

LII reduces two-dimensional (2D) planar suture complexity to a scalar measure[3]. This scalar measure seems to be a logical metric to compare the complexity of the unique interdigitated suture paths and has been adopted by researchers to correlate mechanical testing results[6,7] and generate suture simulation models[8–10]. However, LII fails to acknowledge that the complexity of sutures is not guaranteed to be constant through the thickness of the skull. There is insufficient quantitative analysis focused on the morphometric variability of sutures through the skull thickness or the potential effects that three-dimensional (3D) structure variability could have on the mechanical response of sutures.

Cranial sutures play an important mechanical role in the skull and are the tissue of interest in many clinical applications, including orthodontics where their unique mechanical nature is utilized to reorient bones in the face[11], and in treating suture related pathological conditions that complicate skull development[12]. Creating suture models that produce accurate predictions can aid clinicians in developing efficient and targeted treatment plans. This is especially true when attempting to link mechanical response to loading with subsequent biological adaptations. Morphologically representative suture geometries are important in creating models that characterize their mechanical response. Improving suture morphological representations and complexity quantification methods has potential to improve many research areas involving sutures. Refining complexity quantification methods will provide researchers interested in suture adaptations and development with more robust metrics that increase representation of suture structures compared to current complexity metrics such as a single planar measure of LII. 3D suture complexity information could also provide insight to when 2D simplifying assumptions can be employed reasonably.

Different complexities of cranial sutures on the endocranial and ectocranial surfaces have been noted in literature[7] and are qualitatively apparent when looking the ectocranial and endocranial surfaces of the skull cap shown in Figure 3, for

example. The lack of research into the full 3D quantitative morphometry of sutures through the skull thickness makes 2D geometric simplifications speculative. Due to complexity and variability of biological tissues, simulating their mechanics and characterizing their form is an evolving science pushing towards more representative geometries, material properties, and constitutive model representations. This work aims to better explore the boundaries of 2D vs. 3D assumptions when evaluating suture morphometry and in mechanics. This is important for generating models that balance accuracy and simplicity, understanding cases where 2D simplifications could be employed and when 3D representation is necessary. Advancing knowledge around suture morphometry and mechanical modelling has implications in multiple research areas including clinical treatment, technology advances, and basic research.

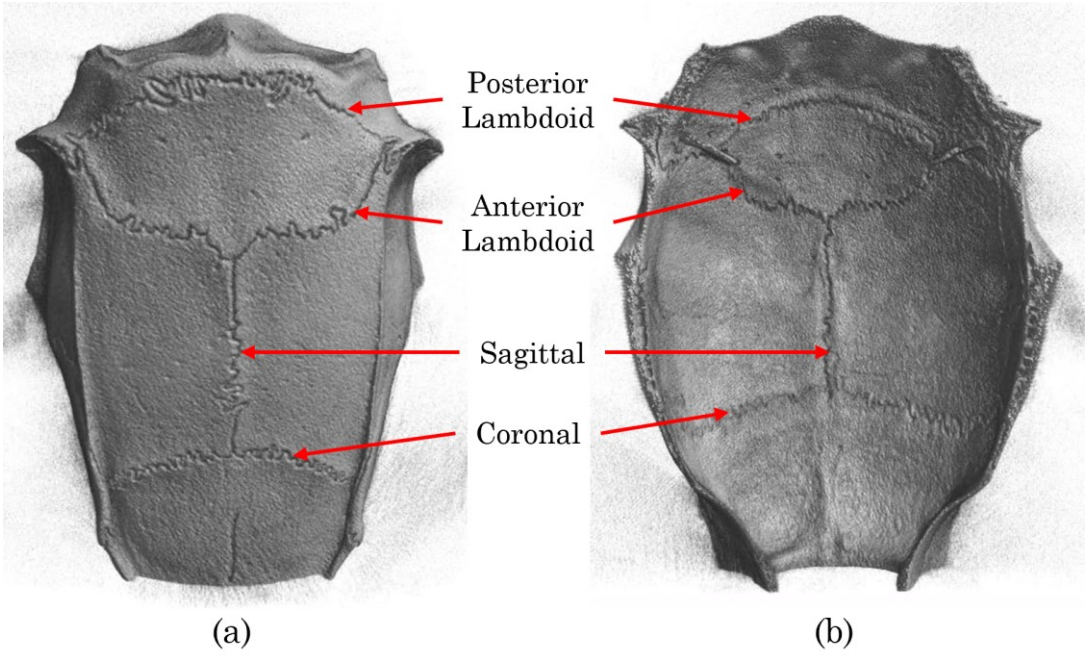

Figure 3 *Solid body μCT reconstruction of isolated rat skull cap with sutures marked; (a) ectocranial view; (b) endocranial view*

Clinically, advancing knowledge of suture mechanics and morphology has the potential to impact fields such as dentistry and general craniofacial surgeries involving suture regions. In dentistry, craniofacial orthodontic devices produce mechanical loads that are transmitted throughout the craniofacial structure as bone

and suture strain[13]. Outcomes of procedures such as maxillary expansion (ME) can be improved with better biomechanical analysis of the procedure. ME is the widening of the upper jaw, accomplished by applying a lateral force to the teeth and maxilla to widen the maxillary suture[14]. Better understanding of suture mechanics could lead to case specific activation methods to expand maxillary sutures in the most physiological manner[15]. Craniosynostosis is a birth defect characterized by the premature ossification of one or more cranial sutures[12], and has been found to occur in a range of 4.3 – 4.8 in 10000 live births[16,17]. Craniosynostosis causes abnormal skull growth due to the prematurely fused sutures[18], often requiring invasive surgical intervention to affected infants and skull molding helmets to be worn for months post operation[19]. Abnormal skull growth due to craniosynostosis has been shown to alter morphology throughout the entire brain volume[20]. Craniosynostosis usually affects a single suture, most commonly the sagittal, followed by the coronal, metopic and lambdoid sutures[21]. Improvements to characterization and mechanical modelling of sutures could provide insight to the mechanical environment of the skull and aid in the treatments of this condition.

Advancements in technology are quickly moving towards wearable and implantable interfaces. Implantable technologies that are located in the skull, such as brain-machine interfaces (BMIs) have been researched for many years and have potential to restore function to those with motor disabilities[22]. These devices also have the potential to change the way that humans interact with technology by using brain signals to interact with computers. With major entrepreneurs recently investing in the technology, BMIs are more likely to progress commercially[23]. Implantable BMIs directly alter skull mechanics by removing a section of skull and replacing it with a neural implant. Increasing the physiological representation of cranial sutures will advance suture mechanical models, which in turn could help optimize the implantation methods and identify any negative structural/biological implications of these implants.

Research of cranial sutures and solidifying a mechanical relationship between suture biological adaptations and applied loading would be benefitted by advancing suture simulations. Verifying mechanical suture adaptation is difficult due to their complex form, however isolated constituent suture components have been found to respond to mechanical stimuli[24–29]. Mechanically induced transcription and expression in sutures has been shown, but determining the exact cells responsible is difficult[30]. To create a validated mechanical relationship between suture adaptations and strains in the suture tissue, accurate morphological representations of sutures and micron scale resolution of strain along the bone-suture interface are necessary.

1.2 Thesis Objectives

The objectives of this thesis were to expand on previous work focused on the mechanical modelling of cranial sutures and gain insight into the 3D morphological form of cranial sutures. The first objective was to develop methods to quantitatively analyze cranial suture morphometry through the skull thickness. This was done by generating methods to process, segment, and extract information from images generated using X-ray-based modalities. Second, to explore the mechanical effects that 2D geometry simplifications have on 3D suture structures from geometric and mechanical perspectives. This was achieved by processing and quantitatively analyzing micro-computed tomography (μCT) data, generating models representing the 2D and 3D assumptions, and performing comparative mechanical finite element (FE) analysis. The third objective of the work focused on analyzing morphometric variability in and between individuals of different age groups using a rat cranial model. This was accomplished by utilizing μCT data and applying the developed methods to analyze sutures from the varying age groups in 3D. The work presented in this thesis advances research surrounding sutures by providing 3D quantitative mechanical and morphometric methods and data currently unavailable in literature. This work aims to guide future works to consider 3D suture representations when

defining suture complexity or modelling suture geometry before 2D simplifications are employed.

1.3 Thesis Organization

This thesis is divided into five chapters. Chapter 2 is composed of a literature review that looks at the general anatomy, composition, current FE modelling techniques, uses of the complexity metric LII, and the anatomy and morphometry of cranial sutures.

Chapter 3 is composed of a morphometric study of the swine coronal and sagittal sutures, and a μCT geometry-based FE case study of the coronal suture. The morphometry study of the coronal and sagittal sutures explores the distribution of LII between the endocranial and ectocranial surfaces of the skull, the average widths of the suture between the endocranial and ectocranial surface, and the local width distribution on a single plane of the suture. The FE case study explores 2D geometric assumptions that are commonly employed in suture geometry modelling. Geometries were extracted from μCT data to generate a representative 3D suture model that accounts for morphometric changes through the thickness of the skull, and three 2D suture models that try to define the entire suture morphometry from a single cross-sectional μCT plane.

Chapter 4 consists of a cranial suture age morphometry analysis on rats of ages 16, 20, and 24 weeks. This section utilizes quantitative methods for extracting suture morphometric data from μCT data. Local and mean planar widths as well as LII was determined at offset planes through the thickness of the skull for coronal, sagittal, anterior lambdoid, and posterior lambdoid sutures. Mean suture width and LII was calculated using the planar data for the coronal, sagittal, anterior lambdoid, and posterior lambdoid sutures. The results of the varying age groups were compared using statistical methods to identify morphological trends within and between sutures.

Chapter 5 discusses the contributions of the work, potential future work that could utilize the findings/methods discussed in this thesis, and the limitations of the work.

Appendix A provides MATLAB code used to process and quantitatively analyze μCT scans, consolidate data, and generate graphics. Appendix B provides information regarding finite element model generation, and numerical results from Chapter 3. Appendix C provides information regarding μCT data manipulation, and numerical results relevant to Chapter 4.

1.4 Thesis Contributions

This thesis provides quantitative methods for analyzing suture complexity in 3D, a mechanical comparison of 2D and 3D geometric models utilizing FE analysis, and a study interested in the variability of 3D suture morphometric complexity with age. The quantitative morphometric analysis methods developed for this thesis can be used to analyze 3D suture morphometry efficiently and is a novel approach for analyzing suture structures providing a more robust representation of their form than current 2D methods. The FE analysis comparing 2D and 3D suture representations highlighted the differences in mechanical results when geometry is defined in 2D using offset reference planes compared to a 3D geometric representation derived from the same specimen. The morphometric age analysis utilized novel methods for calculating suture geometric properties using the entire structure rather than a single cross-section, which provides quantitative 3D data currently unavailable in literature. The presence of 3D morphometric suture variability found in this thesis should prompt researchers interested in suture mechanics, modelling, morphology, development, and adaptations to treat suture structures in a 3D manner or explore 3D structure before employing 2D simplifications when deemed appropriate. This information is necessary in the pursuit of more representative suture models and more accurate relationships between suture morphology, in vivo mechanical loads, and mechanically induced

suture adaptations. 3D morphometric measures can be used to provide more representative relationships between suture adaptations to their environment, this is important in developing meaningful correlations.

Chapter 2: Background

This chapter presents relevant literature surrounding cranial suture function, composition, mechanical environment, morphological and mechanical suture analysis methods, and suture simulation techniques. This review of literature is shown to give background on relevant topics pertaining to the contents of this thesis and current gaps in literature. Information presented in this chapter provides background on topics discussed in Chapters 3 and 4. The unique structure of cranial sutures is discussed to appreciate the complexity and 3D nature of interdigitated sutures which is a focus of this thesis. Background on suture morphometry analysis methods is provided to highlight how suture complexity is typically quantified. The mechanical environment of sutures, as well as research focused on suture mechanics is discussed as they are relevant to the work presented in Chapter 3. Information regarding suture morphometry and structure are presented as they pertain to the work presented in Chapter 4.

2.1 Suture Function, Composition, and Structure

Craniofacial sutures are a network of soft tissue articulations that unite bones in most vertebrates' skulls[1,31]. Sutures are multifunctional, serving as intramembranous bone growth sites that are critical to skull development[32], absorbing mechanical stress[1,2], and allowing for a small amount of compliance that provides the skull with a degree of flexibility[1,2,33]. Suture and adjacent bone structures have been shown to be influenced by mechanical loading conditions they experience in the skull[2]. A wide variety of suture morphologies are found in the skull, ranging from a butt-ended structure where adjacent bones have straight or serrated edges, to complex interdigitated structures where adjacent bones are overlapping and interlocked[5]. A schematic of a rodent model showing the typical locations of the craniofacial sutures of a rat[34], including those of interest for this thesis is shown in Figure 1.

Sutures are complex composite structures primarily composed of extracellular matrix, fibers, and vasculature[2]. Suture composition, morphology, as well as the orientation of the constituent elements change based on functional activity[2,35–39] and age[40–47]. The osteocytic cell population in sutures consists of a bone forming cell (osteoblast), a bone absorbing cell (osteoclast), and a bone maintaining cell (osteocyte)[36]. There is a large population of fibers in the suture space that provide mechanical strength to the suture joint and respond to mechanical loading[40]. Typically, osteocytic populations will be near the bone fronts and the fiber population will be primarily in the middle space between the opposing osteocytic populations and bone fronts[48]. In order to preserve suture patency, there is a delicate balance of osteocytic cell formation and destruction constantly occurring at the osteogenic fronts[48], which is thought to be controlled by programmed cell death, referred to as apoptosis[49]. Apoptosis is thought to be a critical developmental mechanism, removing cells and allowing correct morphogenesis[49]. Sutures are constantly changing at a cellular level, creating, destroying, and maintaining bone, which results in a bone front that responds to age and loading conditions, altering suture morphology[35,39,45,50,51].

2.2 Mechanical Environment and Responses

Sutures in the skull experience complex loading conditions due to the geometry of the cranial vault, the variable geometry and composition of cranial sutures themselves, and the multisource intermittent applied loading they experience through natural (e.g. intracranial pressure) and external (e.g. maxillary expansion appliance) sources[52–55]. Under physiological conditions, the forces primarily responsible for loading cranial sutures are a combination of intracranial pressure, and mastication[2]. Intracranial pressure varies during development due to brain and skull growth[56], but becomes approximately constant in adults, with variations caused primarily by body position and the flow of blood and cerebrospinal fluid[57]. Mastication occurs periodically throughout the day causing complex loading of the

skull that is dependent on ipsilateral, bilateral, or contralateral muscle stimulations[52,53], chewing frequency[58], and the material properties of the food being chewed[35,39,50]. It has been found that masticatory suture strain does change with increasing age; conversely, parietal and frontal bone strain has been found to remain constant with age[59], which emphasizes the role of sutures as strain sinks in the mechanical environment of the skull. External forces also have an influence on cranial suture mechanics and are the most variable of the common loading conditions, with loads ranging from minute magnitudes from various interactions with surroundings (such as wearing glasses), to impacts with potential to cause traumatic brain injury or death[60]. External forces that act on the skull also act on sutures due to their mechanical role in the skull. External forces include impacts, constant loads, dental appliances, or any load that is not present under physiological conditions. The loading conditions that the skull is exposed to results in sutures primarily experiencing three strain regimes[2]. The first is impact which is typically a result of sudden external loading[2]. The second is cyclic, caused by functional activity such as mastication and blood pulsations[2]. The third quasistatic, typically caused by the presence of adjacent tissues, or constant external loading[2]. The loading conditions that a suture experiences are known to affect its structure on cellular and subsequently morphological levels[45]. It is generally thought that exposure to primarily tension leads to straighter morphology with fibers arranged towards the opposing bone fronts, and exposure to primarily compression results in more interdigitated sutures with obliquely arranged fibers[2,3,54]. Fibers can be oriented so that they can resist tension and compression in the same suture[54].

On a cellular level, the composition of sutures is constantly changing due to the presence of osteocytic and fibrocytic cells[36]. Typically, when considering suture biological response to mechanical loading at a cellular level, histological methods[24,44,45,51,61,62] or genetic studies[24,28,49,61–63] will be performed. Histological methods generally give insight to the presence, size, orientation or density of suture cells and fibers. This is useful in understanding how the suture cells respond when

exposed to applied loading and through development. Histological methods have been used to show that fibers within a suture tend to be functionally oriented based on location in order to better resist either tension or compression[2,3,54]. Increasing fiber alignment with age has also been noted[40], which could be interpreted as the suture gradually responding to the changing mechanical environment. The location and density of osteocytic cells have been used to study suture morphological changes[45], responses to mechanical loading[51], and suture growth and fusion[64]. Genetic studies provide valuable information by identifying transcription factors and growth factors/receptors[48]. Elevated gene expressions of several components involved in bone morphogenesis has been noted when exposing mouse cranial sutures to tensile stress[24]. This highlights the mechanical regulation of mesenchymal stem cell proliferation and differentiation into osteocytic cells[24]. This information is valuable in generating relations of mechanical stimulation to cellular response, which is paramount in developing strong links of morphological suture adaptation to mechanical loading.

As previously discussed, sutures are constantly changing at a cellular level, which induces alterations of the morphological form of the apposing bone fronts that bound them[45]. Suture form at a morphometric level is thought to be related to the typical loading and strain regimes it experiences in vivo[2]. Morphological variations related to load magnitude have been described in pigs and fish, with higher levels of interdigitation being reported in compressed sutures than tensed sutures[65,66]. Morphological adaptations are thought to allow the suture to distribute its common loads in a more optimal manner[2]. Due to the complex shape of the skull, and the multitude of loading varieties that could influence a suture, it is no surprise that bending has been found to occur at suture sites in vivo, evident by endocranial surface tension and ectocranial surface compression[53]. With variable loading conditions through the skull thickness, cells are in different mechanical environments at the ectocranial and endocranial surfaces[53]. The differences in the mechanical environment at the endocranial and ectocranial surfaces of the skull would intuitively

alter cellular response at the respective surfaces, and the variable loading through skull thickness could drive differing morphological adaptations that would result in a nonuniform suture structure through the thickness of the skull.

2.3 Morphological Analysis of Cranial Sutures

Morphologically analyzing suture structures can be an ambiguous task due to their unique interdigitated form, enclosed location in the skull, and variability between individuals with age and dependence on previous loading conditions[67]. The unique irregular geometries of cranial sutures makes it difficult to meaningfully define suture morphology using conventional properties with dimensions such as length, wavelength, or amplitude. Wavelength and amplitude are variable along the suture path and using true suture length is dependent on the size of the region of interest (ROI), as shown in Figure 4. Instead, unitless parameters such as LII (Figure 2), that normalize length by incorporating the distance between the sutures ends in the region of interest are more commonly used to describe their 2D complexity[3,5,7,68,69].

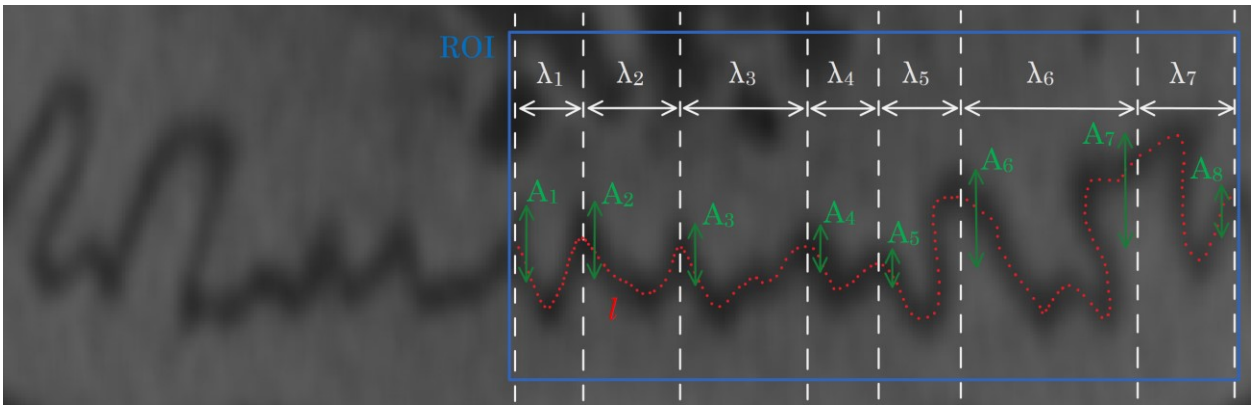

Figure 4 *Analyzing suture morphology within arbitrary region of interest (ROI) using wavelength (λi), amplitude (Ai), and length (l)*

3D suture form is typically neglected entirely or minimally addressed (e.g. considering individual discrete sections instead of the entire structure) when studying suture morphometry in the literature. Instead, 2D representations are commonly used to describe their morphology[3,69]. 2D representations are typically

used because of a given sutures enclosed location in the skull and their complex form, even when viewed in a planar manner. The enclosed position of sutures in the skull makes it difficult to visualize their full 3D form, with only the endocranial and ectocranial surfaces of the suture being visible in a dissected skull. In order to get a full 3D understanding of cranial suture morphometry, utilization of non-destructive imaging techniques or destructive dissections paired with 3D quantitative analysis is necessary. Though 2D representations are commonly used in the literature for morphometric characterization, the assertion that a 2D slice, or group of 2D slices, could be taken as representative for the entire structure has yet to be investigated rigorously. A deeper understanding of 3D suture morphometry will potentially help justify the use of 2D suture representations and provide useful information to studies of suture evolution, development, function, mechanics, and modelling. Studying 2D suture morphometry has been done by visual analysis of dissected skulls[35,70,71], utilizing non-destructive imaging techniques[5,11,38–41,47,66,67,69,72–75], and/or histological methods[3,40,44,45,50].

Visual analysis methods look at dissected skulls by photographic means, which requires less resources than other analysis methods but can still provide valuable information about suture morphology. Visual analysis using photographic methods is limited to analyzing suture complexity at the endocranial and ectocranial surfaces. Byron studied the complexity of sagittal sutures in four cebus species whose diets are known to be materially different by approximately tracing digital photographs of sagittal suture paths on the ectocranial surface of dissected skulls. It was found that dietary specialization on tough foods resulted in greater suture complexity[35]. Nicolay and Vaders were interested in variations of cranial suture complexity of white-tailed deer between males (who have antlers), and females (who lack antlers)[71]. Digital photographs of the ectocranial surface of dried skulls were used to trace suture paths, where they found that the presence of antlers had minimal effects on suture complexity[71]. Both of the studies mentioned were limited to analyzing the morphological form of sutures on the surface of dissected skulls. Exclusively using

the endocranial and ectocranial form limits the utility of this method for 3D morphometric analysis due to the lack of information about the internal suture structure.

Many imaging techniques have been employed to analyze cranial sutures including μCT[5,38,66,76–78], scanning electron microscopy[76], atomic force microscopy[79], and angiograms[1]. The imaging techniques most commonly used analyzing suture morphometry is μCT, due to the large field of view of scan and wide availability of scanners. X-ray techniques are valuable because of the non-destructive nature and ability to see within solid objects. These are important attributes when interested in 3D suture development, response, and morphometry. The limitations of non-destructive imaging techniques are typically their fiscal and computational expenses, as well as the limited view of the cellular structure in conventional machines. Although non-destructive from a bulk physical perspective, X-ray imaging techniques are ionizing, altering molecules within cells, and increasing risks of cancer. This imposes health concerns when using X-rays in-vivo due to the radiation imposed on subjects[80]. The non-destructive nature of imaging methods while limiting radiation exposure is very useful when interested in development and in vivo morphometric responses.

The utilization of imaging techniques has been done in many ways in the literature, depending on the outcomes of interest. Savoldi et al. studied the craniofacial suture morphology of a swine using μCT analysis with 25 μm resolution; the suture morphological properties were calculated on two planes, one perpendicular to the bone surface and one parallel[5]. The study introduced a suture classification method based on bulk morphological properties such as interdigitation and width and noted that morphological parameters such as LII varied within the same suture based on the evaluation plane, however quantitative measures describing the degree of variability through skull thickness were not discussed[5]. Khonsari et al. investigated the micro-structure of cranial sutures using synchrotron X-ray μCT with

approximately 5 μm resolution; where anatomical features such as vasculature, osteocytes, Sharpey's fibres and osteoclast lacunae are noted[78]. The analysis of anatomical features was exclusively qualitative in this study, noting the presence of features rather than quantifying their prevalence or structure in certain areas[78].

Histological methods allow researchers to see the tissue structure and the population of cells and fibers within a suture. These methods are valuable when looking at the cellular response of suture to mechanical loads and through development. The limitations of histology lie in their destructive nature, as well as only providing information on discrete slices that are dissected and stained, which makes it difficult to extract continuous or consistent discrete 3D information.

Histology is commonly utilized in studies to extract information about the conditions that a suture is under in vivo. Rafferty and Herring used histological methods in an in vivo study where a pig's skull was instrumented with strain gauges that bridged various nasal and frontal sutures, strain values were recorded during mastication[3]. The cellular structure in the instrumented regions were analyzed using histological methods where regions of tension and compression were linked with varying levels of interdigitation, cellular populations, bone growth, and fiber configurations/orientations[3]. Burn et al. analyzed the midline suture growth in pigs with varying masticatory function, histological methods were employed to measure the interdigitation, suture width, suture growth rate of the pigs[50]. Anterior, middle, and posterior locations of the internasal and intermaxillary sutures were analyzed, showing varying results, qualitatively highlighting the 3D variability of sutures[50].

As previously mentioned, one of the most common ways to quantify the complexity of sutures is using LII, likely due to its simplicity in providing a single value. It provides a normalized scalar measure of suture complexity by dividing the suture path length by the straight-line path between the suture ends, shown previously in equation (1) and Figure 2. Although LII has been widely used to describe suture complexity[3,5,7,68,69], it does have limitations as a metric. LII does not give any

indication of the traversed path, only the relative complexity to a straight line as shown in Figure 5, where both paths have the same LII but have noticeably different forms. The chosen section or portion of the suture used to determine LII can also have implications, for this value is commonly taken as representing the complexity of the entire suture structure by the single plane it is calculated from.

Figure 5 *Variable forms of suture representation, both with LII=2.8; (a) sinusoidal representation; (b) segmented μCT slice*

LII is typically calculated using a single surface or plane and often used to describe the full complexity of a suture, which completely neglects variable suture form through skull thickness or in different sections. Numerous researchers have noted differing levels of interdigitation within a single suture (i.e. through the thickness or along the length) or limitations with current complexity metrics on a qualitative/anecdotal level but have not quantitatively explored differences[3,5,7,69,70,76], which highlights the necessity of incorporating 3D analysis of these structures. Morphological variability through skull thickness is highlighted in Figure 6, where cross sections of a swine's reconstructed μCT based coronal suture region show variable levels of interdigitation, and subsequently varying LII at different planes through the suture thickness.

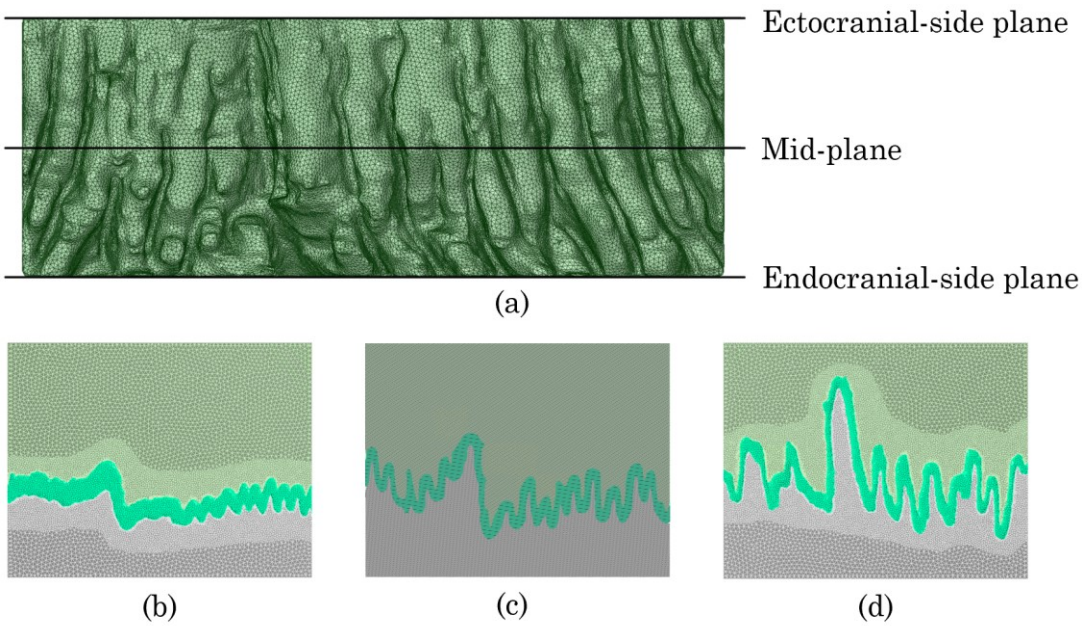

Figure 6 *Reconstructed swine coronal suture, μCT based section; (a) isolated suture viewed from bone; (b)-(d) suture and bone shown, turquoise suture bound by bone; (b) ectocranial-side cross-section, LII=1.6; (c) mid-plane cross section, LII=3.2; (d) endocranial-side cross-section, LII=4.0*

Maloul et al. noted varying levels of LII in the coronal and frontozygomatic sutures of humans in their study that was interested in characterizing the mechanical strength of craniofacial sutures by levels of interdigitation determined from the ectocranial surface[7]. The coronal suture was qualitatively noted as having higher LII on the ectocranial surface and lower on the endocranial surface, while the frontozygomatic suture had higher LII on the endocranial surface and lower on the ectocranial surface; images depicting these differences showed similar complexities on the opposite surfaces of these sutures, which would point to the entire structures having similar complexities[7]. Although this interdigitation variation through the skull thickness was qualitatively noted, there were no measures taken to mitigate the effects of the inversed variation of complexity through the skull thickness between the cranial and facial sutures, and all measures were taken and correlated from the ectocranial side[7]. The results stated that cranial sutures have higher LII and bending strength than facial sutures, however the correlation of LII and bending

strength were skewed due to neglecting the full suture form and describing it exclusively from a single surface. Savoldi et al. studied the midpalatal suture in the premaxillary, maxillary, and palatine region of pigs in the rosto-caudal direction. The properties along the sutures were morphologically and mechanically analyzed where notable differences in mechanics and morphology were found[76]. Markey et al. studied the function and morphology of the interfrontal, interparietal, and frontoparietal sutures of fish, where they qualitatively noted varying levels of interdigitation and concluded that the cross-sectional shape of a suture is not necessarily correlated to the ectocranial appearance of the same suture[69]. These results display the variable complexity of sutures based on where researchers choose to analyze them, however, the 3D morphological form of sutures has been sparsely studied. This variability highlights the necessity for further exploration of the 3D morphometric form of sutures. Further exploration of 3D suture morphometry will provide insight to whether 2D cross-sectional suture representations are appropriate.

2.4 Mechanical Analysis of Cranial Sutures

The mechanical analysis of cranial sutures can be done in a variety of ways, depending on the interests and objectives of the study. Representative geometries are vital for generating useful results in any mechanical analysis, due to geometry, loading conditions, and material properties defining system mechanics. The representativeness of the geometric form defining sutures has an impact on the quality of the results and has the potential to significantly change outcomes depending on the analysis. The typical methods for analyzing suture mechanics are in vivo studies[3,50,51,53,56,62,63,76–80], ex vivo studies[6,7,33,76,79,86,87], and generating analytical and numerical models to describe suture mechanics[8–10,85–116]. Some examples of these methods used in literature are described below in detail.

In vivo studies are performed on living subjects, where biological function and adaptation can be monitored. In vivo mechanical studies of suture are useful for determining anatomical loads and strain states in suture regions[3,50,51,53,56,62,63,76-80] as

well as analyzing suture adaptations to applied loading[35–40,45,50,51,58,59,61,62,93,94]. Mechanical experiments that are interested in anatomical loads and strain states typically instrument strain gauges on live animals to record data from anatomical functions such as mastication[52,53,55,84,85] or external forces[58,81,83]. This information is valuable to researchers interested in modelling mechanics of sutures as it provides a baseline for typical strain values found at specific suture regions, as well as overall strain states in the skull. The typical overall goal of such in vivo work is in linking regions of the skull in specific strain states to their respective morphometry. This is sometimes by a qualitative measure of suture complexity such as describing the suture as "straight"[82], or by quantitative measures such as width[58] or LII[3]. Advancing 3D suture morphology methods and incorporating 3D suture complexity metrics could provide interesting data for linking strain states to suture complexity. Mechanical experiments that analyze suture adaptations to applied loading are crucial for establishing fundamental links between mechanical loads and stress/strain states with the subsequent biological adaptations. Analyses of this type typically are interested in how suture morphometry and cellular populations change with varying loading conditions, often initiated by changing diets[35,39,50,59,94] or instrumenting devices to apply loading[24,36,37,58,62,93]. Herring and Teng analyzed the strain in the braincase during mastication and muscle activation by instrumenting the frontal and parietal bones of live pigs with strain gauges, bridging the interfrontal, interparietal, and coronal sutures[53]. Strains were recorded during mastication and during muscle stimulation of anesthetized animals; it was found the skull bone strain reflected torsion in the braincase and polarity was dependent on which diagonal masseter/temporalis pair was most active[53]. Suture strain was found to not reflect torsion but was primarily impacted by local muscle activation[53]. Histology in this study suggested bending is the primary loading condition at the suture sites. It was proposed that tension was present at the ectocranial surface due to a straight suture path with much of the suture composition lacking a primary orientation, and compression at the endocranial surface due to its interdigitated form with obliquely

oriented fibers[53]. Typically, if suture complexity is of interest, it is treated in 2D, often qualitatively, while sometimes quantitatively analyzing suture complexity on a single plane or surface. Advancing 3D morphological procedures would be beneficial to better understand suture adaptation to applied mechanical loading.

Ex vivo studies utilize samples that have been extracted from an organism and studied in an external environment. Ex vivo mechanical studies of suture typically involve bone-suture complexes being exposed to controlled applied loading[6,7,33,76,79,86,87]. Sutures are often exposed to tension, compression, cyclic loading, or bending in these ex-vivo environments. The results of these studies are paramount in developing material models that describe suture response. Studies often link mechanical results obtained from these experiments to suture complexity, typically by using the parameter LII[6,7,76,79,86]. Jaslow performed ex vivo experiments where sections of goat skull containing cranial sutures were exposed to three-point bending, the bending strength and energy absorption was compared to that of pure bone[6]. Sample age as well as suture interdigitation (calculated from the ectocranial surface) were correlated with the mechanical parameters, and it was found that sutures were not as strong in bending as bone except for highly interdigitated sutures that were loaded slowly. The energy absorption per unit volume of suture was found to have a five-fold increase than that of pure bone[6]. The correlations of suture mechanics to morphology could be improved by developing more representative quantification methods for suture complexity in 3D.

Mechanical modelling of craniofacial sutures is generally done to give insight into the mechanics of clinical procedures[95–108], refine and compare mathematical material models[109–116], explore suture function and response to loading[60,117–120], and/or analyze the effects of suture complexity and morphometry on mechanics[8–10,88–92]. Both analytical and numerical approaches are utilized to model the mechanics of cranial sutures. Analytical methods frame the problem in well understood way and calculate an exact mathematical solution, this often requires substantial assumptions

to be made. Numerical approaches approximate the solutions and test whether solution is acceptable under the user defined conditions. Numerically modelling the mechanics of cranial suture response to applied loading relies heavily on the results of in vivo, and ex vivo mechanical analysis as well as suture morphological studies to obtain appropriate material models and/or geometry. Romanyk et al. employed analytical methods to test whether quasilinear viscoelastic, modified superposition, Schapery's, or Burgers modelling approaches best represented midpalatal suture's viscoelastic expansion behaviour[109]. Romanyk utilized raw experimental data[121] from existing literature in order to compare the models and found that the modified superposition method was best method, replicating experimental data within a standard deviation[109]. The results of the mentioned research provide data for morphometric characteristics, material properties, and loading conditions that are utilized as user defined input parameters in simulations. Simulating suture response using FE methods often requires simplifications to morphology, loading conditions, and material properties due to large computational expenses, lack of access to high resolution images, and non-generic case specific material models.

Morphometric complexity is often simplified to a straight line, or 2D sinusoidal path. Complexity variability is often expressed by altering the amplitude or wavelength of the simplified suture representation[8–10,89,114,116]. In such cases, the appearance of the resulting structures is regular and uniform, which may significantly deviate from the true complex form of sutures, even when viewed on a single plane (Figure 5). Liu et al. introduced irregularities in suture path into similar 2D variable sinusoidal based models using pseudo-random generated numbers[88]. The study was interested in determining the degree that morphological irregularity influenced mechanical properties, and it concluded that morphological irregularities are important features allowing for increased damage tolerance and compliance[88]. Maloul et al. performed an FE analysis where they generated sinusoidal suture models as well as a μCT based model that they qualitatively noted as having variable interdigitation through skull thickness which was treated as a 2D model despite the

clear 3D variability[8]. Mechanical differences of energy absorption between the μCT based 2D models were noted, however results and discussion regarding this were limited and focused more on the regular sinusoidal based models, neglecting the 3D analysis completely[8]. They found that the mechanical behaviour of suture is influenced by morphological factors such as interdigitation and connectivity[8]. Alheit et al. modelled regular 3D suture geometry generated by orthogonal sinusoidal waves that formed a 3D egg tray-like structure to simulate the sutures in turtle shells. The study incorporated 3D variations but neglected suture randomness and thickness variations[90]. They found that sutures absorb more energy than surrounding bone and provide a cushion to avoid fractures[90]. There has been minimal attention in literature to the common 2D treatment of sutures and the implications of neglecting their 3D form. Qualitative conjecture on the complexity variations through the skull thickness is present, but it has typically been ignored when generating suture geometries.

Composition of sutures are typically assumed to be a solid uniform structure rather than its true conglomerate of cells, fibers, and vasculature. Incorporating fibers into the suture bulk to represent the cellular structure has been performed in FE models[8,9,90,114], however mimicking distributions and orientations of fibers found in vivo is a difficult task. This is primarily due to the fiber arrangements found in vivo, where loading magnitude changes from compression to tension with the activation of different muscles in some sutures, often resulting in complex fiber arrangements. Fibers that resist suture tension are typically oriented pointing at the opposing bone fronts, where the fibers that resist suture compression are typically oriented obliquely to the opposing bone fronts; both orientations of fibers are commonly found within a single suture[54]. A wide variety of material models have been explored to represent how sutures respond to loading, including linear elastic, viscoelastic, and hyperelastic models[115]. Linear elastic and viscoelastic are the most common material models used. Linear elastic models represent material response where stress is proportional to strain, and the inputs are computationally simple[115]. Viscoelastic models are more involved, however they best represent in vivo suture

mechanics[2] through incorporating time-dependent and dissipative behaviour[115]. Varying viscoelastic mathematical models have been explored and compared with experimental data with the goal of developing bulk material models that represent suture response[109,110,113,116]. Linear and nonlinear material properties are both used in literature, the latter being more complicated, incorporating time and rate dependent behaviour which has major implications on viscoelastic models[113]. Varying properties directionally is another way to increase model complexity, as isotropic models don't consider directional variability in contrast to anisotropic models[115]. Refinement of material models greatly depends on quality experimental mechanical results for model development and validation. Boundary and loading conditions in FE analysis are typically simplified to look at clinically relevant loads[89,95,97,104,108,122], a single anatomical load such as intracranial pressure or mastication[91,120], an impact load[60,111], or loaded in simple tension, compression, bending, or cyclic loading to contrast response of varying suture geometries[8–10,88] or material models[9,90,114,116,119]. Generating accurate material models is dependent on representative geometric models. Improving the typical 2D representations used in literature to a more representative 3D variable structure could aid in generating more characteristic material models.

Although simulations are commonly used as a method of mechanically analyzing cranial sutures, many simplifications are made in the analysis. Generally, even with simplifications, the outcomes can be useful in the biological and clinical study of suture mechanics. Mechanics of clinical procedures and instruments can be simulated[89,95,97,104,108,122], potentially allowing for refinements that promote specific mechanical environments by interpreting results of clinical FE simulations. FE simulations are useful in generating and refining mathematical material models in conjunction with experimental results[109,120]. Advancing suture geometry modelling in order to be more representative of sutures true 3D form will aid in correlating representative material models with experimental results. As methods for simulating suture response advances, its utility will inevitably increase, with potential to make

significant impacts on clinical advancements and linking suture adaptations with mechanical environments.

Chapter 3: Cranial Suture Morphometry and Mechanical Response to Loading 2D vs. 3D Assumptions and Characterization

The following chapter is a slightly modified version of the manuscript submitted to Biomechanics and Modeling in Mechanobiology in December of 2021 and is currently under review. The alterations made in this thesis are to ensure consistent formatting. The first author of this manuscript is the author of this thesis. In this study the coronal and sagittal sutures of swine were quantitatively analyzed using X-ray μCT *imaging techniques. Geometric models of coronal suture were then generated using 2D and 3D representations. FE methods were used to analyze the mechanical implications of the geometric suture representations under simple loading conditions. This chapter addressed the first objective of the thesis, by developing a method of quantitatively analyzing suture morphometry through the skull thickness and providing quantitative 3D morphometric pilot data. This chapter also addressed the second objective of this thesis, exploring mechanical effects of 2D/3D geometric assumptions of sutures by comparative finite element analysis.*

3.1 Introduction

Cranial sutures are soft connective tissues that join skull bones and play a crucial role in skull development[1,12,32]. Sutures act as a growth site for skull bones during development, and provide the skull with flexibility, and load dampening[2]. They are composed primarily of collagen fibers, extracellular matrix, and vasculature connecting adjacent skull bones[2]. The major cellular types in sutures that regulate bone and fiber populations are osteogenic and fibroblastic respectively[36]. These populations include specific cells responsible for constantly forming and adapting bone and fibers[36], which results in an everchanging suture composition. As such, the mechanical properties of sutures are anisotropic and viscoelastic in

nature[109,110,113,116]. Cranial sutures adapt to their mechanical environment and facilitate bone remodelling and growth to various geometric forms depending on their location in the skull and the magnitude and vectors of loading that they experience[2,3]. Cranial suture morphometry can range from a simple butt-ended structure where adjacent bones are joined with a mostly straight suture, to an interdigitated structure where adjacent bones are joined and sometimes overlapped and interlocked with a highly irregular 3DV serpentine suture between them[5].

Generating models that describe the response of cranial sutures to mechanical loading has proven challenging due to their geometry and mechanical properties, which vary with age and loading[43]. Generating such models could be useful to guide the treatment of pathological conditions of cranial suture growth that can lead to abnormal head shapes and the risk of deleterious increases in intracranial pressure. Birth defects such as craniosynostosis (premature ossification of cranial sutures) result in abnormal development of the skull. Severe cases of abnormal development are often treated with invasive surgery on young patients with varying results[18]. These interventions could be improved by developing a better understanding of the local mechanical loads on a case-by-case basis to promote suture expansion in specific regions. Gaining insight into these local loads to aid in surgical interventions will require improvements to the accuracy of the modelling techniques that are currently described.

Mathematical models interested in predicting suture development or response to applied loading are typically interested in suture and skull morphology and morphological development. Models for suture morphology have been developed that are interested in relating suture growth to structure and function[123], as well as predicting suture width maintenance and interdigitation formation[124]. These mathematical models are bidirectional and predict the suture structure in a planar form, typically how it would be seen in a from the ectocranial surface. This planar representation does not account for potential variability of morphological form

through the skull thickness. Models that predict full skull development and response to applied loading are typically developed utilizing X-ray μCT imaging and landmarking methods to provide data[125,126]. Although skull development models are 3D in nature, the representation of suture areas typically is extracted from discrete ectocranial landmarks that simplify the suture structure to what is seen on the planar skull surface[125,126]. Models interested in suture and skull development could benefit from 3D suture analysis techniques that provide information of suture formation through the thickness of the skull rather than exclusively on the surface.

Extracting quantifiable information describing suture geometry has been handled in various ways in the literature. One approach uses the geometry visible on the external skull surface or through a single plane of the suture and surrounding bone (e.g. through histology)[6,8]. The characteristics of the suture found on the cross-section plane or skull surface are then used to describe the suture complexity. These methods simplify the 3D complexity of the suture structure to a 2D outline of a single plane. A common method of quantifying the complexity of sutures is by determining its LII. LII is a metric that summarises the complexity of a suture plane and is calculated by dividing the path length of the suture by the linear length between the ends of the suture path region of interest, as shown by equation (1) and Figure 2. It is often used in the literature as a parameter to correlate anatomy with mechanical properties or create computer models representing suture mechanics[6–10,79,86,88,89,127]. However, using LII in this manner limits representation of the suture geometry to a single plane of skull thickness assuming a 2D structure. For highly interdigitated sutures this assumption may not be truly representative and is the primary research question to be considered in this study.

Previous experimental work measuring suture mechanical properties has been correlated to the LII of sutures. Three-point bending tests have been used to estimate the flexural strength of the zygomaticotemporal, frontozygomatic, coronal, and sagittal sutures of humans[8], as well as the bending strength and energy absorption

of the internasal and frontoparietal sutures of goats[6]. Tensile suture loading has been used to link suture mechanics to interdigitation levels, and suture LII[86]. These ex vivo experimental data provide insight into how sutures respond to applied loading and help with generating the framework for developing material models but has limitations. The complex in vivo anatomical loads are simplified to bending, compressive, tensile, or cyclic loading conditions, and only the bulk response of the suture is captured.

Suture mechanics have been modelled using finite element methods, often using the LII as the parameter modified for altering suture complexity. Suture paths are commonly modelled with a serpentine pattern using constant wavelength, amplitude, and suture width, typically with changing wavelength for differing interdigitation[8–10,89]. There has been finite element work that incorporated randomness of amplitude and wavelength using constant suture width; in this model, random computer-generated numbers were used to create an irregular sinusoidal suture path that was two dimensional[88]. Simulating suture mechanics using the finite element method can be helpful in determining mechanical response to applied loading and provides high resolution, multidimensional information. Although useful, simulating the mechanical response of sutures using the finite element method also has weaknesses. Simulations are only as good as the input data and assumptions made. Simplifying material properties, composition, anatomical loads, suture connectivity to bone, boundary conditions, and geometry all limit the ability of finite element analysis in predicting mechanical response to applied loading.

Using LII to describe the complexity of a suture requires simplification to a 2D structure and assumes negligible variance in suture form through the thickness of the skull. Differing levels of LII on the transverse plane of sutures through the skull thickness from the ectocranial surface to the endocranial surface has been noted in literature qualitatively for the coronal and frontozygomatic sutures of humans[7]. Varying levels of interdigitation have also been noted in the coronal suture of humans

where finite element analysis was performed but stress results were only shown on a single 2D bone face and values of LII were not reported for the ectocranial and endocranial sides[8]. Varying levels of interdigitation have also been found in the midpalatal suture of swine along the rostro-caudal direction[76]. The variability of suture complexity within a single suture indicates that using a single 2D plane to describe suture complexity may not be adequate.

Our study hypothesis was, for cranial sutures exhibiting high 3D spatial variability, a 2D simplification assumption does not representatively display the true 3D morphological form. The corollary of our hypothesis would be that a 2D simplification does not represent the 3D geometry of a suture and will limit the ability to predict the true 3D morphological form. We posit that local stresses and strains thought to influence growth of sutures[1,59] and mechanically induced biological responses may be overlooked in highly complex sutures that are analyzed using this assumption. This work focuses on advancing the geometric attributes of suture modelling by utilizing quantitative image analysis and the finite element method. Trends in the suture's geometric parameters through the thickness of the skull from ectocranial to endocranial surfaces were analyzed using micro computed tomography (μCT) data to determine if a single 2D measure can represent the 3D morphometry through the thickness of the skull. Subsequently, the effect of 2D geometry simplifications on the mechanics of sutures was investigated using a comparative finite element method. The goal of the comparative work is to gain insight into the structure of interdigitated sutures and how 2D geometric assumptions influence the mechanics of a highly interdigitated suture.

3.2 Materials and Methods

3.2.1 Image Processing and Analysis

Skull samples containing coronal and sagittal sutures were obtained from two female farm bred swine approximately 5 months old. The animals had been used in

unrelated work at University of Washington, where all procedures concerning animal ethics were approved by University of Washington Animal Care and Use Committee. The samples were scanned at 9 µm nominal resolution with 74 kV source voltage, 129 µA source current, and 0.5° rotational steps using a Skyscan 1076 µCT (Bruker-SkyScan, Kontich, Belgium). Raw image projections were Gaussian filtered and reconstructed using a modified Feldkamp back projection algorithm bundled with the imager software (NRecon, version 1.7.0.4, Bruker-Skyscan). Samples 1 and 2 had thicknesses of 2.66mm and 1.77mm respectively. Eleven evenly spaced reconstructed slices at 10% increments through the skull thickness were selected for image analysis. The eleven images from the planes at 10% increments were then imported to MATLAB R2020A (MathWorks, Natick, USA) where the image processing and segmentation was performed using a custom script developed for this application (Appendix A1, A2, A3, A4). A single slice of sample 1 coronal suture will be used to show the process and results that are generated at each thickness location.

Reconstructed µCT images were binarized to extract an isolated suture area suitable for quantitative analysis (Figure 7, Appendix A1). That process commenced with the raw image projection (Figure 7a), that was thresholded and reconstructed with cross-section to image conversion values set from 0.0 - 0.06 in the NRecon software. (Figure 7b). The image was then binarized (Figure 7c) and cropped to the region of interest (Figure 7d). The binarization and cropping allowed for the isolation of the suture (Figure 7e). The filtered image was then manually segmented along the suture (Figure 7f). This process was completed for the coronal and sagittal suture from both animals.

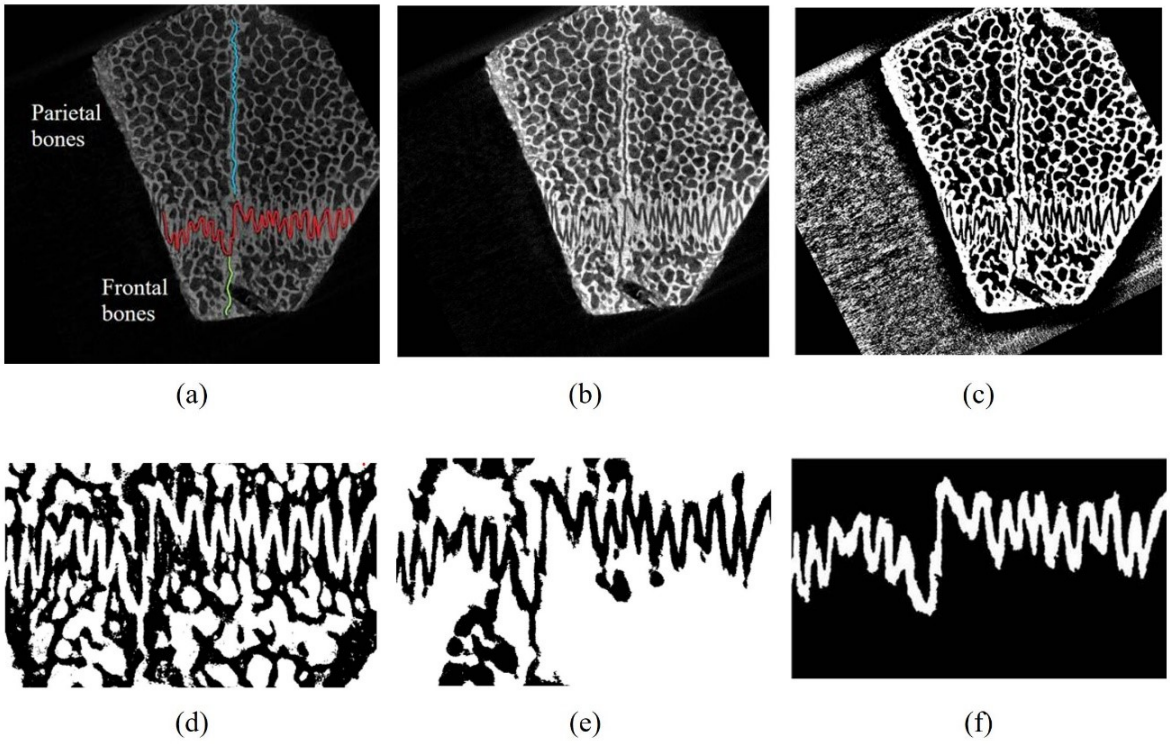

Figure 7 *Image processing of coronal suture, (a)-(c) show the entire sample, (d)-(f) show the cropped area; (a) Raw reconstructed μCT image, sagittal suture shown in blue, coronal in red, and interfrontal in green; (b) Contrast adjusted image; (c) Binarized image; (d) Cropped binarized image; (e) Area filtered image; (f) Final processed and segmented coronal suture*

After the processing and segmentation was completed, binary images of the sutures on each of the 11 planes through the skull thickness were then used for quantitative analysis of suture morphometry. Each image was analyzed using a custom MATLAB script that was generated for this application, and it used the top and bottom edges of the segmented sutures and smoothed those lines for analysis (Appendix A2, A3). The script used a method that started on the left side of the suture slice and traversed along the suture path measuring and storing local center point locations between bone surfaces and widths along the way. The script worked by taking a linear step of 3 pixels normal to the previous width's center point and scanning a 90° range with 1° angular steps to find the closest distance between the top and bottom smoothed curves that intersected the location of the linear step taken

normal to the previous width. Once the new local width was found, the center of the local width was determined, and the process was repeated from the new center point. A visualization of the script's functionality for a single slice section of the coronal suture of sample 1 can be seen in Figure 8.

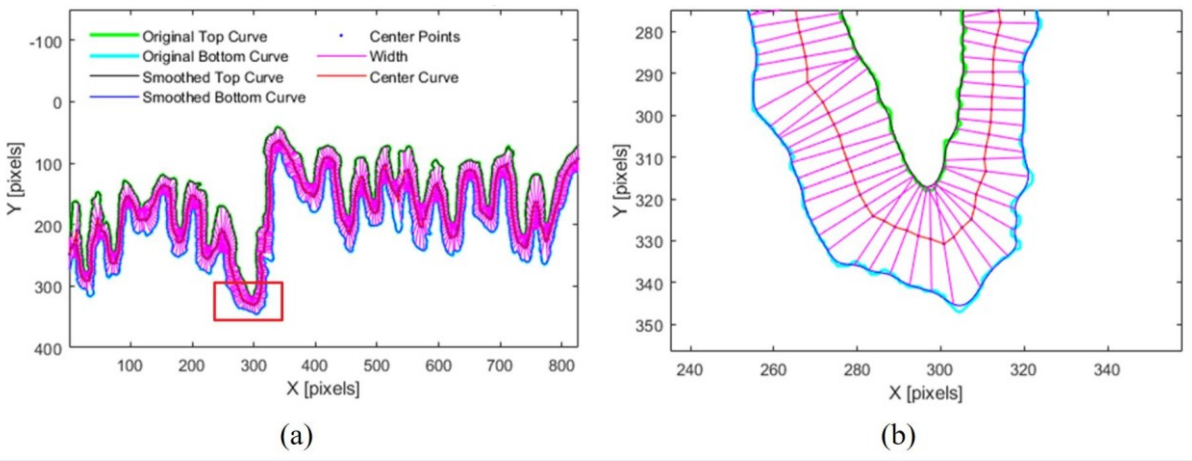

Figure 8 *Visualization of MATLAB script analysis; (a) Overall view of code function on single slice of coronal suture; (b) Detailed view of red box in Figure 8a*

3.2.2 Finite Element Analysis

To determine the mechanical implications of considering only the suture outline of a single plane when analyzing their structure, a comparative mechanical approach was used. The first step in this comparative analysis was obtaining the suture model geometries to compare. This was achieved by extracting information from the µCT scans to generate solid models with different levels of complexity. The suture geometries were analyzed in a simplified rectangular bone block section, as shown in Figure 9. Both the bone and suture material properties were simplified to have isotropic linear elastic properties. This required Young's modulus, E, and Poisson's ratio, ν, to be defined for the bone and suture. There is a large range of material properties for suture reported in literature, for instance Young's modulus has been reported ranging from 1.16 MPa – 610.3 MPa[9,79,87,115,128]. The largest values in literature were reported by Margulies & Thibault where a Young's modulus of 610.3 MPa was measured for suture-bone complex undergoing three-point-bending

at 2540 mm/min, 194.2 MPa for suture-bone complex undergoing three-point-bending at 25.4 mm/min, and 171.5 MPa for suture-bone complex under tension at 25.4 mm/min. The smallest values in literature were reported by Radhakrishnan & Mao, to be 1.16 MPa, they applied nano-indentation forces to suture where Young's modulus was calculated from individual force volume images according to the Hertz model. The larger values of Young's modulus found were reported from measuring suture-bone complex, giving a better indication of the material properties of the structure rather than solely the suture tissue. These large variations have the potential to affect the results of models and should be considered. An analysis including 5 values of suture Young's modulus, 1MPa, 6MPa, 15MPa, 100MPa, and 600MPa, was performed to ensure the relationship between models is consistent regardless of Young's modulus' magnitude. The general results presented use material property values set to the following for suture and bone, $E_{bone} = 2 \cdot 10^9\ Pa$, $E_{suture} = 6 \cdot 10^6\ Pa$, $\nu_{bone} = 0.27$, and $\nu_{suture} = 0.4$.

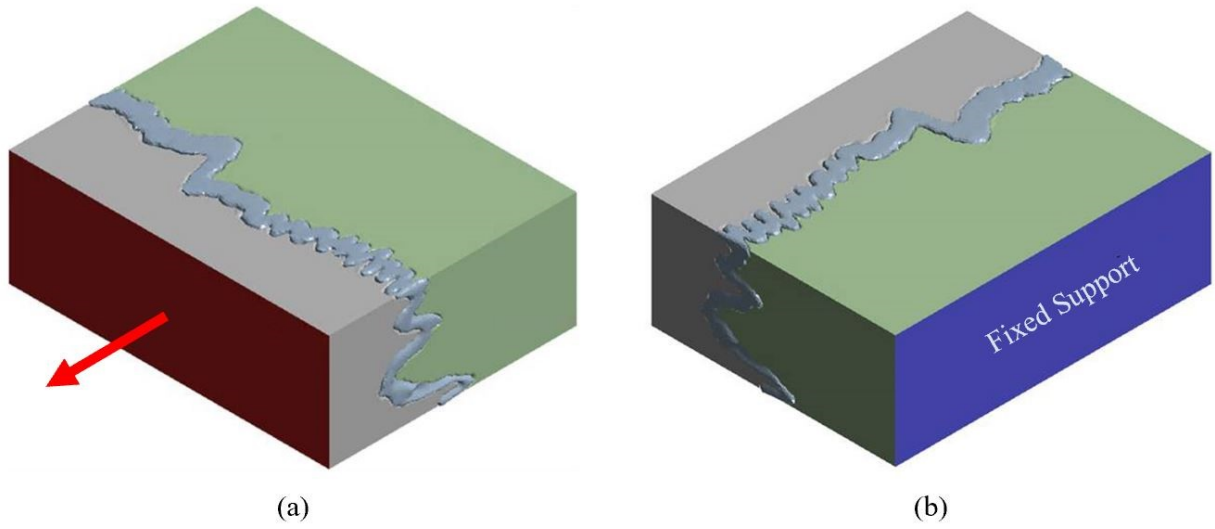

Figure 9 *Model boundary conditions, grey and green are apposing bone surfaces, light blue is sutural ligament. (a) Normal outward distributed load resulting in tension is applied on grey bone surface, red; (b) Fixed support is applied on green bone surface, blue*

The finite element method was implemented to compare the mechanical response of constant cross-section 2DV models based on the sections from the ectocranial, midplane, and endocranial regions to a 3DV model representing true geometry. The constant cross-section 2DV models represent a suture analyzed from a single transverse plane and the 3DV model represents a suture where the full geometry is considered. The three 2DV models were generated by extruding the suture outline geometry generated by isolating and binarizing the µCT scans at the ectocranial most, midplane, and endocranial most planes (Appendix B1). These models were generated in SolidWorks 2019 (Dassault Systemes, Velizy-Villacoublay, France) and the isolated suture, without the adjacent bone can be seen in Figure 10 b, c, and d respectively.

The 3DV model was generated using Mimics Innovation Suite 23 (Materialize NV, Leuven, Belgium) using the same dataset that the 2DV models were constructed with (Appendix B2). The full µCT dataset was imported to Mimics, and the scan was oriented and cropped to match the image analysis area used to generate the constant cross section models. The suture was then isolated in the bone complex within each slice of the µCT dataset. A mask for the suture was then created by filling the void between bone surfaces where the suture resides in each plane of the µCT dataset. Dilation and erosion morphological operations were performed on the suture mask, as it was in the 2D image analysis. Next, the processed suture mask was used to generate an initial surface of the suture. The surface was generated by lofting the suture mask profiles on each µCT plane to the adjacent suture mask to obtain a continuous surface. The reconstructed µCT slices used orthotropic voxels, therefore the distance between adjacent planes of the suture mask is equivalent to the scan resolution, 8.9 µm. This small distance between planes allowed for accurate model generation of the suture geometry through the thickness of the skull and can be seen in Figure 10a. A detailed walkthrough of the process can be seen in Appendix B2.

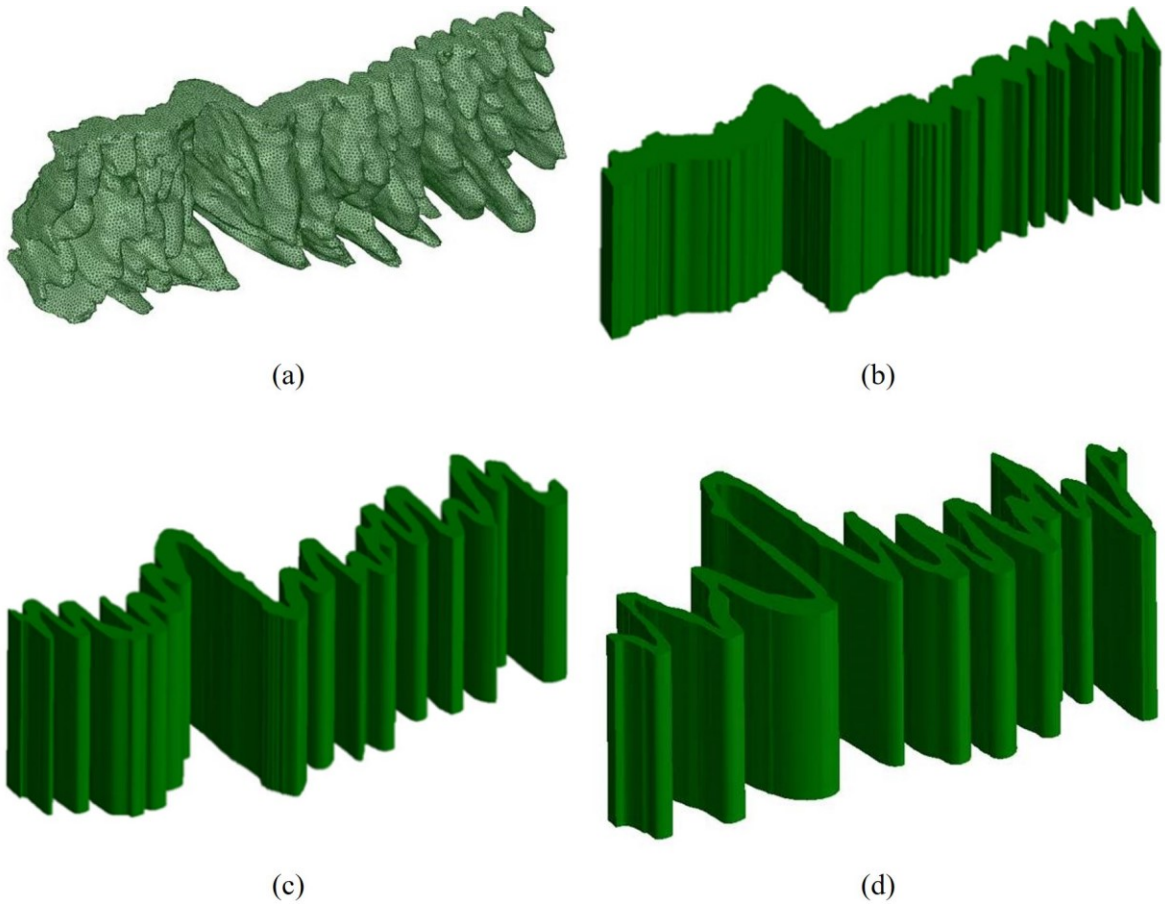

Figure 10 *Coronal suture models generated from Sample 1. (a) 3DV model; (b) 2DV ectocranial model; (c) 2DV midplane model; (d) 2DV endocranial model*

The 3DV suture model was then imported to SpaceClaim 2020 R2 (ANSYS, Canonsburg, USA) where the suture surface mesh was generated, and the bone was created by extruding a rectangular block that encompassed the suture geometry and subtracting the suture volume. This created face to face contact between the bone and the suture and ensured no voids. The model was then imported to Workbench 2020 R2 (ANSYS, Canonsburg, USA), where the mechanical analysis was performed in Mechanical 2020 R2 (ANSYS, Canonsburg, USA). A unit load of 1N converted to a uniformly applied distributed load resulting in suture tension was applied at one of the bone faces, as shown in Figure 9a. Sutures may be exposed to a wide range of loading regimes from low magnitude intracranial pressure to rapid high force impact loads; however, a static uniaxial tensile load was chosen in order to demonstrate the

different mechanics of the geometric assumptions, even with a simplified load. The loading magnitude of 1N was chosen as a unit force for these purposes, but has also been used in previous *in vivo* work studying sutural expansion [121]. The opposite bone face was defined with a fixed support, as shown in Figure 9b.

For the comparative analysis, the 3DV model was taken as the true result as it was based on the actual suture geometry. The mesh was generated using quadratic tetrahedron elements. The 3DV model was used for the mesh sensitivity analysis as the geometry is the most complex. Suture elements of sizes of 100 µm (265861 elements and 447516 nodes), 75 µm (499632 elements and 826350 nodes), 60 µm (839521 elements and 1359706 nodes), and 50 µm (1361742 elements and 2173586 nodes) were selected for the analysis (Appendix B3). The results among the varying mesh size models were compared at 5 locations that included nodes in a 100 µm edge length cuboid region of interest for mesh refinement. The results that were compared included the equivalent strain, maximum principal strain, and minimum principal strain. The average values at these points were compared and there was a relative difference of less than 3% for the refinement between the 60 µm model and 50 µm model. The 50 µm model was chosen and the results were converged and stable.

Finite element results were considered to analyze the implications that 2DV vs. 3DV geometric model assumptions have for mechanical response. The loaded bone face deformation was of interest in this study to compare the average and extreme deformation values between models. The equivalent, as well as the maximum, middle, and minimum principal strains were also considered to gain insight into how these geometric model assumptions affect strain distribution as well as average and extreme values. Because of the simplified loading conditions, the absolute strain and displacement values are not considered important, rather the relative difference of the 2DV models to the 3DV model was of interest. Positive relative difference values correspond to values of 2DV models that are larger than those found in the 3DV model. Negative relative difference values correspond to values in the 2DV models

that are smaller than those found in the 3DV model. The relative difference of the 2DV from the 3DV model was calculated using equation (2).

$$R.D. = \frac{\delta_{2DV} - \delta_{3DV}}{\delta_{3DV}} \cdot 100\% \qquad (2)$$

3.3 Results

3.3.1 Image Analysis

The variation in LII through the sample thickness can be seen in Figure 11a. For both individuals there is a trend of increasing LII from the ectocranial surface to the endocranial surface for the highly interdigitated coronal sutures, whereas the butt-ended sagittal sutures are relatively unchanged through the skull thickness. The approximately linear variation in average suture width through the skull thickness can be seen in Figure 11b. The interdigitated coronal suture shows a continuous variation through skull thickness, where the butt-ended sagittal suture is relatively unchanged through the thickness. For the coronal suture, the average width takes the opposite trend from LII, where the suture average width is higher in the more butt-ended ectocranial region of the suture, and lower in the more interdigitated endocranial region. The distribution through the thickness of the skull appears to be fairly linear for the coronal, and quite constant for the sagittal.

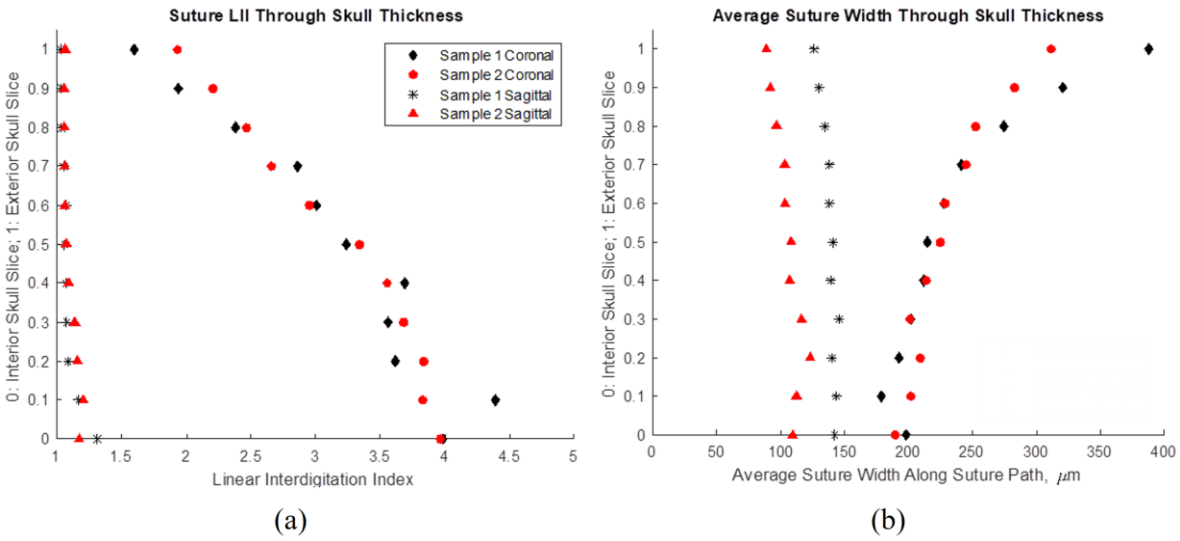

Figure 11 *Suture properties through thickness. (a) Linear interdigitation index through skull thickness. (b) Average suture width through skull thickness*

The suture width was calculated at each center point. The widths were stored and the average width value for each μCT section was found by taking the average value of the widths along the suture path. An example of the suture width distribution along the suture path for the same suture section shown in the methods section can be seen in Figure 12. In interdigitated regions the local sutural width increases at locations where the sutures path changes direction.

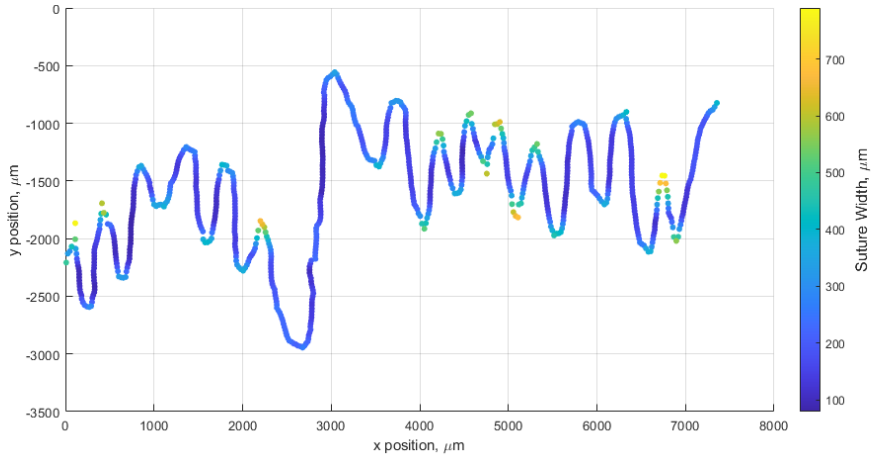

Figure 12 *Suture width along the suture lateral-medial length, colormap of variations in coronal suture width along suture lateral-medial path on a single transverse section plane*

A visualization of how the suture path changes through the skull thickness can be seen in the 3D figures that illustrate how the suture traverses through the skull thickness in Figure 13. The more interdigitated coronal suture centerlines appear to amplify and shift as position changes through the thickness. The less interdigitated sagittal sutures show consistency in centerline form through the thickness.

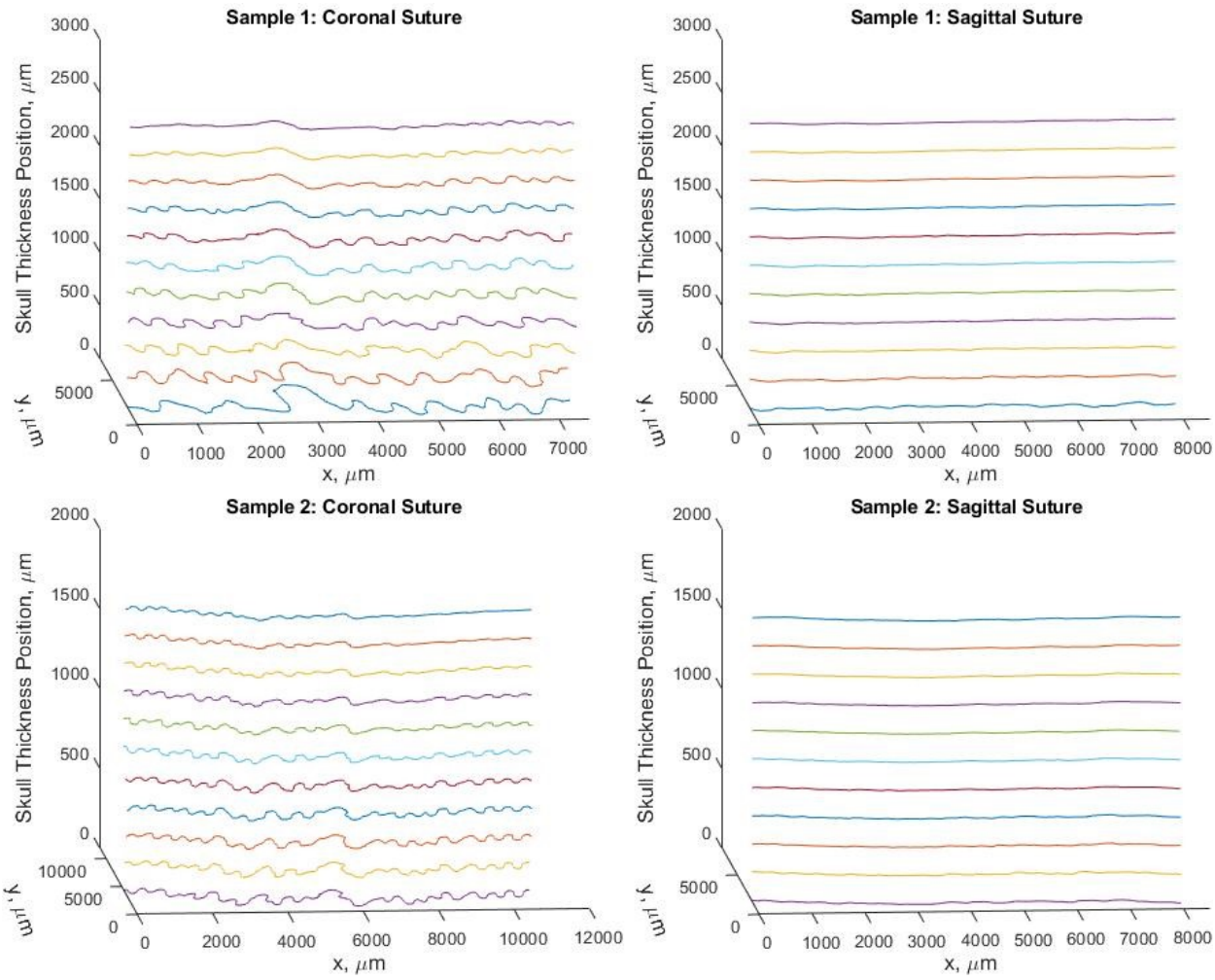

Figure 13 *Suture center line paths through skull thickness, measurement datum on the y-axis is the endocranial region of the dataset*

3.3.2 Finite Element Analysis

The suture volumes for each of the models are comparable and are summarised in Table 1. The similarity in suture volume reduces the likelihood that variations in

results are due to a variable amount of compliant suture material in the different models rather than geometric differences. The suture model that varied the most was the endocranial 2DV model.

Table 1 *Suture model volumes*

Suture Model	Suture Volume, μm³
3DV	1.17 e+10
Endocranial 2DV	1.40 e+10
Mid-plane 2DV	1.13 e+10
Ectocranial 2DV	1.10 e+10

Material property dependency was analyzed by running FE on each geometric model five times, once for each value of Young's modulus intially considered. The overall qualitative trends and relationships between the 2DV and 3DV model results were found to be similar between the different material properties, despite the magnitudes of deformation and strain decreasing with increasing Young's modulus. The equivalent strain results of each model with varying material properties is shown in Figure 14 (Appendix B4).

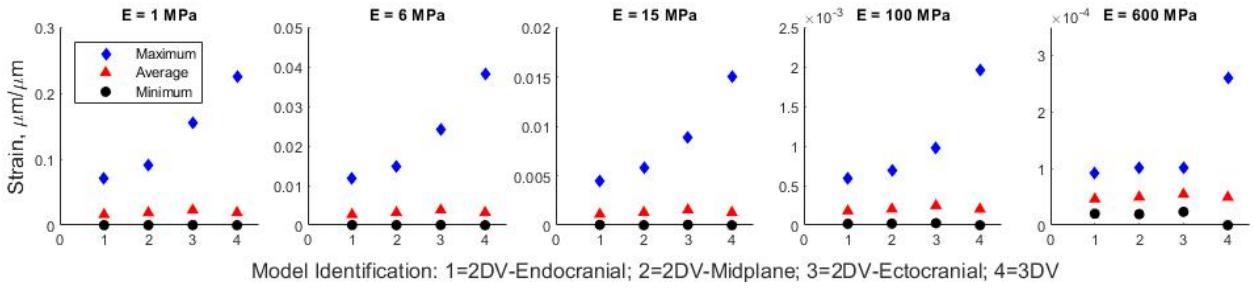

Figure 14 *Equivalent strain, material refinement results*

3.3.2.1 Loaded Bone Face Deformation

The deformation of the bone face that the evenly distributed load was applied to (shown in red in Figure 9a) was analyzed to gain insight into how the different

suture models deform under loading. There were some notable differences in the model results, the deformation ranges, and the deformation gradient. The results of the minimum, average and maximum deformation for each model can be seen in Figure 15. The 3D model had the largest range between the minimum and maximum deformations on the loaded bone face. The maximum relative difference in average deformation from the 3DV model was found in the ectocranial 2DV model with a relative difference of 56.5%, followed by the endocranial 2DV model with a relative difference of -28.2%, the closest average value was found using the midplane 2DV model where the relative difference was found to be -19.9% from the 3DV model.

The deformation gradient direction and magnitude differed between the 2DV and 3DV models. The loaded bone face deformation gradient in the 3DV model (Figure 15a) was in the endocranial-ectocranial direction, orthogonal to the lateral-medial gradient found in the ectocranial 2DV model (Figure 15b). The mid-plane 2DV and endocranial 2DV models had more uniform responses, having relatively constant deformation across the entire loaded bone shown in Figure 15c and Figure 15d respectively.

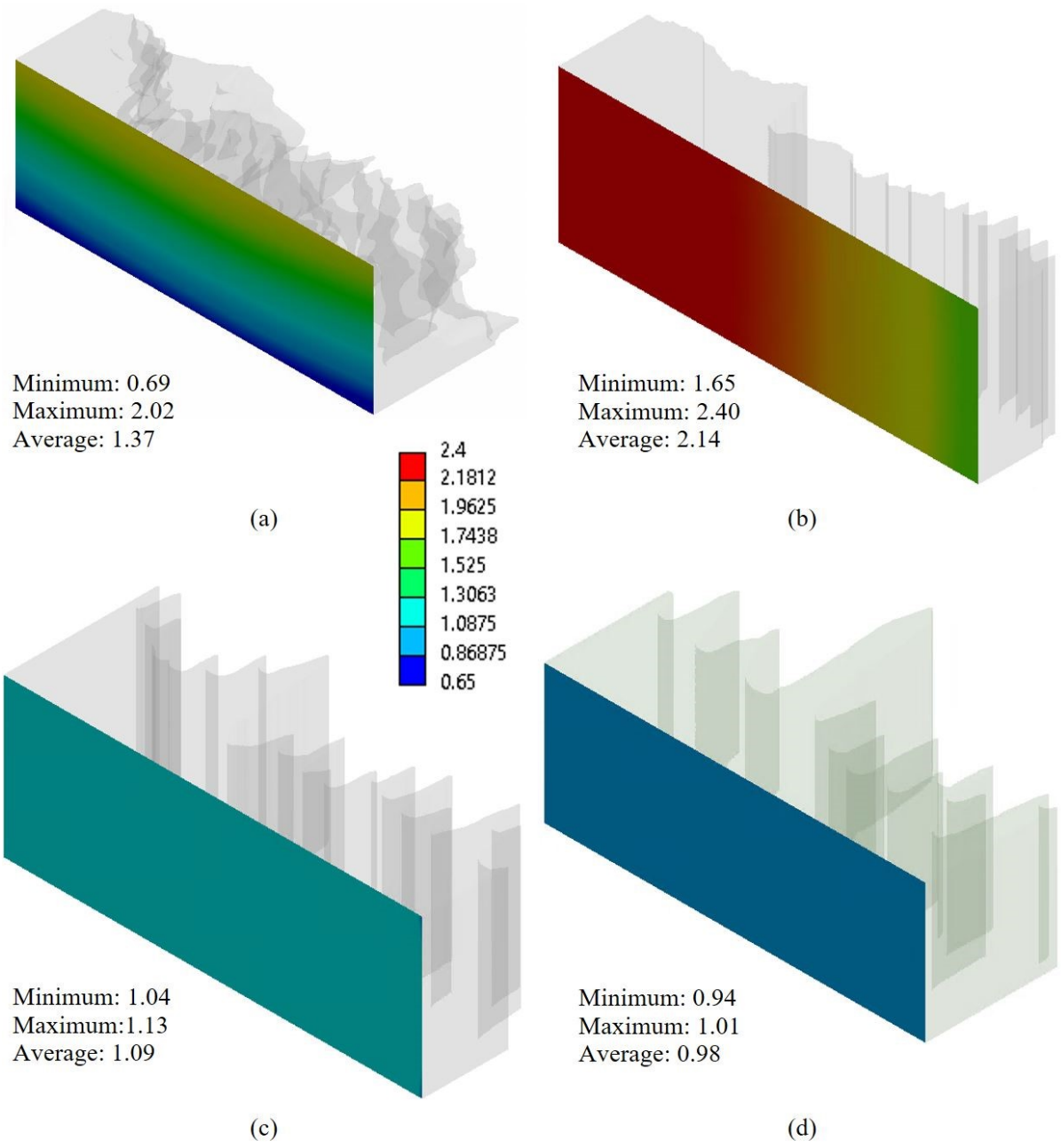

Figure 15 *Finite element deformation results at loaded bone face in the direction of the applied distributed load, using a suture elastic modulus of 6 MPa. (a) 3DV model, (b) 2DV ectocranial model, (c) 2DV mid-plane model, (d) 2DV endocranial model*

3.3.2.2 Suture Strain

The equivalent, maximum principal, middle principal, and minimum principal strains within the suture material were analyzed in this study. Due to the linear elastic material properties chosen for this model, the strain and stress results were correlated and only the strain results are presented to avoid redundancy. In the comparison of strain for the 2DV models and the 3DV model, the 3DV model will be taken as the control as it most closely represents the true morphological form of the suture. The relative difference of 2DV model response to the 3DV model can be seen in Table 2.

The equivalent strain relative difference results show minimum equivalent strain values were orders of magnitude larger in the 2DV models than the 3DV model. Maximum equivalent strain values were consistently lower in the 2DV models compared with the 3DV model. Average equivalent strain values were found to be smaller than 3DV model values for the highly interdigitated endocranial 2DV model, very similar to 3DV model results in the moderately interdigitated midplane 2DV model, and larger in the less interdigitated ectocranial 2DV model. (Table 2 and Figure 16)

Minimum values of maximum principal strain were found to be lower than 3DV results in the highly interdigitated endocranial 2DV model and less interdigitated ectocranial 2DV model, but fairly close in the 2DV midplane model. Maximum values of maximum principal strain for 2DV models were consistently lower than 3DV results. Average values of maximum principal strain showed a similar trend to that found in the average equivalent strain results. (Table 2 and Figure 16)

For the minimum and maximum values of middle principal strain the 2DV model results were all lower than was determined for the 3DV model. The average values for middle principal strain were lower than the 3DV results in the highly

interdigitated endocranial 2DV and moderately interdigitated midplane 2DV models, and slightly larger in the less interdigitated ectocranial 2DV model. (Table 2 and Figure 16)

Similar to the minimum and maximum values of middle principal strain, the minimum and maximum 2DV model values found for the minimum principal strain were all lower than the 3DV model results. The average minimum principal strain was lower for the 2DV endocranial and ectocranial models, and very similar to the 3DV model results for the midplane 2DV model. (Table 2 and Figure 16)

Table 2 *Relative differences for suture strain values of 2DV model responses to 3DV model response (6 MPa suture elastic modulus)*

		Suture Models		
		Endocranial	Midplane	Ectocranial
Equivalent Strain RD (%)	Minimum	13051.7%	8218.3%	16540.6%
	Maximum	-69.1%	-61.2%	-36.5%
	Average	-15.7%	0.2%	20.5%
Maximum Principal Strain RD (%)	Minimum	-388.1%	30.3%	-794.9%
	Maximum	-68.3%	-60.3%	-34.8%
	Average	-17.1%	1.5%	37.0%
Middle Principal Strain RD (%)	Minimum	-65.3%	-55.7%	-31.0%
	Maximum	-87.2%	-81.8%	-59.9%
	Average	-42.2%	-24.0%	6.1%
Minimum Principal Strain RD (%)	Minimum	-66.0%	-62.5%	-40.5%
	Maximum	-70.5%	-53.7%	-10.6%
	Average	-7.6%	0.8%	-19.6%

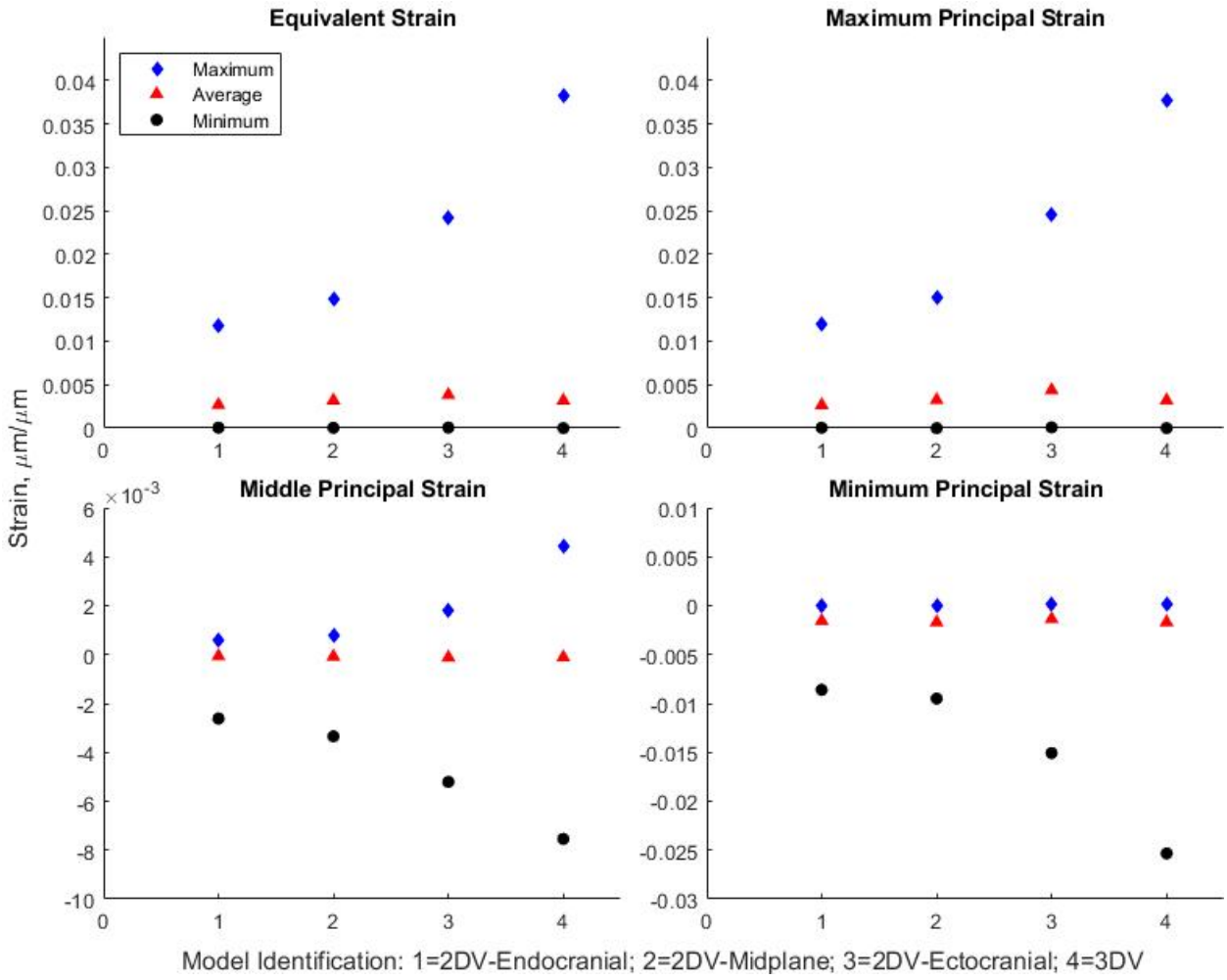

Figure 16 *Suture strain results for different suture models of sample 1 coronal sutures (6 MPa suture elastic modulus)*

The finite element results showed some key differences between the 2DV models and the 3DV model. The main difference seen was the lack of variability in strain distribution through the thickness of the 2DV models due to their constant geometry through the skull thickness. This caused the results to look like vertical bands of strain with little differences in strain values through the thickness of the suture. The suture models and corresponding strain on the suture-bone interface can be seen in Figure 17.

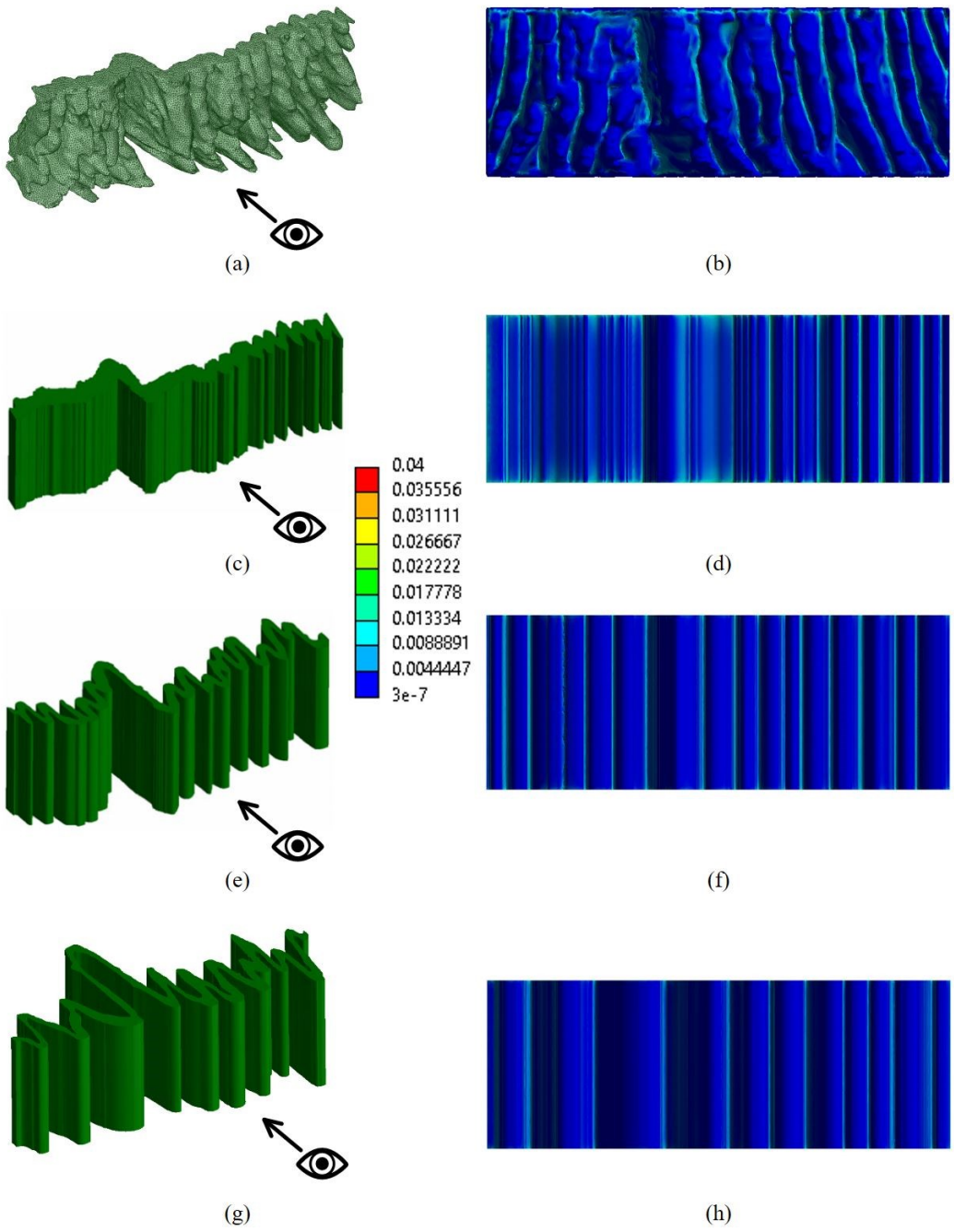

Figure 17 *Suture geometry and corresponding equivalent suture strain on the suture at the bone-suture interface FE results beside each geometry, eye shows the orientation that the finite element results are viewed (6 MPa suture elastic modulus); (a) 3DV geometry; (b) 3DV equivalent strain result; (c) 2DV ectocranial geometry; (d) 2DV ectocranial strain result; (e) 2DV midplane model geometry; (f) 2DV midplane model equivalent strain result; (g) 2DV endocranial geometry; (h) 2DV endocranial model equivalent strain result*

3.4 Discussion

Modelling the mechanics and geometry of cranial sutures is challenging given their complex tortuous geometry and their inhomogeneous and anisotropic structure. This study was interested in whether the simplification to a 2D geometry that is commonly practiced in the modelling and study of cranial sutures is appropriate[8–10,38,89,114]. 2D simplification defines a suture's geometry by a single plane of the suture, acquired from either the ectocranial surface[6], a CT section[86], or a histological slice[3]. Quantitative image analysis was used to describe cranial suture linear interdigitation through the thickness of the skull, and finite element methods compared the mechanical results of three segmented 2DV geometries of a coronal suture based on different locations in the skull thickness and a fully segmented 3DV model that captured the geometry throughout the thickness. Given the primary overall objective of this work to elucidate how 2D geometric assumptions can differ from the true 3D suture geometry, only the more interdigitated coronal suture was considered for mechanical analysis. Considering the high level of interdigitation and through-skull variation of the coronal samples compared with the sagittal, it is anticipated that any notable differences in mechanical response would manifest when studying the more complex structure, and thus only the coronal geometry was considered.

The variable nature of the analyzed coronal suture cross section through the thickness of the skull has been observed qualitatively[7,8], however implications of the variable form through thickness on mechanics have not been investigated and documented quantitatively using representative geometries. Having a quantitative measure of 3D variability within a suture better elucidates how much variation may be expected when proposing a 2D simplification of the suture compared to its true 3D geometry. The results of the image analysis illustrate the 3D structure of interdigitated sutures, which challenges the use of generic 2D suture representations. Researchers interested in relating interdigitation levels to other

parameters of interest need be aware of the variable levels of interdigitation through the skull thickness and take measures to analyze the suture using its full form.

For each of the outcomes discussed in the FEA results, there is a consistent relationship between the 3DV model and the 2DV models. In each case, the 3DV average value lies within the range of average values that were found from the 2DV models. A consistent difference that is seen in the 3DV model is the increased range of values between the minimum and maximum values found for each result compared with the 2DV models. The relationships between 2DV and 3DV models were supported in the material refinement, where the material properties ranging multiple orders of magnitude were analyzed with similar relationships between the model complexities. This is not necessarily a surprising result due to the increased complexity of the 3DV model geometry, where the increased geometric complexity drives a more variable response of the suture, generating larger maximums and smaller minimums than the more uniformly responding 2DV models. From the results of this study, a 2DV model could be viable if average results are of interest.

Of the three 2DV models, the midplane model produced the closest results to the 3DV models. This makes sense when comparing the coronal suture model that has a fairly linear distribution of LII through the thickness, the midplane model balances the results of the 3D results the best of the 2DV models through the continuous structure. This was also shown with its more consistent relationship to the 3DV model through the range of material properties analyzed, with 2.1% deformation R.D. and 1.5% equivalent strain R.D. variability across the range of material properties analyzed. This shows more consistent deformation and equivalent strain to the 3DV model across the range of material properties than the endocranial model where R.D. values of 36.7% and 22.1% were found for the deformation and equivalent strain respectively, or the ectocranial model where ranges of 104.2% and 9.9% were found, respectively. However, it cannot be said that the linear LII trend through the thickness for all interdigitated sutures as only 2

coronal suture samples were analyzed. Trends of LII through skull thickness should be explored before making assumptions on a plane used to create a 2DV model.

From the results of the image and finite element analysis it can confidently be said that considering a cranial suture as a 2DV structure affects the results obtained from simulations considering mechanical loading. Researchers considering sutures as 2D structures may be able to justify treating them as such based on their topic of interest. If a researcher is interested in bulk properties such as average displacement, strain, or stress, a 2D model could be a suitable fit. The vastly decreased time and resources required to create a 2DV model, and the fact that the average values found in this study are comparable between the models gives the 2DV models the edge in this case. If a researcher is interested in the distribution of stress and strain and mechanical links to suture adaptation, then a 3DV model would be a more suitable choice. This is due to the increased range of values found in the 3DV model, as well as the more complex distributions along the bone-suture interface. This finite element study does have several limitations from being anatomically and mechanically identical to an in-vivo swine coronal suture. The geometry of the bone block that houses the suture creates a solid rectangular structure, which is simplified from the true irregular geometry and heterogeneity of bone. The loading magnitude and conditions are simplified, the suture is in pure tension rather than the complex combined loading from muscle activation, intracranial pressure, and external applied forces. Investigating a range of dynamic and quasi-static loading conditions/magnitudes could be considered in future works, with appropriate associated assumptions for material models (e.g., incorporating suture viscoelasticity when studying rapid load application through impact), to better understand their influence on suture geometric assumptions. The material properties of the model are isotropic linear elastic, whereas an anisotropic nonlinear viscoelastic model would more accurately describe the material properties[109,110,113], our approach neglects transient and time dependent effects. However, mechanical response of varying geometric complexities was the primary objective of the study. This was captured by

only varying suture geometry between the 2DV and 3DV models and keeping boundary conditions, loading, and material properties consistent.

3.5 Conclusions

The results of the image analysis show consistency through the skull in the butt-ended sagittal sutures but illustrate the variability in interdigitation and suture width through the thickness of the skull in the highly interdigitated coronal sutures. The finite element results showed that the average values of stress/strain were similar among all the models, where the 2DV midplane model showed variations of 0.2% to -24.0% from the 3DV model. The key difference in results between the 2DV and 3DV models were the maximum and minimum values, which were more extreme in the 3DV model. This was shown by the variations in the 2DV midplane model minimum parameter values which were found from 30.3% to 8218.3%, and maximum parameter values ranged from -53.7% to -81.8%. Researchers interested in studying cranial sutures using finite element methods should consider morphological variability throughout the structure which could affect their results. If the average values for mechanical response to applied loading are of interest and the distribution of mechanical response is not, a 2DV model utilizing the midplane geometry can be appropriate. If the researcher is interested in the distribution of parameters along the suture bone interface or a more complete understanding of suture response is desired, a 3DV suture model may be required.

Chapter 4: 3D Age Based Rat Morphology Analysis

A version of the following chapter is under preparation for submission to a peer-reviewed journal at a later date. The first author of this manuscript is also the author of this thesis. This chapter contains a study where 3D cranial suture morphology was analyzed in three age groups of rats. The results are qualitatively and quantitatively compared and contrasted. This chapter addressed the first objective of the thesis, by refining the methods presented in Chapter 3 in order to semi-automatically analyze full datasets, this improves the efficiency of this method for quantitatively analyzing suture morphometry through the skull thickness. This chapter also addresses the third objective of the thesis, studying 3D suture morphometry variability between individuals of the same and varying ages.

4.1 Introduction

Craniofacial sutures are a network of soft tissues that serve a crucial role in the development and mechanical environment of the skull[1,2], acting as a growth site[32] and strain sink[2]. Sutures are typically composed of extracellular matrix, fibers, and vasculature[2]; their structure connects and integrates them into adjacent bones. Sutures adapt at cellular[45,51], and, subsequently, morphological[3,65] levels based on the loads experienced in vivo. Morphological adaptations of sutures to applied loading has been noted in literature, where sutures that are compressed in vivo typically exhibit higher levels of interdigitation than sutures that are tensed[65,66]. Researchers who are interested in suture morphology typically are interested in exploring ex vivo properties of suture bone complexes[6,7,79], in vivo suture loads and loading conditions[3,82,84], in vivo suture morphological adaptations[2,58,59,93], developing and improving clinical applications[12–14,89], or generating numerical and analytical modelling techniques involving suture complexity and mechanics[8–10,88].

Suture morphology is typically analyzed with visual/photographic analysis[35,70,71], histology[44,50,59,76], and/or X-ray imaging modalities[5,38,66,76,78]. Skull

dissection and visual methods allows for morphological analysis of the endocranial and ectocranial surfaces of suture but is limited to the skull surfaces. Histological methods allow researchers to see the cellular populations at the location of the histological slice but are limited to planar information. X-ray modalities such as μCT can give information of sutures by a subtractive measure, assuming that the spaces between the bones on the scan is where the suture resides. μCT data provides 3D information for bulk suture morphometry, which is why it was chosen as the method for this study.

LII is a method for determining normalized planar suture complexity that has been used widely in literature[3,5,9,69,76]. Typically, LII is determined at a section plane, or from the endocranial or ectocranial surfaces of the skull. LII is determined by dividing the curved path length of the suture by the linear length between the ends of the region of interest (as shown in Figure 2). Although LII is commonly used to express levels of suture interdigitation, single plane expressions may not be a suitable way to convey the complexity of 3D spatially variable suture structures.

Many researchers have analyzed cranial suture morphology and composition using X-ray modalities[5,38,66,76,78]. The analysis is typically done in a quantitative or qualitative manner. For instance, Savoldi et al. were interested in craniofacial suture morphology of swine where they utilized μCT with 25 μm resolution in order to quantitatively analyze the sutures[5]. Their methods analyzed the middle most cross-sectional plane on both the perpendicular and parallel planes to the bone surface. Measures such as LII and width were analyzed, and results were grouped into facial, craniofacial, and cranial sutures[5]. Although this method noted bulk differences in morphometric features from varying parts of the skull, and the 3D form of sutures was acknowledged by analyzing orthogonal planes, it did not provide insight to the degree of variability that is seen through the thickness of the skull in a single location or compare morphometric features between individuals. In another instance, Khonsari et al. used synchrotron μCT with 5 μm resolution in order to qualitatively

investigate the structure of cranial sutures[78]. The analysis methods used were purely qualitative, noting progressive changes in interdigitation, uneven distributions of fibers and cells in the suture, and the presence of bone growth lines. Although these are interesting findings, quantifying their values would help other researchers find utility in these results. Although both quantitative and qualitative morphometric analysis has been performed with varying X-ray imaging modalities, studies interested in 3D suture morphometry are sparse in literature and work focused on generating robust 3D morphometric data within sutures is not present.

Cranial sutures are known to change with age, which is why it was a topic of interest in this study. Henderson et al. were interested in age dependent morphological and mechanical properties of sagittal sutures in rats[43]. The study was interested in morphometric features such as suture length, and width, as well as mechanics related to suture stiffness and in-vivo quasi static strain in rats aged 2 to 60 days[43]. They found that both geometric and mechanical properties are age dependent[43], however the analysis was conducted in a 2D manner, and didn't provide any systematic methods for determining morphometric properties.

Cranial sutures are known to be complex 3D structures that alter throughout life. There has been limited quantitative work focused on 3D morphology of cranial sutures or justifying 2D analysis simplifications despite variable levels of interdigitation at the endocranial and ectocranial skull surfaces being qualitatively noted in literature[7,8,70]. This work intends to provide insight to how suture structures vary through the skull thickness, and the degree that they vary in three age groups of rats. It is hypothesized that local and mean planar suture widths as well as planar LII will vary within and between the cranial sutures studied. This is hypothesized because sutures experience complex loading conditions and have been shown to morphologically respond to their mechanical environment. It has generally been shown sutures become more interdigitated in compression and straighter in tension. Bending has been shown to occur at suture sites[85], which could cause tension at one

surface and compression at the other, driving morphological variability through the skull thickness. It is also hypothesized that statistically significant differences in mean suture width and LII between age groups will be present. Bulk morphological properties of rat sutures have been shown to change throughout development, however the measurement techniques used to analyze their changes are simplified to local measurements on a single plane[43]. This work aims to improve measurement methods and consider 3D morphological properties in rats in order to advance suture complexity quantification and provide 3D data for suture modelling.

4.2 Materials and Methods

4.2.1 Data Manipulation

Sprague–Dawley strain rats were used for all data collected in this study. These animals were originally part of a study interested in evaluating osteoarthritis progression, where all animal procedures were carried out in full compliance with the standards of the animal care and use committee of the University of Alberta[129]. µCT scans were performed on 15 female rat carcasses euthanized at ages 16, 20, and 24 weeks. This age range was chosen due to the availability from the previous study as well as the sutures having distinct bone margins which is crucial for quantitatively analyzing the morphology of the suture space. An equal number of samples for each age group was analyzed, with n=5 for each age. The samples were scanned at 18 µm nominal resolutions with 90 kV source voltage, 278 µA source amperage, and 0.7° rotational steps using a Skyscan 1176 µCT (Bruker-SkyScan, Kontich, Belgium). The raw datasets were reconstructed using NRecon Version 1.6.3.3 (Bruker-SkyScan, Kontich, Belgium) where they were converted into orthotropic datasets. The cranial sutures of interest in this study are the coronal, sagittal, anterior lambdoid, and posterior lambdoid sutures, as shown on the 3D rendered skull in Figure 18 which was generated using reconstructed µCT data and CTVox Version 2.0 (Bruker-SkyScan, Kontich, Belgium). The regions that were studied are the right-hand side coronal (C RHS), left-hand side coronal (C LHS), sagittal (S), left-hand side anterior

lambdoid (AL LHS), right-hand side anterior lambdoid (AL RHS), and posterior lambdoid (PL) sutures, marked on Figure 18.

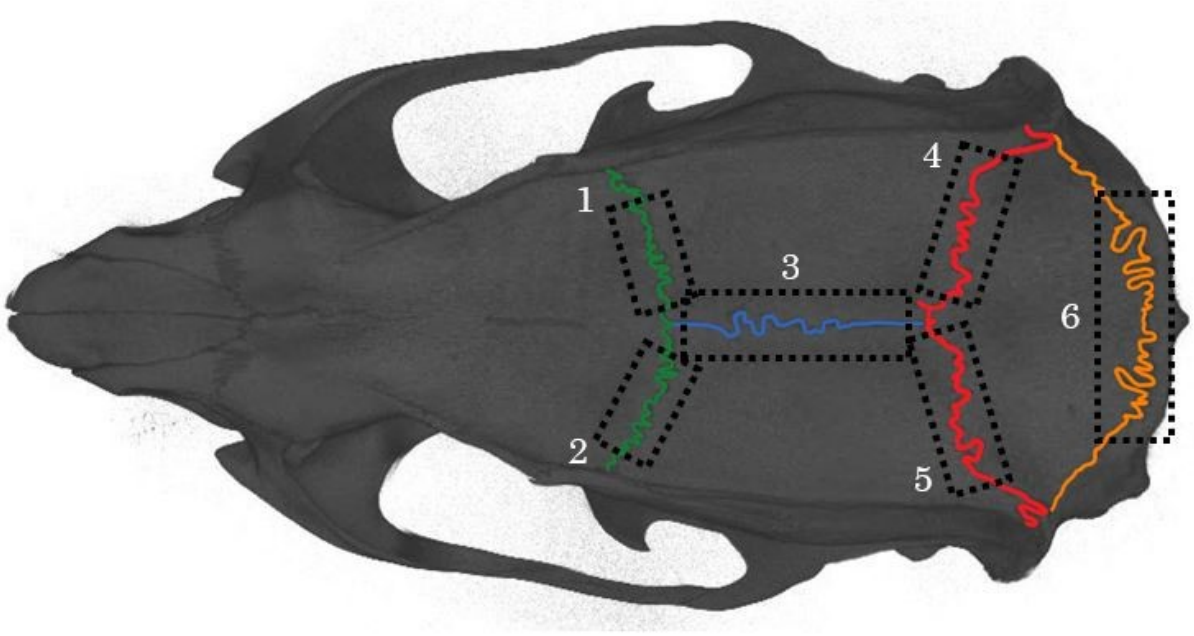

Figure 18 *Sutures of interest; coronal, green; sagittal, blue; anterior lambdoid, red; posterior lambdoid, orange. The approximate regions of interest are labeled as follows; 1, C RHS; 2, C LHS; 3, S; 4, A RHS; 5, A LHS; 6, PL*

The reconstructed datasets were imported to DataViewer Version 1.4.3.2 (Bruker-SkyScan, Kontich, Belgium). All the reconstructed files were rotated using DataViewer in the coronal, sagittal, and transaxial planes in order to orient the µCT dataset to be approximately orthogonal to the suture of interest as shown in Figure 19. The reoriented output datasets contain a discrete set of images that shows the skull cross section in the reoriented transaxial plane at 18 µm intervals through the entire dataset. Due to the curvature of the skull, a separate dataset was collected for the left and right portions of the coronal and anterior lambdoid sutures in order to obtain more data through the skull thickness. The Euler rotations applied to reorient the µCT data for each rat can be found in Table 16, Table 17 and Table 18 in Appendix C1.

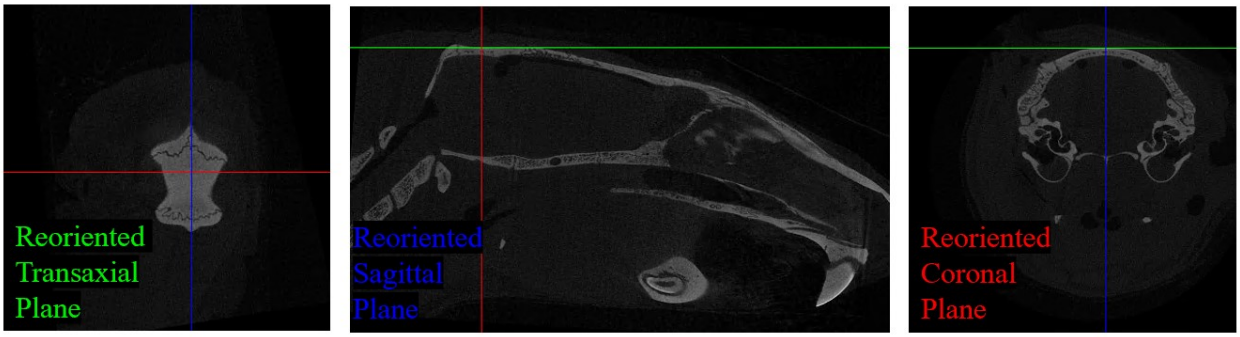

Figure 19 *DataViewer interface for reorienting datasets. A single plane of the output dataset for the posterior lambdoid suture is shown in the transaxial plane. The location of the transaxial image in this instance can be seen in the sagittal and coronal planes*

After the datasets were reoriented as described above, they were converted to a binary form where the suture of interest was isolated using a method developed using MATLAB R2020A (MathWorks, Natick, USA), (Appendix A3, A5, A6). The range of planes in the reoriented transaxial dataset that contained the suture of interest were noted, and then copied to the corresponding MATLAB image processing folder. The process is shown using a representative plane of a 24-week-old posterior lambdoid suture in Figure 20 to Figure 23. First, a suitable cropping region of interest was determined by manually ensuring the suture of interest was in frame in the ectocranial-most and endocranial-most planes of the dataset. Each image in the stack was processed using an automated systematic image processing method developed for this application, where consistent parameter values were used to ensure consistent processing results. The processing started by cropping the ectocranial-most image obtained from the reoriented transaxial dataset (Figure 19) to the cropped image shown in Figure 20a. The cropped image was then equalized to increase the dynamic range and contrast of the image (Figure 20b). The equalized image was then adjusted, where a consistent range of intensity values were used in order to further increase the contrast of the image (Figure 20c). Next, the adjusted image was binarized (Figure 20d) and stray pixels within the suture were filled (Figure 20e). The filled image was then inverted in order to use built in MATLAB

functions, then eroded and dilated using the same structuring element in order to smooth contours and eliminate thin protrusions from the suture outline while maintaining the outline size and shape (Figure 20f). Erosion and dilation are morphological operations that, respectively, remove and add pixels on the object boundary; when performed in succession this operation is typically called morphological opening, which is useful in removing small objects from an image (stray pixels) while preserving the size and shape of larger objects (the suture). The suture was then segmented, to ensure suture connectivity (Figure 20g) and extraneous information was removed (Figure 20h). An overlay of the isolated segmented suture outline (shown in Figure 20f) at 65% transparency on the cropped image (shown in Figure 20a) can be seen in Figure 20i. This process was repeated for each reoriented transaxial image by sequentially analyzing the 18 µm spaced images from ectocranial to endocranial ends of the dataset containing the suture of interest.

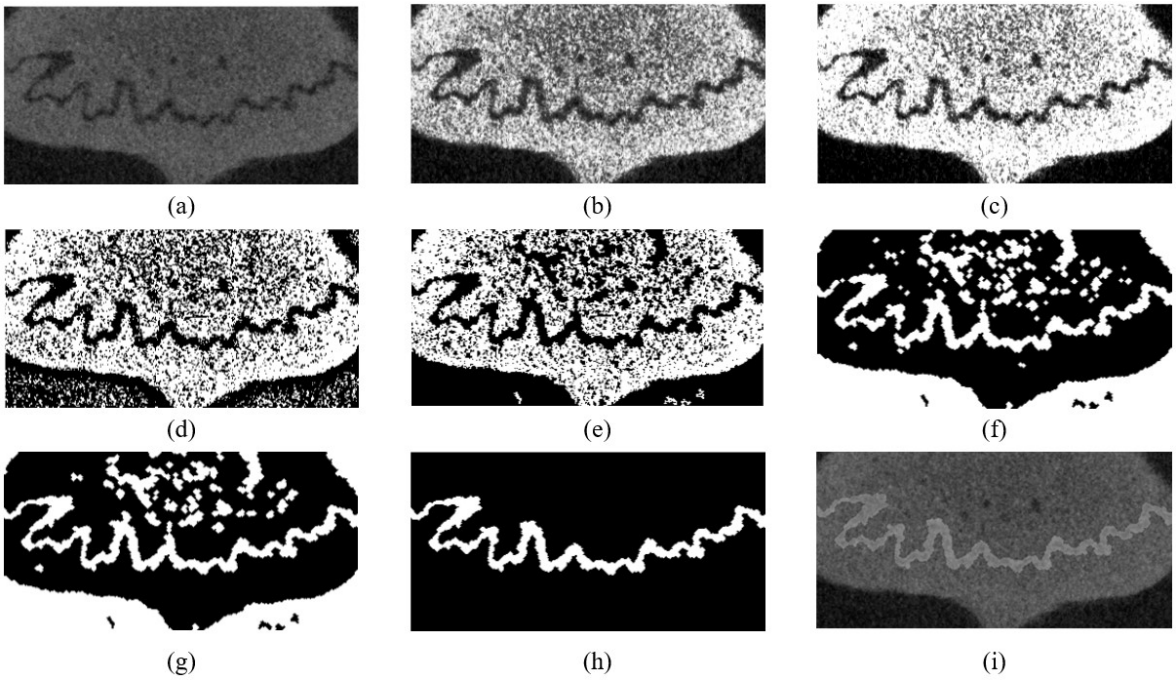

Figure 20 *Image processing of posterior lambdoid suture. (a) cropped image of reoriented scan; (b) histogram equalized; (c) adjusted; (d) binarized; (e) filled; (f) morphologically opened; (g) segmentation, black to white; (h) segmentation, white to black, final binary image; (i) isolated suture area (65% transparency) shown in (h) overlay on cropped image shown in (a).*

After the processing and segmentation was complete, the isolated binary suture outlines were available for quantitative analysis for each of the 18 µm spaced images through the skull thickness. Each image was analyzed using a custom MATLAB script that generated lines using the top and bottom edges of the binarized segmented sutures. The script used a method that started on the left side of the suture image and traversed along the suture path measuring and storing local center point locations and widths between bone surfaces along the way (Figure 21a and b). The script worked by taking a linear step of 1 pixel normal to the previous width's orientation from the width center point, then scanning a 90° range with 1° angular steps to find the closest distance between the top and bottom smoothed curves. The minimum distance between the top and bottom curve that intersected the location of the linear step taken normal to the previous width becomes the new local width. Once the new local width was found, the center of the local width was determined, and the process was repeated from the new center point. Once the entire suture was analyzed by this method, the center points were connected to create the suture path, where the length of this path is the suture length shown by the red centerline in Figure 21c. An overlay of the suture analysis result (Figure 21c) at 50% transparency on the cropped image (shown in Figure 20a) can be seen in Figure 21d. This analysis method was iterated for each of the image planes in the reoriented transaxial dataset.

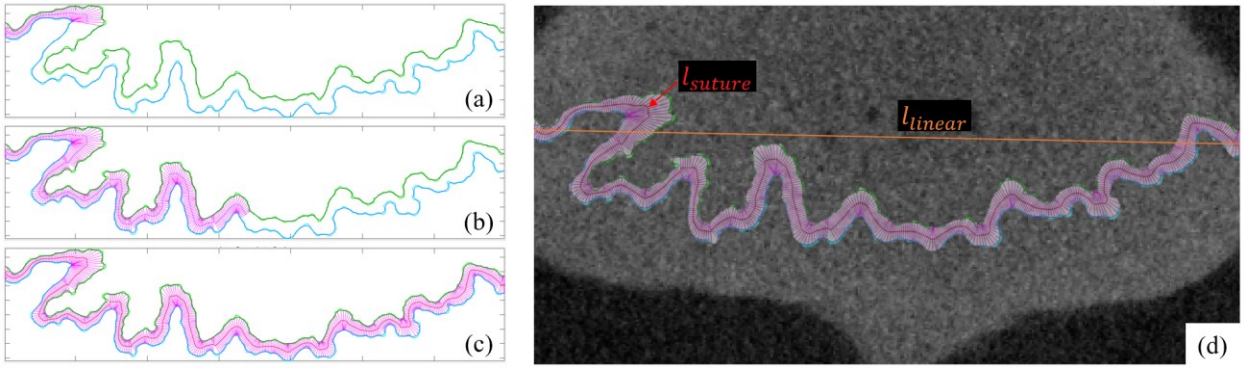

Figure 21 *Analysis of processed binary image of suture. (a) analysis code in progress (early); (b) analysis code in progress (middle); (c) completed analysis; (d) overlay of quantitative analysis on cropped image, suture length and linear length marked*

4.2.2 Data Analysis

Similar to the image processing, the analysis starts with the data closest to the ectocranial side and works iteratively through the dataset until it reaches the endocranial side. The script determines information regarding local suture widths, average planar widths, planar LII, mean suture widths, and mean suture LII.

Planar LII is found as a single measure for each plane of the reoriented µCT datasets by dividing the path length of the suture by the linear length between the end points as previously discussed and shown in equation (1). The local planar LII values can be expressed mathematically as $LII_{i,j}$, where i represents the specific sample that the local planar LII values were determined from (e.g., i=BML-3), and j represents the specific plane that the local planar LII values were determined at (e.g., ectocranial j=1, endocranial j=n). The mean suture LII, $\overline{LII}_i$, was determined from the planar LII data using equation (3).

$$\overline{LII}_i = \frac{\sum_{j=1}^{n} LII_{i,j}}{n} \qquad (3)$$

Local widths are computed along the suture path as shown in pink in Figure 21, where each local width, $W_{i,j,k}$, is specific to a singular center point along the traversed suture path between the opposing bone fronts. Where i represents the specific sample that the local widths were determined from (e.g., i=BML-3), j represents the specific plane that the local width was determined at (e.g., ectocranial j=1, endocranial j=n), and k represents the location along the suture path that the local width was determined at (e.g., left hand side (LHS) starting point k=1, right hand side (RHS) end point k=m). The local widths are used to determine the mean planar width, $\overline{W}_{i,j}$, using equation (4).

$$\overline{W}_{i,j} = \frac{\sum_{k=1}^{m} W_{i,j,k}}{m} \qquad (4)$$

The mean planar widths are then used to determine the mean suture width, $\overline{\overline{W}}_i$, using equation (5).

$$\bar{\bar{W}}_i = \frac{\sum_{j=1}^{n} \bar{W}_{i,j}}{n} \quad (5)$$

The Kruskal-Wallis test was used to determine if there was statistically significant variability between the age groups for each suture with respect to the mean suture LII and mean suture width. The Kruskal-Wallis test was selected for this analysis due to the small sample sizes and inability to confirm normal distributions and equal variance among the populations. The null and alternative hypotheses used for the Kruskal-Wallis tests are as follows:

Mean suture LII Kruskal-Wallis:

- $H_{0,LII}$: There is no difference in mean suture LII between the age groups.
- $H_{1,LII}$: There is a difference in mean suture LII between the age groups.

Mean suture width Kruskal-Wallis:

- $H_{0,W}$: There is no difference in mean suture width between the age groups.
- $H_{1,WI}$: There is a difference in mean suture width between the age groups.

The analysis was completed using 95% confidence level, and 2 degrees of freedom due to the 3 age groups. Due to the different sample sizes of age groups in the posterior lambdoid suture, equation (6) was used to determine the test statistic, *H*.

$$H = (N-1)\frac{\sum_{i=1}^{g} n_i(\bar{r}_i - \bar{r})^2}{\sum_{i=1}^{g}\sum_{j=1}^{n_i}(r_{ij} - \bar{r})^2} \quad (6)$$

Where, N is total number of observations across all groups, g is the number of groups, n_i is the number of observations in group i, r_{ij} is the rank (among all observations) of observation j from group i, $\bar{r}_i = \frac{\sum_{j=1}^{n_i} r_{ij}}{n_i}$ is the average rank of all observations in group i, *and* $\bar{r} = \frac{1}{2}(N+1)$ is the average of all the r_{ij}.

4.3 Results

4.3.1 Local Planar Widths

The local planar widths were found at each center point location as mentioned in the materials and methods section. The local planar widths vary along a single plane, typically the maximum local widths are found at locations that the suture changes direction, and the minimum local widths are found in straight running regions of the suture. Figure 22 shows the local width distribution along the same plane of the representative 24-week-old posterior lambdoid suture shown in Figure 20 and Figure 21. Variations of local widths in a single suture were found to range from 798.3%-1902.4% for the anterior lambdoid suture samples, 556.4%-2457.5% for the coronal suture samples, 404.8%-1360.2% for sagittal suture samples, and from 670.4%-1597.6% for posterior lambdoid suture samples.

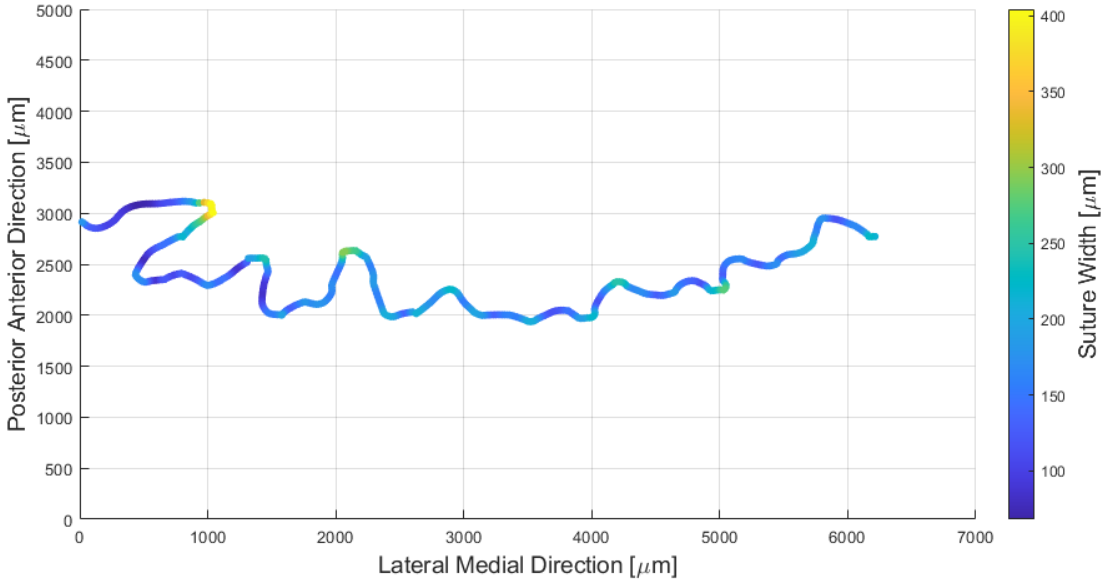

Figure 22 *Representative local planar widths along planar suture outline*

4.3.2 Planar LII and Mean Planar Width

Representative plots of the 3D centerline paths of the six regions of interest in the same representative specimen shown previously are displayed in Figure 23.

These plots qualitatively show the suture centerline path variability as the planar position in the skull thickness changes. The anterior lambdoid, coronal, sagittal, and posterior lambdoid suture centerlines all vary through the skull thickness, showing a dependence of planar suture form with position in the skull thickness. Due to a single posterior lambdoid sample being out of frame on a scan, a sample size n=4 was used for the 24-week-old posterior lambdoid datasets.

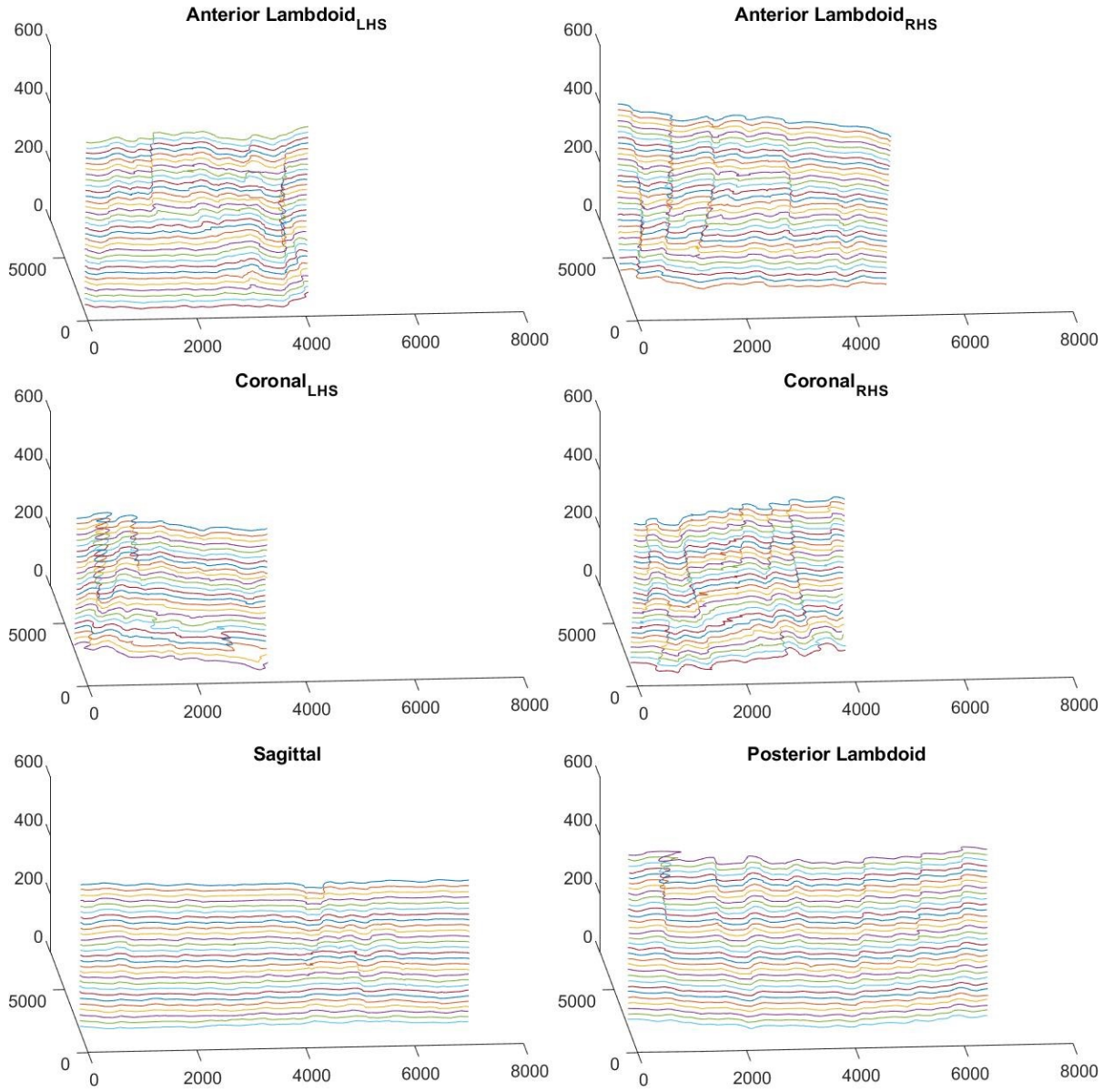

Figure 23 *Representative 3D centerlines of suture regions of interest from a single sample, scale is in μm*

Quantitative planar LII data shown through the skull thickness of the 16, 20, and 24-week-old rats can be found in Figure 24, Figure 25, and Figure 26 respectively. Variations of LII through the thickness of a single specimen were found to range from 20.5%-115.4% for the anterior lambdoid suture samples, 17.8%-107.1% for the coronal suture samples, 15.8%-62.5% for sagittal suture samples, and from 9.5%-109.7% for posterior lambdoid suture samples.

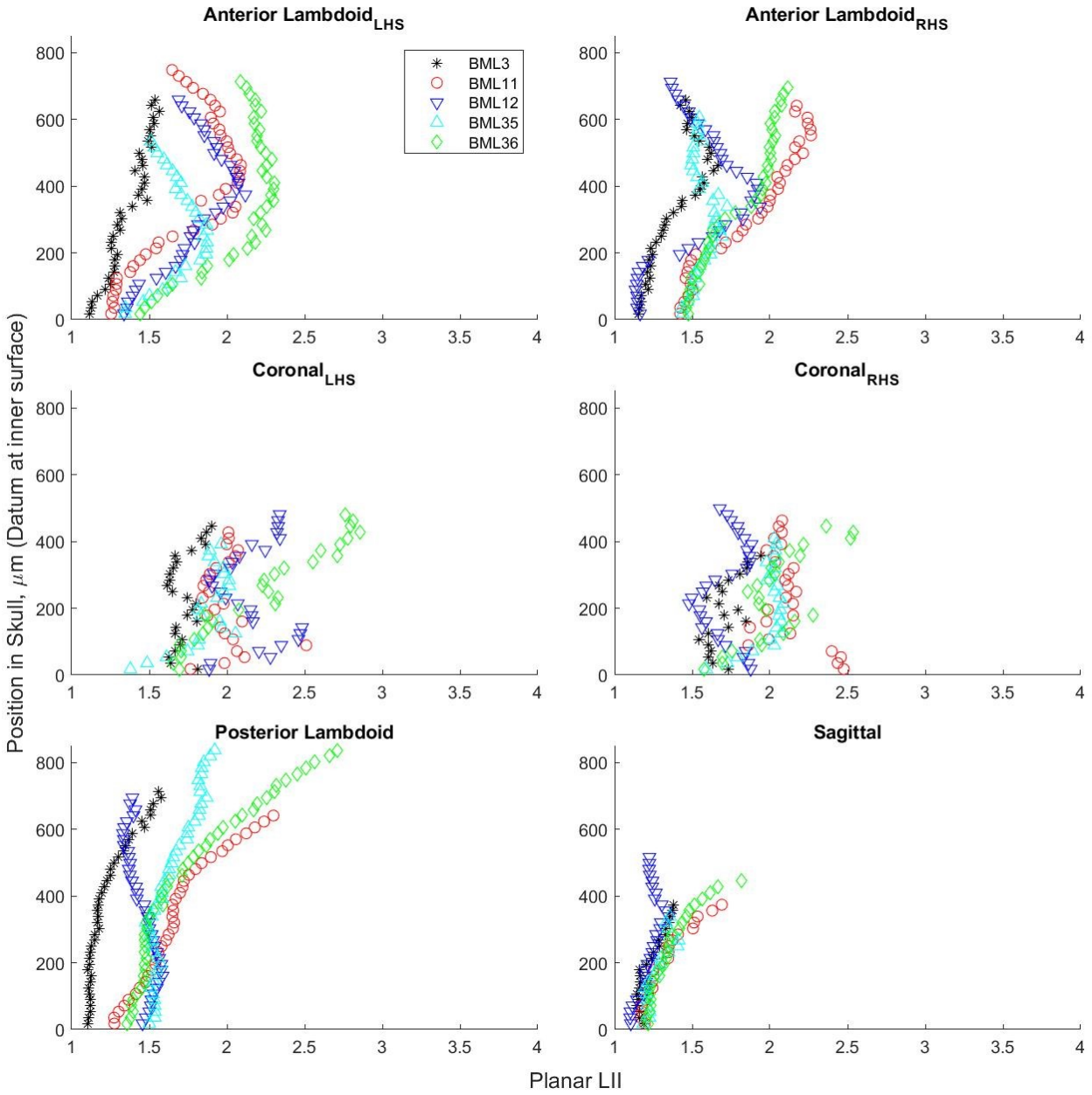

Figure 24 *16-week-old rats: Planar LII*

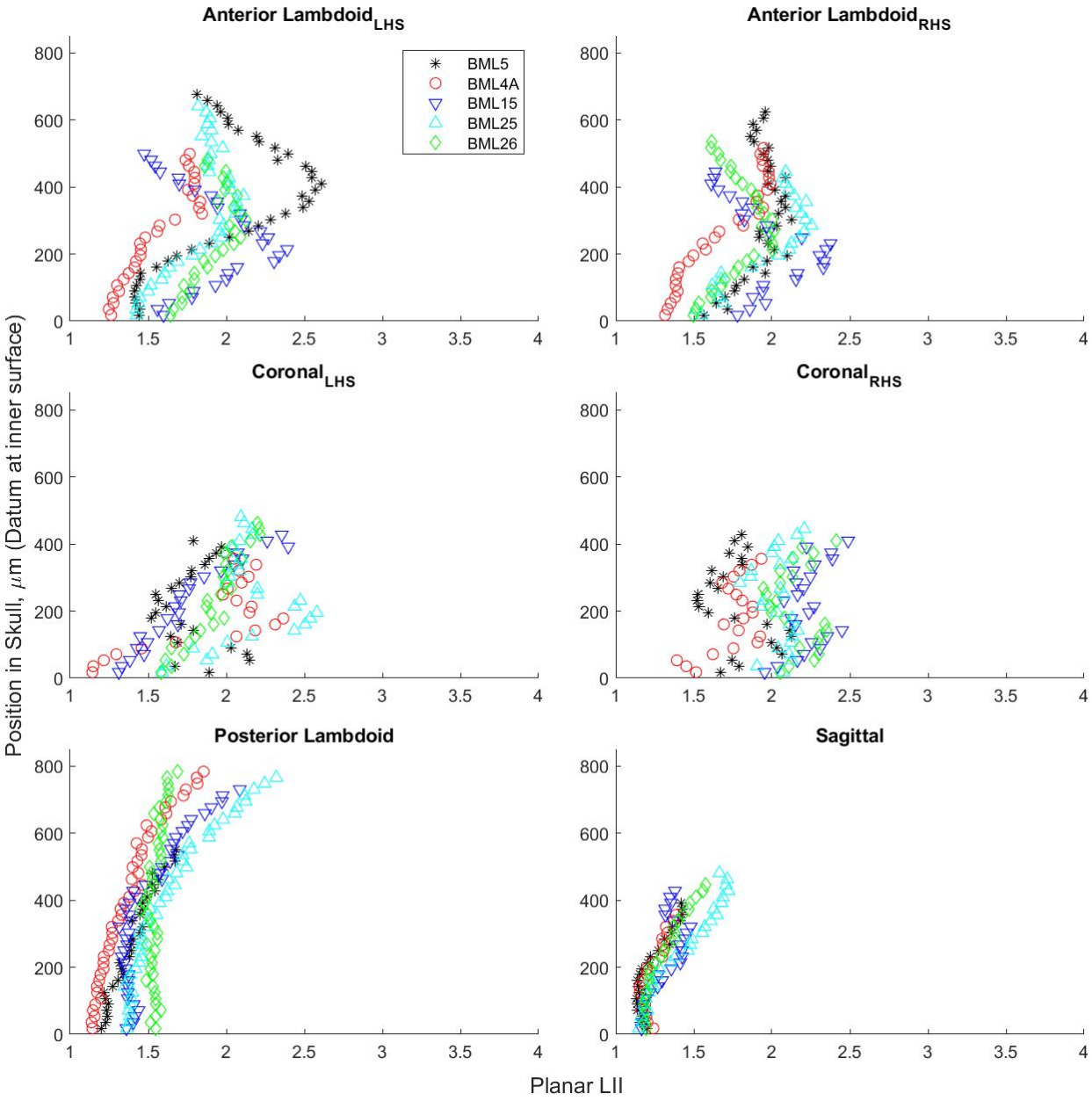

Figure 25 *20-week-old rats: Planar LII*

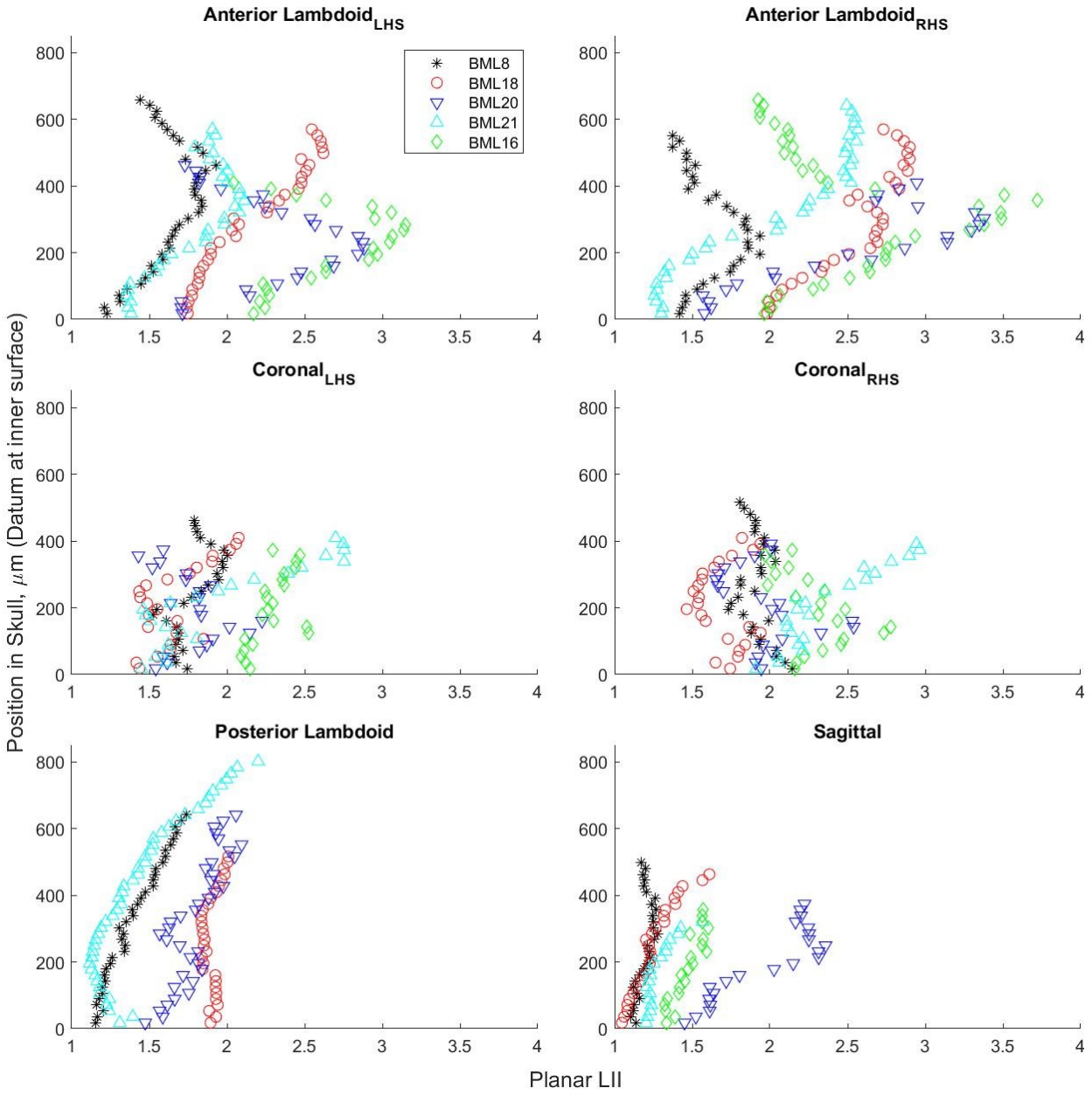

Figure 26 *24-week-old rats: Planar LII*

The mean planar width data provides quantitative information through the skull thickness of the 16, 20, and 24-week-old rats, shown below in Figure 27, Figure 28, and Figure 29 respectively. Variations of mean planar width through the thickness of a single specimen were found to range from 24.1%-180.5% for the anterior lambdoid suture samples, 14.8%-136.7% for the coronal suture samples,

15.3%-99.7% for sagittal suture samples, and from 17.4%-61.6% for posterior lambdoid suture samples.

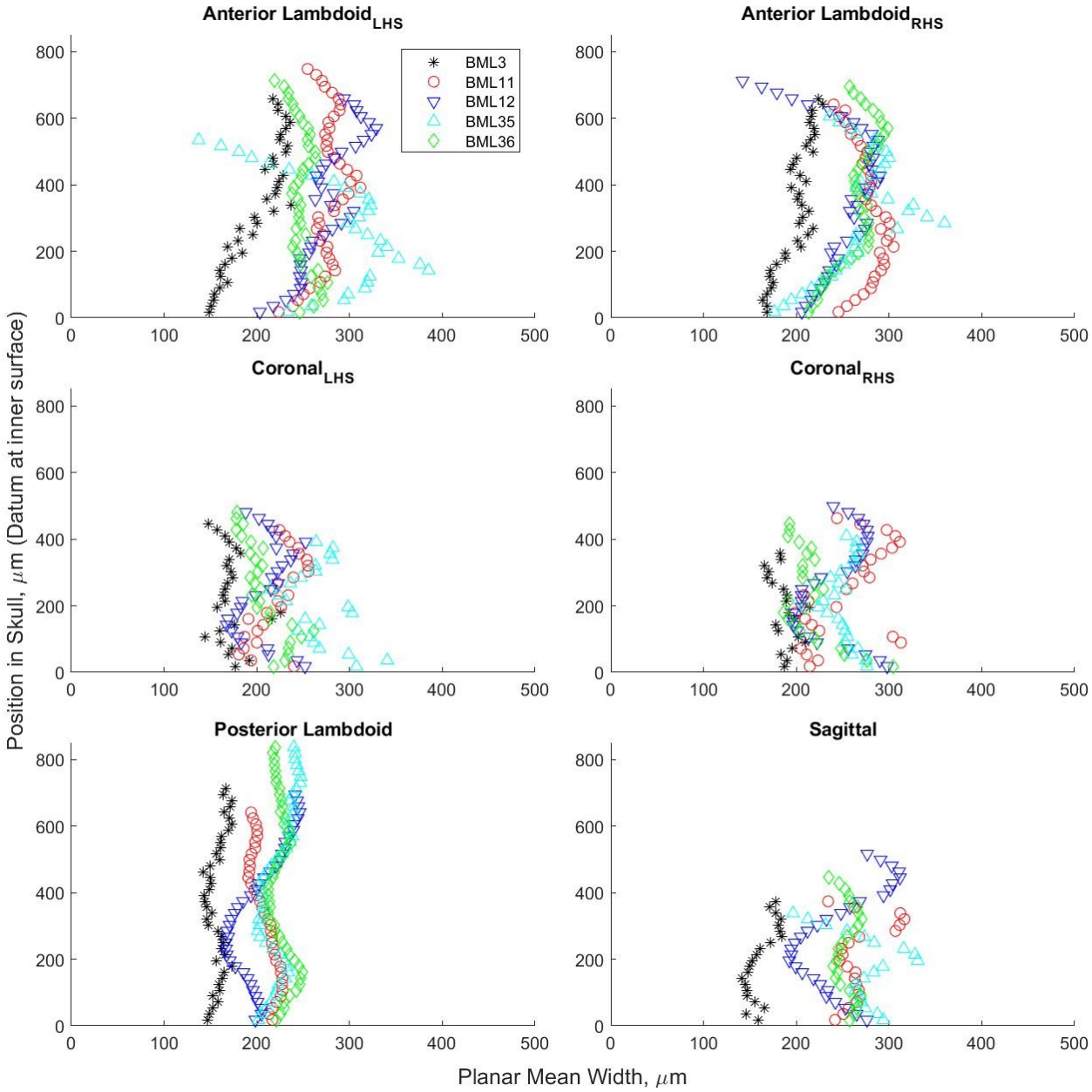

Figure 27 *16-week-old rats: Mean planar widths*

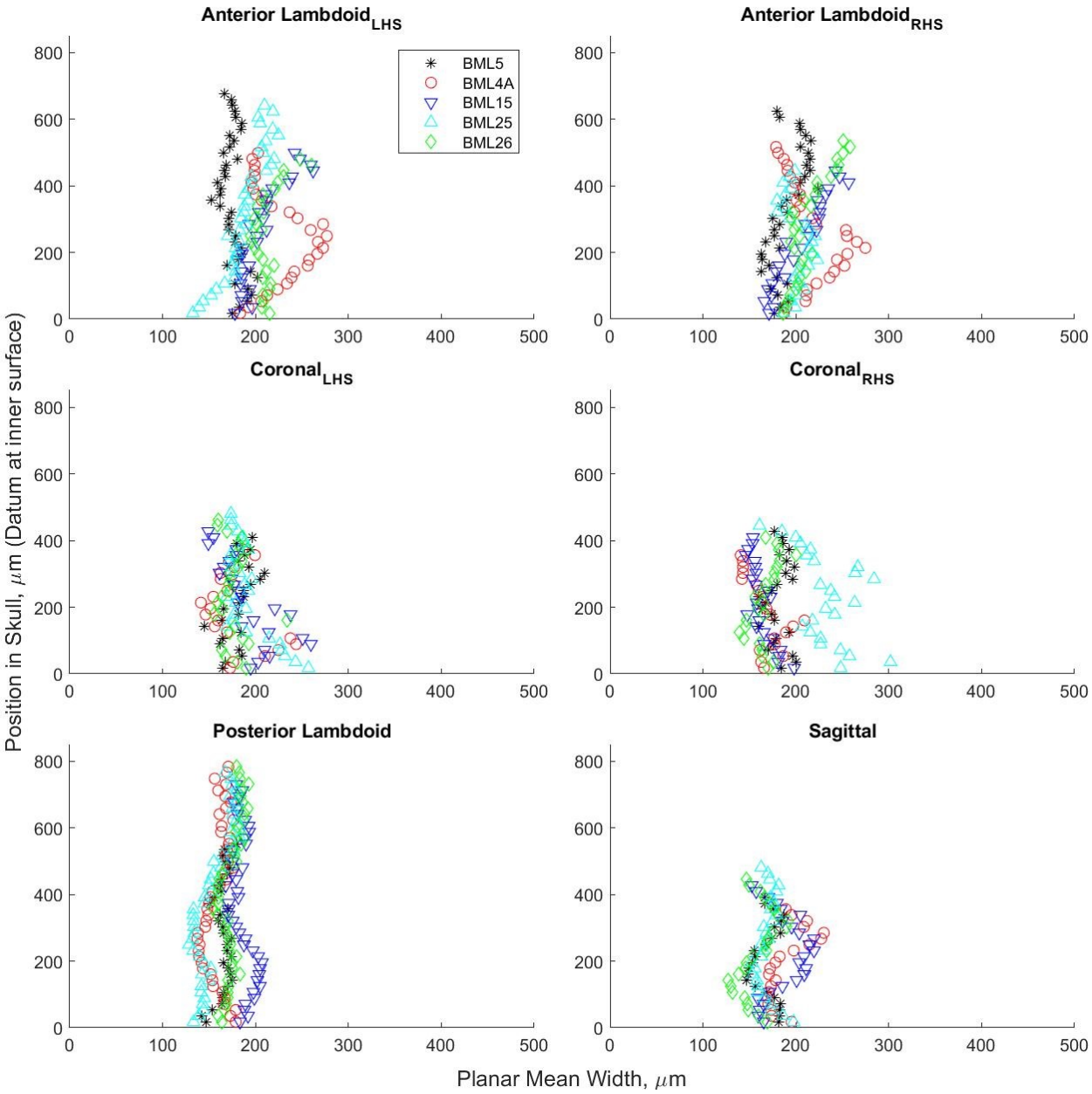

Figure 28 *20-week-old rats: Mean planar widths*

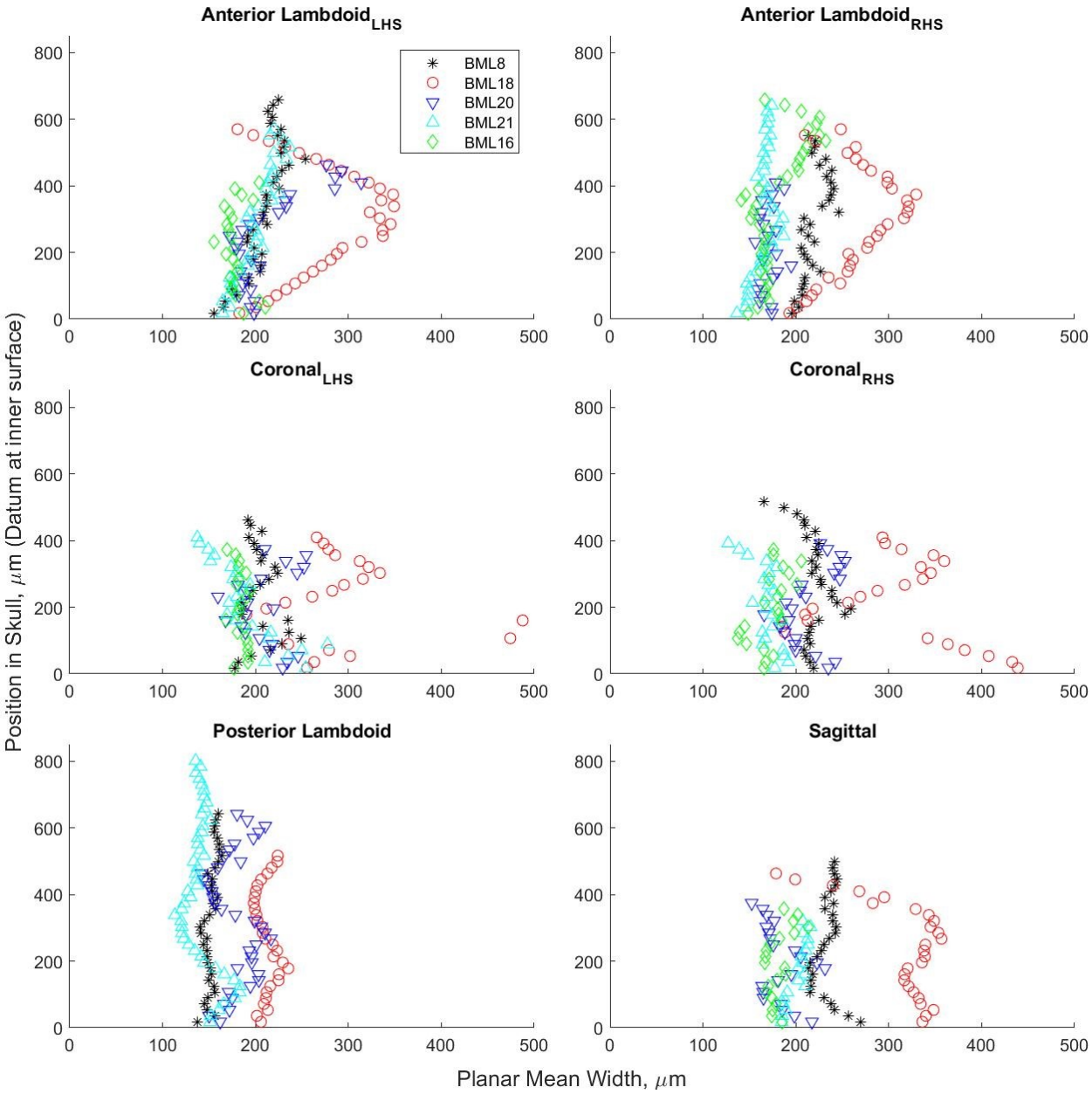

Figure 29 *24-week-old rats: Mean planar widths*

4.3.3 Mean Suture LII and Width

The mean suture LIIs and mean suture widths of the 6 regions of interest analyzed, can be found in Figure 30 and Figure 31 respectively. The values corresponding to the individual specimens for the mean suture LII and widths can be found in Table 19-Table 21 in Appendix C2. The mean suture LII appears to be constant between the age groups for the coronal, sagittal and posterior lambdoid

sutures. The anterior lambdoid suture qualitatively appears to have increased levels of mean suture LII with increased age, however the statistical significance of this trend will be explored.

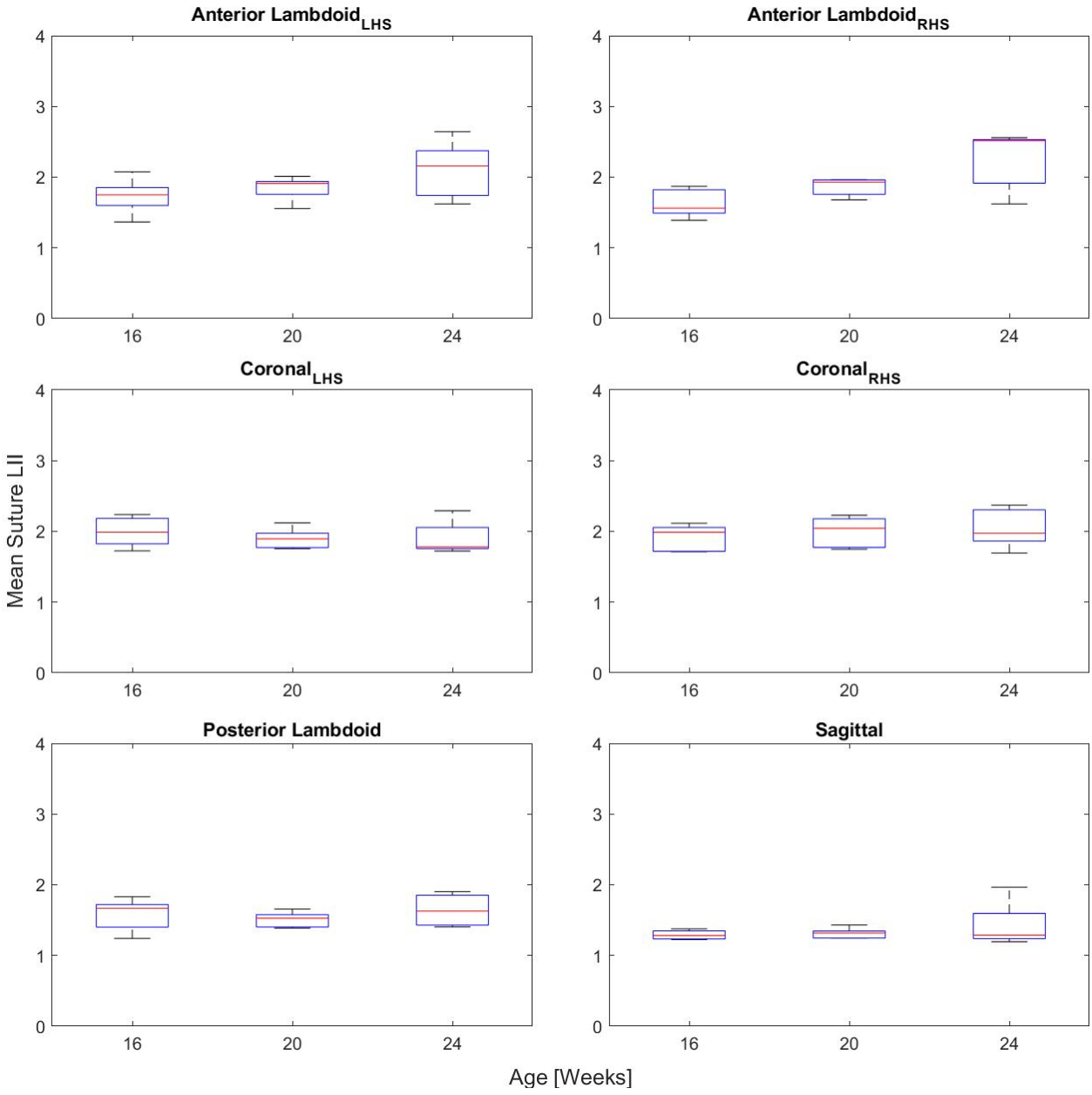

Figure 30 *Mean suture LII boxplots for suture regions of interest, grouped by age*

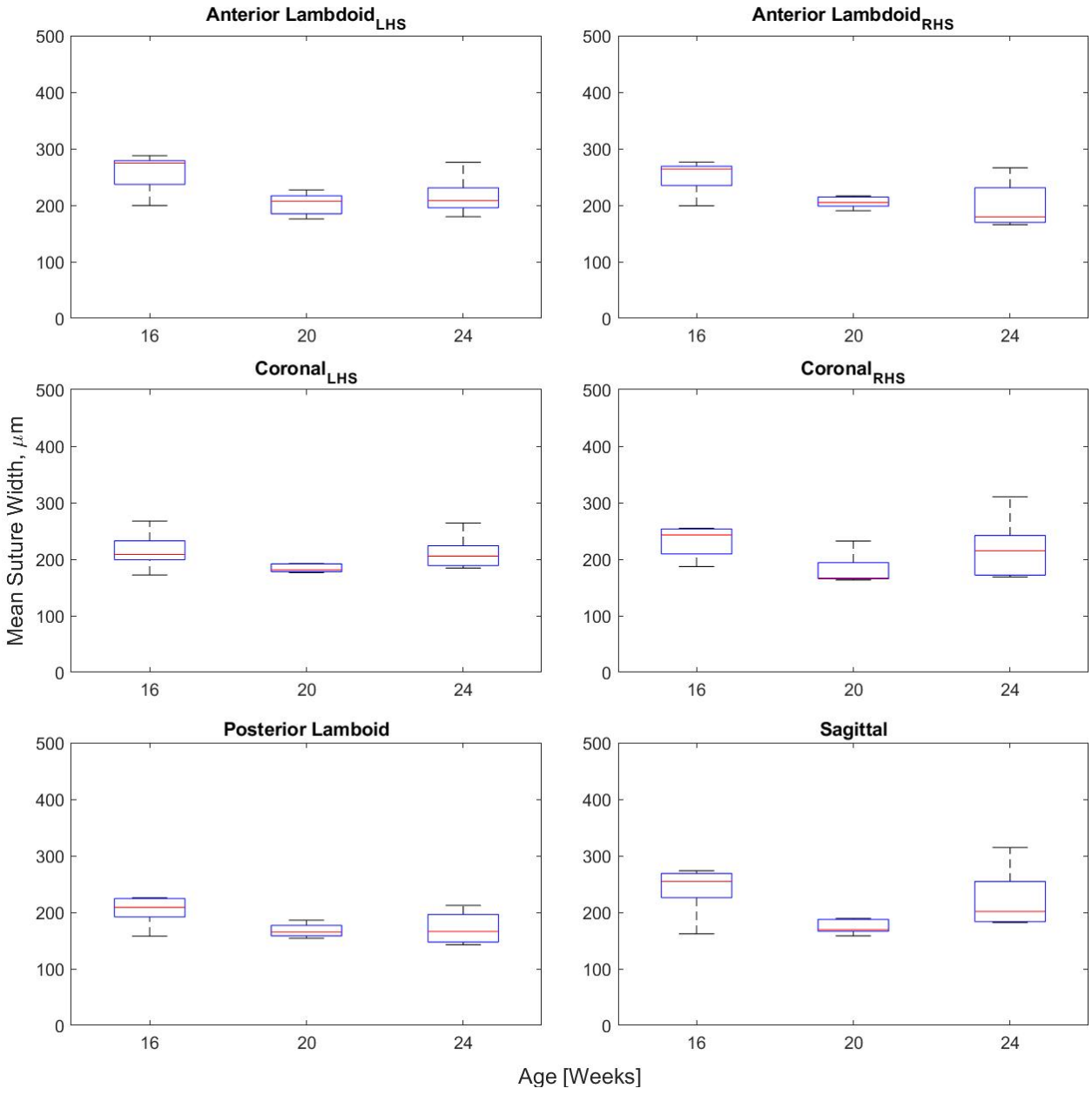

Figure 31 *Mean suture width boxplots for suture regions of interest, grouped by age*

The results of the Kruskal-Wallis test of the mean suture LII and mean suture widths between the age groups are shown below in Table 3. The Chi-Square (χ^2) value was determined to be χ^2=5.991 from the Chi-Square Distribution using 2 degrees of freedom, and 95% confidence level. With the exception of the mean suture LII of the right-hand side of the anterior lambdoid suture, all of the test statistic values determined from the statistical analysis showed no significant difference among the

three age groups in mean suture LII or width. This largely points to no significance in age with respect to mean suture LII, and points to no significance of age with respect to mean suture width.

Table 3 *Test statistics, H, relating mean suture LII and mean suture width between rat age groups determined using Kruskal-Wallis tests*

Suture	H, Suture LII	H, Mean Suture Width
PL	1.01	3.75
AL RHS	6.86	4.46
AL LHS	2.88	3.78
S	0.42	4.58
C RHS	0.74	5.18
C LHS	0.74	3.86

4.4 Discussion

Representatively conveying cranial suture complexity is challenging due to the 3D variable structure that is hidden by adjacent bones. A primary focus of this study was to develop methods for quantitatively analyzing X-ray μCT images of the cranium at different suture locations to evaluate their LII and width through the bone thickness. Development of these methods advances the literature surrounding cranial suture morphometrics by presenting a systematic method through which sutures can be quantitatively compared when studying differences/changes in a range of applications. Using these methods, it was then of interest to compare cranial suture changes with age in a rat model. Planar and mean suture LII as well as local, mean planar, and mean suture widths were determined for six regions of interest on 15 rats divided into 3 age groups. This provided 3D information regarding suture complexity and width trends through the skull thickness. This information is useful to researchers interested in suture development, relating suture mechanics to morphology, and/or modelling suture mechanics.

Cranial sutures are typically considered as 2D structures when modelled[9,10,88] and morphologically analyzed[3,76]. Furthermore, when the geometry is modelled, they

are commonly represented as being 2D with constant width and a normal sinusoidal morphology[9,10]. There have been models developed that incorporate irregularities in suture path, however constant width and 2D assumptions are still in place[88]. The results of this work showed substantial local and mean planar width variability within sutures; with local width variability of up to 2427.5% and mean planar width variability up to 180.5% through the skull thickness in single specimens. This supports part of the hypothesis of this study, that width variability is exhibited within sutures; variability between sutures is also evident by comparing the quantitative data presented in Figure 27 to Figure 29. The mean planar sagittal suture widths measured in this study (142 μm - 357 μm) are similar to results of Henderson et al., where they found rat sagittal suture widths of approximately 100 μm - 450 μm. This helps to validate the results of this work. The results indicate that if approximate suture widths are of interest, an average of multiple surface suture width measurements could represent the entire sagittal suture in rats.

The work also presented quantitative through thickness LII data, demonstrating planar LII variability of up to 115.4% through the thickness of a single specimen. Results of this work support the hypothesis that LII will spatially vary through the skull thickness within a single suture and variability between sutures is also evident in by comparing the quantitative data presented in Figure 24 to Figure 26. This study also determined mean suture widths and LII of different age groups by averaging planar data. The statistical results of the Kruskal-Wallis test did not, in general, support the hypothesis that mean suture LII, and width will vary between age groups of 16 to 24 weeks. Although there was some variability shown between ages, the results in most instances were found to be statistically insignificant. When interpreting the lack of differences, it is suspected that since rats considered in this study were nearing the end of their skeletal maturity[130], there may have been less drastic changes compared to the early stages of growth/development where more rapid skeletal changes occur[130].

The results of this work indicate that rat cranial suture width and LII can be variable through the thickness of the skull. This variability could have effects on studies that rely on measuring, characterizing, or modelling the morphological form of sutures. The through thickness distributions of width and LII were not present in every suture, it is recommended that sutures be analyzed qualitatively to ensure there is no significant through thickness variability. If no significant variability is found from the endocranial and ectocranial surfaces, planar analysis of the suture is recommended in order to save computational resources. The methods presented in this thesis could be employed when analyzing suture response to loading, as they would provide a high-resolution displacement map of how sutures are reacting if the subject is scanned before and after loading. The methods could also be utilized in studies interested in suture development and functional alterations by providing 3D morphological data.

This study did have several limitations. The sample size of 5 for each suture region of interest per age group could certainly be improved to a higher number, however the large computational costs associated with the analysis limited the ability to have a higher number of sample sizes. The age groups analyzed were all near the final period of a rats skeletal maturity[130], future works should consider a wider age range in order to track full suture development. The analysis also did not consider the surfaces of the skull, as a full plane of suture was required to perform the analysis, including this would improve the range of analysis in the study. These are all limitations of the study, but they do not discount the width and LII variability through skull thickness presented in this study. The results of this work should prompt researchers interested in suture development, mechanics, morphology, and modelling to consider how this variability affects results based on the complexity metrics being used.

4.5 Conclusions

The image analysis results show variations in local planar widths, mean planar widths, and planar LII through the thickness of the skull of individual sutures. The data shown regarding mean planar widths, planar LII, and sutures centerlines through the skull thickness highlight the 3D variability of cranial suture morphology. In the sutures analyzed there is some variability in mean suture width and LII between different aged individuals, however this was determined to be statistically insignificant via Kruskal-Wallis test in the majority of the data. Future works related to this study could include single animal 3D morphometric development analysis, in vivo 3D morphological analysis to applied loading, increasing sample sizes, increasing the age range, or analyzing different species. If researchers are interested in suture morphometry, measures should be taken to account for 3D suture morphology.

Chapter 5: Conclusions, Limitations, and Future Work

This chapter discusses the conclusions that were drawn from the morphometric and FE suture studies presented in this thesis. The limitations of the methods and results as well as potential future works that could utilize the methods presented in this work are discussed.

5.1 Conclusions

The objectives of this thesis were to expand on previous work interested in quantitative cranial suture morphology and mechanical modelling. The work presented in this thesis is primarily focused on studying the validity of 2D representations commonly used in describing cranial suture morphometry[3,69] through the development of quantitative measures using X-ray μCT imaging to explore the true 3D nature of suture structures. The investigation utilized μCT based geometric models of suture to assess the effects of 2D assumptions in FE analysis. A 3D age-based morphometry analysis was conducted to provide through thickness information in order to assess the assumption of 2D suture geometry.

Image processing methods were developed to convert reconstructed μCT images into a binarized form better suited for quantitative analysis. The method isolated suture outlines in the planar view of the scan, this allowed for the suture widths and path length to be determined. The measurements of suture width and length were determined by a script that traversed the suture path, defining local center points and measuring widths at each step. The center points were then connected to generate a suture center line path length, this was normalized to obtain LII by dividing suture path length by the linear length between the suture ends. This method was iterated through the planes of the reconstructed μCT data from the ectocranial to endocranial sides of the skull in order to obtain 3D morphometric

suture data. This method provided quantitative data that can be directly used to make better informed decisions when representing suture geometry.

A FE analysis was performed using μCT datasets to generate suture models of different levels of complexity. Swine coronal suture geometries were generated under the assumption of 2D suture representations, and a 3D suture representation. 2DV suture models were generated at the ectocranial, midplane, and endocranial regions of a swine coronal suture μCT dataset by using processed binarized suture outlines obtained from the method described above. The 2D suture outlines were extruded to generate 2DV suture models. These three 2DV suture models characterized a 2D suture representation. A 3DV suture model was also generated by utilizing the entire μCT dataset, rather than discrete planes as was done for the 2DV models. The 3DV model conveys a 3D suture representation. For each suture model, bone was generated, and mechanical FE analysis was performed on the suture-bone complex. Each suture representation was exposed to tension, and the resulting stress/strain distributions and quantities were compared and contrasted. This study provided novel information for quantifying the effects of 2D suture representations on mechanical response as compared to the true 3D geometry. It was found that 2D midplane suture representations may be sufficient for approximating bulk suture mechanics, however, were found to be insufficient if the distribution of parameters along the suture-bone interface is of interest.

A morphological study was performed on the coronal, sagittal, anterior lambdoid, and posterior lambdoid sutures of 16-, 20- and 24-week-old rats. This study utilized μCT scan data in order to perform 3D analysis on the sutures of interest. Five specimens of each age group were considered, and six regions of interest in the skull were analyzed through the skull thickness at discrete 18μm spaced planes. Local planar widths, planar LII, mean planar widths, mean suture widths, and mean suture LII were determined for each region of interest. This provided local, mean 2D, and mean 3D information regarding suture morphometry. This is a novel approach

in suture morphometry studies, which are typically conducted in a 2D manner[3,69]. It was found that suture morphometry is variable through the skull thickness, with varying levels of suture complexity through skull thickness found between, and within sutures. Variations of planar LII through the skull thickness of a single suture specimen were found to have values of up to 115.4%. Variations of local planar widths within a single suture had variations of up to 2457.5%. Variations of mean planar suture widths through the skull thickness of a single suture specimen were found to have values up to 180.5%. These large variations highlight the potential dependence of 2D suture representations to the region that they are extracted from rather than their representativeness of the entire suture structure, and that 3D suture structure should at least be qualitatively analyzed before employing 2D simplifications. For this reason, 3D suture representations, or multiple discrete measures that incorporate the entire structure are important for representing the form of interdigitated sutures.

It was concluded that 2D suture representations do not completely exemplify all suture morphometry and can provide misleading information regarding complexity. Researchers interested in quantifying suture complexity should be aware of the variability in suture form and take measures to mitigate its effects on their complexity metrics. 3D quantification is the best option for describing suture complexity, however, it is taxing of both time and computational resources. If 2D analysis is a more realistic option for a study, measures should be taken to consistently analyze sutures at the same location, ideally at both the endocranial and ectocranial surfaces if a dissected skull is the only resource. 3D morphometric and mechanical analysis of sutures could help generate stronger links between applied loading and suture adaptations, aid in developing better understanding of suture development and growth and provide more representative anatomical data for correlating with experimental results.

5.2 Limitations and Future Works

The FE analysis conducted in this thesis provided useful information for comparing mechanics of 2D and 3D suture representations, however, it did have several limitations from being fully anatomically and mechanically representative. The bone that housed the suture was modeled as a solid rectangular structure, which is not representative of the variable thickness, curved, and porous structure of bone. The suture was modelled as a solid structure, rather than its true composite form consisting of cells, fibers, and vasculature[32,36]. Small sections of the skull at the endocranial and ectocranial regions were neglected in this study, which was done to ensure consistent suture dimensions between the 2DV and 3DV models. Simplified isotropic linear elastic material properties were used to describe suture and bone properties rather than the true anisotropic nonlinear viscoelastic material properties that more accurately describe their response to loading[109,110,113]. Although these limitations were present in the study, they do not disregard the variability in mechanical results within the 2DV models, and between the 2DV and 3DV models.

Modelling cranial sutures is constantly evolving, moving towards more representative geometries, material models, and loading conditions. Some future works that have the potential to advance the field are discussed. Correlating ex vivo controlled suture loading data with 3D μCT based FE geometric models could help to develop better material models by utilizing experimental mechanical results and more representative geometric models. Increasing the sample size using a similar method for developing 3DV models would give interesting insight to the variability in suture form and mechanical response between individuals. Generating full skull models that incorporate 3D suture geometries could provide insight to the transmission of loads in the skull. As 3D modelling of sutures is quite novel, the opportunities for improving the modelling techniques and minimizing variations from true anatomical suture form are tremendous.

The age-based 3D morphology analysis was useful in providing more robust information of suture form; however, the study did have its limitations. The age range used in the study was from 16 to 24 weeks, this could be a limitation in detecting age differences due to the narrow range nearing the end of skeletal maturity. The sample size of this study could be increased from five of each age group in order to generate stronger statistical relationships and more confidence in the results. The orientation of the analysis planes for each suture was rotated and aligned manually, a landmarking process that automates the rotation of the datasets in order for more consistent normal orientations would improve the methods of this study. The methods used in this study required the suture to fully bridge the region of interest from left to right, this limited the ability to include the curved surfaces of the skulls in the analysis. Incorporating analysis of those regions would improve the range study, however, the distinct variability in complexity found through the skull thickness in the limited range is still valid information, even if it is potentially understated. Another limitation of this study was the metric used to quantify suture complexity, LII. Although it provides useful information, and the variations are clearly notable with this metric, it is a 2D metric that does not give any indication of the path traversed, only its variation from a straight line.

Future works involving 3D morphometry analyses of suture could be improved in many ways. Automated landmarking methods should also be developed in order to ensure consistent suture orientations in the analysis. Future works could involve a similar study to the one presented in this thesis, on a different species of animal. A similar study to the one performed in this thesis could also be performed on live animals, periodically scanning the specimen at different stages of development. This would provide valuable information regarding suture development timelines, and processes. Another potential application of this work could be developing more meaningful 3D complexity metrics for sutures that can robustly describe the tortuous nature of interdigitated suture.

References

1. Persson, M. The role of sutures in normal and abnormal craniofacial growth. *Acta Odontol. Scand.* **53**, 152–161 (1995).

2. Herring, S. W. Mechanical influences on suture development and patency. *Front. Oral Biol.* **12**, 41–56 (2008).

3. Rafferty, K. L. & Herring, S. W. Craniofacial sutures: Morphology, growth, and in vivo masticatory strains. *J. Morphol.* **242**, 167–179 (1999).

4. Al Dayeh, A. A., Rafferty, K. L., Egbert, M. & Herring, S. W. Real-time monitoring of the growth of the nasal septal cartilage and the nasofrontal suture. *Am. J. Orthod. Dentofac. Orthop.* **143**, 773–783 (2013).

5. Savoldi, F., Tsoi, J. K. H., Paganelli, C. & Matinlinna, J. P. Sutural Morphology in the Craniofacial Skeleton: A Descriptive Microcomputed Tomography Study in a Swine Model. *Anat. Rec.* **302**, 2156–2163 (2019).

6. Jaslow, C. R. Mechanical properties of cranial sutures. *J. Biomech.* **23**, 313–321 (1990).

7. Maloul, A., Fialkov, J. & Whyne, C. M. Characterization of the bending strength of craniofacial sutures. *J. Biomech.* **46**, 912–917 (2013).

8. Maloul, A., Fialkov, J., Wagner, D. & Whyne, C. M. Characterization of craniofacial sutures using the finite element method. *J. Biomech.* **47**, 245–252 (2014).

9. Jasinoski, S. C., Reddy, B. D., Louw, K. K. & Chinsamy, A. Mechanics of cranial sutures using the finite element method. *J. Biomech.* **43**, 3104–3111 (2010).

10. Jasinoski, S. C. & Reddy, B. D. Mechanics of cranial sutures during simulated cyclic loading. *J. Biomech.* **45**, 2050–2054 (2012).

11. Garrett, B. J. *et al.* Skeletal effects to the maxilla after rapid maxillary expansion assessed with cone-beam computed tomography. *Am. J. Orthod. Dentofac. Orthop.* **134**, 8.e1-8.e11 (2008).

12. Cohen, M. M. Sutural biology and the correlates of craniosynostosis. *Am. J. Med. Genet.* **47**, 581–616 (1993).

13. Mao, J. J., Wang, X. & Kopher, R. A. Biomechanics of craniofacial sutures: Orthopedic implications. *Angle Orthod.* **73**, 128–135 (2003).

14. Bishara, S. E. & Staley, R. N. Maxillary expansion: Clinical implications. *Am. J. Orthod. Dentofac. Orthop.* **91**, 3–14 (1987).

15. Romanyk, D. L., Lagravere, M. O., Toogood, R. W., Major, P. W. & Carey, J. P.

Review of maxillary expansion appliance activation methods: Engineering and clinical perspectives. *J. Dent. Biomech.* **1**, 1–7 (2010).

16. Lajeunie, E., Le Merrer, M., Bonaiti-Pellie, C., Marchac, D. & Renier, D. Genetic study of nonsyndromic coronal craniosynostosis. *Am. J. Med. Genet.* **55**, 500–504 (1995).

17. Boulet, S. L., Rasmussen, S. A. & Honein, M. A. A population-based study of craniosynostosis in metropolitan Atlanta, 1989-2003. *Am. J. Med. Genet. Part A* **146**, 984–991 (2008).

18. Sgouros, S. Skull vault growth in craniosynostosis. *Child's Nerv. Syst.* **21**, 861–870 (2005).

19. Cohen, S. R. Endoscopic craniectomy for early correction of craniosynostosis: Discussion. *Plast. Reconstr. Surg.* **104**, 1974–1975 (1999).

20. Aldridge, K. *et al.* Brain morphology in nonsyndromic unicoronal craniosynostosis. *Anat. Rec. - Part A Discov. Mol. Cell. Evol. Biol.* **285**, 690–698 (2005).

21. Johnson, D. & Wilkie, A. O. M. Craniosynostosis. *Eur. J. Hum. Genet.* **19**, 369–376 (2011).

22. McFarland, D. J. & Wolpaw, J. R. Brain-computer interfaces for communication and control. *Commun. ACM* **54**, 60–66 (2011).

23. Musk, E. An integrated brain-machine interface platform with thousands of channels. *J. Med. Internet Res.* **21**, 1–14 (2019).

24. Ikegame, M. *et al.* Tensile stress induces bone morphogenetic protein 4 in preosteoblastic and fibroblastic cells, which later differentiate into osteoblasts leading to osteogenesis in the mouse calvariae in organ culture. *J. Bone Miner. Res.* **16**, 24–32 (2001).

25. Wang, J. H. C., Yang, G., Li, Z. & Shen, W. Fibroblast responses to cyclic mechanical stretching depend on cell orientation to the stretching direction. *J. Biomech.* **37**, 573–576 (2004).

26. Wang, J. H. C., Yang, G. & Li, Z. Controlling cell responses to cyclic mechanical stretching. *Ann. Biomed. Eng.* **33**, 337–342 (2005).

27. Vining, K. H. & Mooney, D. J. Mechanical forces direct stem cell behaviour in development and regeneration. *Nat. Rev. Mol. Cell Biol.* **18**, 728–742 (2017).

28. Redlich, M. *et al.* Expression of tropoelastin in human periodontal ligament fibroblasts after simulation of orthodontic force. *Arch. Oral Biol.* **49**, 119–124 (2004).

29. Von Den Hoff, J. W. Effects of mechanical tension on matrix degradation by

human periodontal ligament cells cultured in collagen gels. *J. Periodontal Res.* **38**, 449–457 (2003).

30. Shimomura, J. *et al.* Tensile stress induces α-adaptin C production in mouse calvariae in an organ culture: Possible involvement of endocytosis in mechanical stress-stimulated osteoblast differentiation. *J. Cell. Physiol.* **195**, 488–496 (2003).

31. Morris-Kay, G. M. Derivation of the mammalian skull vault. *Journal of Anatomy* **199**, 143–151 (2001).

32. Opperman, L. A. Cranial sutures as intramembranous bone growth sites. *Dev. Dyn.* **219**, 472–485 (2000).

33. Hubbard, R. P., Melvin, J. W. & Barodawala, I. T. Flexure of cranial sutures. *J. Biomech.* **4**, (1971).

34. White, H. E., Goswami, A. & Tucker, A. S. The Intertwined Evolution and Development of Sutures and Cranial Morphology. *Front. Cell Dev. Biol.* **9**, 1–20 (2021).

35. Byron, C. D. Cranial Suture Morphology and its Relationship to Diet in Cebus. *J. Hum. Evol.* **57**, 649–655 (2009).

36. Ten Cate, A. R., Freeman, E. & Dickinson, J. B. Sutural development: Structure and its response to rapid expansion. *Am. J. Orthod.* **71**, 622–636 (1977).

37. Persing, J. A., Babler, W. J., Jane, J. A. & Paul F. Duckworth. Experimental Unilateral Coronal Synostosis in Rabbits. *Plast. Reconstr. Surg.* 369–376 (1986). doi:10.1097/00006534-198603000-00003

38. Wu, B. H. *et al.* Stretch force guides finger-like pattern of bone formation in Suture. *PLoS One* **12**, 1–15 (2017).

39. Katsaros, C., Kiliaridis, S. & Berg, R. Functional influence on sutural growth. A morphometric study in the anterior facial skeleton of the growing rat. *Eur. J. Orthod.* **16**, 353–360 (1994).

40. Adamski, K. N. *et al.* Pediatric Coronal Suture Fiber Alignment and the Effect of Interdigitation on Coronal Suture Mechanical Properties. *Ann. Biomed. Eng.* **43**, 2101–2111 (2015).

41. Angelieri, F. *et al.* Cone beam computed tomography evaluation of midpalatal suture maturation in adults. *Int. J. Oral Maxillofac. Surg.* **46**, 1557–1561 (2017).

42. Weinzweig, J. *et al.* Metopic synostosis: Defining the temporal sequence of normal suture fusion and differentiating it from synostosis on the basis of computed tomography images. *Plast. Reconstr. Surg.* **112**, 1211–1218 (2003).

43. Henderson, J. H., Chang, L. Y., Song, H. J. M., Longaker, M. T. & Carter, D. R. Age-dependent properties and quasi-static strain in the rat sagittal suture. *J. Biomech.* **38**, 2294–2301 (2005).

44. Willershausen, I. *et al.* Development of a novel histological and histomorphometric evaluation protocol for a standardized description of the mid-palatal suture – An ex vivo study. *J. Anat.* **235**, 180–188 (2019).

45. Byron, C. D. Role of the osteoclast in cranial suture waveform patterning. *Anat. Rec. - Part A Discov. Mol. Cell. Evol. Biol.* **288**, 552–563 (2006).

46. Vu, H. L., Panchal, J., Parker, E. E., Levine, N. S. & Francel, P. The timing of physiologic closure of the metopic suture: A review of 159 patients using reconstructed 3D CT scans of the craniofacial region. *J. Craniofac. Surg.* **12**, 527–532 (2001).

47. Korbmacher, H., Schilling, A., Püschel, K., Amling, M. & Kahl-Nieke, B. Age-dependent Three-dimensional Micro-computed Tomography Analysis of the Human Midpalatal Suture. *J. Orofac. Orthop.* **68**, 364–376 (2007).

48. Mao, J. J. & Nah, H. D. Growth and development: Hereditary and mechanical modulations. *Am. J. Orthod. Dentofac. Orthop.* **125**, 676–689 (2004).

49. Rice, D., Kim, H. & Apoptosis, T. I. Apoptosis in murine calvarial bone and suture development. *Eur. J. Oral Sci.* **107**, 265–275 (1999).

50. Burn, A. K. *et al.* Dietary consistency and the midline sutures in growing pigs. *Orthod. Craniofacial Res.* **13**, 106–113 (2010).

51. Vij, K. & Mao, J. J. Geometry and cell density of rat craniofacial sutures during early postnatal development and upon in vivo cyclic loading. *Bone* **38**, 722–730 (2006).

52. Herring, S. W., Teng, S., Huang, X., Mucci, R. J. & Freeman, J. Patterns of bone strain in the zygomatic arch. *Anat. Rec.* **246**, 446–457 (1996).

53. Herring, S. W. & Teng, S. Strain in the braincase and its sutures during function. *Am. J. Phys. Anthropol.* **112**, 575–593 (2000).

54. Popowics, T. E. & Herring, S. W. Load transmission in the nasofrontal suture of the pig, Sus scrofa. *J. Biomech.* **40**, 837–844 (2007).

55. Behrents, R. G., Carlson, D. S. & Abdelnour, T. In Vivo Analysis of Bone Strain about the Sagittal Suture in Macaca mulatta during Masticatory Movements. *J. Dent. Res.* **57**, 904–908 (1978).

56. Moazen, M. *et al.* Intracranial pressure changes during mouse development. *J. Biomech.* **49**, 123–126 (2016).

57. Goriely, A. *et al.* Mechanics of the brain: perspectives, challenges, and

opportunities. *Biomech. Model. Mechanobiol.* **14**, 931–965 (2015).

58. Soh, S. H., Rafferty, K. & Herring, S. Cyclic loading effects on craniofacial strain and sutural growth in pigs. *Am. J. Orthod. Dentofac. Orthop.* **154**, 270–282 (2018).

59. Sun, Z., Lee, E. & Herring, S. W. Cranial Sutures and Bones: Growth and Fusion in Relation to Masticatory Strain. *Anat. Rec. - Part A Discov. Mol. Cell. Evol. Biol.* **276**, 150–161 (2004).

60. Burgos-Flórez, F. J. & Garzón-Alvarado, D. A. Stress and strain propagation on infant skull from impact loads during falls: a finite element analysis. *Int. Biomech.* **7**, 19–34 (2020).

61. Ikegame, M. *et al.* Tensile stress stimulates the expression of osteogenic cytokines/growth factors and matricellular proteins in the mouse cranial suture at the site of osteoblast differentiation. *Biomed. Res.* **37**, 117–126 (2016).

62. Takeshita, N. *et al.* In vivo expression and regulation of genes associated with vascularization during early response of sutures to tensile force. *J. Bone Miner. Metab.* **35**, 40–51 (2017).

63. Chiquet, M., Renedo, A. S., Huber, F. & Flück, M. How do fibroblasts translate mechanical signals into changes in extracellular matrix production? *Matrix Biol.* **22**, 73–80 (2003).

64. Sun, Z., Lee, E. & Herring, S. W. Cell proliferation and osteogenic differentiation of growing pig cranial sutures. 280–289 (2007). doi:10.1111/j.1469-7580.2007.00761.x

65. Herring, S. W. & Ochareon, P. Bone – special problems of the craniofacial region. *Orthod. Craniofacial Res.* **8**, 174–182 (2005).

66. Markey, M. J., Main, R. P. & Marshall, C. R. In vivo cranial suture function and suture morphology in the extant fish Polypterus: Implications for inferring skull function in living and fossil fish. *J. Exp. Biol.* **209**, 2085–2102 (2006).

67. Miura, T. *et al.* Mechanism of skull suture maintenance and interdigitation. *J. Anat.* **215**, 642–655 (2009).

68. Kammerer, C. F. Elevated Cranial Sutural Complexity in Burrowing Dicynodonts. *Front. Ecol. Evol.* **9**, 1–11 (2021).

69. Markey, M. J. & Marshall, C. R. Linking Form and Function of the Fibrous Joints in the Skull: A New Quantification Scheme for Cranial Sutures Using the Extant Fish Polypt. *J. Morphol.* **268**, 89–102 (2007).

70. Jayaprakash, P. T. & Srinivasan, G. J. Skull sutures: Changing morphology during preadolescent growth and its implications in forensic identification.

Forensic Sci. Int. **229**, 166.e1-166.e13 (2013).

71. Nicolay, C. W. & Vaders, M. J. Cranial Suture Complexity in White-Tailed Deer (Odocoileus virginianus). *J. Morphol.* **267**, 841–849 (2006).

72. Koesling, S., Kunkel, P. & Schul, T. Vascular anomalies, sutures and small canals of the temporal bone on axial CT. *Eur. J. Radiol.* **54**, 335–343 (2005).

73. Maloul, A., Fialkov, J., Hojjat, S. P. & Whyne, C. M. A technique for the quantification of the 3D connectivity of thin articulations in Bony sutures. *J. Biomech.* **43**, 1227–1230 (2010).

74. Markey, M. J. & Marshall, C. R. Terrestrial-style feeding in a very early aquatic tetrapod is supported by evidence from experimental analysis of suture morphology. *Proc. Natl. Acad. Sci. U. S. A.* **104**, 7134–7138 (2007).

75. Furuya, Y. *et al.* Computerized tomography of cranial sutures. *J. Neurosurg.* **61**, 59–70 (2009).

76. Savoldi, F., Xu, B., Tsoi, J. K. H., Paganelli, C. & Matinlinna, J. P. Anatomical and mechanical properties of swine midpalatal suture in the premaxillary, maxillary, and palatine region. *Sci. Rep.* **8**, 1–12 (2018).

77. Khonsari, R. H. *et al.* A mathematical model for mechanotransduction at the early steps of suture formation. *Proc. R. Soc. B Biol. Sci.* **280**, (2013).

78. Khonsari, R. H., Di Rocco, F., Arnaud, É., Sanchez, S. & Tafforeau, P. High-resolution imaging of craniofacial sutures: New tools for understanding the origins of craniosynostoses. *Child's Nerv. Syst.* **28**, 1465–1469 (2012).

79. Radhakrishnan, P. & Mao, J. J. Nanomechanical Properties of Facial Sutures and Sutural Mineralization Front. *J. Dent. Res.* **83**, 470–475 (2004).

80. Berrington De González, A. *et al.* Projected Cancer Risks from Computed Tomographic Scans Performed in the United States in 2007. *Arch. Intern. Med.* **169**, 2071–2077 (2009).

81. Kopher, R. A., Nudera, J. A., Wang, X., O'Grady, K. & Mao, J. J. Expression of In Vivo Mechanical Strain upon Different Wave Forms of Exogenous Forces in Rabbit Craniofacial Sutures. *Ann. Biomed. Eng.* **31**, 1125–1131 (2003).

82. Rafferty, K. L., Baldwin, M. C., Soh, S. H. & Herring, S. W. Mechanobiology of bone and suture – Results from a pig model. *Orthod. Craniofacial Res.* **22**, 82–89 (2019).

83. Freeman, J. A., Teng, S. & Herring, S. W. Rigid fixation and strain patterns in the pig zygomatic arch and suture. *J. Oral Maxillofac. Surg.* **55**, 496–504 (1997).

84. Herring, S. W. & Mucci, R. J. In vivo strain in cranial sutures: The zygomatic

arch. *J. Morphol.* **207**, 225–239 (1991).

85. Rafferty, K. L., Herring, S. W. & Marshall, C. D. Biomechanics of the rostrum and the role of facial sutures. *J. Morphol.* **257**, 33–44 (2003).

86. Savoldi, F., Tsoi, J. K. H., Paganelli, C. & Matinlinna, J. P. Biomechanical behaviour of craniofacial sutures during distraction: An evaluation all over the entire craniofacial skeleton. *Dent. Mater.* **33**, e290–e300 (2017).

87. Margulies, S. S. & Thibault, K. L. Infant skull and suture properties: Measurements and implications for mechanisms of pediatric brain injury. *J. Biomech. Eng.* **122**, 364–371 (2000).

88. Liu, L. *et al.* The effects of morphological irregularity on the mechanical behavior of interdigitated biological sutures under tension. *J. Biomech.* **58**, 71–78 (2017).

89. Guerrero-vargas, J. A., Silva, T. A., Macari, S., Casas, E. B. D. Las & Garzón-alvarado, D. A. Influence of interdigitation and expander type in the mechanical response of the midpalatal suture during maxillary expansion. *Comput. Methods Programs Biomed.* **176**, 195–209 (2019).

90. Alheit, B., Bargmann, S. & Reddy, B. D. Computationally modelling the mechanical behaviour of turtle shell sutures—A natural interlocking structure. *J. Mech. Behav. Biomed. Mater.* **110**, 103973 (2020).

91. Moazen, M., Costantini, D. & Bruner, E. A Sensitivity Analysis to the Role of the Fronto-Parietal Suture in Lacerta Bilineata: A Preliminary Finite Element Study. *Anat. Rec.* **296**, 198–209 (2013).

92. Rayfield, E. J. Using finite-element analysis to investigate suture morphology: A case study using large carnivorous dinosaurs. *Anat. Rec. - Part A Discov. Mol. Cell. Evol. Biol.* **283**, 349–365 (2005).

93. Peptan, A. I., Lopez, A., Kopher, R. A. & Mao, J. J. Responses of intramembranous bone and sutures upon in vivo cyclic tensile and compressive loading. *Bone* **42**, 432–438 (2008).

94. Huang, X., Zhang, G. & Herring, S. W. Age Changes in mastication in the pig. *Comp. Biochem. Physiol.* **107A**, 647–654 (1994).

95. Carvalho Trojan, L., Andrés González-Torres, L., Claudia Moreira Melo, A. & Barbosa de Las Casas, E. Stresses and Strains Analysis Using Different Palatal Expander Appliances in Upper Jaw and Midpalatal Suture. *Artif. Organs* **41**, E41–E51 (2017).

96. Priyadarshini, J. *et al.* Stress and displacement patterns in the craniofacial skeleton with rapid maxillary expansion—a finite element method study. *Prog. Orthod.* **18**, (2017).

97. Jain, V., Shyagali, T. R., Kambalyal, P., Rajpara, Y. & Doshi, J. Comparison and evaluation of stresses generated by rapid maxillary expansion and the implant-supported rapid maxillary expansion on the craniofacial structures using finite element method of stress analysis. *Prog. Orthod.* **18**, (2017).

98. Borghi, A. *et al.* A population-specific material model for sagittal craniosynostosis to predict surgical shape outcomes. *Biomech. Model. Mechanobiol.* **19**, 1319–1329 (2020).

99. Bozkurt, S. *et al.* Computational modelling of patient specific spring assisted lambdoid craniosynostosis correction. *Sci. Rep.* **10**, 1–9 (2020).

100. Boryor, A. *et al.* In-vitro results of rapid maxillary expansion on adults compared with finite element simulations. *J. Biomech.* **43**, 1237–1242 (2010).

101. Hartono, N., Soegiharto, B. M. & Widayati, R. The difference of stress distribution of maxillary expansion using rapid maxillary expander (RME) and maxillary skeletal expander (MSE)—a finite element analysis. *Prog. Orthod.* **19**, (2018).

102. Moon, W. *et al.* The efficacy of maxillary protraction protocols with the micro-implant-assisted rapid palatal expander (MARPE) and the novel N2 mini-implant—a finite element study. *Prog. Orthod.* **16**, (2015).

103. Barbeito-Andrés, J., Bonfili, N., Nogué, J. M., Bernal, V. & Gonzalez, P. N. Modeling the effect of brain growth on cranial bones using finite-element analysis and geometric morphometrics. *Surg. Radiol. Anat.* **42**, 741–748 (2020).

104. André, C. B., Rino-Neto, J., Iared, W., Pasqua, B. P. M. & Nascimento, F. D. Stress distribution and displacement of three different types of micro-implant assisted rapid maxillary expansion (MARME): a three-dimensional finite element study. *Prog. Orthod.* **22**, (2021).

105. Lee, H., Ting, K., Nelson, M., Sun, N. & Sung, S. J. Maxillary expansion in customized finite element method models. *Am. J. Orthod. Dentofac. Orthop.* **136**, 367–374 (2009).

106. You, J. *et al.* The bone slot effect study of PI procedure for craniosynostosis correction plan based on finite element method. *Proc. - 2010 3rd Int. Conf. Biomed. Eng. Informatics, BMEI 2010* **2**, 605–608 (2010).

107. Malde, O., Libby, J. & Moazen, M. An overview of modelling craniosynostosis using the finite element method. *Mol. Syndromol.* **10**, 74–82 (2019).

108. Mathew, A., Nagachandran, K. S. & Vijayalakshmi, D. Stress and displacement pattern evaluation using two different palatal expanders in unilateral cleft lip and palate: a three-dimensional finite element analysis. *Prog. Orthod.* **17**, (2016).

109. Romanyk, D. L. *et al.* Towards a viscoelastic model for the unfused midpalatal suture: Development and validation using the midsagittal suture in New Zealand white Rabbits. *J. Biomech.* **46**, 1618–1625 (2013).

110. Romanyk, D. L. *et al.* Viscoelastic response of the midpalatal suture during maxillary expansion treatment. *Orthod. Craniofacial Res.* **19**, 28–35 (2016).

111. Li, X., Sandler, H. & Kleiven, S. The importance of nonlinear tissue modelling in finite element simulations of infant head impacts. *Biomech. Model. Mechanobiol.* **16**, 823–840 (2017).

112. Savoldi, F., Tsoi, J. K. H., Paganelli, C. & Matinlinna, J. P. The Biomechanical Properties of Human Craniofacial Sutures and Relevant Variables in Sutural Distraction Osteogenesis: A Critical Review. *Tissue Eng. - Part B Rev.* **24**, 25–36 (2018).

113. Romanyk, D. L., Liu, S. S., Long, R. & Carey, J. P. Considerations for determining relaxation constants from creep modeling of nonlinear suture tissue. *Int. J. Mech. Sci.* **85**, 179–186 (2014).

114. Miroshnichenko, K., Liu, L., Tsukrov, I. & Li, Y. Mechanical model of suture joints with fibrous connective layer. *J. Mech. Phys. Solids* **111**, 490–502 (2018).

115. Brooks, T. *et al.* Finite element models and material data for analysis of infant head impacts. *Heliyon* **4**, e01010 (2018).

116. Fuhrer, R. S., Romanyk, D. L. & Carey, J. P. A comparative finite element analysis of maxillary expansion with and without midpalatal suture viscoelasticity using a representative skeletal geometry. *Sci. Rep.* **9**, 1–11 (2019).

117. Dzialo, C. *et al.* Functional implications of squamosal suture size in paranthropus boisei. *Am. J. Phys. Anthropol.* **153**, 260–268 (2014).

118. Jasinoski, S. C., Rayfield, E. J. & Chinsamy, A. Functional implications of dicynodont cranial suture morphology. *J. Morphol.* **271**, 705–728 (2010).

119. Curtis, N., Jones, M. E. H., Evans, S. E., O'Higgins, P. & Fagan, M. J. Cranial sutures work collectively to distribute strain throughout the reptile skull. *J. R. Soc. Interface* **10**, 1–8 (2013).

120. Bright, J. A. & Gröning, F. Strain accommodation in the zygomatic arch of the pig: A validation study using digital speckle pattern interferometry and finite element analysis. *J. Morphol.* **272**, 1388–1398 (2011).

121. Liu, S. S. Y., Opperman, L. A., Kyung, H. M. & Buschang, P. H. Is there an optimal force level for sutural expansion? *Am. J. Orthod. Dentofac. Orthop.* **139**, 446–455 (2011).

122. Kumar, A., Ghafoor, H. & Khanam, A. A comparison of three-dimensional stress distribution and displacement of naso- maxillary complex on application of forces using quad-helix and nickel titanium palatal expander 2 (NPE2): a FEM study. *Prog. Orthod.* **2**, (2016).

123. Zollikofer, C. P. E. & Weissmann, J. D. A bidirectional interface growth model for cranial interosseous suture morphogenesis. *J. Anat.* **219**, 100–114 (2011).

124. Yoshimura, K., Kobayashi, R., Ohmura, T., Kajimoto, Y. & Miura, T. A new mathematical model for pattern formation by cranial sutures. *J. Theor. Biol.* **408**, 66–74 (2016).

125. Mercan, E., Hopper, R. A. & Maga, A. M. Cranial growth in isolated sagittal craniosynostosis compared with normal growth in the first 6 months of age. *J. Anat.* **236**, 105–116 (2020).

126. Li, Z. *et al.* A statistical skull geometry model for children 0-3 years old. *PLoS One* **10**, 1–13 (2015).

127. Burgos-Flórez, F. J., Gavilán-Alfonso, M. E. & Garzón-Alvarado, D. A. Flat bones and sutures formation in the human cranial vault during prenatal development and infancy: A computational model. *J. Theor. Biol.* **393**, 127–144 (2016).

128. Coats, B. & Margulies, S. S. Material properties of human infant skull and suture at high rates. *J. Neurotrauma* **23**, 1222–1232 (2006).

129. Panahifar, A. *et al.* Development and reliability of a multi-modality scoring system for evaluation of disease progression in pre-clinical models of osteoarthritis: Celecoxib may possess disease-modifying properties. *Osteoarthr. Cartil.* **22**, 1639–1650 (2014).

130. Hughes, P. C. & Tanner, J. M. The assessment of skeletal maturity in the growing rat. *J. Anat.* **106**, 371–402 (1970).

Appendix A: MATLAB Scripts

Data analysis and image processing presented in this work was done using MATLAB unless otherwise specified. This appendix includes relevant scripts and functions that were used to process, segment, and quantitatively analyze images as well as compile results and generate figures.

A1 Individual Image Processing

This script converts individual μCT files into a binarized form better suited for quantitative analysis, used in Chapter 3.

```
% This will be used for image segmentation of swine cranial sutures.

%----- Initializing steps -----
% Clean up
clc;
close all;
workspace; % Display the workspace panel.
fontSize = 20;

% Ensuring that user has necessary apps
% (Image Processing Toolbox is required)
hasIPT = license('test', 'image_toolbox');
if ~hasIPT
    % User does not have the toolbox installed.
    message = sprintf('Sorry, but you do not seem to have the Image Processing
Toolbox.\nDo you want to try to continue anyway?');
    reply = questdlg(message, 'Toolbox missing', 'Yes', 'No', 'Yes');
    if strcmpi(reply, 'No')
        % User said No, so exit.
        return;
    end
end

% CHANGE INPUT IMAGE FILE HERE:
% Reading raw images
Raw = imread('FILENAME.bmp');
% figure
% imshow(Raw)
% title('Raw Image')

% Adjusting raw images so they can be turned into binary
Raw_Adjusted = imadjust(Raw);
% figure
% imshow(Raw_Adjusted)
% title('Adjusted Image')

% Converting to black and white images
```

```
BW_Original = imbinarize(Raw_Adjusted,'adaptive','Sensitivity',0.6);
% figure
% imshow(BW_Original)
% title('Binary Image')

% Inverting the black and white image
BW_Inverse = imcomplement(BW_Original);
% figure
% imshow(BW_Inverse)
% title('Inverted Binary Image')

% Cropping the image
BW_Cropped = imcrop(BW_Inverse,[900,1000,825,500]);
% figure
% imshow(BW_Cropped)
% title('Cropped Image')

% Segmenting
Filtered = bwpropfilt(BW_Cropped,'Area',1);
% figure
% imshow(Filtered)
% title('Cropped Image Filtered by Area')

% Preparing the Segmented image for burning
preprocess = imcomplement(Filtered);
figure
imshow(preprocess)
title('Binary Cropped Image')


%%%%%%%%%%%%%%%%%%%%%%%%%%%%%%%%%%%%%%%%%%%%%%%%%%%%%%%%%%%%%%%%%%%%%%%%%%%%%%%
% Determining the area of the pre-processed suture
measurements = regionprops(logical(preprocess), 'Area');
area_preprocessed = sum([measurements.Area]);
%%%%%%%%%%%%%%%%%%%%%%%%%%%%%%%%%%%%%%%%%%%%%%%%%%%%%%%%%%%%%%%%%%%%%%%%%%%%%%%

% Saving the modified cropped image
imwrite(preprocess, 'Segmented.tif');

% Display images to prepare for ease of use
BurnedImage = imread('Segmented.tif');
subplot(2, 2, 1);
imshow(BurnedImage);
title('Original Image', 'FontSize', fontSize);
subplot(2, 2, 2);
imshow(BurnedImage);
title('DRAW LINE HERE!!!', 'FontSize', fontSize);
subplot(2, 2, 4);
imshow(BurnedImage);
title('Original Image with regions burned into image', 'FontSize', fontSize);
set(gcf, 'units','normalized','outerposition',[0 0 1 1]); % Maximize figure.
set(gcf,'name','Manual Suture Segmentation','numbertitle','off')

%----- Burn region into image -----
burnedImage = imread('Segmented.tif');
```

```
% Create a binary image for all the regions we will draw.
cumulativeBinaryImage = false(size(burnedImage));
subplot(2, 2, 3);
imshow(BurnedImage);
title('Binary Image', 'FontSize', fontSize);
% Create region mask, h, as an ROI object over the second image in the bottom
row.
axis on;
again = true;
regionCount = 0;
while again && regionCount < 20
    promptMessage = sprintf('Draw region #%d in the upper right image,\nor
Quit?', regionCount + 1);
    titleBarCaption = 'Continue?';
    button = questdlg(promptMessage, titleBarCaption, 'Draw', 'Quit', 'Draw');
    if strcmpi(button, 'Quit')
        break;
    end
    regionCount = regionCount + 1;
    subplot(2, 2, 2);

    % Ask user to draw freehand mask.
    message = sprintf('Left click and hold to begin drawing.\nSimply lift the
mouse button to finish');
    uiwait(msgbox(message));
    hFH = imfreehand(); % Actual line of code to do the drawing.
    % Create a binary image ("mask") from the ROI object.
    singleRegionBinaryImage = hFH.createMask();
    xy = hFH.getPosition;

    caption = sprintf('DRAW HERE.  Original Image with %d regions in overlay.',
regionCount);
    title(caption, 'FontSize', fontSize);

    % OR it in to the "all regions" binary image mask we're building up.
    cumulativeBinaryImage = cumulativeBinaryImage | singleRegionBinaryImage;
    % Display the regions mask.
    subplot(2, 2, 3);
    imshow(cumulativeBinaryImage);
    caption = sprintf('Binary mask of the %d regions', regionCount);
    title(caption, 'FontSize', fontSize);

    % Burn region into image by setting it to 255 wherever the mask is true.
    burnedImage(cumulativeBinaryImage) = 255;
    % Display the image with the "burned in" region.
    subplot(2, 2, 4);
    cla;
    imshow(burnedImage);
    caption = sprintf('New image with %d regions burned into image',
regionCount);
    title(caption, 'FontSize', fontSize);
end

% Filtering to the largest area only
BurnFilter = bwpropfilt(imcomplement(burnedImage),'Area',1);
```

```
% Smoothing edges
se = strel('disk',2);
postprocess1 = imclose(BurnFilter,se);
% figure
% imshowpair(BurnFilter,postprocess1,'montage')

% Closing holes
% CHANGE NAME OF VARIABLE BELOW BASED ON WHAT FILE YOU EXPORT
SUTURE_ID = imfill(postprocess1,'holes');
% figure
% imshow(VARIABLE NAME) % Change to SUTURE_ID variable
```

A2 Quantitative Analysis Function

This function traverses the suture outline, generating a center path of the suture which can be used to determine LII. It also determines local widths at every point along the way, this can be used to determine width distributions along the suture path of a single plane as well as average suture width of a single plane. This function was used in Chapter 3 and Chapter 4.

```
function [Center,Width] = SutureAnalysis(ProcessedData)

LoadedImage=ProcessedData;

% Getting Size of Image
[Row,Col]=size(LoadedImage);
% Applying edge detection
Edge=edge(LoadedImage);

% Finding the coordinates of the edge elements
Elements=find(Edge);
Line=zeros(length(Elements),2);
for i=1:length(Elements)
    Line(i,1)=ceil(Elements(i)/Row);
    Line(i,2)=Elements(i)-floor(Elements(i)/Row)*Row;
end

%% ------------------------------------------------------------------------
% Rearranging points based on the distance from each other to get
% continuous curve
% It will get the points until there is minimum distance of 3 or more
% occurs. at that point it will be reaching the end of top curve.

R=length(Line);
Top=zeros(R,2);
base=Line(2:end,:);
point=Line(1,:);
Top(1,:)=point;
for i=1:R-1
```

```
    temp=base-repmat(point,R-i,1);
    distance=sqrt(temp(:,1).^2+temp(:,2).^2);
    Min=min(distance);
    if Min < 5
        closest=min(find(distance==Min));
        Top(i+1,:)=base(closest,:);
        point=base(closest,:);
        base(closest,:)=[];
    else
        Top(i+1:end,:)=[];
        break;
    end
end

% Starting the rearrangement of the bottom curve
R=length(base);
Bottom=zeros(R,2);
point=base(1,:);
base(1,:)=[];
Bottom(1,:)=point;
for i=1:R-1
    temp=base-repmat(point,R-i,1);
    distance=sqrt(temp(:,1).^2+temp(:,2).^2);
    Min=min(distance);
    if Min < 5
        closest=min(find(distance==Min));
        Bottom(i+1,:)=base(closest,:);
        point=base(closest,:);
        base(closest,:)=[];
    else
        Bottom(i+1:end,:)=[];
        break;
    end
end

% Smoothing the top and bottom curves
TopS(:,1)=smooth(smooth(smooth(Top(:,1))));
TopS(:,2)=smooth(smooth(smooth(Top(:,2))));
BottomS(:,1)=smooth(smooth(smooth(Bottom(:,1))));
BottomS(:,2)=smooth(smooth(smooth(Bottom(:,2))));

figure();
Plot=plot(Top(:,1),Top(:,2),'g','LineWidth',2);
hold on;
Plot=[Plot,plot(Bottom(:,1),Bottom(:,2),'c','LineWidth',2)];
xlabel('X [pixels]');
ylabel('Y [pixels]');

Plot=[Plot,plot(TopS(:,1),TopS(:,2),'k')];
Plot=[Plot,plot(BottomS(:,1),BottomS(:,2),'b')];
axis ij;
axis tight;
axis equal;

%% ------------------------------------------------------------------------
```

```
% Finding closest distance between 2 curves through given point

lstep=1; %Linear step size along normal direction
lspan=30; %Linear search span. -Span to +Span with an step equal to astep
astep=1; %Angular step size along search span
aspan=45; %Angular search span. -Span to +Span with an step equal to astep
vlength=100;
TopIndex=1; %Index of initial point of top curve
BottomIndex=1; %Index of initial point of bottom curve
T=TopS(TopIndex,:); % Top initial point
B=BottomS(BottomIndex,:); % Bottom initial point
Width=norm(T(1,:)-B(1,:));
Center=mean([T(1,:);B(1,:)]);
Plot=[Plot,scatter(Center(1,1),Center(1,2),'b .')];
Plot=[Plot,plot([T(1,1);B(1,1)],[T(1,2);B(1,2)],'m')];
tic
while Center(end,1)<Col
    V1=vlength*(T(end,:)-Center(end,:))/norm(T(end,:)-Center(end,:));
    V2=vlength*(B(end,:)-Center(end,:))/norm(B(end,:)-Center(end,:));
    Normal=lstep*[-V1(2),V1(1)]/norm([-V1(2),V1(1)]);
    P=Center(end,:)+Normal;
    TopRange=(TopIndex-0.5*lspan:TopIndex+2*lspan);
    TopRange=TopRange(TopRange>0&TopRange<=length(TopS));

    BottomRange=(BottomIndex-0.5*lspan:BottomIndex+2*lspan);
    BottomRange=BottomRange(BottomRange>0&BottomRange<=length(BottomS));

    Rot=@(a)[cosd(a) -sind(a);
             sind(a)  cosd(a)];
    for i=-aspan:astep:aspan
        V1_1=(Rot(i)*V1')';
        V2_1=(Rot(i)*V2')';

        % Detecting intersection with top curve

[X1,Y1,K1]=polyxpoly([P(1),P(1)+V1_1(1)],[P(2),P(2)+V1_1(2)],TopS(TopRange,1)
,TopS(TopRange,2));
        if ~isempty(K1)
            if length(X1)==1
                Tnew(i+aspan+1,1)=X1(1);
                Tnew(i+aspan+1,2)=Y1(1);
            else
                IntersectDistance=sqrt((X1-P(1)).^2+(Y1-P(2)).^2);

IntersectIndex=find(IntersectDistance==min(IntersectDistance));
                Tnew(i+aspan+1,1)=X1(IntersectIndex);
                Tnew(i+aspan+1,2)=Y1(IntersectIndex);
            end
        else
            Tnew(i+aspan+1,1)=nan;
            Tnew(i+aspan+1,2)=nan;
        end

        % Detecting intersection with bottom curve
```

```
[X2,Y2,K2]=polyxpoly([P(1),P(1)+V2_1(1)],[P(2),P(2)+V2_1(2)],BottomS(BottomRa
nge,1),BottomS(BottomRange,2));
        if ~isempty(K2)
            if length(X2)==1
                Bnew(i+aspan+1,1)=X2(1);
                Bnew(i+aspan+1,2)=Y2(1);
            else
                IntersectDistance=sqrt((X2-P(1)).^2+(Y2-P(2)).^2);

IntersectIndex=find(IntersectDistance==min(IntersectDistance));
                Bnew(i+aspan+1,1)=X2(IntersectIndex);
                Bnew(i+aspan+1,2)=Y2(IntersectIndex);
            end
        else
            Bnew(i+aspan+1,1)=nan;
            Bnew(i+aspan+1,2)=nan;
        end
        BT=Tnew-Bnew;
        LocalWidth=sqrt(BT(:,1).^2+BT(:,2).^2);
    end
    Index=find(LocalWidth==min(LocalWidth));
    T=[T;Tnew(Index,:)];
    B=[B;Bnew(Index,:)];
    Width=[Width;LocalWidth(Index,:)];
    if ~isempty(Index)
        Center=[Center;mean([Tnew(Index,:);Bnew(Index,:)])];
        [~,TopIndex]=ClosestPoint(Tnew(Index,:),TopS);
        [~,BottomIndex]=ClosestPoint(Bnew(Index,:),BottomS);
    else
        break;
    end
    scatter(Center(end,1),Center(end,2),'b .');
    plot([T(end,1);B(end,1)],[T(end,2);B(end,2)],'m');
    drawnow;
end
T=[T;TopS(end,:)];
B=[B;BottomS(end,:)];
Width=[Width;norm(T(end,:)-B(end,:))];
WidthAverage=mean(Width);
Center=[Center;mean([TopS(end,:);BottomS(end,:)])];
scatter(Center(end,1),Center(end,2),'b .');
plot([T(end,1);B(end,1)],[T(end,2);B(end,2)],'m');
Plot=[Plot,plot(Center(:,1),Center(:,2),'r')];
title(['Linear step ',num2str(lstep),', Angular step ',num2str(astep),', Angle
span ',num2str(-aspan),' ~ ',num2str(aspan)]);
CenterDistance=diff(Center);
CenterDistance=sqrt(CenterDistance(:,1).^2+CenterDistance(:,2).^2);
SutureLength=sum(CenterDistance);
Lengths=0;
for i=1:length(CenterDistance)
    Lengths=[Lengths;Lengths(end,1)+CenterDistance(i,1)];
end

figure();
```

```
stem(Lengths,Width,'b','MarkerSize',1);
hold on;
Plot=plot([0,Lengths(end,1)],[WidthAverage,WidthAverage],'r');
title('Sutural width along the sutural length');
legend('Width of the sutures along the sutural length','Average
with','Location','NorthWest','Box','off');
xlabel('Sutural length [pixels]');
ylabel('Sutural width [pixels]');
toc
```

A3 Closest Point Measurements

This function finds the closest distance that intersects a specific point between two curves. Used in Chapter 3 and Chapter 4.

```
% This function finds the closest point to the given point among given curves
function [P,ii]=ClosestPoint(Point,Data)
[row,~]=size(Data);
SubVector=Data-repmat(Point,row,1);

Distance=sqrt(SubVector(:,1).^2+SubVector(:,2).^2);
ii=find(Distance==min(Distance));
P=Data(ii,:);
```

A4 Compiling Individual Results

This script compiled the results of the individual planes of the swine analysis, data from the A1 script was first compiled in Microsoft excel. This script was used in Chapter 3.

```
clear;
close all;
clc;

% Importing Data from CompiledData.xlsx file
Data3351 = readtable('CompiledData.xlsx','Range','B18:H29');
Data3355 = readtable('CompiledData.xlsx','Range','K18:Q29');

% CORONAL
% Plotting Coronal LII vs Suture Position:
% 3351 (30 slices per 10% through thickness)
figure
% scatter(Data3351.Percentage,Data3351.Coronal_LII)
scatter(Data3351.Coronal_LII,Data3351.Percentage)
title('3351: Coronal Suture LII Through Skull Thickness')
xlabel('Linear Interdigitation Index')
ylabel('0: Interior Skull Slice; 1: Exterior Skull Slice')
ylim([0 1]);
```

```
xlim([1 5]);
% 3355 (20 slices per 10% through thickness)
figure
% scatter(Data3355.Percentage,Data3355.Coronal_LII)
scatter(Data3355.Coronal_LII,Data3355.Percentage)
title('3355: Coronal Suture LII Through Skull Thickness')
xlabel('Linear Interdigitation Index')
ylabel('0: Interior Skull Slice; 1: Exterior Skull Slice')
ylim([0 1]);
xlim([1 5]);
% Plotting Coronal Width vs Suture Position:
% 3351 (30 slices per 10% through thickness)
figure
% scatter(Data3351.Percentage,Data3351.Coronal_W)
scatter(Data3351.Coronal_W,Data3351.Percentage)
title('3351: Coronal Suture Average Width Through Skull Thickness')
xlabel('Average Suture Width [um]')
ylabel('0: Interior Skull Slice; 1: Exterior Skull Slice')
ylim([0 1]);
xlim([50 400]);
% 3355 (20 slices per 10% through thickness)
figure
scatter(Data3355.Coronal_W, Data3355.Percentage)
% scatter(Data3355.Percentage,Data3355.Coronal_W)
title('3355: Coronal Suture Average Width Through Skull Thickness')
xlabel('Average Suture Width [um]')
ylabel('0: Interior Skull Slice; 1: Exterior Skull Slice')
ylim([0 1]);
xlim([50 400]);


% SAGITTAL
% Plotting Sagittal LII vs Suture Position:
% 3351 (30 slices per 10% through thickness)
figure
% scatter(Data3351.Percentage,Data3351.Sagittal_LII)
scatter(Data3351.Sagittal_LII,Data3351.Percentage)
title('3351: Sagittal Suture LII Through Skull Thickness')
xlabel('Linear Interdigitation Index')
ylabel('0: Interior Skull Slice; 1: Exterior Skull Slice')
ylim([0 1]);
xlim([1 5]);
% 3355 (20 slices per 10% through thickness)
figure
% scatter(Data3355.Percentage,Data3355.Sagittal_LII)
scatter(Data3355.Sagittal_LII,Data3355.Percentage)
title('3355: Sagittal Suture LII Through Skull Thickness')
xlabel('Linear Interdigitation Index')
ylabel('0: Interior Skull Slice; 1: Exterior Skull Slice')
ylim([0 1]);
xlim([1 5]);
% Plotting Sagittal Width vs Suture Position:
% 3351 (30 slices per 10% through thickness)
figure
% scatter(Data3351.Percentage,Data3351.Sagittal_W)
```

```
scatter(Data3351.Sagittal_W,Data3351.Percentage)
title('3351: Sagittal Suture Average Width Through Skull Thickness')
xlabel('Average Suture Width [um]')
ylabel('0: Interior Skull Slice; 1: Exterior Skull Slice')
ylim([0 1]);
xlim([50 400]);
% 3355 (20 slices per 10% through thickness)
figure
% scatter(Data3355.Percentage,Data3355.Sagittal_W)
scatter(Data3355.Sagittal_W,Data3355.Percentage)
title('3355: Sagittal Suture Average Width Through Skull Thickness')
xlabel('Average Suture Width [um]')
ylabel('0: Interior Skull Slice; 1: Exterior Skull Slice')
ylim([0 1]);
xlim([50 400]);

% Thickness Combined
figure
scatter(Data3351.Coronal_W,Data3351.Percentage,'kd','filled')
hold on
scatter(Data3355.Coronal_W,Data3355.Percentage,'ro','filled')
hold on
scatter(Data3351.Sagittal_W,Data3351.Percentage,'k*')
hold on
scatter(Data3355.Sagittal_W,Data3355.Percentage,'r^','filled')
title('Average Suture Width Through Skull Thickness')
xlabel('Average Suture Width Along Suture Path, \mum')
ylabel('0: Interior Skull Slice; 1: Exterior Skull Slice')
legend('3351:      Coronal','3355:      Coronal','3351:      Sagittal','3355:
Sagittal','Location','southeast')
ylim([0 1.05]);
xlim([0 400]);

% LII Combined
figure
scatter(Data3351.Coronal_LII,Data3351.Percentage,'kd','filled')
hold on
scatter(Data3355.Coronal_LII,Data3355.Percentage,'ro','filled')
hold on
scatter(Data3351.Sagittal_LII,Data3351.Percentage,'k*')
hold on
scatter(Data3355.Sagittal_LII,Data3355.Percentage,'r^','filled')
title('Suture LII Through Skull Thickness')
xlabel('Linear Interdigitation Index')
ylabel('0: Interior Skull Slice; 1: Exterior Skull Slice')
legend('3351: Coronal','3355: Coronal','3351: Sagittal','3355: Sagittal')
ylim([0 1.05]);
xlim([1 5]);

% Thickness Combined
figure
scatter(Data3351.Coronal_W,Data3351.Percentage,'kd','filled')
hold on
scatter(Data3355.Coronal_W,Data3355.Percentage,'ro','filled')
hold on
```

```
scatter(Data3351.Sagittal_W,Data3351.Percentage,'k*')
hold on
scatter(Data3355.Sagittal_W,Data3355.Percentage,'r^','filled')
title('Average Suture Width Through Skull Thickness')
xlabel('Average Suture Width Along Suture Path, \mum')
ylabel('0: Interior Skull Slice; 1: Exterior Skull Slice')
legend('Sample 1 Coronal','Sample 2 Coronal','Sample 1 Sagittal','Sample 2
Sagittal','Location','southeast')
ylim([0 1.05]);
xlim([0 400]);

% LII Combined
figure
scatter(Data3351.Coronal_LII,Data3351.Percentage,'kd','filled')
hold on
scatter(Data3355.Coronal_LII,Data3355.Percentage,'ro','filled')
hold on
scatter(Data3351.Sagittal_LII,Data3351.Percentage,'k*')
hold on
scatter(Data3355.Sagittal_LII,Data3355.Percentage,'r^','filled')
title('Suture LII Through Skull Thickness')
xlabel('Linear Interdigitation Index')
ylabel('0: Interior Skull Slice; 1: Exterior Skull Slice')
legend('Sample 1 Coronal','Sample 2 Coronal','Sample 1 Sagittal','Sample 2
Sagittal')
ylim([0 1.05]);
xlim([1 5]);
```

A5 Dataset Image Processing

This script converts entire μCT datasets into a binarized form better suited for quantitative analysis, it was used in Chapter 4.

```
% Multiple Scan Analysis

%----- Initializing steps -----
% Clean up
clc;
close all;
workspace; % Display the workspace panel.
fontSize = 20;

% USER INPUTS:
se = strel('disk',2);  % STRUCTURING ELEMENT: NOTE SHOULD BE APPROXIMATE SIZE
AS OBJECTS
sens = 0.6;     % SENSITIVITY FACTOR FOR ADAPTIVE THRESHOLDING
resolution = 8.9;   % CT SCAN RESOLUTION, 1 pixel = 8.9 um
resize = 2;  % Intervals between adjacent scans sampled (this is 2 if resized
x2)
Data = imageDatastore('Scans'); % DATA INPUT, CHANGE NAME TO NESTED FOLDER
scanData = struct();
% Cropping information
```

```
crop = [777.5000 695.0000 208 144.0000]; % Change for every unique suture
suture = 'BML-XX, SUTURE_NAME'; % This puts the suture of interest into titles
suturesave = 'BMLXX_SUTURENAME_';

% Ensuring that user has necessary apps
% (Image Processing Toolbox is required)
hasIPT = license('test', 'image_toolbox');
if ~hasIPT
    % User does not have the toolbox installed.
    message = sprintf('Sorry, but you do not seem to have the Image Processing
Toolbox.\nDo you want to try to continue anyway?');
    reply = questdlg(message, 'Toolbox missing', 'Yes', 'No', 'Yes');
    if strcmpi(reply, 'No')
        % User said No, so exit.
        return;
    end
end

%%%%%%%%%%%%%%%%%%%%%%%%%%%%%%%%%%%%%%%%%%%%%%%%%%%%%%%%%%%%%%%%%%%%%%%%%%%%
%%%%% SEGMENTATION %%%%%%%%%%%%%%%%%%%%%%%%%%%%%%%%%%%%%%%%%%%%%%%%%%%%%%%%
%%%%%%%%%%%%%%%%%%%%%%%%%%%%%%%%%%%%%%%%%%%%%%%%%%%%%%%%%%%%%%%%%%%%%%%%%%%%

% Creating loop to handle the dataset.
for i=1:(length(Data.Files))
    % Extracting file number from the Data input
    % INPUTS REQUIRED:
    % Look at the file name of string and input the string before and after
    % the marker/file number
    before = "SUTURE IDENTIFYING TEXT";
    after = ".bmp";
    scanData.ID{i} = char(extractBetween(Data.Files{i},before,after));
    scanData.FileName{i} = join(['Processed',scanData.ID{i},'.tif']);

    % Cropping the image
    scanData.Cropped{i} = imcrop(imread(Data.Files{i}),crop);
%         figure, imshow(scanData.Cropped{i})
%         title(['Cropped Image of ',suture,num2str(scanData.ID{i})])

    % Equalizing the GSV histograms so consistant adjustments will work
    scanData.Equalized{i} = histeq(scanData.Cropped{i},256);
%         figure, imshow(scanData.Equalized{i})
%         title(['Histogram Equalization ',suture,num2str(scanData.ID{i})])

    % Adjust the image intesity values to increase contrast
    scanData.Adjust{i} = imadjust(scanData.Equalized{i},[0.1,0.6],[0,1],1);
%         figure, imshow(scanData.Adjust{i})
%         title(['Adjusted Image of ',suture,scanData.ID{i}])

    % Binarizing the adjusted image
    scanData.BW{i}                                                          =
imbinarize(scanData.Adjust{i},'adaptive','Sensitivity',sens);
%         figure, imshow(scanData.BW{i})
%         title(['Binary Image of ',suture,scanData.ID{i}])

    % Filling the holes in the image
```

```
    scanData.Filled{i} = bwareaopen(scanData.BW{i}, 30, 4);
%         figure, imshow(scanData.Filled{i})
%         title(['Filled Image of ',suture,scanData.ID{i}])

%     % Morphologically opening image (sequential eriosion and dilation)
    scanData.Opened{i} = imopen(~scanData.Filled{i},se);
%         figure, imshow(scanData.Opened{i})
%         title(['Morphologically Opened ',suture,scanData.ID{i}])

    % Filling the holes in the image
    scanData.Filled2{i} = bwareaopen(scanData.Opened{i}, 30, 8);
%         figure, imshow(scanData.Filled2{i})
%         title(['Filled Image of Opened ',suture,scanData.ID{i}])


    %%%%%%%%%%%%%%%%%%%%%%%%%%%%%%%%%%%%%%%%%%%%%%%%%%%%%%%%%%%%%%%%%%%%%%%%%%%
    % BURNING WHITE REGION
    % Display images to prepare for ease of use
    burnedImage = scanData.Filled2{i};
    OGImage = scanData.Cropped{i};
    subplot(2, 2, 1);
    imshow(OGImage);
    title('Original Image', 'FontSize', fontSize);
    subplot(2, 2, 2);
    imshow(burnedImage);
    current=i;
    total=length(Data.Files);
    title(['Burn       White       Region,       Draw       Here:       Scan
',num2str(current),'/',num2str(total)], 'FontSize', fontSize);
    subplot(2, 2, 4);
    imshow(burnedImage);
    title('Original  Image  with  regions  burned  into  image',  'FontSize',
fontSize);
    set(gcf,  'units','normalized','outerposition',[0  0  1  1]);  %  Maximize
figure.
    set(gcf,'name','Manual Suture Segmentation','numbertitle','off')

    %----- Burn region into image -----
    % Create a binary image for all the regions we will draw.
    cumulativeBinaryImage = false(size(burnedImage));
    subplot(2, 2, 3);
    imshow(burnedImage);
    title('Binary Image', 'FontSize', fontSize);
    % Create region mask, h, as an ROI object over the second image in the
bottom row.
    axis on;
    again = true;
    regionCount = 0;
    while again && regionCount < 20
        promptMessage = sprintf('Draw region #%d in the upper right image,\nor
Quit?', regionCount + 1);
        titleBarCaption = 'Continue?';
        button  =  questdlg(promptMessage,  titleBarCaption,  'Draw',  'Quit',
'Draw');
        if strcmpi(button, 'Quit')
```

```
            break;
        end
        regionCount = regionCount + 1;
        subplot(2, 2, 2);

        % Ask user to draw freehand mask.
        message = sprintf('Left click and hold to begin drawing.\nSimply lift
the mouse button to finish');
        uiwait(msgbox(message));
        hFH = imfreehand(); % Actual line of code to do the drawing.
        % Create a binary image ("mask") from the ROI object.
        singleRegionBinaryImage = hFH.createMask();
        xy = hFH.getPosition;

        caption = sprintf('DRAW HERE.  Original Image with %d regions in
overlay.', regionCount);
        title(caption, 'FontSize', fontSize);

        % OR it in to the "all regions" binary image mask we're building up.
        cumulativeBinaryImage = cumulativeBinaryImage |
singleRegionBinaryImage;
        % Display the regions mask.
        subplot(2, 2, 3);
        imshow(cumulativeBinaryImage);
        caption = sprintf('Binary mask of the %d regions', regionCount);
        title(caption, 'FontSize', fontSize);

        % Burn region into image by setting it to 255 wherever the mask is true.
        burnedImage(cumulativeBinaryImage) = 255;
        % Display the image with the "burned in" region.
        subplot(2, 2, 4);
        cla;
        imshow(burnedImage);
        caption = sprintf('New image with %d regions burned into image',
regionCount);
        title(caption, 'FontSize', fontSize);
    end
    % Saving the Segmented Images
    scanData.PreSegmented{i}=burnedImage;

    %%%%%%%%%%%%%%%%%%%%%%%%%%%%%%%%%%%%%%%%%%%%%%%%%%%%%%%%%%%%%%%%%%%%%%%%%%%
    % BURNING BLACK REGION
    % Display images to prepare for ease of use
    burnedImage = scanData.PreSegmented{i};
    OGImage = scanData.Cropped{i};
    subplot(2, 2, 1);
    imshow(OGImage);
    title('Original Image', 'FontSize', fontSize);
    subplot(2, 2, 2);
    imshow(burnedImage);
    current=i;
    total=length(Data.Files);
    title(['Burn Black Region, Draw Here: Scan
',num2str(current),'/',num2str(total)], 'FontSize', fontSize);
    subplot(2, 2, 4);
```

```
    imshow(burnedImage);
    title('Original Image with regions burned into image', 'FontSize',
fontSize);
    set(gcf, 'units','normalized','outerposition',[0 0 1 1]); % Maximize
figure.
    set(gcf,'name','Manual Suture Segmentation','numbertitle','off')

    %----- Burn region into image -----
    % Create a binary image for all the regions we will draw.
    cumulativeBinaryImage = false(size(burnedImage));
    subplot(2, 2, 3);
    imshow(burnedImage);
    title('Binary Image', 'FontSize', fontSize);
    % Create region mask, h, as an ROI object over the second image in the
bottom row.
    axis on;
    again = true;
    regionCount = 0;
    while again && regionCount < 20
        promptMessage = sprintf('Draw region #%d in the upper right image,\nor
Quit?', regionCount + 1);
        titleBarCaption = 'Continue?';
        button = questdlg(promptMessage, titleBarCaption, 'Draw', 'Quit',
'Draw');
        if strcmpi(button, 'Quit')
            break;
        end
        regionCount = regionCount + 1;
        subplot(2, 2, 2);

        % Ask user to draw freehand mask.
        message = sprintf('Left click and hold to begin drawing.\nSimply lift
the mouse button to finish');
        uiwait(msgbox(message));
        hFH = imfreehand(); % Actual line of code to do the drawing.
        % Create a binary image ("mask") from the ROI object.
        singleRegionBinaryImage = hFH.createMask();
        xy = hFH.getPosition;

        caption = sprintf('DRAW HERE. Original Image with %d regions in
overlay.', regionCount);
        title(caption, 'FontSize', fontSize);

        % OR it in to the "all regions" binary image mask we're building up.
        cumulativeBinaryImage = cumulativeBinaryImage |
singleRegionBinaryImage;
        % Display the regions mask.
        subplot(2, 2, 3);
        imshow(cumulativeBinaryImage);
        caption = sprintf('Binary mask of the %d regions', regionCount);
        title(caption, 'FontSize', fontSize);

        % Burn region into image by setting it to 0 wherever the mask is true.
        burnedImage(cumulativeBinaryImage) = 0;
        % Display the image with the "burned in" region.
```

```
        subplot(2, 2, 4);
        cla;
        imshow(burnedImage);
        caption = sprintf('New image with %d regions burned into image',
regionCount);
        title(caption, 'FontSize', fontSize);
    end

    % Saving the Segmented Images
    scanData.ManualSegmented{i}=burnedImage;
        figure, imshow(scanData.ManualSegmented{i})
        title(['Post-Segmentation ',suture,scanData.ID{i}])

    % Isolating the largest area
    scanData.FinalArea{i} = bwpropfilt(scanData.ManualSegmented{i},'Area',1);
%         figure, imshow(scanData.FinalArea{i})
%         title(['Final Area ',suture,scanData.ID{i}])

    % Filling potential stray pixels within the ROI:
    scanData.SegSmooth{i} = imfill(scanData.FinalArea{i},'holes');
%         figure, imshow(scanData.SegSmooth{i})
%         title(['Fully Segmented ',suture,scanData.ID{i}])
end



%%%%%%%%%%%%%%%%%%%%%%%%%%%%%%%%%%%%%%%%%%%%%%%%%%%%%%%%%%%%%%%%%%%%%%%%%%%%%%%
%%%%% ANALYSIS %%%%%%%%%%%%%%%%%%%%%%%%%%%%%%%%%%%%%%%%%%%%%%%%%%%%%%%%%%%%%%%
%%%%%%%%%%%%%%%%%%%%%%%%%%%%%%%%%%%%%%%%%%%%%%%%%%%%%%%%%%%%%%%%%%%%%%%%%%%%%%%

% Looping though the segmented files
for i=1:(length(Data.Files))

[scanData.Center{i},scanData.Width{i}]=SutureAnalysis(scanData.SegSmooth{i});
end

h=length(Data.Files)*resize*resolution;      % Setting the initial height to
maximum
fig=figure;
for i=1:(length(Data.Files))
    scanData.h_LII{i}=h;
    height=h*ones(length(scanData.Center{i}(:,1)),1);

plot3(resize*resolution*scanData.Center{i}(:,1),(crop(1,4)*resolution*resize)
-resize*resolution*scanData.Center{i}(:,2),height)
    hold on
    h=h-resolution*resize;
end
hold off
ylim([0 4000]);
xlim([0 4000]);
title(['Centerlines Through Thickness, ',suture])
caz = -5;
cel = 30;
view([caz,cel]);
```

```
saveas(fig,[suturesave,'3D_Centerlines.jpg'])


% Determining the suture length
for i=1:(length(Data.Files))
scanData.CenterDistance{i}=diff(scanData.Center{i});
scanData.CenterDistance{i}=sqrt(scanData.CenterDistance{i}(:,1).^2+scanData.C
enterDistance{i}(:,2).^2);
scanData.SutureLength{i}=sum(scanData.CenterDistance{i});
end

% Determining LII (keeping in units of pixels)
scanData.SumLII=0;
for i=1:(length(Data.Files))
    scanData.LinDist{i}=sqrt((scanData.Center{1,i}(end,1)-
scanData.Center{1,i}(1,1))^2+(scanData.Center{1,i}(end,2)-
scanData.Center{1,i}(1,2))^2);
    scanData.LII{i}=scanData.SutureLength{i}/scanData.LinDist{i};
    scanData.SumLII=scanData.SumLII+scanData.LII{i};
end
% Mean LII of Dataset
for i=1:(length(Data.Files))
    scanData.MeanLII{i}=scanData.SumLII/length(Data.Files);
end

% Plotting LII vs Height
fig=figure;
scatter([scanData.LII{:}], [scanData.h_LII{:}], 'filled')
hold on
plot([scanData.MeanLII{:}], [scanData.h_LII{:}], 'r', 'LineWidth', 1);
hold off
title(['Suture LII Through Skull Thickness, ',suture])
xlabel('Linear Interdigitation Index')
ylabel('Position in Skull, \mum (Datum at inner surface)')
ylim([0 500]);
xlim([1 3]);
legend('LII at Slice','Average LII of Suture')
saveas(fig,[suturesave,'LII_Thickness.jpg'])

% Determining Average Width of Each Slice
scanData.SumWidth=0;
for i=1:(length(Data.Files))

scanData.AvgWidth{i}=resize*resolution.*sum(scanData.Width{i})/length(scanDat
a.Width{i});
    scanData.SumWidth=scanData.SumWidth+scanData.AvgWidth{i};
end
% Mean Average Width of Dataset
for i=1:(length(Data.Files))
    scanData.MeanWidth{i}=scanData.SumWidth/length(Data.Files);
end

% Plotting Average Width  vs. Height
fig=figure;
scatter([scanData.AvgWidth{:}], [scanData.h_LII{:}], 'filled')
```

```
hold on
plot([scanData.MeanWidth{:}], [scanData.h_LII{:}], 'r', 'LineWidth', 1);
hold off
title(['Suture Average Width Through Thickness, ',suture])
xlabel('Average Width, \mum')
ylabel('Position in Skull, \mum (Datum at inner surface)')
ylim([0 500]);
xlim([100 400]);
legend('Average Width at Slice','Average Width of Suture')
saveas(fig,[suturesave,'Width_Thickness.jpg'])

% Saving Data
save('scanData.mat','scanData')
```

A6 Compiling Dataset Results

This script compiles the full suture data from the 15 rats considered in the analysis, it was used in Chapter 4.

```
% THIS SCRIPT IS USED TO COMPILE THE RESULTS OF THE INDIVIDUAL SUTURE
ANALYSIS

close all
clear
clc

%%%%%%%%%%%%%%%%%%%%%%%%%%%%%%%%%%%%%%%%%%%%%%%%%%%%%%%%%%%%%%%%%%%%%%%%%%%%%%%
%%% LOADING DATASETS %%%%%%%%%%%%%%%%%%%%%%%%%%%%%%%%%%%%%%%%%%%%%%%%%%%%%%%%%%
%%%%%%%%%%%%%%%%%%%%%%%%%%%%%%%%%%%%%%%%%%%%%%%%%%%%%%%%%%%%%%%%%%%%%%%%%%%%%%%

%%% 16 WEEK DATA %%%%%%%%%%%%%%%%%%%%%%%%%%%%%%%%%%%%%%%%%%%%%%%%%%%%%%%%%%%%%%%
% BML3:
load('E:\Ross\Rats\MATLAB Analysis\Combined Analysis\Data\16
Week\BML3\BML3_AL_LHS.mat')
load('E:\Ross\Rats\MATLAB Analysis\Combined Analysis\Data\16
Week\BML3\BML3_AL_RHS.mat')
load('E:\Ross\Rats\MATLAB Analysis\Combined Analysis\Data\16
Week\BML3\BML3_Cor_LHS.mat')
load('E:\Ross\Rats\MATLAB Analysis\Combined Analysis\Data\16
Week\BML3\BML3_Cor_RHS.mat')
load('E:\Ross\Rats\MATLAB Analysis\Combined Analysis\Data\16
Week\BML3\BML3_PL.mat')
load('E:\Ross\Rats\MATLAB Analysis\Combined Analysis\Data\16
Week\BML3\BML3_Sag.mat')
% BML11:
load('E:\Ross\Rats\MATLAB Analysis\Combined Analysis\Data\16
Week\BML11\BML11_AL_LHS.mat')
load('E:\Ross\Rats\MATLAB Analysis\Combined Analysis\Data\16
Week\BML11\BML11_AL_RHS.mat')
load('E:\Ross\Rats\MATLAB Analysis\Combined Analysis\Data\16
Week\BML11\BML11_Cor_LHS.mat')
load('E:\Ross\Rats\MATLAB Analysis\Combined Analysis\Data\16
Week\BML11\BML11_Cor_RHS.mat')
```

```
load('E:\Ross\Rats\MATLAB Analysis\Combined Analysis\Data\16
Week\BML11\BML11_PL.mat')
load('E:\Ross\Rats\MATLAB Analysis\Combined Analysis\Data\16
Week\BML11\BML11_Sag.mat')
% BML12:
load('E:\Ross\Rats\MATLAB Analysis\Combined Analysis\Data\16
Week\BML12\BML12_AL_LHS.mat')
load('E:\Ross\Rats\MATLAB Analysis\Combined Analysis\Data\16
Week\BML12\BML12_AL_RHS.mat')
load('E:\Ross\Rats\MATLAB Analysis\Combined Analysis\Data\16
Week\BML12\BML12_Cor_LHS.mat')
load('E:\Ross\Rats\MATLAB Analysis\Combined Analysis\Data\16
Week\BML12\BML12_Cor_RHS.mat')
load('E:\Ross\Rats\MATLAB Analysis\Combined Analysis\Data\16
Week\BML12\BML12_PL.mat')
load('E:\Ross\Rats\MATLAB Analysis\Combined Analysis\Data\16
Week\BML12\BML12_Sag.mat')
% % BML35
load('E:\Ross\Rats\MATLAB Analysis\Combined Analysis\Data\16
Week\BML35\BML35_AL_LHS.mat')
load('E:\Ross\Rats\MATLAB Analysis\Combined Analysis\Data\16
Week\BML35\BML35_AL_RHS.mat')
load('E:\Ross\Rats\MATLAB Analysis\Combined Analysis\Data\16
Week\BML35\BML35_Cor_LHS.mat')
load('E:\Ross\Rats\MATLAB Analysis\Combined Analysis\Data\16
Week\BML35\BML35_Cor_RHS.mat')
load('E:\Ross\Rats\MATLAB Analysis\Combined Analysis\Data\16
Week\BML35\BML35_PL.mat')
load('E:\Ross\Rats\MATLAB Analysis\Combined Analysis\Data\16
Week\BML35\BML35_Sag.mat')
% % BML36
load('E:\Ross\Rats\MATLAB Analysis\Combined Analysis\Data\16
Week\BML36\BML36_AL_LHS.mat')
load('E:\Ross\Rats\MATLAB Analysis\Combined Analysis\Data\16
Week\BML36\BML36_AL_RHS.mat')
load('E:\Ross\Rats\MATLAB Analysis\Combined Analysis\Data\16
Week\BML36\BML36_Cor_LHS.mat')
load('E:\Ross\Rats\MATLAB Analysis\Combined Analysis\Data\16
Week\BML36\BML36_Cor_RHS.mat')
load('E:\Ross\Rats\MATLAB Analysis\Combined Analysis\Data\16
Week\BML36\BML36_PL.mat')
load('E:\Ross\Rats\MATLAB Analysis\Combined Analysis\Data\16
Week\BML36\BML36_Sag.mat')

%%% 20 WEEK DATA %%%%%%%%%%%%%%%%%%%%%%%%%%%%%%%%%%%%%%%%%%%%%%%%%%%%%%%%%%%%
% BML4A:
load('E:\Ross\Rats\MATLAB Analysis\Combined Analysis\Data\20
Week\BML4A\BML4A_AL_LHS.mat')
load('E:\Ross\Rats\MATLAB Analysis\Combined Analysis\Data\20
Week\BML4A\BML4A_AL_RHS.mat')
load('E:\Ross\Rats\MATLAB Analysis\Combined Analysis\Data\20
Week\BML4A\BML4A_Cor_LHS.mat')
load('E:\Ross\Rats\MATLAB Analysis\Combined Analysis\Data\20
Week\BML4A\BML4A_Cor_RHS.mat')
```

```
load('E:\Ross\Rats\MATLAB Analysis\Combined Analysis\Data\20
Week\BML4A\BML4A_PL.mat')
load('E:\Ross\Rats\MATLAB Analysis\Combined Analysis\Data\20
Week\BML4A\BML4A_Sag.mat')
% BML5:
load('E:\Ross\Rats\MATLAB Analysis\Combined Analysis\Data\20
Week\BML5\BML5_AL_LHS.mat')
load('E:\Ross\Rats\MATLAB Analysis\Combined Analysis\Data\20
Week\BML5\BML5_AL_RHS.mat')
load('E:\Ross\Rats\MATLAB Analysis\Combined Analysis\Data\20
Week\BML5\BML5_Cor_LHS.mat')
load('E:\Ross\Rats\MATLAB Analysis\Combined Analysis\Data\20
Week\BML5\BML5_Cor_RHS.mat')
load('E:\Ross\Rats\MATLAB Analysis\Combined Analysis\Data\20
Week\BML5\BML5_PL.mat')
load('E:\Ross\Rats\MATLAB Analysis\Combined Analysis\Data\20
Week\BML5\BML5_Sag.mat')
% BML15:
load('E:\Ross\Rats\MATLAB Analysis\Combined Analysis\Data\20
Week\BML15\BML15_AL_LHS.mat')
load('E:\Ross\Rats\MATLAB Analysis\Combined Analysis\Data\20
Week\BML15\BML15_AL_RHS.mat')
load('E:\Ross\Rats\MATLAB Analysis\Combined Analysis\Data\20
Week\BML15\BML15_Cor_LHS.mat')
load('E:\Ross\Rats\MATLAB Analysis\Combined Analysis\Data\20
Week\BML15\BML15_Cor_RHS.mat')
load('E:\Ross\Rats\MATLAB Analysis\Combined Analysis\Data\20
Week\BML15\BML15_PL.mat')
load('E:\Ross\Rats\MATLAB Analysis\Combined Analysis\Data\20
Week\BML15\BML15_Sag.mat')
% BML25:
load('E:\Ross\Rats\MATLAB Analysis\Combined Analysis\Data\20
Week\BML25\BML25_AL_LHS.mat')
load('E:\Ross\Rats\MATLAB Analysis\Combined Analysis\Data\20
Week\BML25\BML25_AL_RHS.mat')
load('E:\Ross\Rats\MATLAB Analysis\Combined Analysis\Data\20
Week\BML25\BML25_Cor_LHS.mat')
load('E:\Ross\Rats\MATLAB Analysis\Combined Analysis\Data\20
Week\BML25\BML25_Cor_RHS.mat')
load('E:\Ross\Rats\MATLAB Analysis\Combined Analysis\Data\20
Week\BML25\BML25_PL.mat')
load('E:\Ross\Rats\MATLAB Analysis\Combined Analysis\Data\20
Week\BML25\BML25_Sag.mat')
% % BML26:
load('E:\Ross\Rats\MATLAB Analysis\Combined Analysis\Data\20
Week\BML26\BML26_AL_LHS.mat')
load('E:\Ross\Rats\MATLAB Analysis\Combined Analysis\Data\20
Week\BML26\BML26_AL_RHS.mat')
load('E:\Ross\Rats\MATLAB Analysis\Combined Analysis\Data\20
Week\BML26\BML26_Cor_LHS.mat')
load('E:\Ross\Rats\MATLAB Analysis\Combined Analysis\Data\20
Week\BML26\BML26_Cor_RHS.mat')
load('E:\Ross\Rats\MATLAB Analysis\Combined Analysis\Data\20
Week\BML26\BML26_PL.mat')
```

```
load('E:\Ross\Rats\MATLAB Analysis\Combined Analysis\Data\20
Week\BML26\BML26_Sag.mat')

%%% 24 WEEK DATA %%%%%%%%%%%%%%%%%%%%%%%%%%%%%%%%%%%%%%%%%%%%%%%%%%%%%%%%%%%%
% BML8:
load('E:\Ross\Rats\MATLAB Analysis\Combined Analysis\Data\24
Week\BML8\BML8_AL_LHS.mat')
load('E:\Ross\Rats\MATLAB Analysis\Combined Analysis\Data\24
Week\BML8\BML8_AL_RHS.mat')
load('E:\Ross\Rats\MATLAB Analysis\Combined Analysis\Data\24
Week\BML8\BML8_Cor_LHS.mat')
load('E:\Ross\Rats\MATLAB Analysis\Combined Analysis\Data\24
Week\BML8\BML8_Cor_RHS.mat')
load('E:\Ross\Rats\MATLAB Analysis\Combined Analysis\Data\24
Week\BML8\BML8_PL.mat')
load('E:\Ross\Rats\MATLAB Analysis\Combined Analysis\Data\24
Week\BML8\BML8_Sag.mat')
% BML18:
load('E:\Ross\Rats\MATLAB Analysis\Combined Analysis\Data\24
Week\BML18\BML18_AL_LHS.mat')
load('E:\Ross\Rats\MATLAB Analysis\Combined Analysis\Data\24
Week\BML18\BML18_AL_RHS.mat')
load('E:\Ross\Rats\MATLAB Analysis\Combined Analysis\Data\24
Week\BML18\BML18_Cor_LHS.mat')
load('E:\Ross\Rats\MATLAB Analysis\Combined Analysis\Data\24
Week\BML18\BML18_Cor_RHS.mat')
load('E:\Ross\Rats\MATLAB Analysis\Combined Analysis\Data\24
Week\BML18\BML18_PL.mat')
load('E:\Ross\Rats\MATLAB Analysis\Combined Analysis\Data\24
Week\BML18\BML18_Sag.mat')
% BML20:
load('E:\Ross\Rats\MATLAB Analysis\Combined Analysis\Data\24
Week\BML20\BML20_AL_LHS.mat')
load('E:\Ross\Rats\MATLAB Analysis\Combined Analysis\Data\24
Week\BML20\BML20_AL_RHS.mat')
load('E:\Ross\Rats\MATLAB Analysis\Combined Analysis\Data\24
Week\BML20\BML20_Cor_LHS.mat')
load('E:\Ross\Rats\MATLAB Analysis\Combined Analysis\Data\24
Week\BML20\BML20_Cor_RHS.mat')
load('E:\Ross\Rats\MATLAB Analysis\Combined Analysis\Data\24
Week\BML20\BML20_PL.mat')
load('E:\Ross\Rats\MATLAB Analysis\Combined Analysis\Data\24
Week\BML20\BML20_Sag.mat')
% BML21:
load('E:\Ross\Rats\MATLAB Analysis\Combined Analysis\Data\24
Week\BML21\BML21_AL_LHS.mat')
load('E:\Ross\Rats\MATLAB Analysis\Combined Analysis\Data\24
Week\BML21\BML21_AL_RHS.mat')
load('E:\Ross\Rats\MATLAB Analysis\Combined Analysis\Data\24
Week\BML21\BML21_Cor_LHS.mat')
load('E:\Ross\Rats\MATLAB Analysis\Combined Analysis\Data\24
Week\BML21\BML21_Cor_RHS.mat')
load('E:\Ross\Rats\MATLAB Analysis\Combined Analysis\Data\24
Week\BML21\BML21_PL.mat')
```

```
load('E:\Ross\Rats\MATLAB Analysis\Combined Analysis\Data\24
Week\BML21\BML21_Sag.mat')
% BML16:
load('E:\Ross\Rats\MATLAB Analysis\Combined Analysis\Data\24
Week\BML16\BML16_AL_LHS.mat')
load('E:\Ross\Rats\MATLAB Analysis\Combined Analysis\Data\24
Week\BML16\BML16_AL_RHS.mat')
load('E:\Ross\Rats\MATLAB Analysis\Combined Analysis\Data\24
Week\BML16\BML16_Cor_LHS.mat')
load('E:\Ross\Rats\MATLAB Analysis\Combined Analysis\Data\24
Week\BML16\BML16_Cor_RHS.mat')
load('E:\Ross\Rats\MATLAB Analysis\Combined Analysis\Data\24
Week\BML16\BML16_Sag.mat')

%%%%%%%%%%%%%%%%%%%%%%%%%%%%%%%%%%%%%%%%%%%%%%%%%%%%%%%%%%%%%%%%%%%%%%%%%%%%%%%
%%% STATISTICAL MEASURES %%%%%%%%%%%%%%%%%%%%%%%%%%%%%%%%%%%%%%%%%%%%%%%%%%%%%
%%%%%%%%%%%%%%%%%%%%%%%%%%%%%%%%%%%%%%%%%%%%%%%%%%%%%%%%%%%%%%%%%%%%%%%%%%%%%%%

% 16 WEEK
% BML3:
BML3_AL_LHS.LII_StdDev = std([BML3_AL_LHS.LII{:}]);
BML3_AL_LHS.AvgWidth_StdDev = std([BML3_AL_LHS.AvgWidth{:}]);
BML3_AL_RHS.LII_StdDev = std([BML3_AL_RHS.LII{:}]);
BML3_AL_RHS.AvgWidth_StdDev = std([BML3_AL_RHS.AvgWidth{:}]);
BML3_Cor_LHS.LII_StdDev = std([BML3_Cor_LHS.LII{:}]);
BML3_Cor_LHS.AvgWidth_StdDev = std([BML3_Cor_LHS.AvgWidth{:}]);
BML3_Cor_RHS.LII_StdDev = std([BML3_Cor_RHS.LII{:}]);
BML3_Cor_RHS.AvgWidth_StdDev = std([BML3_Cor_RHS.AvgWidth{:}]);
BML3_PL.LII_StdDev = std([BML3_PL.LII{:}]);
BML3_PL.AvgWidth_StdDev = std([BML3_PL.AvgWidth{:}]);
BML3_Sag.LII_StdDev = std([BML3_Sag.LII{:}]);
BML3_Sag.AvgWidth_StdDev = std([BML3_Sag.AvgWidth{:}]);
% BML 11:
BML11_AL_LHS.LII_StdDev = std([BML11_AL_LHS.LII{:}]);
BML11_AL_LHS.AvgWidth_StdDev = std([BML11_AL_LHS.AvgWidth{:}]);
BML11_AL_RHS.LII_StdDev = std([BML11_AL_RHS.LII{:}]);
BML11_AL_RHS.AvgWidth_StdDev = std([BML11_AL_RHS.AvgWidth{:}]);
BML11_Cor_LHS.LII_StdDev = std([BML11_Cor_LHS.LII{:}]);
BML11_Cor_LHS.AvgWidth_StdDev = std([BML11_Cor_LHS.AvgWidth{:}]);
BML11_Cor_RHS.LII_StdDev = std([BML11_Cor_RHS.LII{:}]);
BML11_Cor_RHS.AvgWidth_StdDev = std([BML11_Cor_RHS.AvgWidth{:}]);
BML11_PL.LII_StdDev = std([BML11_PL.LII{:}]);
BML11_PL.AvgWidth_StdDev = std([BML11_PL.AvgWidth{:}]);
BML11_Sag.LII_StdDev = std([BML11_Sag.LII{:}]);
BML11_Sag.AvgWidth_StdDev = std([BML11_Sag.AvgWidth{:}]);
% BML 12:
BML12_AL_LHS.LII_StdDev = std([BML12_AL_LHS.LII{:}]);
BML12_AL_LHS.AvgWidth_StdDev = std([BML12_AL_LHS.AvgWidth{:}]);
BML12_AL_RHS.LII_StdDev = std([BML12_AL_RHS.LII{:}]);
BML12_AL_RHS.AvgWidth_StdDev = std([BML12_AL_RHS.AvgWidth{:}]);
BML12_Cor_LHS.LII_StdDev = std([BML12_Cor_LHS.LII{:}]);
BML12_Cor_LHS.AvgWidth_StdDev = std([BML12_Cor_LHS.AvgWidth{:}]);
BML12_Cor_RHS.LII_StdDev = std([BML12_Cor_RHS.LII{:}]);
BML12_Cor_RHS.AvgWidth_StdDev = std([BML12_Cor_RHS.AvgWidth{:}]);
BML12_PL.LII_StdDev = std([BML12_PL.LII{:}]);
```

```
BML12_PL.AvgWidth_StdDev = std([BML12_PL.AvgWidth{:}]);
BML12_Sag.LII_StdDev = std([BML12_Sag.LII{:}]);
BML12_Sag.AvgWidth_StdDev = std([BML12_Sag.AvgWidth{:}]);
% BML 35:
BML35_AL_LHS.LII_StdDev = std([BML35_AL_LHS.LII{:}]);
BML35_AL_LHS.AvgWidth_StdDev = std([BML35_AL_LHS.AvgWidth{:}]);
BML35_AL_RHS.LII_StdDev = std([BML35_AL_RHS.LII{:}]);
BML35_AL_RHS.AvgWidth_StdDev = std([BML35_AL_RHS.AvgWidth{:}]);
BML35_Cor_LHS.LII_StdDev = std([BML35_Cor_LHS.LII{:}]);
BML35_Cor_LHS.AvgWidth_StdDev = std([BML35_Cor_LHS.AvgWidth{:}]);
BML35_Cor_RHS.LII_StdDev = std([BML35_Cor_RHS.LII{:}]);
BML35_Cor_RHS.AvgWidth_StdDev = std([BML35_Cor_RHS.AvgWidth{:}]);
BML35_PL.LII_StdDev = std([BML35_PL.LII{:}]);
BML35_PL.AvgWidth_StdDev = std([BML35_PL.AvgWidth{:}]);
BML35_Sag.LII_StdDev = std([BML35_Sag.LII{:}]);
BML35_Sag.AvgWidth_StdDev = std([BML35_Sag.AvgWidth{:}]);
% BML 36:
BML36_AL_LHS.LII_StdDev = std([BML36_AL_LHS.LII{:}]);
BML36_AL_LHS.AvgWidth_StdDev = std([BML36_AL_LHS.AvgWidth{:}]);
BML36_AL_RHS.LII_StdDev = std([BML36_AL_RHS.LII{:}]);
BML36_AL_RHS.AvgWidth_StdDev = std([BML36_AL_RHS.AvgWidth{:}]);
BML36_Cor_LHS.LII_StdDev = std([BML36_Cor_LHS.LII{:}]);
BML36_Cor_LHS.AvgWidth_StdDev = std([BML36_Cor_LHS.AvgWidth{:}]);
BML36_Cor_RHS.LII_StdDev = std([BML36_Cor_RHS.LII{:}]);
BML36_Cor_RHS.AvgWidth_StdDev = std([BML36_Cor_RHS.AvgWidth{:}]);
BML36_PL.LII_StdDev = std([BML36_PL.LII{:}]);
BML36_PL.AvgWidth_StdDev = std([BML36_PL.AvgWidth{:}]);
BML36_Sag.LII_StdDev = std([BML36_Sag.LII{:}]);
BML36_Sag.AvgWidth_StdDev = std([BML36_Sag.AvgWidth{:}]);

% 20 WEEK
% BML5:
BML5_AL_LHS.LII_StdDev = std([BML5_AL_LHS.LII{:}]);
BML5_AL_LHS.AvgWidth_StdDev = std([BML5_AL_LHS.AvgWidth{:}]);
BML5_AL_RHS.LII_StdDev = std([BML5_AL_RHS.LII{:}]);
BML5_AL_RHS.AvgWidth_StdDev = std([BML5_AL_RHS.AvgWidth{:}]);
BML5_Cor_LHS.LII_StdDev = std([BML5_Cor_LHS.LII{:}]);
BML5_Cor_LHS.AvgWidth_StdDev = std([BML5_Cor_LHS.AvgWidth{:}]);
BML5_Cor_RHS.LII_StdDev = std([BML5_Cor_RHS.LII{:}]);
BML5_Cor_RHS.AvgWidth_StdDev = std([BML5_Cor_RHS.AvgWidth{:}]);
BML5_PL.LII_StdDev = std([BML5_PL.LII{:}]);
BML5_PL.AvgWidth_StdDev = std([BML5_PL.AvgWidth{:}]);
BML5_Sag.LII_StdDev = std([BML5_Sag.LII{:}]);
BML5_Sag.AvgWidth_StdDev = std([BML5_Sag.AvgWidth{:}]);
% BML 4A:
BML4A_AL_LHS.LII_StdDev = std([BML4A_AL_LHS.LII{:}]);
BML4A_AL_LHS.AvgWidth_StdDev = std([BML4A_AL_LHS.AvgWidth{:}]);
BML4A_AL_RHS.LII_StdDev = std([BML4A_AL_RHS.LII{:}]);
BML4A_AL_RHS.AvgWidth_StdDev = std([BML4A_AL_RHS.AvgWidth{:}]);
BML4A_Cor_LHS.LII_StdDev = std([BML4A_Cor_LHS.LII{:}]);
BML4A_Cor_LHS.AvgWidth_StdDev = std([BML4A_Cor_LHS.AvgWidth{:}]);
BML4A_Cor_RHS.LII_StdDev = std([BML4A_Cor_RHS.LII{:}]);
BML4A_Cor_RHS.AvgWidth_StdDev = std([BML4A_Cor_RHS.AvgWidth{:}]);
BML4A_PL.LII_StdDev = std([BML4A_PL.LII{:}]);
BML4A_PL.AvgWidth_StdDev = std([BML4A_PL.AvgWidth{:}]);
```

```
BML4A_Sag.LII_StdDev = std([BML4A_Sag.LII{:}]);
BML4A_Sag.AvgWidth_StdDev = std([BML4A_Sag.AvgWidth{:}]);
% BML 15:
BML15_AL_LHS.LII_StdDev = std([BML15_AL_LHS.LII{:}]);
BML15_AL_LHS.AvgWidth_StdDev = std([BML15_AL_LHS.AvgWidth{:}]);
BML15_AL_RHS.LII_StdDev = std([BML15_AL_RHS.LII{:}]);
BML15_AL_RHS.AvgWidth_StdDev = std([BML15_AL_RHS.AvgWidth{:}]);
BML15_Cor_LHS.LII_StdDev = std([BML15_Cor_LHS.LII{:}]);
BML15_Cor_LHS.AvgWidth_StdDev = std([BML15_Cor_LHS.AvgWidth{:}]);
BML15_Cor_RHS.LII_StdDev = std([BML15_Cor_RHS.LII{:}]);
BML15_Cor_RHS.AvgWidth_StdDev = std([BML15_Cor_RHS.AvgWidth{:}]);
BML15_PL.LII_StdDev = std([BML15_PL.LII{:}]);
BML15_PL.AvgWidth_StdDev = std([BML15_PL.AvgWidth{:}]);
BML15_Sag.LII_StdDev = std([BML15_Sag.LII{:}]);
BML15_Sag.AvgWidth_StdDev = std([BML15_Sag.AvgWidth{:}]);
% BML 25:
BML25_AL_LHS.LII_StdDev = std([BML25_AL_LHS.LII{:}]);
BML25_AL_LHS.AvgWidth_StdDev = std([BML25_AL_LHS.AvgWidth{:}]);
BML25_AL_RHS.LII_StdDev = std([BML25_AL_RHS.LII{:}]);
BML25_AL_RHS.AvgWidth_StdDev = std([BML25_AL_RHS.AvgWidth{:}]);
BML25_Cor_LHS.LII_StdDev = std([BML25_Cor_LHS.LII{:}]);
BML25_Cor_LHS.AvgWidth_StdDev = std([BML25_Cor_LHS.AvgWidth{:}]);
BML25_Cor_RHS.LII_StdDev = std([BML25_Cor_RHS.LII{:}]);
BML25_Cor_RHS.AvgWidth_StdDev = std([BML25_Cor_RHS.AvgWidth{:}]);
BML25_PL.LII_StdDev = std([BML25_PL.LII{:}]);
BML25_PL.AvgWidth_StdDev = std([BML25_PL.AvgWidth{:}]);
BML25_Sag.LII_StdDev = std([BML25_Sag.LII{:}]);
BML25_Sag.AvgWidth_StdDev = std([BML25_Sag.AvgWidth{:}]);
% BML 26:
BML26_AL_LHS.LII_StdDev = std([BML26_AL_LHS.LII{:}]);
BML26_AL_LHS.AvgWidth_StdDev = std([BML26_AL_LHS.AvgWidth{:}]);
BML26_AL_RHS.LII_StdDev = std([BML26_AL_RHS.LII{:}]);
BML26_AL_RHS.AvgWidth_StdDev = std([BML26_AL_RHS.AvgWidth{:}]);
BML26_Cor_LHS.LII_StdDev = std([BML26_Cor_LHS.LII{:}]);
BML26_Cor_LHS.AvgWidth_StdDev = std([BML26_Cor_LHS.AvgWidth{:}]);
BML26_Cor_RHS.LII_StdDev = std([BML26_Cor_RHS.LII{:}]);
BML26_Cor_RHS.AvgWidth_StdDev = std([BML26_Cor_RHS.AvgWidth{:}]);
BML26_PL.LII_StdDev = std([BML26_PL.LII{:}]);
BML26_PL.AvgWidth_StdDev = std([BML26_PL.AvgWidth{:}]);
BML26_Sag.LII_StdDev = std([BML26_Sag.LII{:}]);
BML26_Sag.AvgWidth_StdDev = std([BML26_Sag.AvgWidth{:}]);

% 24 WEEK
% BML8:
BML8_AL_LHS.LII_StdDev = std([BML8_AL_LHS.LII{:}]);
BML8_AL_LHS.AvgWidth_StdDev = std([BML8_AL_LHS.AvgWidth{:}]);
BML8_AL_RHS.LII_StdDev = std([BML8_AL_RHS.LII{:}]);
BML8_AL_RHS.AvgWidth_StdDev = std([BML8_AL_RHS.AvgWidth{:}]);
BML8_Cor_LHS.LII_StdDev = std([BML8_Cor_LHS.LII{:}]);
BML8_Cor_LHS.AvgWidth_StdDev = std([BML8_Cor_LHS.AvgWidth{:}]);
BML8_Cor_RHS.LII_StdDev = std([BML8_Cor_RHS.LII{:}]);
BML8_Cor_RHS.AvgWidth_StdDev = std([BML8_Cor_RHS.AvgWidth{:}]);
BML8_PL.LII_StdDev = std([BML8_PL.LII{:}]);
BML8_PL.AvgWidth_StdDev = std([BML8_PL.AvgWidth{:}]);
BML8_Sag.LII_StdDev = std([BML8_Sag.LII{:}]);
```

```
BML8_Sag.AvgWidth_StdDev = std([BML8_Sag.AvgWidth{:}]);
% BML 18:
BML18_AL_LHS.LII_StdDev = std([BML18_AL_LHS.LII{:}]);
BML18_AL_LHS.AvgWidth_StdDev = std([BML18_AL_LHS.AvgWidth{:}]);
BML18_AL_RHS.LII_StdDev = std([BML18_AL_RHS.LII{:}]);
BML18_AL_RHS.AvgWidth_StdDev = std([BML18_AL_RHS.AvgWidth{:}]);
BML18_Cor_LHS.LII_StdDev = std([BML18_Cor_LHS.LII{:}]);
BML18_Cor_LHS.AvgWidth_StdDev = std([BML18_Cor_LHS.AvgWidth{:}]);
BML18_Cor_RHS.LII_StdDev = std([BML18_Cor_RHS.LII{:}]);
BML18_Cor_RHS.AvgWidth_StdDev = std([BML18_Cor_RHS.AvgWidth{:}]);
BML18_PL.LII_StdDev = std([BML18_PL.LII{:}]);
BML18_PL.AvgWidth_StdDev = std([BML18_PL.AvgWidth{:}]);
BML18_Sag.LII_StdDev = std([BML18_Sag.LII{:}]);
BML18_Sag.AvgWidth_StdDev = std([BML18_Sag.AvgWidth{:}]);
% BML 20:
BML20_AL_LHS.LII_StdDev = std([BML20_AL_LHS.LII{:}]);
BML20_AL_LHS.AvgWidth_StdDev = std([BML20_AL_LHS.AvgWidth{:}]);
BML20_AL_RHS.LII_StdDev = std([BML20_AL_RHS.LII{:}]);
BML20_AL_RHS.AvgWidth_StdDev = std([BML20_AL_RHS.AvgWidth{:}]);
BML20_Cor_LHS.LII_StdDev = std([BML20_Cor_LHS.LII{:}]);
BML20_Cor_LHS.AvgWidth_StdDev = std([BML20_Cor_LHS.AvgWidth{:}]);
BML20_Cor_RHS.LII_StdDev = std([BML20_Cor_RHS.LII{:}]);
BML20_Cor_RHS.AvgWidth_StdDev = std([BML20_Cor_RHS.AvgWidth{:}]);
BML20_PL.LII_StdDev = std([BML20_PL.LII{:}]);
BML20_PL.AvgWidth_StdDev = std([BML20_PL.AvgWidth{:}]);
BML20_Sag.LII_StdDev = std([BML20_Sag.LII{:}]);
BML20_Sag.AvgWidth_StdDev = std([BML20_Sag.AvgWidth{:}]);
% BML 21:
BML21_AL_LHS.LII_StdDev = std([BML21_AL_LHS.LII{:}]);
BML21_AL_LHS.AvgWidth_StdDev = std([BML21_AL_LHS.AvgWidth{:}]);
BML21_AL_RHS.LII_StdDev = std([BML21_AL_RHS.LII{:}]);
BML21_AL_RHS.AvgWidth_StdDev = std([BML21_AL_RHS.AvgWidth{:}]);
BML21_Cor_LHS.LII_StdDev = std([BML21_Cor_LHS.LII{:}]);
BML21_Cor_LHS.AvgWidth_StdDev = std([BML21_Cor_LHS.AvgWidth{:}]);
BML21_Cor_RHS.LII_StdDev = std([BML21_Cor_RHS.LII{:}]);
BML21_Cor_RHS.AvgWidth_StdDev = std([BML21_Cor_RHS.AvgWidth{:}]);
BML21_PL.LII_StdDev = std([BML21_PL.LII{:}]);
BML21_PL.AvgWidth_StdDev = std([BML21_PL.AvgWidth{:}]);
BML21_Sag.LII_StdDev = std([BML21_Sag.LII{:}]);
BML21_Sag.AvgWidth_StdDev = std([BML21_Sag.AvgWidth{:}]);
% BML 16:
BML16_AL_LHS.LII_StdDev = std([BML16_AL_LHS.LII{:}]);
BML16_AL_LHS.AvgWidth_StdDev = std([BML16_AL_LHS.AvgWidth{:}]);
BML16_AL_RHS.LII_StdDev = std([BML16_AL_RHS.LII{:}]);
BML16_AL_RHS.AvgWidth_StdDev = std([BML16_AL_RHS.AvgWidth{:}]);
BML16_Cor_LHS.LII_StdDev = std([BML16_Cor_LHS.LII{:}]);
BML16_Cor_LHS.AvgWidth_StdDev = std([BML16_Cor_LHS.AvgWidth{:}]);
BML16_Cor_RHS.LII_StdDev = std([BML16_Cor_RHS.LII{:}]);
BML16_Cor_RHS.AvgWidth_StdDev = std([BML16_Cor_RHS.AvgWidth{:}]);
BML16_Sag.LII_StdDev = std([BML16_Sag.LII{:}]);
BML16_Sag.AvgWidth_StdDev = std([BML16_Sag.AvgWidth{:}]);


%%%%%%%%%%%%%%%%%%%%%%%%%%%%%%%%%%%%%%%%%%%%%%%%%%%%%%%%%%%%%%%%%%%%%%%%%%%%%%%
%%% COMPILING MEAN LII %%%%%%*%%%%%%%%%%%%%%%%%%%%%%%%%%%%%%%%%%%%%%%%%%%%%%%%
```

```
%%%%%%%%%%%%%%%%%%%%%%%%%%%%%%%%%%%%%%%%%%%%%%%%%%%%%%%%%%%%%%%%%%%%%%%%%%%%

% Restructuring LII Data:
LII = struct();
% 16 Week Samples (NOTE NEED TO MODIFY THIS TO ADD THE LAST 2 RATS WHEN  I
GET THEM
LII.W16_AL_LHS =
[BML3_AL_LHS.MeanLII{1},BML11_AL_LHS.MeanLII{1},BML12_AL_LHS.MeanLII{1},BML35
_AL_LHS.MeanLII{1},BML36_AL_LHS.MeanLII{1}];
LII.W16_AL_RHS =
[BML3_AL_RHS.MeanLII{1},BML11_AL_RHS.MeanLII{1},BML12_AL_RHS.MeanLII{1},BML35
_AL_RHS.MeanLII{1},BML36_AL_RHS.MeanLII{1}];
LII.W16_Cor_LHS =
[BML3_Cor_LHS.MeanLII{1},BML11_Cor_LHS.MeanLII{1},BML12_Cor_LHS.MeanLII{1},BM
L35_Cor_LHS.MeanLII{1},BML36_Cor_LHS.MeanLII{1}];
LII.W16_Cor_RHS =
[BML3_Cor_RHS.MeanLII{1},BML11_Cor_RHS.MeanLII{1},BML12_Cor_RHS.MeanLII{1},BM
L35_Cor_RHS.MeanLII{1},BML36_Cor_RHS.MeanLII{1}];
LII.W16_PL =
[BML3_PL.MeanLII{1},BML11_PL.MeanLII{1},BML12_PL.MeanLII{1},BML35_PL.MeanLII{
1},BML36_PL.MeanLII{1}];
LII.W16_Sag =
[BML3_Sag.MeanLII{1},BML11_Sag.MeanLII{1},BML12_Sag.MeanLII{1},BML35_Sag.Mean
LII{1},BML36_Sag.MeanLII{1}];
% 20 Week Samples
LII.W20_AL_LHS =
[BML5_AL_LHS.MeanLII{1},BML4A_AL_LHS.MeanLII{1},BML15_AL_LHS.MeanLII{1},BML25
_AL_LHS.MeanLII{1},BML26_AL_LHS.MeanLII{1}];
LII.W20_AL_RHS =
[BML5_AL_RHS.MeanLII{1},BML4A_AL_RHS.MeanLII{1},BML15_AL_RHS.MeanLII{1},BML25
_AL_RHS.MeanLII{1},BML26_AL_RHS.MeanLII{1}];
LII.W20_Cor_LHS =
[BML5_Cor_LHS.MeanLII{1},BML4A_Cor_LHS.MeanLII{1},BML15_Cor_LHS.MeanLII{1},BM
L25_Cor_LHS.MeanLII{1},BML26_Cor_LHS.MeanLII{1}];
LII.W20_Cor_RHS =
[BML5_Cor_RHS.MeanLII{1},BML4A_Cor_RHS.MeanLII{1},BML15_Cor_RHS.MeanLII{1},BM
L25_Cor_RHS.MeanLII{1},BML26_Cor_RHS.MeanLII{1}];
LII.W20_PL =
[BML5_PL.MeanLII{1},BML4A_PL.MeanLII{1},BML15_PL.MeanLII{1},BML25_PL.MeanLII{
1},BML26_PL.MeanLII{1}];
LII.W20_Sag =
[BML5_Sag.MeanLII{1},BML4A_Sag.MeanLII{1},BML15_Sag.MeanLII{1},BML25_Sag.Mean
LII{1},BML26_Sag.MeanLII{1}];
% 24 Week Samples
LII.W24_AL_LHS =
[BML8_AL_LHS.MeanLII{1},BML18_AL_LHS.MeanLII{1},BML20_AL_LHS.MeanLII{1},BML21
_AL_LHS.MeanLII{1},BML16_AL_LHS.MeanLII{1}];
LII.W24_AL_RHS =
[BML8_AL_RHS.MeanLII{1},BML18_AL_RHS.MeanLII{1},BML20_AL_RHS.MeanLII{1},BML21
_AL_RHS.MeanLII{1},BML16_AL_RHS.MeanLII{1}];
LII.W24_Cor_LHS =
[BML8_Cor_LHS.MeanLII{1},BML18_Cor_LHS.MeanLII{1},BML20_Cor_LHS.MeanLII{1},BM
L21_Cor_LHS.MeanLII{1},BML16_Cor_LHS.MeanLII{1}];
```

```
LII.W24_Cor_RHS =
[BML8_Cor_RHS.MeanLII{1},BML18_Cor_RHS.MeanLII{1},BML20_Cor_RHS.MeanLII{1},BM
L21_Cor_RHS.MeanLII{1},BML16_Cor_RHS.MeanLII{1}];
LII.W24_PL =
[BML8_PL.MeanLII{1},BML18_PL.MeanLII{1},BML20_PL.MeanLII{1},BML21_PL.MeanLII{
1}];
LII.W24_Sag =
[BML8_Sag.MeanLII{1},BML18_Sag.MeanLII{1},BML20_Sag.MeanLII{1},BML21_Sag.Mean
LII{1},BML16_Sag.MeanLII{1}];

% Generating boxplots to show LII Variations between age groups for each
suture:
warning('off','MATLAB:handle_graphics:Layout:NoPositionSetInTiledChartLayout'
)
% Creating single tiled figure to display results
f = figure;
f.Position = [100 0 800 800];
tBP_LII = tiledlayout('flow','TileSpacing','compact','Padding','none');
tBP_LII.YLabel.String = 'Mean Suture LII';
tBP_LII.XLabel.String = 'Age [Weeks]';

% Anterior Lambdoid LHS:
nexttile;
X=[LII.W16_AL_LHS';LII.W20_AL_LHS';LII.W24_AL_LHS'];
G=[16*ones(length(LII.W16_AL_LHS),1);20*ones(length(LII.W20_AL_LHS),1);24*one
s(length(LII.W24_AL_LHS),1)];
boxplot(X,G)
title('Anterior Lambdoid_L_H_S');
ylim([0 4]);
% Anterior Lambdoid RHS:
nexttile;
X=[LII.W16_AL_RHS';LII.W20_AL_RHS';LII.W24_AL_RHS'];
G=[16*ones(length(LII.W16_AL_RHS),1);20*ones(length(LII.W20_AL_RHS),1);24*one
s(length(LII.W24_AL_RHS),1)];
boxplot(X,G)
title('Anterior Lambdoid_R_H_S');
ylim([0 4]);
% Coronal LHS:
nexttile;
X=[LII.W16_Cor_LHS';LII.W20_Cor_LHS';LII.W24_Cor_LHS'];
G=[16*ones(length(LII.W16_Cor_LHS),1);20*ones(length(LII.W20_Cor_LHS),1);24*o
nes(length(LII.W24_Cor_LHS),1)];
boxplot(X,G)
title('Coronal_L_H_S');
ylim([0 4]);
% Coronal RHS:
nexttile;
X=[LII.W16_Cor_RHS';LII.W20_Cor_RHS';LII.W24_Cor_RHS'];
G=[16*ones(length(LII.W16_Cor_RHS),1);20*ones(length(LII.W20_Cor_RHS),1);24*o
nes(length(LII.W24_Cor_RHS),1)];
boxplot(X,G)
title('Coronal_R_H_S');
ylim([0 4]);
% Posterior Lambdoid:
nexttile;
```

```
X=[LII.W16_PL';LII.W20_PL';LII.W24_PL'];
G=[16*ones(length(LII.W16_PL),1);20*ones(length(LII.W20_PL),1);24*ones(length
(LII.W24_PL),1)];
boxplot(X,G)
title('Posterior Lambdoid');
ylim([0 4]);
% Sagittal:
nexttile;
X=[LII.W16_Sag';LII.W20_Sag';LII.W24_Sag'];
G=[16*ones(length(LII.W16_Sag),1);20*ones(length(LII.W20_Sag),1);24*ones(leng
th(LII.W24_Sag),1)];
boxplot(X,G)
title('Sagittal');
ylim([0 4]);

saveas(f,'BP_SutureLII.jpg')

%%%%%%%%%%%%%%%%%%%%%%%%%%%%%%%%%%%%%%%%%%%%%%%%%%%%%%%%%%%%%%%%%%%%%%%%%%%%
%%% COMPILED MEAN WIDTHS %%%%%%%%%%%%%%%%%%%%%%%%%%%%%%%%%%%%%%%%%%%%%%%%%%
%%%%%%%%%%%%%%%%%%%%%%%%%%%%%%%%%%%%%%%%%%%%%%%%%%%%%%%%%%%%%%%%%%%%%%%%%%%%

% Restructuring Average Width Data:
% Restructuring LII Data:
WIDTH = struct();
% 16 Week Samples
WIDTH.W16_AL_LHS =
[BML3_AL_LHS.MeanWidth{1},BML11_AL_LHS.MeanWidth{1},BML12_AL_LHS.MeanWidth{1}
,BML35_AL_LHS.MeanWidth{1},BML36_AL_LHS.MeanWidth{1}];
WIDTH.W16_AL_RHS =
[BML3_AL_RHS.MeanWidth{1},BML11_AL_RHS.MeanWidth{1},BML12_AL_RHS.MeanWidth{1}
,BML35_AL_RHS.MeanWidth{1},BML36_AL_RHS.MeanWidth{1}];
WIDTH.W16_Cor_LHS =
[BML3_Cor_LHS.MeanWidth{1},BML11_Cor_LHS.MeanWidth{1},BML12_Cor_LHS.MeanWidth
{1},BML35_Cor_LHS.MeanWidth{1},BML36_Cor_LHS.MeanWidth{1}];
WIDTH.W16_Cor_RHS =
[BML3_Cor_RHS.MeanWidth{1},BML11_Cor_RHS.MeanWidth{1},BML12_Cor_RHS.MeanWidth
{1},BML35_Cor_RHS.MeanWidth{1},BML36_Cor_RHS.MeanWidth{1}];
WIDTH.W16_PL =
[BML3_PL.MeanWidth{1},BML11_PL.MeanWidth{1},BML12_PL.MeanWidth{1},BML35_PL.Me
anWidth{1},BML36_PL.MeanWidth{1}];
WIDTH.W16_Sag =
[BML3_Sag.MeanWidth{1},BML11_Sag.MeanWidth{1},BML12_Sag.MeanWidth{1},BML35_Sa
g.MeanWidth{1},BML36_Sag.MeanWidth{1}];
% 20 Week Samples
WIDTH.W20_AL_LHS =
[BML5_AL_LHS.MeanWidth{1},BML4A_AL_LHS.MeanWidth{1},BML15_AL_LHS.MeanWidth{1}
,BML25_AL_LHS.MeanWidth{1},BML26_AL_LHS.MeanWidth{1}];
WIDTH.W20_AL_RHS =
[BML5_AL_RHS.MeanWidth{1},BML4A_AL_RHS.MeanWidth{1},BML15_AL_RHS.MeanWidth{1}
,BML25_AL_RHS.MeanWidth{1},BML26_AL_RHS.MeanWidth{1}];
WIDTH.W20_Cor_LHS =
[BML5_Cor_LHS.MeanWidth{1},BML4A_Cor_LHS.MeanWidth{1},BML15_Cor_LHS.MeanWidth
{1},BML25_Cor_LHS.MeanWidth{1},BML26_Cor_LHS.MeanWidth{1}];
```

```
WIDTH.W20_Cor_RHS =
[BML5_Cor_RHS.MeanWidth{1},BML4A_Cor_RHS.MeanWidth{1},BML15_Cor_RHS.MeanWidth
{1},BML25_Cor_RHS.MeanWidth{1},BML26_Cor_RHS.MeanWidth{1}];
WIDTH.W20_PL =
[BML5_PL.MeanWidth{1},BML4A_PL.MeanWidth{1},BML15_PL.MeanWidth{1},BML25_PL.Me
anWidth{1},BML26_PL.MeanWidth{1}];
WIDTH.W20_Sag =
[BML5_Sag.MeanWidth{1},BML4A_Sag.MeanWidth{1},BML15_Sag.MeanWidth{1},BML25_Sa
g.MeanWidth{1},BML26_Sag.MeanWidth{1}];
% 24 Week Samples
WIDTH.W24_AL_LHS =
[BML8_AL_LHS.MeanWidth{1},BML18_AL_LHS.MeanWidth{1},BML20_AL_LHS.MeanWidth{1}
,BML21_AL_LHS.MeanWidth{1},BML16_AL_LHS.MeanWidth{1}];
WIDTH.W24_AL_RHS =
[BML8_AL_RHS.MeanWidth{1},BML18_AL_RHS.MeanWidth{1},BML20_AL_RHS.MeanWidth{1}
,BML21_AL_RHS.MeanWidth{1},BML16_AL_RHS.MeanWidth{1}];
WIDTH.W24_Cor_LHS =
[BML8_Cor_LHS.MeanWidth{1},BML18_Cor_LHS.MeanWidth{1},BML20_Cor_LHS.MeanWidth
{1},BML21_Cor_LHS.MeanWidth{1},BML16_Cor_LHS.MeanWidth{1}];
WIDTH.W24_Cor_RHS =
[BML8_Cor_RHS.MeanWidth{1},BML18_Cor_RHS.MeanWidth{1},BML20_Cor_RHS.MeanWidth
{1},BML21_Cor_RHS.MeanWidth{1},BML16_Cor_RHS.MeanWidth{1}];
WIDTH.W24_PL =
[BML8_PL.MeanWidth{1},BML18_PL.MeanWidth{1},BML20_PL.MeanWidth{1},BML21_PL.Me
anWidth{1}];
WIDTH.W24_Sag =
[BML8_Sag.MeanWidth{1},BML18_Sag.MeanWidth{1},BML20_Sag.MeanWidth{1},BML21_Sa
g.MeanWidth{1},BML16_Sag.MeanWidth{1}];

% Generating boxplots to show width Variations between age groups:
% Creating single tiled figure to display results
f = figure;
f.Position = [100 0 800 800];
tBP_LII = tiledlayout('flow','TileSpacing','compact','Padding','none');
tBP_LII.YLabel.String = 'Mean Suture Width, \mum';
tBP_LII.XLabel.String = 'Age [Weeks]';

% Anterior Lambdoid LHS:
nexttile;
X=[WIDTH.W16_AL_LHS';WIDTH.W20_AL_LHS';WIDTH.W24_AL_LHS'];
G=[16*ones(length(WIDTH.W16_AL_LHS),1);20*ones(length(WIDTH.W20_AL_LHS),1);24
*ones(length(WIDTH.W24_AL_LHS),1)];
boxplot(X,G)
title('Anterior Lambdoid_L_H_S');
ylim([0 500]);
% Anterior Lambdoid RHS:
nexttile;
X=[WIDTH.W16_AL_RHS';WIDTH.W20_AL_RHS';WIDTH.W24_AL_RHS'];
G=[16*ones(length(WIDTH.W16_AL_RHS),1);20*ones(length(WIDTH.W20_AL_RHS),1);24
*ones(length(WIDTH.W24_AL_RHS),1)];
boxplot(X,G)
title('Anterior Lambdoid_R_H_S');
ylim([0 500]);
% Coronal LHS:
nexttile;
```

```
X=[WIDTH.W16_Cor_LHS';WIDTH.W20_Cor_LHS';WIDTH.W24_Cor_LHS'];
G=[16*ones(length(WIDTH.W16_AL_LHS),1);20*ones(length(WIDTH.W20_AL_LHS),1);24
*ones(length(WIDTH.W24_AL_LHS),1)];
boxplot(X,G)
title('Coronal_L_H_S');
ylim([0 500]);
% Coronal RHS:
nexttile;
X=[WIDTH.W16_Cor_RHS';WIDTH.W20_Cor_RHS';WIDTH.W24_Cor_RHS'];
G=[16*ones(length(WIDTH.W16_Cor_RHS),1);20*ones(length(WIDTH.W20_Cor_RHS),1);
24*ones(length(WIDTH.W24_Cor_RHS),1)];
boxplot(X,G)
title('Coronal_R_H_S');
ylim([0 500]);
% Posterior Lambdoid:
nexttile;
X=[WIDTH.W16_PL';WIDTH.W20_PL';WIDTH.W24_PL'];
G=[16*ones(length(WIDTH.W16_PL),1);20*ones(length(WIDTH.W20_PL),1);24*ones(le
ngth(WIDTH.W24_PL),1)];
boxplot(X,G)
title('Posterior Lamboid');
ylim([0 500]);
% Sagittal:
nexttile;
X=[WIDTH.W16_Sag';WIDTH.W20_Sag';WIDTH.W24_Sag'];
G=[16*ones(length(WIDTH.W16_Sag),1);20*ones(length(WIDTH.W20_Sag),1);24*ones(
length(WIDTH.W24_Sag),1)];
boxplot(X,G)
title('Sagittal');
ylim([0 500]);

saveas(f,'BP_SutureWidth.jpg')

%%%%%%%%%%%%%%%%%%%%%%%%%%%%%%%%%%%%%%%%%%%%%%%%%%%%%%%%%%%%%%%%%%%%%%%%%%%%
%%% COMPILED (24 WEEK) LII ANALYSIS %%%%%%%%%%%%%%%%%%%%%%%%%%%%%%%%%%%%%%%
%%%%%%%%%%%%%%%%%%%%%%%%%%%%%%%%%%%%%%%%%%%%%%%%%%%%%%%%%%%%%%%%%%%%%%%%%%%%

% Creating single tiled figure to display results
f = figure;
f.Position = [100 0 800 800];
t24_LII = tiledlayout(3,2,'TileSpacing','compact','Padding','none');
t24_LII.XLabel.String = 'Planar LII';
t24_LII.YLabel.String = 'Position in Skull, \mum (Datum at inner surface)';
ylim24=850;
LIIlim24=4;

% Anterior Lambdoid LHS
nexttile;
scatter([BML8_AL_LHS.LII{:}],[BML8_AL_LHS.h_LII{:}],'k*')
hold on
scatter([BML18_AL_LHS.LII{:}],[BML18_AL_LHS.h_LII{:}],'ro')
scatter([BML20_AL_LHS.LII{:}],[BML20_AL_LHS.h_LII{:}],'bv')
scatter([BML21_AL_LHS.LII{:}],[BML21_AL_LHS.h_LII{:}],'c^')
scatter([BML16_AL_LHS.LII{:}],[BML16_AL_LHS.h_LII{:}],'gd')
hold off
```

```
ylim([0 ylim24])
xlim([1 LIIlim24])
title('Anterior Lambdoid_L_H_S')
legend('BML8','BML18','BML20','BML21','BML16')

% Anterior Lambdoid RHS
nexttile;
scatter([BML8_AL_RHS.LII{:}],[BML8_AL_RHS.h_LII{:}],'k*')
hold on
scatter([BML18_AL_RHS.LII{:}],[BML18_AL_RHS.h_LII{:}],'ro')
scatter([BML20_AL_RHS.LII{:}],[BML20_AL_RHS.h_LII{:}],'bv')
scatter([BML21_AL_RHS.LII{:}],[BML21_AL_RHS.h_LII{:}],'c^')
scatter([BML16_AL_RHS.LII{:}],[BML16_AL_RHS.h_LII{:}],'gd')
hold off
legend('off')
ylim([0 ylim24])
xlim([1 LIIlim24])
title('Anterior Lambdoid_R_H_S')

% Coronal LHS
nexttile;
scatter([BML8_Cor_LHS.LII{:}],[BML8_Cor_LHS.h_LII{:}],'k*')
hold on
scatter([BML18_Cor_LHS.LII{:}],[BML18_Cor_LHS.h_LII{:}],'ro')
scatter([BML20_Cor_LHS.LII{:}],[BML20_Cor_LHS.h_LII{:}],'bv')
scatter([BML21_Cor_LHS.LII{:}],[BML21_Cor_LHS.h_LII{:}],'c^')
scatter([BML16_Cor_LHS.LII{:}],[BML16_Cor_LHS.h_LII{:}],'gd')
hold off
legend('off')
ylim([0 ylim24])
xlim([1 LIIlim24])
title('Coronal_L_H_S')

% Coronal RHS
nexttile;
scatter([BML8_Cor_RHS.LII{:}],[BML8_Cor_RHS.h_LII{:}],'k*')
hold on
scatter([BML18_Cor_RHS.LII{:}],[BML18_Cor_RHS.h_LII{:}],'ro')
scatter([BML20_Cor_RHS.LII{:}],[BML20_Cor_RHS.h_LII{:}],'bv')
scatter([BML21_Cor_RHS.LII{:}],[BML21_Cor_RHS.h_LII{:}],'c^')
scatter([BML16_Cor_RHS.LII{:}],[BML16_Cor_RHS.h_LII{:}],'gd')
hold off
legend('off')
ylim([0 ylim24])
xlim([1 LIIlim24])
title('Coronal_R_H_S')

% Posterior Lambdoid
nexttile;
scatter([BML8_PL.LII{:}],[BML8_PL.h_LII{:}],'k*')
hold on
scatter([BML18_PL.LII{:}],[BML18_PL.h_LII{:}],'ro')
scatter([BML20_PL.LII{:}],[BML20_PL.h_LII{:}],'bv')
scatter([BML21_PL.LII{:}],[BML21_PL.h_LII{:}],'c^')
hold off
```

```
legend('off')
ylim([0 ylim24])
xlim([1 LIIlim24])
title('Posterior Lambdoid')

% Sagittal
nexttile;
scatter([BML8_Sag.LII{:}],[BML8_Sag.h_LII{:}],'k*')
hold on
scatter([BML18_Sag.LII{:}],[BML18_Sag.h_LII{:}],'ro')
scatter([BML20_Sag.LII{:}],[BML20_Sag.h_LII{:}],'bv')
scatter([BML21_Sag.LII{:}],[BML21_Sag.h_LII{:}],'c^')
scatter([BML16_Sag.LII{:}],[BML16_Sag.h_LII{:}],'gd')
hold off
legend('off')
title('Sagittal')
ylim([0 ylim24])
xlim([1 LIIlim24])

saveas(f,'24W_PlanarLII.jpg')

%%%%%%%%%%%%%%%%%%%%%%%%%%%%%%%%%%%%%%%%%%%%%%%%%%%%%%%%%%%%%%%%%%%%%%%%%%%%%%%
%%% COMPILED (24 WEEK) WIDTH ANALYSIS %%%%%%%%%%%%%%%%%%%%%%%%%%%%%%%%%%%%%%%%
%%%%%%%%%%%%%%%%%%%%%%%%%%%%%%%%%%%%%%%%%%%%%%%%%%%%%%%%%%%%%%%%%%%%%%%%%%%%%%%

% Creating single tiled figure to display results
f = figure;
f.Position = [100 0 800 800];
t24_W=tiledlayout(3,2,'TileSpacing','compact','Padding','none');
t24_W.XLabel.String = 'Planar Mean Width, \mum';
t24_W.YLabel.String = 'Position in Skull, \mum (Datum at inner surface)';
Wlim24=500;

% Anterior Lambdoid LHS
nexttile;
scatter([BML8_AL_LHS.AvgWidth{:}],[BML8_AL_LHS.h_LII{:}],'k*')
hold on
scatter([BML18_AL_LHS.AvgWidth{:}],[BML18_AL_LHS.h_LII{:}],'ro')
scatter([BML20_AL_LHS.AvgWidth{:}],[BML20_AL_LHS.h_LII{:}],'bv')
scatter([BML21_AL_LHS.AvgWidth{:}],[BML21_AL_LHS.h_LII{:}],'c^')
scatter([BML16_AL_LHS.AvgWidth{:}],[BML16_AL_LHS.h_LII{:}],'gd')
hold off
legend
ylim([0 ylim24])
xlim([0 Wlim24])
title('Anterior Lambdoid_L_H_S')
legend('BML8','BML18','BML20','BML21','BML16')

% Anterior Lambdoid RHS
nexttile;
scatter([BML8_AL_RHS.AvgWidth{:}],[BML8_AL_RHS.h_LII{:}],'k*')
hold on
scatter([BML18_AL_RHS.AvgWidth{:}],[BML18_AL_RHS.h_LII{:}],'ro')
scatter([BML20_AL_RHS.AvgWidth{:}],[BML20_AL_RHS.h_LII{:}],'bv')
```

```
scatter([BML21_AL_RHS.AvgWidth{:}],[BML21_AL_RHS.h_LII{:}],'c^')
scatter([BML16_AL_RHS.AvgWidth{:}],[BML16_AL_RHS.h_LII{:}],'gd')
hold off
legend
ylim([0 ylim24])
xlim([0 Wlim24])
title('Anterior Lambdoid_R_H_S')
legend('off')

% Coronal LHS
nexttile;
scatter([BML8_Cor_LHS.AvgWidth{:}],[BML8_Cor_LHS.h_LII{:}],'k*')
hold on
scatter([BML18_Cor_LHS.AvgWidth{:}],[BML18_Cor_LHS.h_LII{:}],'ro')
scatter([BML20_Cor_LHS.AvgWidth{:}],[BML20_Cor_LHS.h_LII{:}],'bv')
scatter([BML21_Cor_LHS.AvgWidth{:}],[BML21_Cor_LHS.h_LII{:}],'c^')
scatter([BML16_Cor_LHS.AvgWidth{:}],[BML16_Cor_LHS.h_LII{:}],'gd')
hold off
hold off
legend
ylim([0 ylim24])
xlim([0 Wlim24])
title('Coronal_L_H_S')
legend('off')

% Coronal RHS
nexttile;
scatter([BML8_Cor_RHS.AvgWidth{:}],[BML8_Cor_RHS.h_LII{:}],'k*')
hold on
scatter([BML18_Cor_RHS.AvgWidth{:}],[BML18_Cor_RHS.h_LII{:}],'ro')
scatter([BML20_Cor_RHS.AvgWidth{:}],[BML20_Cor_RHS.h_LII{:}],'bv')
scatter([BML21_Cor_RHS.AvgWidth{:}],[BML21_Cor_RHS.h_LII{:}],'c^')
scatter([BML16_Cor_RHS.AvgWidth{:}],[BML16_Cor_RHS.h_LII{:}],'gd')
hold off
hold off
legend
ylim([0 ylim24])
xlim([0 Wlim24])
title('Coronal_R_H_S')
legend('off')

% 24 Week Posterior Lambdoid
nexttile;
scatter([BML8_PL.AvgWidth{:}],[BML8_PL.h_LII{:}],'k*')
hold on
scatter([BML18_PL.AvgWidth{:}],[BML18_PL.h_LII{:}],'ro')
scatter([BML20_PL.AvgWidth{:}],[BML20_PL.h_LII{:}],'bv')
scatter([BML21_PL.AvgWidth{:}],[BML21_PL.h_LII{:}],'c^')
hold off
legend
ylim([0 ylim24])
xlim([0 Wlim24])
title('Posterior Lambdoid')
legend('off')
```

```
% Sagittal
nexttile;
scatter([BML8_Sag.AvgWidth{:}],[BML8_Sag.h_LII{:}],'k*')
hold on
scatter([BML18_Sag.AvgWidth{:}],[BML18_Sag.h_LII{:}],'ro')
scatter([BML20_Sag.AvgWidth{:}],[BML20_Sag.h_LII{:}],'bv')
scatter([BML21_Sag.AvgWidth{:}],[BML21_Sag.h_LII{:}],'c^')
scatter([BML16_Sag.AvgWidth{:}],[BML16_Sag.h_LII{:}],'gd')
hold off
legend
ylim([0 ylim24])
xlim([0 500])
title('Sagittal')
legend('off')

saveas(f,'24W_MeanPlanarWidth.jpg')

%%%%%%%%%%%%%%%%%%%%%%%%%%%%%%%%%%%%%%%%%%%%%%%%%%%%%%%%%%%%%%%%%%%%%%%%%%%%%%%
%%% COMPILED (20 WEEK) LII ANALYSIS %%%%%%%%%%%%%%%%%%%%%%%%%%%%%%%%%%%%%%%%%%%
%%%%%%%%%%%%%%%%%%%%%%%%%%%%%%%%%%%%%%%%%%%%%%%%%%%%%%%%%%%%%%%%%%%%%%%%%%%%%%%

% Creating single tiled figure to display results
f = figure;
f.Position = [100 0 800 800];
t20_LII = tiledlayout(3,2,'TileSpacing','compact','Padding','none');
t20_LII.XLabel.String = 'Planar LII';
t20_LII.YLabel.String = 'Position in Skull, \mum (Datum at inner surface)';
ylim20=850;
LIIlim20=4;

% Anterior Lambdoid LHS
nexttile;
scatter([BML5_AL_LHS.LII{:}],[BML5_AL_LHS.h_LII{:}],'k*')
hold on
scatter([BML4A_AL_LHS.LII{:}],[BML4A_AL_LHS.h_LII{:}],'ro')
scatter([BML15_AL_LHS.LII{:}],[BML15_AL_LHS.h_LII{:}],'bv')
scatter([BML25_AL_LHS.LII{:}],[BML25_AL_LHS.h_LII{:}],'c^')
scatter([BML26_AL_LHS.LII{:}],[BML26_AL_LHS.h_LII{:}],'gd')
hold off
ylim([0 ylim20])
xlim([1 LIIlim20])
title('Anterior Lambdoid_L_H_S')
legend('BML5','BML4A','BML15','BML25','BML26')

% Anterior Lambdoid RHS
nexttile;
scatter([BML5_AL_RHS.LII{:}],[BML5_AL_RHS.h_LII{:}],'k*')
hold on
scatter([BML4A_AL_RHS.LII{:}],[BML4A_AL_RHS.h_LII{:}],'ro')
scatter([BML15_AL_RHS.LII{:}],[BML15_AL_RHS.h_LII{:}],'bv')
scatter([BML25_AL_RHS.LII{:}],[BML25_AL_RHS.h_LII{:}],'c^')
scatter([BML26_AL_RHS.LII{:}],[BML26_AL_RHS.h_LII{:}],'gd')
hold off
legend('off')
```

```
ylim([0 ylim20])
xlim([1 LIIlim20])
title('Anterior Lambdoid_R_H_S')

% Coronal LHS
nexttile;
scatter([BML5_Cor_LHS.LII{:}],[BML5_Cor_LHS.h_LII{:}],'k*')
hold on
scatter([BML4A_Cor_LHS.LII{:}],[BML4A_Cor_LHS.h_LII{:}],'ro')
scatter([BML15_Cor_LHS.LII{:}],[BML15_Cor_LHS.h_LII{:}],'bv')
scatter([BML25_Cor_LHS.LII{:}],[BML25_Cor_LHS.h_LII{:}],'c^')
scatter([BML26_Cor_LHS.LII{:}],[BML26_Cor_LHS.h_LII{:}],'gd')
hold off
legend('off')
ylim([0 ylim20])
xlim([1 LIIlim20])
title('Coronal_L_H_S')

% Coronal RHS
nexttile;
scatter([BML5_Cor_RHS.LII{:}],[BML5_Cor_RHS.h_LII{:}],'k*')
hold on
scatter([BML4A_Cor_RHS.LII{:}],[BML4A_Cor_RHS.h_LII{:}],'ro')
scatter([BML15_Cor_RHS.LII{:}],[BML15_Cor_RHS.h_LII{:}],'bv')
scatter([BML25_Cor_RHS.LII{:}],[BML25_Cor_RHS.h_LII{:}],'c^')
scatter([BML26_Cor_RHS.LII{:}],[BML26_Cor_RHS.h_LII{:}],'gd')
hold off
legend('off')
ylim([0 ylim20])
xlim([1 LIIlim20])
title('Coronal_R_H_S')

% Posterior Lambdoid
nexttile;
scatter([BML5_PL.LII{:}],[BML5_PL.h_LII{:}],'k*')
hold on
scatter([BML4A_PL.LII{:}],[BML4A_PL.h_LII{:}],'ro')
scatter([BML15_PL.LII{:}],[BML15_PL.h_LII{:}],'bv')
scatter([BML25_PL.LII{:}],[BML25_PL.h_LII{:}],'c^')
scatter([BML26_PL.LII{:}],[BML26_PL.h_LII{:}],'gd')
hold off
legend('off')
ylim([0 ylim20])
xlim([1 LIIlim20])
title('Posterior Lambdoid')

% Sagittal
nexttile;
scatter([BML5_Sag.LII{:}],[BML5_Sag.h_LII{:}],'k*')
hold on
scatter([BML4A_Sag.LII{:}],[BML4A_Sag.h_LII{:}],'ro')
scatter([BML15_Sag.LII{:}],[BML15_Sag.h_LII{:}],'bv')
scatter([BML25_Sag.LII{:}],[BML25_Sag.h_LII{:}],'c^')
scatter([BML26_Sag.LII{:}],[BML26_Sag.h_LII{:}],'gd')
hold off
```

```
legend('off')
title('Sagittal')
ylim([0 ylim20])
xlim([1 LIIlim20])

saveas(f,'20W_PlanarLII.jpg')

%%%%%%%%%%%%%%%%%%%%%%%%%%%%%%%%%%%%%%%%%%%%%%%%%%%%%%%%%%%%%%%%%%%%%%%%%%%%%%%
%%% COMPILED (20 WEEK) WIDTH ANALYSIS %%%%%%%%%%%%%%%%%%%%%%%%%%%%%%%%%%%%%%%%
%%%%%%%%%%%%%%%%%%%%%%%%%%%%%%%%%%%%%%%%%%%%%%%%%%%%%%%%%%%%%%%%%%%%%%%%%%%%%%%

% Creating single tiled figure to display results
f = figure;
f.Position = [100 0 800 800];
t20_W=tiledlayout(3,2,'TileSpacing','compact','Padding','none');
t20_W.XLabel.String = 'Planar Mean Width, \mum';
t20_W.YLabel.String = 'Position in Skull, \mum (Datum at inner surface)';
Wlim20=500;

% Anterior Lambdoid LHS
nexttile;
scatter([BML5_AL_LHS.AvgWidth{:}],[BML5_AL_LHS.h_LII{:}],'k*')
hold on
scatter([BML4A_AL_LHS.AvgWidth{:}],[BML4A_AL_LHS.h_LII{:}],'ro')
scatter([BML15_AL_LHS.AvgWidth{:}],[BML15_AL_LHS.h_LII{:}],'bv')
scatter([BML25_AL_LHS.AvgWidth{:}],[BML25_AL_LHS.h_LII{:}],'c^')
scatter([BML26_AL_LHS.AvgWidth{:}],[BML26_AL_LHS.h_LII{:}],'gd')
hold off
legend
ylim([0 ylim20])
xlim([0 Wlim20])
title('Anterior Lambdoid_L_H_S')
legend('BML5','BML4A','BML15','BML25','BML26')

% Anterior Lambdoid RHS
nexttile;
scatter([BML5_AL_RHS.AvgWidth{:}],[BML5_AL_RHS.h_LII{:}],'k*')
hold on
scatter([BML4A_AL_RHS.AvgWidth{:}],[BML4A_AL_RHS.h_LII{:}],'ro')
scatter([BML15_AL_RHS.AvgWidth{:}],[BML15_AL_RHS.h_LII{:}],'bv')
scatter([BML25_AL_RHS.AvgWidth{:}],[BML25_AL_RHS.h_LII{:}],'c^')
scatter([BML26_AL_RHS.AvgWidth{:}],[BML26_AL_RHS.h_LII{:}],'gd')
hold off
legend
ylim([0 ylim20])
xlim([0 Wlim20])
title('Anterior Lambdoid_R_H_S')
legend('off')

% Coronal LHS
nexttile;
scatter([BML5_Cor_LHS.AvgWidth{:}],[BML5_Cor_LHS.h_LII{:}],'k*')
hold on
scatter([BML4A_Cor_LHS.AvgWidth{:}],[BML4A_Cor_LHS.h_LII{:}],'ro')
```

```
scatter([BML15_Cor_LHS.AvgWidth{:}],[BML15_Cor_LHS.h_LII{:}],'bv')
scatter([BML25_Cor_LHS.AvgWidth{:}],[BML25_Cor_LHS.h_LII{:}],'c^')
scatter([BML26_Cor_LHS.AvgWidth{:}],[BML26_Cor_LHS.h_LII{:}],'gd')
hold off
hold off
legend
ylim([0 ylim20])
xlim([0 Wlim20])
title('Coronal_L_H_S')
legend('off')

% Coronal RHS
nexttile;
scatter([BML5_Cor_RHS.AvgWidth{:}],[BML5_Cor_RHS.h_LII{:}],'k*')
hold on
scatter([BML4A_Cor_RHS.AvgWidth{:}],[BML4A_Cor_RHS.h_LII{:}],'ro')
scatter([BML15_Cor_RHS.AvgWidth{:}],[BML15_Cor_RHS.h_LII{:}],'bv')
scatter([BML25_Cor_RHS.AvgWidth{:}],[BML25_Cor_RHS.h_LII{:}],'c^')
scatter([BML26_Cor_RHS.AvgWidth{:}],[BML26_Cor_RHS.h_LII{:}],'gd')
hold off
hold off
legend
ylim([0 ylim20])
xlim([0 Wlim20])
title('Coronal_R_H_S')
legend('off')

% 24 Week Posterior Lambdoid
nexttile;
scatter([BML5_PL.AvgWidth{:}],[BML5_PL.h_LII{:}],'k*')
hold on
scatter([BML4A_PL.AvgWidth{:}],[BML4A_PL.h_LII{:}],'ro')
scatter([BML15_PL.AvgWidth{:}],[BML15_PL.h_LII{:}],'bv')
scatter([BML25_PL.AvgWidth{:}],[BML25_PL.h_LII{:}],'c^')
scatter([BML26_PL.AvgWidth{:}],[BML26_PL.h_LII{:}],'gd')
hold off
legend
ylim([0 ylim20])
xlim([0 Wlim20])
title('Posterior Lambdoid')
legend('off')

% Sagittal
nexttile;
scatter([BML5_Sag.AvgWidth{:}],[BML5_Sag.h_LII{:}],'k*')
hold on
scatter([BML4A_Sag.AvgWidth{:}],[BML4A_Sag.h_LII{:}],'ro')
scatter([BML15_Sag.AvgWidth{:}],[BML15_Sag.h_LII{:}],'bv')
scatter([BML25_Sag.AvgWidth{:}],[BML25_Sag.h_LII{:}],'c^')
scatter([BML26_Sag.AvgWidth{:}],[BML26_Sag.h_LII{:}],'gd')
hold off
legend
ylim([0 ylim20])
xlim([0 Wlim20])
title('Sagittal')
```

```
legend('off')

saveas(f,'20W_MeanPlanarWidth.jpg')

%%%%%%%%%%%%%%%%%%%%%%%%%%%%%%%%%%%%%%%%%%%%%%%%%%%%%%%%%%%%%%%%%%%%%%%%%%%%%%%%
%%% COMPILED (16 WEEK) LII ANALYSIS %%%%%%%%%%%%%%%%%%%%%%%%%%%%%%%%%%%%%%%%%%%%
%%%%%%%%%%%%%%%%%%%%%%%%%%%%%%%%%%%%%%%%%%%%%%%%%%%%%%%%%%%%%%%%%%%%%%%%%%%%%%%%

% Creating single tiled figure to display results
f = figure;
f.Position = [100 0 800 800];
t16_LII = tiledlayout(3,2,'TileSpacing','compact','Padding','none');
t16_LII.XLabel.String = 'Planar LII';
t16_LII.YLabel.String = 'Position in Skull, \mum (Datum at inner surface)';
ylim16=850;
LIIlim16=4;

% Anterior Lambdoid LHS
nexttile;
scatter([BML3_AL_LHS.LII{:}],[BML3_AL_LHS.h_LII{:}],'k*')
hold on
scatter([BML11_AL_LHS.LII{:}],[BML11_AL_LHS.h_LII{:}],'ro')
scatter([BML12_AL_LHS.LII{:}],[BML12_AL_LHS.h_LII{:}],'bv')
scatter([BML35_AL_LHS.LII{:}],[BML35_AL_LHS.h_LII{:}],'c^')
scatter([BML36_AL_LHS.LII{:}],[BML36_AL_LHS.h_LII{:}],'gd')
hold off
ylim([0 ylim16])
xlim([1 LIIlim16])
title('Anterior Lambdoid_L_H_S')
legend('BML3','BML11','BML12','BML35','BML36')

% Anterior Lambdoid RHS
nexttile;
scatter([BML3_AL_RHS.LII{:}],[BML3_AL_RHS.h_LII{:}],'k*')
hold on
scatter([BML11_AL_RHS.LII{:}],[BML11_AL_RHS.h_LII{:}],'ro')
scatter([BML12_AL_RHS.LII{:}],[BML12_AL_RHS.h_LII{:}],'bv')
scatter([BML35_AL_RHS.LII{:}],[BML35_AL_RHS.h_LII{:}],'c^')
scatter([BML36_AL_RHS.LII{:}],[BML36_AL_RHS.h_LII{:}],'gd')
hold off
legend('off')
ylim([0 ylim16])
xlim([1 LIIlim16])
title('Anterior Lambdoid_R_H_S')

% Coronal LHS
nexttile;
scatter([BML3_Cor_LHS.LII{:}],[BML3_Cor_LHS.h_LII{:}],'k*')
hold on
scatter([BML11_Cor_LHS.LII{:}],[BML11_Cor_LHS.h_LII{:}],'ro')
scatter([BML12_Cor_LHS.LII{:}],[BML12_Cor_LHS.h_LII{:}],'bv')
scatter([BML35_Cor_LHS.LII{:}],[BML35_Cor_LHS.h_LII{:}],'c^')
scatter([BML36_Cor_LHS.LII{:}],[BML36_Cor_LHS.h_LII{:}],'gd')
hold off
```

```
legend('off')
ylim([0 ylim16])
xlim([1 LIIlim16])
title('Coronal_L_H_S')

% Coronal RHS
nexttile;
scatter([BML3_Cor_RHS.LII{:}],[BML3_Cor_RHS.h_LII{:}],'k*')
hold on
scatter([BML11_Cor_RHS.LII{:}],[BML11_Cor_RHS.h_LII{:}],'ro')
scatter([BML12_Cor_RHS.LII{:}],[BML12_Cor_RHS.h_LII{:}],'bv')
scatter([BML35_Cor_RHS.LII{:}],[BML35_Cor_RHS.h_LII{:}],'c^')
scatter([BML36_Cor_RHS.LII{:}],[BML36_Cor_RHS.h_LII{:}],'gd')
hold off
legend('off')
ylim([0 ylim16])
xlim([1 LIIlim16])
title('Coronal_R_H_S')

% Posterior Lambdoid
nexttile;
scatter([BML3_PL.LII{:}],[BML3_PL.h_LII{:}],'k*')
hold on
scatter([BML11_PL.LII{:}],[BML11_PL.h_LII{:}],'ro')
scatter([BML12_PL.LII{:}],[BML12_PL.h_LII{:}],'bv')
scatter([BML35_PL.LII{:}],[BML35_PL.h_LII{:}],'c^')
scatter([BML36_PL.LII{:}],[BML36_PL.h_LII{:}],'gd')
hold off
legend('off')
ylim([0 ylim16])
xlim([1 LIIlim16])
title('Posterior Lambdoid')

% Sagittal
nexttile;
scatter([BML3_Sag.LII{:}],[BML3_Sag.h_LII{:}],'k*')
hold on
scatter([BML11_Sag.LII{:}],[BML11_Sag.h_LII{:}],'ro')
scatter([BML12_Sag.LII{:}],[BML12_Sag.h_LII{:}],'bv')
scatter([BML35_Sag.LII{:}],[BML35_Sag.h_LII{:}],'c^')
scatter([BML36_Sag.LII{:}],[BML36_Sag.h_LII{:}],'gd')
hold off
legend('off')
title('Sagittal')
ylim([0 ylim16])
xlim([1 LIIlim16])

saveas(f,'16W_PlanarLII.jpg')

%%%%%%%%%%%%%%%%%%%%%%%%%%%%%%%%%%%%%%%%%%%%%%%%%%%%%%%%%%%%%%%%%%%%%%%%%%%%%%%
%%% COMPILED (16 WEEK) WIDTH ANALYSIS %%%%%%%%%%%%%%%%%%%%%%%%%%%%%%%%%%%%%%%%
%%%%%%%%%%%%%%%%%%%%%%%%%%%%%%%%%%%%%%%%%%%%%%%%%%%%%%%%%%%%%%%%%%%%%%%%%%%%%%%

% Creating single tiled figure to display results
```

```
f = figure;
f.Position = [100 0 800 800];
t16_W=tiledlayout(3,2,'TileSpacing','compact','Padding','none');
t16_W.XLabel.String = 'Planar Mean Width, \mum';
t16_W.YLabel.String = 'Position in Skull, \mum (Datum at inner surface)';
Wlim16=500;

% Anterior Lambdoid LHS
nexttile;
scatter([BML3_AL_LHS.AvgWidth{:}],[BML3_AL_LHS.h_LII{:}],'k*')
hold on
scatter([BML11_AL_LHS.AvgWidth{:}],[BML11_AL_LHS.h_LII{:}],'ro')
scatter([BML12_AL_LHS.AvgWidth{:}],[BML12_AL_LHS.h_LII{:}],'bv')
scatter([BML35_AL_LHS.AvgWidth{:}],[BML35_AL_LHS.h_LII{:}],'c^')
scatter([BML36_AL_LHS.AvgWidth{:}],[BML36_AL_LHS.h_LII{:}],'gd')
hold off
legend
ylim([0 ylim16])
xlim([0 Wlim16])
title('Anterior Lambdoid_L_H_S')
legend('BML3','BML11','BML12','BML35','BML36')

% Anterior Lambdoid RHS
nexttile;
scatter([BML3_AL_RHS.AvgWidth{:}],[BML3_AL_RHS.h_LII{:}],'k*')
hold on
scatter([BML11_AL_RHS.AvgWidth{:}],[BML11_AL_RHS.h_LII{:}],'ro')
scatter([BML12_AL_RHS.AvgWidth{:}],[BML12_AL_RHS.h_LII{:}],'bv')
scatter([BML35_AL_RHS.AvgWidth{:}],[BML35_AL_RHS.h_LII{:}],'c^')
scatter([BML36_AL_RHS.AvgWidth{:}],[BML36_AL_RHS.h_LII{:}],'gd')
hold off
legend
ylim([0 ylim16])
xlim([0 Wlim16])
title('Anterior Lambdoid_R_H_S')
legend('off')

% Coronal LHS
nexttile;
scatter([BML3_Cor_LHS.AvgWidth{:}],[BML3_Cor_LHS.h_LII{:}],'k*')
hold on
scatter([BML11_Cor_LHS.AvgWidth{:}],[BML11_Cor_LHS.h_LII{:}],'ro')
scatter([BML12_Cor_LHS.AvgWidth{:}],[BML12_Cor_LHS.h_LII{:}],'bv')
scatter([BML35_Cor_LHS.AvgWidth{:}],[BML35_Cor_LHS.h_LII{:}],'c^')
scatter([BML36_Cor_LHS.AvgWidth{:}],[BML36_Cor_LHS.h_LII{:}],'gd')
hold off
hold off
legend
ylim([0 ylim16])
xlim([0 Wlim16])
title('Coronal_L_H_S')
legend('off')

% Coronal RHS
nexttile;
```

```
scatter([BML3_Cor_RHS.AvgWidth{:}],[BML3_Cor_RHS.h_LII{:}],'k*')
hold on
scatter([BML11_Cor_RHS.AvgWidth{:}],[BML11_Cor_RHS.h_LII{:}],'ro')
scatter([BML12_Cor_RHS.AvgWidth{:}],[BML12_Cor_RHS.h_LII{:}],'bv')
scatter([BML35_Cor_RHS.AvgWidth{:}],[BML35_Cor_RHS.h_LII{:}],'c^')
scatter([BML36_Cor_RHS.AvgWidth{:}],[BML36_Cor_RHS.h_LII{:}],'gd')
hold off
hold off
legend
ylim([0 ylim16])
xlim([0 Wlim16])
title('Coronal_R_H_S')
legend('off')

% 24 Week Posterior Lambdoid
nexttile;
scatter([BML3_PL.AvgWidth{:}],[BML3_PL.h_LII{:}],'k*')
hold on
scatter([BML11_PL.AvgWidth{:}],[BML11_PL.h_LII{:}],'ro')
scatter([BML12_PL.AvgWidth{:}],[BML12_PL.h_LII{:}],'bv')
scatter([BML35_PL.AvgWidth{:}],[BML35_PL.h_LII{:}],'c^')
scatter([BML36_PL.AvgWidth{:}],[BML36_PL.h_LII{:}],'gd')
hold off
legend
ylim([0 ylim16])
xlim([0 Wlim16])
title('Posterior Lambdoid')
legend('off')

% Sagittal
nexttile;
scatter([BML3_Sag.AvgWidth{:}],[BML3_Sag.h_LII{:}],'k*')
hold on
scatter([BML11_Sag.AvgWidth{:}],[BML11_Sag.h_LII{:}],'ro')
scatter([BML12_Sag.AvgWidth{:}],[BML12_Sag.h_LII{:}],'bv')
scatter([BML35_Sag.AvgWidth{:}],[BML35_Sag.h_LII{:}],'c^')
scatter([BML36_Sag.AvgWidth{:}],[BML36_Sag.h_LII{:}],'gd')
hold off
legend
ylim([0 ylim16])
xlim([0 Wlim16])
title('Sagittal')
legend('off')

saveas(f,'16W_MeanPlanarWidth.jpg')

%%%%%%%%%%%%%%%%%%%%%%%%%%%%%%%%%%%%%%%%%%%%%%%%%%%%%%%%%%%%%%%%%%%%%%%%%%%%%%%
%%% PLOTTING ALL 3D CENTERLINES %%%%%%%%%%%%%%%%%%%%%%%%%%%%%%%%%%%%%%%%%%%%%%
%%%%%%%%%%%%%%%%%%%%%%%%%%%%%%%%%%%%%%%%%%%%%%%%%%%%%%%%%%%%%%%%%%%%%%%%%%%%%%%
caz = -5;
cel = 30;
f = figure;
f.Position = [100 0 800 800];
BML8_3D = tiledlayout(3,2,'TileSpacing','compact','Padding','none');
res=17.8;
```

```
% AL LHS
nexttile
h=BML8_AL_LHS.h_LII{1};    % Setting the initial height to maximum
for i=1:(length(BML8_AL_LHS.h_LII))
    height=h*ones(length(BML8_AL_LHS.Center{i}(:,1)),1);

plot3(res*BML8_AL_LHS.Center{i}(:,1),(length(BML8_AL_LHS.Cropped{i}(:,1))*res
)-res*BML8_AL_LHS.Center{i}(:,2),height)
    hold on
    h=h-res;
end
hold off
ylim([0 8000]);
xlim([0 8000]);
zlim([0 600]);
title('Anterior Lambdoid_L_H_S');
view([caz,cel]);
% AL RHS
nexttile
h=BML8_AL_RHS.h_LII{1};    % Setting the initial height to maximum
for i=1:(length(BML8_AL_RHS.h_LII))
    height=h*ones(length(BML8_AL_RHS.Center{i}(:,1)),1);

plot3(res*BML8_AL_RHS.Center{i}(:,1),(length(BML8_AL_RHS.Cropped{i}(:,1))*res
)-res*BML8_AL_RHS.Center{i}(:,2),height)
    hold on
    h=h-res;
end
hold off
ylim([0 8000]);
xlim([0 8000]);
zlim([0 600]);
title('Anterior Lambdoid_R_H_S');
view([caz,cel]);
% C LHS
nexttile
h=BML8_Cor_LHS.h_LII{1};    % Setting the initial height to maximum
for i=1:(length(BML8_Cor_LHS.h_LII))
    height=h*ones(length(BML8_Cor_LHS.Center{i}(:,1)),1);

plot3(res*BML8_Cor_LHS.Center{i}(:,1),(length(BML8_Cor_LHS.Cropped{i}(:,1))*r
es)-res*BML8_Cor_LHS.Center{i}(:,2),height)
    hold on
    h=h-res;
end
hold off
ylim([0 8000]);
xlim([0 8000]);
zlim([0 600]);
title('Coronal_L_H_S');
view([caz,cel]);
% C RHS
nexttile
h=BML8_Cor_RHS.h_LII{1};    % Setting the initial height to maximum
for i=1:(length(BML8_Cor_RHS.h_LII))
```

```
    height=h*ones(length(BML8_Cor_RHS.Center{i}(:,1)),1);

plot3(res*BML8_Cor_RHS.Center{i}(:,1),(length(BML8_Cor_RHS.Cropped{i}(:,1))*r
es)-res*BML8_Cor_RHS.Center{i}(:,2),height)
    hold on
    h=h-res;
end
hold off
ylim([0 8000]);
xlim([0 8000]);
zlim([0 600]);
title('Coronal_R_H_S');
view([caz,cel]);
% S
nexttile
h=BML8_Sag.h_LII{1};    % Setting the initial height to maximum
for i=1:(length(BML8_Sag.h_LII))
    height=h*ones(length(BML8_Sag.Center{i}(:,1)),1);
    plot3(res*BML8_Sag.Center{i}(:,1),(length(BML8_Sag.Cropped{i}(:,1))*res)-
res*BML8_Sag.Center{i}(:,2),height)
    hold on
    h=h-res;
end
hold off
ylim([0 8000]);
xlim([0 8000]);
zlim([0 600]);
title('Sagittal');
view([caz,cel]);
% PL
nexttile
h=BML8_PL.h_LII{1};    % Setting the initial height to maximum
for i=1:(length(BML8_PL.h_LII))
    height=h*ones(length(BML8_PL.Center{i}(:,1)),1);
    plot3(res*BML8_PL.Center{i}(:,1),(length(BML8_PL.Cropped{i}(:,1))*res)-
res*BML8_PL.Center{i}(:,2),height)
    hold on
    h=h-res;
end
hold off
ylim([0 8000]);
xlim([0 8000]);
zlim([0 600]);
title('Posterior Lambdoid');
view([caz,cel]);
saveas(f,'3Drepresentations.jpg');

%%%%%%%%%%%%%%%%%%%%%%%%%%%%%%%%%%%%%%%%%%%%%%%%%%%%%%%%%%%%%%%%%%%%%%%%%%%%%%%
%%% CREATING FIGURE SHOWING LOCAL WIDTH VARIABILITY %%%%%%%%%%%%%%%%%%%%%%%%%%
%%%%%%%%%%%%%%%%%%%%%%%%%%%%%%%%%%%%%%%%%%%%%%%%%%%%%%%%%%%%%%%%%%%%%%%%%%%%%%%

figure
scatter3(res*BML8_PL.Center{1}(:,1),4000-
res*BML8_PL.Center{1}(:,2),res*BML8_PL.Width{1}(:),20,res*BML8_PL.Width{1}(:)
, 'filled');
```

```
colorbar
set(get(colorbar,'label'),'string','Suture Width [\mum]','FontSize',14);
xlabel('\mum', 'FontSize', 14)
ylabel('\mum', 'FontSize', 14)
ylim([0 5000])
view([0 90]);
set(gcf, 'Position',  [0, 0, 1000, 500])
saveas(gcf,'BML8_PL_LocalWidth_i=1.jpg')

%%%%%%%%%%%%%%%%%%%%%%%%%%%%%%%%%%%%%%%%%%%%%%%%%%%%%%%%%%%%%%%%%%%%%%%%%%%%%%%
%%% MAX AND MIN VALUES OF LII %%%%%%%%%%%%%%%%%%%%%%%%%%%%%%%%%%%%%%%%%%%%%%%%
%%%%%%%%%%%%%%%%%%%%%%%%%%%%%%%%%%%%%%%%%%%%%%%%%%%%%%%%%%%%%%%%%%%%%%%%%%%%%%%

%%% Anterior Lambdoid
% 16 Week
LII_ALvar(1)=(max(cell2mat(BML3_AL_LHS.LII(:)))-
min(cell2mat(BML3_AL_LHS.LII(:))))/min(cell2mat(BML3_AL_LHS.LII(:)));
LII_ALvar(2)=(max(cell2mat(BML3_AL_RHS.LII(:)))-
min(cell2mat(BML3_AL_RHS.LII(:))))/min(cell2mat(BML3_AL_RHS.LII(:)));
LII_ALvar(3)=(max(cell2mat(BML11_AL_LHS.LII(:)))-
min(cell2mat(BML11_AL_LHS.LII(:))))/min(cell2mat(BML11_AL_LHS.LII(:)));
LII_ALvar(4)=(max(cell2mat(BML11_AL_RHS.LII(:)))-
min(cell2mat(BML11_AL_RHS.LII(:))))/min(cell2mat(BML11_AL_RHS.LII(:)));
LII_ALvar(5)=(max(cell2mat(BML12_AL_LHS.LII(:)))-
min(cell2mat(BML12_AL_LHS.LII(:))))/min(cell2mat(BML12_AL_LHS.LII(:)));
LII_ALvar(6)=(max(cell2mat(BML12_AL_RHS.LII(:)))-
min(cell2mat(BML12_AL_RHS.LII(:))))/min(cell2mat(BML12_AL_RHS.LII(:)));
LII_ALvar(7)=(max(cell2mat(BML35_AL_LHS.LII(:)))-
min(cell2mat(BML35_AL_LHS.LII(:))))/min(cell2mat(BML35_AL_LHS.LII(:)));
LII_ALvar(8)=(max(cell2mat(BML35_AL_RHS.LII(:)))-
min(cell2mat(BML35_AL_RHS.LII(:))))/min(cell2mat(BML35_AL_RHS.LII(:)));
LII_ALvar(9)=(max(cell2mat(BML36_AL_LHS.LII(:)))-
min(cell2mat(BML36_AL_LHS.LII(:))))/min(cell2mat(BML36_AL_LHS.LII(:)));
LII_ALvar(10)=(max(cell2mat(BML36_AL_RHS.LII(:)))-
min(cell2mat(BML36_AL_RHS.LII(:))))/min(cell2mat(BML36_AL_RHS.LII(:)));
% 20 Week
LII_ALvar(11)=(max(cell2mat(BML5_AL_LHS.LII(:)))-
min(cell2mat(BML5_AL_LHS.LII(:))))/min(cell2mat(BML5_AL_LHS.LII(:)));
LII_ALvar(12)=(max(cell2mat(BML5_AL_RHS.LII(:)))-
min(cell2mat(BML5_AL_RHS.LII(:))))/min(cell2mat(BML5_AL_RHS.LII(:)));
LII_ALvar(13)=(max(cell2mat(BML4A_AL_LHS.LII(:)))-
min(cell2mat(BML4A_AL_LHS.LII(:))))/min(cell2mat(BML4A_AL_LHS.LII(:)));
LII_ALvar(14)=(max(cell2mat(BML4A_AL_RHS.LII(:)))-
min(cell2mat(BML4A_AL_RHS.LII(:))))/min(cell2mat(BML4A_AL_RHS.LII(:)));
LII_ALvar(15)=(max(cell2mat(BML15_AL_LHS.LII(:)))-
min(cell2mat(BML15_AL_LHS.LII(:))))/min(cell2mat(BML15_AL_LHS.LII(:)));
LII_ALvar(16)=(max(cell2mat(BML15_AL_RHS.LII(:)))-
min(cell2mat(BML15_AL_RHS.LII(:))))/min(cell2mat(BML15_AL_RHS.LII(:)));
LII_ALvar(17)=(max(cell2mat(BML25_AL_LHS.LII(:)))-
min(cell2mat(BML25_AL_LHS.LII(:))))/min(cell2mat(BML25_AL_LHS.LII(:)));
LII_ALvar(18)=(max(cell2mat(BML25_AL_RHS.LII(:)))-
min(cell2mat(BML25_AL_RHS.LII(:))))/min(cell2mat(BML25_AL_RHS.LII(:)));
LII_ALvar(19)=(max(cell2mat(BML26_AL_LHS.LII(:)))-
min(cell2mat(BML26_AL_LHS.LII(:))))/min(cell2mat(BML26_AL_LHS.LII(:)));
```

```
LII_ALvar(20)=(max(cell2mat(BML26_AL_RHS.LII(:)))-
min(cell2mat(BML26_AL_RHS.LII(:))))/min(cell2mat(BML26_AL_RHS.LII(:)));
% 24 Week
LII_ALvar(21)=(max(cell2mat(BML8_AL_LHS.LII(:)))-
min(cell2mat(BML8_AL_LHS.LII(:))))/min(cell2mat(BML8_AL_LHS.LII(:)));
LII_ALvar(22)=(max(cell2mat(BML8_AL_RHS.LII(:)))-
min(cell2mat(BML8_AL_RHS.LII(:))))/min(cell2mat(BML8_AL_RHS.LII(:)));
LII_ALvar(23)=(max(cell2mat(BML18_AL_LHS.LII(:)))-
min(cell2mat(BML18_AL_LHS.LII(:))))/min(cell2mat(BML18_AL_LHS.LII(:)));
LII_ALvar(24)=(max(cell2mat(BML18_AL_RHS.LII(:)))-
min(cell2mat(BML18_AL_RHS.LII(:))))/min(cell2mat(BML18_AL_RHS.LII(:)));
LII_ALvar(25)=(max(cell2mat(BML20_AL_LHS.LII(:)))-
min(cell2mat(BML20_AL_LHS.LII(:))))/min(cell2mat(BML20_AL_LHS.LII(:)));
LII_ALvar(26)=(max(cell2mat(BML20_AL_RHS.LII(:)))-
min(cell2mat(BML20_AL_RHS.LII(:))))/min(cell2mat(BML20_AL_RHS.LII(:)));
LII_ALvar(27)=(max(cell2mat(BML21_AL_LHS.LII(:)))-
min(cell2mat(BML21_AL_LHS.LII(:))))/min(cell2mat(BML21_AL_LHS.LII(:)));
LII_ALvar(28)=(max(cell2mat(BML21_AL_RHS.LII(:)))-
min(cell2mat(BML21_AL_RHS.LII(:))))/min(cell2mat(BML21_AL_RHS.LII(:)));
LII_ALvar(29)=(max(cell2mat(BML16_AL_LHS.LII(:)))-
min(cell2mat(BML16_AL_LHS.LII(:))))/min(cell2mat(BML16_AL_LHS.LII(:)));
LII_ALvar(30)=(max(cell2mat(BML16_AL_RHS.LII(:)))-
min(cell2mat(BML16_AL_RHS.LII(:))))/min(cell2mat(BML16_AL_RHS.LII(:)));
LII_maxALvar=max(LII_ALvar)
LII_minALvar=min(LII_ALvar)

%%% Coronal
% 16 Week
LII_Corvar(1)=(max(cell2mat(BML3_Cor_LHS.LII(:)))-
min(cell2mat(BML3_Cor_LHS.LII(:))))/min(cell2mat(BML3_Cor_LHS.LII(:)));
LII_Corvar(2)=(max(cell2mat(BML3_Cor_RHS.LII(:)))-
min(cell2mat(BML3_Cor_RHS.LII(:))))/min(cell2mat(BML3_Cor_RHS.LII(:)));
LII_Corvar(3)=(max(cell2mat(BML11_Cor_LHS.LII(:)))-
min(cell2mat(BML11_Cor_LHS.LII(:))))/min(cell2mat(BML11_Cor_LHS.LII(:)));
LII_Corvar(4)=(max(cell2mat(BML11_Cor_RHS.LII(:)))-
min(cell2mat(BML11_Cor_RHS.LII(:))))/min(cell2mat(BML11_Cor_RHS.LII(:)));
LII_Corvar(5)=(max(cell2mat(BML12_Cor_LHS.LII(:)))-
min(cell2mat(BML12_Cor_LHS.LII(:))))/min(cell2mat(BML12_Cor_LHS.LII(:)));
LII_Corvar(6)=(max(cell2mat(BML12_Cor_RHS.LII(:)))-
min(cell2mat(BML12_Cor_RHS.LII(:))))/min(cell2mat(BML12_Cor_RHS.LII(:)));
LII_Corvar(7)=(max(cell2mat(BML35_Cor_LHS.LII(:)))-
min(cell2mat(BML35_Cor_LHS.LII(:))))/min(cell2mat(BML35_Cor_LHS.LII(:)));
LII_Corvar(8)=(max(cell2mat(BML35_Cor_RHS.LII(:)))-
min(cell2mat(BML35_Cor_RHS.LII(:))))/min(cell2mat(BML35_Cor_RHS.LII(:)));
LII_Corvar(9)=(max(cell2mat(BML36_Cor_LHS.LII(:)))-
min(cell2mat(BML36_Cor_LHS.LII(:))))/min(cell2mat(BML36_Cor_LHS.LII(:)));
LII_Corvar(10)=(max(cell2mat(BML36_Cor_RHS.LII(:)))-
min(cell2mat(BML36_Cor_RHS.LII(:))))/min(cell2mat(BML36_Cor_RHS.LII(:)));
% 20 Week
LII_Corvar(11)=(max(cell2mat(BML5_Cor_LHS.LII(:)))-
min(cell2mat(BML5_Cor_LHS.LII(:))))/min(cell2mat(BML5_Cor_LHS.LII(:)));
LII_Corvar(12)=(max(cell2mat(BML5_Cor_RHS.LII(:)))-
min(cell2mat(BML5_Cor_RHS.LII(:))))/min(cell2mat(BML5_Cor_RHS.LII(:)));
LII_Corvar(13)=(max(cell2mat(BML4A_Cor_LHS.LII(:)))-
min(cell2mat(BML4A_Cor_LHS.LII(:))))/min(cell2mat(BML4A_Cor_LHS.LII(:)));
```

```
LII_Corvar(14)=(max(cell2mat(BML4A_Cor_RHS.LII(:)))-
min(cell2mat(BML4A_Cor_RHS.LII(:))))/min(cell2mat(BML4A_Cor_RHS.LII(:)));
LII_Corvar(15)=(max(cell2mat(BML15_Cor_LHS.LII(:)))-
min(cell2mat(BML15_Cor_LHS.LII(:))))/min(cell2mat(BML15_Cor_LHS.LII(:)));
LII_Corvar(16)=(max(cell2mat(BML15_Cor_RHS.LII(:)))-
min(cell2mat(BML15_Cor_RHS.LII(:))))/min(cell2mat(BML15_Cor_RHS.LII(:)));
LII_Corvar(17)=(max(cell2mat(BML25_Cor_LHS.LII(:)))-
min(cell2mat(BML25_Cor_LHS.LII(:))))/min(cell2mat(BML25_Cor_LHS.LII(:)));
LII_Corvar(18)=(max(cell2mat(BML25_Cor_RHS.LII(:)))-
min(cell2mat(BML25_Cor_RHS.LII(:))))/min(cell2mat(BML25_Cor_RHS.LII(:)));
LII_Corvar(19)=(max(cell2mat(BML26_Cor_LHS.LII(:)))-
min(cell2mat(BML26_Cor_LHS.LII(:))))/min(cell2mat(BML26_Cor_LHS.LII(:)));
LII_Corvar(20)=(max(cell2mat(BML26_Cor_RHS.LII(:)))-
min(cell2mat(BML26_Cor_RHS.LII(:))))/min(cell2mat(BML26_Cor_RHS.LII(:)));
% 24 Week
LII_Corvar(21)=(max(cell2mat(BML8_Cor_LHS.LII(:)))-
min(cell2mat(BML8_Cor_LHS.LII(:))))/min(cell2mat(BML8_Cor_LHS.LII(:)));
LII_Corvar(22)=(max(cell2mat(BML8_Cor_RHS.LII(:)))-
min(cell2mat(BML8_Cor_RHS.LII(:))))/min(cell2mat(BML8_Cor_RHS.LII(:)));
LII_Corvar(23)=(max(cell2mat(BML18_Cor_LHS.LII(:)))-
min(cell2mat(BML18_Cor_LHS.LII(:))))/min(cell2mat(BML18_Cor_LHS.LII(:)));
LII_Corvar(24)=(max(cell2mat(BML18_Cor_RHS.LII(:)))-
min(cell2mat(BML18_Cor_RHS.LII(:))))/min(cell2mat(BML18_Cor_RHS.LII(:)));
LII_Corvar(25)=(max(cell2mat(BML20_Cor_LHS.LII(:)))-
min(cell2mat(BML20_Cor_LHS.LII(:))))/min(cell2mat(BML20_Cor_LHS.LII(:)));
LII_Corvar(26)=(max(cell2mat(BML20_Cor_RHS.LII(:)))-
min(cell2mat(BML20_Cor_RHS.LII(:))))/min(cell2mat(BML20_Cor_RHS.LII(:)));
LII_Corvar(27)=(max(cell2mat(BML21_Cor_LHS.LII(:)))-
min(cell2mat(BML21_Cor_LHS.LII(:))))/min(cell2mat(BML21_Cor_LHS.LII(:)));
LII_Corvar(28)=(max(cell2mat(BML21_Cor_RHS.LII(:)))-
min(cell2mat(BML21_Cor_RHS.LII(:))))/min(cell2mat(BML21_Cor_RHS.LII(:)));
LII_Corvar(29)=(max(cell2mat(BML16_Cor_LHS.LII(:)))-
min(cell2mat(BML16_Cor_LHS.LII(:))))/min(cell2mat(BML16_Cor_LHS.LII(:)));
LII_Corvar(30)=(max(cell2mat(BML16_Cor_RHS.LII(:)))-
min(cell2mat(BML16_Cor_RHS.LII(:))))/min(cell2mat(BML16_Cor_RHS.LII(:)));
LII_maxCorvar=max(LII_Corvar)
LII_minCorvar=min(LII_Corvar)

% Sagittal
% 16 Week
LII_Sagvar(1)=(max(cell2mat(BML3_Sag.LII(:)))-
min(cell2mat(BML3_Sag.LII(:))))/min(cell2mat(BML3_Sag.LII(:)));
LII_Sagvar(2)=(max(cell2mat(BML11_Sag.LII(:)))-
min(cell2mat(BML11_Sag.LII(:))))/min(cell2mat(BML11_Sag.LII(:)));
LII_Sagvar(3)=(max(cell2mat(BML12_Sag.LII(:)))-
min(cell2mat(BML12_Sag.LII(:))))/min(cell2mat(BML12_Sag.LII(:)));
LII_Sagvar(4)=(max(cell2mat(BML35_Sag.LII(:)))-
min(cell2mat(BML35_Sag.LII(:))))/min(cell2mat(BML35_Sag.LII(:)));
LII_Sagvar(5)=(max(cell2mat(BML36_Sag.LII(:)))-
min(cell2mat(BML36_Sag.LII(:))))/min(cell2mat(BML36_Sag.LII(:)));
% 20 Week
LII_Sagvar(6)=(max(cell2mat(BML5_Sag.LII(:)))-
min(cell2mat(BML5_Sag.LII(:))))/min(cell2mat(BML5_Sag.LII(:)));
LII_Sagvar(7)=(max(cell2mat(BML4A_Sag.LII(:)))-
min(cell2mat(BML4A_Sag.LII(:))))/min(cell2mat(BML4A_Sag.LII(:)));
```

```
LII_Sagvar(8)=(max(cell2mat(BML15_Sag.LII(:)))-
min(cell2mat(BML15_Sag.LII(:))))/min(cell2mat(BML15_Sag.LII(:)));
LII_Sagvar(9)=(max(cell2mat(BML25_Sag.LII(:)))-
min(cell2mat(BML25_Sag.LII(:))))/min(cell2mat(BML25_Sag.LII(:)));
LII_Sagvar(10)=(max(cell2mat(BML26_Sag.LII(:)))-
min(cell2mat(BML26_Sag.LII(:))))/min(cell2mat(BML26_Sag.LII(:)));
% 24 Week
LII_Sagvar(11)=(max(cell2mat(BML8_Sag.LII(:)))-
min(cell2mat(BML8_Sag.LII(:))))/min(cell2mat(BML8_Sag.LII(:)));
LII_Sagvar(12)=(max(cell2mat(BML18_Sag.LII(:)))-
min(cell2mat(BML18_Sag.LII(:))))/min(cell2mat(BML18_Sag.LII(:)));
LII_Sagvar(13)=(max(cell2mat(BML20_Sag.LII(:)))-
min(cell2mat(BML20_Sag.LII(:))))/min(cell2mat(BML20_Sag.LII(:)));
LII_Sagvar(14)=(max(cell2mat(BML21_Sag.LII(:)))-
min(cell2mat(BML21_Sag.LII(:))))/min(cell2mat(BML21_Sag.LII(:)));
LII_Sagvar(15)=(max(cell2mat(BML16_Sag.LII(:)))-
min(cell2mat(BML16_Sag.LII(:))))/min(cell2mat(BML16_Sag.LII(:)));
LII_maxSagvar=max(LII_Sagvar)
LII_minSagvar=min(LII_Sagvar)

% Posterior Lambdoid
% 16 Week
LII_PLvar(1)=(max(cell2mat(BML3_PL.LII(:)))-
min(cell2mat(BML3_PL.LII(:))))/min(cell2mat(BML3_PL.LII(:)));
LII_PLvar(2)=(max(cell2mat(BML11_PL.LII(:)))-
min(cell2mat(BML11_PL.LII(:))))/min(cell2mat(BML11_PL.LII(:)));
LII_PLvar(3)=(max(cell2mat(BML12_PL.LII(:)))-
min(cell2mat(BML12_PL.LII(:))))/min(cell2mat(BML12_PL.LII(:)));
LII_PLvar(4)=(max(cell2mat(BML35_PL.LII(:)))-
min(cell2mat(BML35_PL.LII(:))))/min(cell2mat(BML35_PL.LII(:)));
LII_PLvar(5)=(max(cell2mat(BML36_PL.LII(:)))-
min(cell2mat(BML36_PL.LII(:))))/min(cell2mat(BML36_PL.LII(:)));
% 20 Week
LII_PLvar(6)=(max(cell2mat(BML5_PL.LII(:)))-
min(cell2mat(BML5_PL.LII(:))))/min(cell2mat(BML5_PL.LII(:)));
LII_PLvar(7)=(max(cell2mat(BML4A_PL.LII(:)))-
min(cell2mat(BML4A_PL.LII(:))))/min(cell2mat(BML4A_PL.LII(:)));
LII_PLvar(8)=(max(cell2mat(BML15_PL.LII(:)))-
min(cell2mat(BML15_PL.LII(:))))/min(cell2mat(BML15_PL.LII(:)));
LII_PLvar(9)=(max(cell2mat(BML25_PL.LII(:)))-
min(cell2mat(BML25_PL.LII(:))))/min(cell2mat(BML25_PL.LII(:)));
LII_PLvar(10)=(max(cell2mat(BML26_PL.LII(:)))-
min(cell2mat(BML26_PL.LII(:))))/min(cell2mat(BML26_PL.LII(:)));
% 24 Week
LII_PLvar(11)=(max(cell2mat(BML8_PL.LII(:)))-
min(cell2mat(BML8_PL.LII(:))))/min(cell2mat(BML8_PL.LII(:)));
LII_PLvar(12)=(max(cell2mat(BML18_PL.LII(:)))-
min(cell2mat(BML18_PL.LII(:))))/min(cell2mat(BML18_PL.LII(:)));
LII_PLvar(13)=(max(cell2mat(BML20_PL.LII(:)))-
min(cell2mat(BML20_PL.LII(:))))/min(cell2mat(BML20_PL.LII(:)));
LII_PLvar(14)=(max(cell2mat(BML21_PL.LII(:)))-
min(cell2mat(BML21_PL.LII(:))))/min(cell2mat(BML21_PL.LII(:)));
% LII_PLvar(15)=(max(cell2mat(BML16_PL.LII(:)))-
min(cell2mat(BML16_PL.LII(:))))/min(cell2mat(BML16_PL.LII(:))); % N/A
LII_maxPLvar=max(LII_PLvar)
```

```
LII_minPLvar=min(LII_PLvar)

%%%%%%%%%%%%%%%%%%%%%%%%%%%%%%%%%%%%%%%%%%%%%%%%%%%%%%%%%%%%%%%%%%%%%%%%%%%%
%%% MAX AND MIN VALUES OF WIDTHS %%%%%%%%%%%%%%%%%%%%%%%%%%%%%%%%%%%%%%%%%%%
%%%%%%%%%%%%%%%%%%%%%%%%%%%%%%%%%%%%%%%%%%%%%%%%%%%%%%%%%%%%%%%%%%%%%%%%%%%%

%%% Anterior Lambdoid
% 16 Week
AvgWidth_ALvar(1)=(max(cell2mat(BML3_AL_LHS.AvgWidth(:)))-
min(cell2mat(BML3_AL_LHS.AvgWidth(:))))/min(cell2mat(BML3_AL_LHS.AvgWidth(:))
);
AvgWidth_ALvar(2)=(max(cell2mat(BML3_AL_RHS.AvgWidth(:)))-
min(cell2mat(BML3_AL_RHS.AvgWidth(:))))/min(cell2mat(BML3_AL_RHS.AvgWidth(:))
);
AvgWidth_ALvar(3)=(max(cell2mat(BML11_AL_LHS.AvgWidth(:)))-
min(cell2mat(BML11_AL_LHS.AvgWidth(:))))/min(cell2mat(BML11_AL_LHS.AvgWidth(:
)));
AvgWidth_ALvar(4)=(max(cell2mat(BML11_AL_RHS.AvgWidth(:)))-
min(cell2mat(BML11_AL_RHS.AvgWidth(:))))/min(cell2mat(BML11_AL_RHS.AvgWidth(:
)));
AvgWidth_ALvar(5)=(max(cell2mat(BML12_AL_LHS.AvgWidth(:)))-
min(cell2mat(BML12_AL_LHS.AvgWidth(:))))/min(cell2mat(BML12_AL_LHS.AvgWidth(:
)));
AvgWidth_ALvar(6)=(max(cell2mat(BML12_AL_RHS.AvgWidth(:)))-
min(cell2mat(BML12_AL_RHS.AvgWidth(:))))/min(cell2mat(BML12_AL_RHS.AvgWidth(:
)));
AvgWidth_ALvar(7)=(max(cell2mat(BML35_AL_LHS.AvgWidth(:)))-
min(cell2mat(BML35_AL_LHS.AvgWidth(:))))/min(cell2mat(BML35_AL_LHS.AvgWidth(:
)));
AvgWidth_ALvar(8)=(max(cell2mat(BML35_AL_RHS.AvgWidth(:)))-
min(cell2mat(BML35_AL_RHS.AvgWidth(:))))/min(cell2mat(BML35_AL_RHS.AvgWidth(:
)));
AvgWidth_ALvar(9)=(max(cell2mat(BML36_AL_LHS.AvgWidth(:)))-
min(cell2mat(BML36_AL_LHS.AvgWidth(:))))/min(cell2mat(BML36_AL_LHS.AvgWidth(:
)));
AvgWidth_ALvar(10)=(max(cell2mat(BML36_AL_RHS.AvgWidth(:)))-
min(cell2mat(BML36_AL_RHS.AvgWidth(:))))/min(cell2mat(BML36_AL_RHS.AvgWidth(:
)));
% 20 Week
AvgWidth_ALvar(11)=(max(cell2mat(BML5_AL_LHS.AvgWidth(:)))-
min(cell2mat(BML5_AL_LHS.AvgWidth(:))))/min(cell2mat(BML5_AL_LHS.AvgWidth(:))
);
AvgWidth_ALvar(12)=(max(cell2mat(BML5_AL_RHS.AvgWidth(:)))-
min(cell2mat(BML5_AL_RHS.AvgWidth(:))))/min(cell2mat(BML5_AL_RHS.AvgWidth(:))
);
AvgWidth_ALvar(13)=(max(cell2mat(BML4A_AL_LHS.AvgWidth(:)))-
min(cell2mat(BML4A_AL_LHS.AvgWidth(:))))/min(cell2mat(BML4A_AL_LHS.AvgWidth(:
)));
AvgWidth_ALvar(14)=(max(cell2mat(BML4A_AL_RHS.AvgWidth(:)))-
min(cell2mat(BML4A_AL_RHS.AvgWidth(:))))/min(cell2mat(BML4A_AL_RHS.AvgWidth(:
)));
AvgWidth_ALvar(15)=(max(cell2mat(BML15_AL_LHS.AvgWidth(:)))-
min(cell2mat(BML15_AL_LHS.AvgWidth(:))))/min(cell2mat(BML15_AL_LHS.AvgWidth(:
)));
```

```
AvgWidth_ALvar(16)=(max(cell2mat(BML15_AL_RHS.AvgWidth(:)))-
min(cell2mat(BML15_AL_RHS.AvgWidth(:))))/min(cell2mat(BML15_AL_RHS.AvgWidth(:
)));
AvgWidth_ALvar(17)=(max(cell2mat(BML25_AL_LHS.AvgWidth(:)))-
min(cell2mat(BML25_AL_LHS.AvgWidth(:))))/min(cell2mat(BML25_AL_LHS.AvgWidth(:
)));
AvgWidth_ALvar(18)=(max(cell2mat(BML25_AL_RHS.AvgWidth(:)))-
min(cell2mat(BML25_AL_RHS.AvgWidth(:))))/min(cell2mat(BML25_AL_RHS.AvgWidth(:
)));
AvgWidth_ALvar(19)=(max(cell2mat(BML26_AL_LHS.AvgWidth(:)))-
min(cell2mat(BML26_AL_LHS.AvgWidth(:))))/min(cell2mat(BML26_AL_LHS.AvgWidth(:
)));
AvgWidth_ALvar(20)=(max(cell2mat(BML26_AL_RHS.AvgWidth(:)))-
min(cell2mat(BML26_AL_RHS.AvgWidth(:))))/min(cell2mat(BML26_AL_RHS.AvgWidth(:
)));
% 24 Week
AvgWidth_ALvar(21)=(max(cell2mat(BML8_AL_LHS.AvgWidth(:)))-
min(cell2mat(BML8_AL_LHS.AvgWidth(:))))/min(cell2mat(BML8_AL_LHS.AvgWidth(:))
);
AvgWidth_ALvar(22)=(max(cell2mat(BML8_AL_RHS.AvgWidth(:)))-
min(cell2mat(BML8_AL_RHS.AvgWidth(:))))/min(cell2mat(BML8_AL_RHS.AvgWidth(:))
);
AvgWidth_ALvar(23)=(max(cell2mat(BML18_AL_LHS.AvgWidth(:)))-
min(cell2mat(BML18_AL_LHS.AvgWidth(:))))/min(cell2mat(BML18_AL_LHS.AvgWidth(:
)));
AvgWidth_ALvar(24)=(max(cell2mat(BML18_AL_RHS.AvgWidth(:)))-
min(cell2mat(BML18_AL_RHS.AvgWidth(:))))/min(cell2mat(BML18_AL_RHS.AvgWidth(:
)));
AvgWidth_ALvar(25)=(max(cell2mat(BML20_AL_LHS.AvgWidth(:)))-
min(cell2mat(BML20_AL_LHS.AvgWidth(:))))/min(cell2mat(BML20_AL_LHS.AvgWidth(:
)));
AvgWidth_ALvar(26)=(max(cell2mat(BML20_AL_RHS.AvgWidth(:)))-
min(cell2mat(BML20_AL_RHS.AvgWidth(:))))/min(cell2mat(BML20_AL_RHS.AvgWidth(:
)));
AvgWidth_ALvar(27)=(max(cell2mat(BML21_AL_LHS.AvgWidth(:)))-
min(cell2mat(BML21_AL_LHS.AvgWidth(:))))/min(cell2mat(BML21_AL_LHS.AvgWidth(:
)));
AvgWidth_ALvar(28)=(max(cell2mat(BML21_AL_RHS.AvgWidth(:)))-
min(cell2mat(BML21_AL_RHS.AvgWidth(:))))/min(cell2mat(BML21_AL_RHS.AvgWidth(:
)));
AvgWidth_ALvar(29)=(max(cell2mat(BML16_AL_LHS.AvgWidth(:)))-
min(cell2mat(BML16_AL_LHS.AvgWidth(:))))/min(cell2mat(BML16_AL_LHS.AvgWidth(:
)));
AvgWidth_ALvar(30)=(max(cell2mat(BML16_AL_RHS.AvgWidth(:)))-
min(cell2mat(BML16_AL_RHS.AvgWidth(:))))/min(cell2mat(BML16_AL_RHS.AvgWidth(:
)));
AvgWidth_maxALvar=max(AvgWidth_ALvar)
AvgWidth_minALvar=min(AvgWidth_ALvar)

%%% Coronal
% 16 Week
AvgWidth_Corvar(1)=(max(cell2mat(BML3_Cor_LHS.AvgWidth(:)))-
min(cell2mat(BML3_Cor_LHS.AvgWidth(:))))/min(cell2mat(BML3_Cor_LHS.AvgWidth(:
)));
```

```
AvgWidth_Corvar(2)=(max(cell2mat(BML3_Cor_RHS.AvgWidth(:)))-
min(cell2mat(BML3_Cor_RHS.AvgWidth(:))))/min(cell2mat(BML3_Cor_RHS.AvgWidth(:
)));
AvgWidth_Corvar(3)=(max(cell2mat(BML11_Cor_LHS.AvgWidth(:)))-
min(cell2mat(BML11_Cor_LHS.AvgWidth(:))))/min(cell2mat(BML11_Cor_LHS.AvgWidth
(:)));
AvgWidth_Corvar(4)=(max(cell2mat(BML11_Cor_RHS.AvgWidth(:)))-
min(cell2mat(BML11_Cor_RHS.AvgWidth(:))))/min(cell2mat(BML11_Cor_RHS.AvgWidth
(:)));
AvgWidth_Corvar(5)=(max(cell2mat(BML12_Cor_LHS.AvgWidth(:)))-
min(cell2mat(BML12_Cor_LHS.AvgWidth(:))))/min(cell2mat(BML12_Cor_LHS.AvgWidth
(:)));
AvgWidth_Corvar(6)=(max(cell2mat(BML12_Cor_RHS.AvgWidth(:)))-
min(cell2mat(BML12_Cor_RHS.AvgWidth(:))))/min(cell2mat(BML12_Cor_RHS.AvgWidth
(:)));
AvgWidth_Corvar(7)=(max(cell2mat(BML35_Cor_LHS.AvgWidth(:)))-
min(cell2mat(BML35_Cor_LHS.AvgWidth(:))))/min(cell2mat(BML35_Cor_LHS.AvgWidth
(:)));
AvgWidth_Corvar(8)=(max(cell2mat(BML35_Cor_RHS.AvgWidth(:)))-
min(cell2mat(BML35_Cor_RHS.AvgWidth(:))))/min(cell2mat(BML35_Cor_RHS.AvgWidth
(:)));
AvgWidth_Corvar(9)=(max(cell2mat(BML36_Cor_LHS.AvgWidth(:)))-
min(cell2mat(BML36_Cor_LHS.AvgWidth(:))))/min(cell2mat(BML36_Cor_LHS.AvgWidth
(:)));
AvgWidth_Corvar(10)=(max(cell2mat(BML36_Cor_RHS.AvgWidth(:)))-
min(cell2mat(BML36_Cor_RHS.AvgWidth(:))))/min(cell2mat(BML36_Cor_RHS.AvgWidth
(:)));
% 20 Week
AvgWidth_Corvar(11)=(max(cell2mat(BML5_Cor_LHS.AvgWidth(:)))-
min(cell2mat(BML5_Cor_LHS.AvgWidth(:))))/min(cell2mat(BML5_Cor_LHS.AvgWidth(:
)));
AvgWidth_Corvar(12)=(max(cell2mat(BML5_Cor_RHS.AvgWidth(:)))-
min(cell2mat(BML5_Cor_RHS.AvgWidth(:))))/min(cell2mat(BML5_Cor_RHS.AvgWidth(:
)));
AvgWidth_Corvar(13)=(max(cell2mat(BML4A_Cor_LHS.AvgWidth(:)))-
min(cell2mat(BML4A_Cor_LHS.AvgWidth(:))))/min(cell2mat(BML4A_Cor_LHS.AvgWidth
(:)));
AvgWidth_Corvar(14)=(max(cell2mat(BML4A_Cor_RHS.AvgWidth(:)))-
min(cell2mat(BML4A_Cor_RHS.AvgWidth(:))))/min(cell2mat(BML4A_Cor_RHS.AvgWidth
(:)));
AvgWidth_Corvar(15)=(max(cell2mat(BML15_Cor_LHS.AvgWidth(:)))-
min(cell2mat(BML15_Cor_LHS.AvgWidth(:))))/min(cell2mat(BML15_Cor_LHS.AvgWidth
(:)));
AvgWidth_Corvar(16)=(max(cell2mat(BML15_Cor_RHS.AvgWidth(:)))-
min(cell2mat(BML15_Cor_RHS.AvgWidth(:))))/min(cell2mat(BML15_Cor_RHS.AvgWidth
(:)));
AvgWidth_Corvar(17)=(max(cell2mat(BML25_Cor_LHS.AvgWidth(:)))-
min(cell2mat(BML25_Cor_LHS.AvgWidth(:))))/min(cell2mat(BML25_Cor_LHS.AvgWidth
(:)));
AvgWidth_Corvar(18)=(max(cell2mat(BML25_Cor_RHS.AvgWidth(:)))-
min(cell2mat(BML25_Cor_RHS.AvgWidth(:))))/min(cell2mat(BML25_Cor_RHS.AvgWidth
(:)));
AvgWidth_Corvar(19)=(max(cell2mat(BML26_Cor_LHS.AvgWidth(:)))-
min(cell2mat(BML26_Cor_LHS.AvgWidth(:))))/min(cell2mat(BML26_Cor_LHS.AvgWidth
(:)));
```

```
AvgWidth_Corvar(20)=(max(cell2mat(BML26_Cor_RHS.AvgWidth(:)))-
min(cell2mat(BML26_Cor_RHS.AvgWidth(:))))/min(cell2mat(BML26_Cor_RHS.AvgWidth
(:)));
% 24 Week
AvgWidth_Corvar(21)=(max(cell2mat(BML8_Cor_LHS.AvgWidth(:)))-
min(cell2mat(BML8_Cor_LHS.AvgWidth(:))))/min(cell2mat(BML8_Cor_LHS.AvgWidth(:
)));
AvgWidth_Corvar(22)=(max(cell2mat(BML8_Cor_RHS.AvgWidth(:)))-
min(cell2mat(BML8_Cor_RHS.AvgWidth(:))))/min(cell2mat(BML8_Cor_RHS.AvgWidth(:
)));
AvgWidth_Corvar(23)=(max(cell2mat(BML18_Cor_LHS.AvgWidth(:)))-
min(cell2mat(BML18_Cor_LHS.AvgWidth(:))))/min(cell2mat(BML18_Cor_LHS.AvgWidth
(:)));
AvgWidth_Corvar(24)=(max(cell2mat(BML18_Cor_RHS.AvgWidth(:)))-
min(cell2mat(BML18_Cor_RHS.AvgWidth(:))))/min(cell2mat(BML18_Cor_RHS.AvgWidth
(:)));
AvgWidth_Corvar(25)=(max(cell2mat(BML20_Cor_LHS.AvgWidth(:)))-
min(cell2mat(BML20_Cor_LHS.AvgWidth(:))))/min(cell2mat(BML20_Cor_LHS.AvgWidth
(:)));
AvgWidth_Corvar(26)=(max(cell2mat(BML20_Cor_RHS.AvgWidth(:)))-
min(cell2mat(BML20_Cor_RHS.AvgWidth(:))))/min(cell2mat(BML20_Cor_RHS.AvgWidth
(:)));
AvgWidth_Corvar(27)=(max(cell2mat(BML21_Cor_LHS.AvgWidth(:)))-
min(cell2mat(BML21_Cor_LHS.AvgWidth(:))))/min(cell2mat(BML21_Cor_LHS.AvgWidth
(:)));
AvgWidth_Corvar(28)=(max(cell2mat(BML21_Cor_RHS.AvgWidth(:)))-
min(cell2mat(BML21_Cor_RHS.AvgWidth(:))))/min(cell2mat(BML21_Cor_RHS.AvgWidth
(:)));
AvgWidth_Corvar(29)=(max(cell2mat(BML16_Cor_LHS.AvgWidth(:)))-
min(cell2mat(BML16_Cor_LHS.AvgWidth(:))))/min(cell2mat(BML16_Cor_LHS.AvgWidth
(:)));
AvgWidth_Corvar(30)=(max(cell2mat(BML16_Cor_RHS.AvgWidth(:)))-
min(cell2mat(BML16_Cor_RHS.AvgWidth(:))))/min(cell2mat(BML16_Cor_RHS.AvgWidth
(:)));
AvgWidth_maxCorvar=max(AvgWidth_Corvar)
AvgWidth_minCorvar=min(AvgWidth_Corvar)

% Sagittal
% 16 Week
AvgWidth_Sagvar(1)=(max(cell2mat(BML3_Sag.AvgWidth(:)))-
min(cell2mat(BML3_Sag.AvgWidth(:))))/min(cell2mat(BML3_Sag.AvgWidth(:)));
AvgWidth_Sagvar(2)=(max(cell2mat(BML11_Sag.AvgWidth(:)))-
min(cell2mat(BML11_Sag.AvgWidth(:))))/min(cell2mat(BML11_Sag.AvgWidth(:)));
AvgWidth_Sagvar(3)=(max(cell2mat(BML12_Sag.AvgWidth(:)))-
min(cell2mat(BML12_Sag.AvgWidth(:))))/min(cell2mat(BML12_Sag.AvgWidth(:)));
AvgWidth_Sagvar(4)=(max(cell2mat(BML35_Sag.AvgWidth(:)))-
min(cell2mat(BML35_Sag.AvgWidth(:))))/min(cell2mat(BML35_Sag.AvgWidth(:)));
AvgWidth_Sagvar(5)=(max(cell2mat(BML36_Sag.AvgWidth(:)))-
min(cell2mat(BML36_Sag.AvgWidth(:))))/min(cell2mat(BML36_Sag.AvgWidth(:)));
% 20 Week
AvgWidth_Sagvar(6)=(max(cell2mat(BML5_Sag.AvgWidth(:)))-
min(cell2mat(BML5_Sag.AvgWidth(:))))/min(cell2mat(BML5_Sag.AvgWidth(:)));
AvgWidth_Sagvar(7)=(max(cell2mat(BML4A_Sag.AvgWidth(:)))-
min(cell2mat(BML4A_Sag.AvgWidth(:))))/min(cell2mat(BML4A_Sag.AvgWidth(:)));
```

```
AvgWidth_Sagvar(8)=(max(cell2mat(BML15_Sag.AvgWidth(:)))-
min(cell2mat(BML15_Sag.AvgWidth(:))))/min(cell2mat(BML15_Sag.AvgWidth(:)));
AvgWidth_Sagvar(9)=(max(cell2mat(BML25_Sag.AvgWidth(:)))-
min(cell2mat(BML25_Sag.AvgWidth(:))))/min(cell2mat(BML25_Sag.AvgWidth(:)));
AvgWidth_Sagvar(10)=(max(cell2mat(BML26_Sag.AvgWidth(:)))-
min(cell2mat(BML26_Sag.AvgWidth(:))))/min(cell2mat(BML26_Sag.AvgWidth(:)));
% 24 Week
AvgWidth_Sagvar(11)=(max(cell2mat(BML8_Sag.AvgWidth(:)))-
min(cell2mat(BML8_Sag.AvgWidth(:))))/min(cell2mat(BML8_Sag.AvgWidth(:)));
AvgWidth_Sagvar(12)=(max(cell2mat(BML18_Sag.AvgWidth(:)))-
min(cell2mat(BML18_Sag.AvgWidth(:))))/min(cell2mat(BML18_Sag.AvgWidth(:)));
AvgWidth_Sagvar(13)=(max(cell2mat(BML20_Sag.AvgWidth(:)))-
min(cell2mat(BML20_Sag.AvgWidth(:))))/min(cell2mat(BML20_Sag.AvgWidth(:)));
AvgWidth_Sagvar(14)=(max(cell2mat(BML21_Sag.AvgWidth(:)))-
min(cell2mat(BML21_Sag.AvgWidth(:))))/min(cell2mat(BML21_Sag.AvgWidth(:)));
AvgWidth_Sagvar(15)=(max(cell2mat(BML16_Sag.AvgWidth(:)))-
min(cell2mat(BML16_Sag.AvgWidth(:))))/min(cell2mat(BML16_Sag.AvgWidth(:)));
AvgWidth_maxSagvar=max(AvgWidth_Sagvar)
AvgWidth_minSagvar=min(AvgWidth_Sagvar)

% Posterior Lambdoid
% 16 Week
AvgWidth_PLvar(1)=(max(cell2mat(BML3_PL.AvgWidth(:)))-
min(cell2mat(BML3_PL.AvgWidth(:))))/min(cell2mat(BML3_PL.AvgWidth(:)));
AvgWidth_PLvar(2)=(max(cell2mat(BML11_PL.AvgWidth(:)))-
min(cell2mat(BML11_PL.AvgWidth(:))))/min(cell2mat(BML11_PL.AvgWidth(:)));
AvgWidth_PLvar(3)=(max(cell2mat(BML12_PL.AvgWidth(:)))-
min(cell2mat(BML12_PL.AvgWidth(:))))/min(cell2mat(BML12_PL.AvgWidth(:)));
AvgWidth_PLvar(4)=(max(cell2mat(BML35_PL.AvgWidth(:)))-
min(cell2mat(BML35_PL.AvgWidth(:))))/min(cell2mat(BML35_PL.AvgWidth(:)));
AvgWidth_PLvar(5)=(max(cell2mat(BML36_PL.AvgWidth(:)))-
min(cell2mat(BML36_PL.AvgWidth(:))))/min(cell2mat(BML36_PL.AvgWidth(:)));
% 20 Week
AvgWidth_PLvar(6)=(max(cell2mat(BML5_PL.AvgWidth(:)))-
min(cell2mat(BML5_PL.AvgWidth(:))))/min(cell2mat(BML5_PL.AvgWidth(:)));
AvgWidth_PLvar(7)=(max(cell2mat(BML4A_PL.AvgWidth(:)))-
min(cell2mat(BML4A_PL.AvgWidth(:))))/min(cell2mat(BML4A_PL.AvgWidth(:)));
AvgWidth_PLvar(8)=(max(cell2mat(BML15_PL.AvgWidth(:)))-
min(cell2mat(BML15_PL.AvgWidth(:))))/min(cell2mat(BML15_PL.AvgWidth(:)));
AvgWidth_PLvar(9)=(max(cell2mat(BML25_PL.AvgWidth(:)))-
min(cell2mat(BML25_PL.AvgWidth(:))))/min(cell2mat(BML25_PL.AvgWidth(:)));
AvgWidth_PLvar(10)=(max(cell2mat(BML26_PL.AvgWidth(:)))-
min(cell2mat(BML26_PL.AvgWidth(:))))/min(cell2mat(BML26_PL.AvgWidth(:)));
% 24 Week
AvgWidth_PLvar(11)=(max(cell2mat(BML8_PL.AvgWidth(:)))-
min(cell2mat(BML8_PL.AvgWidth(:))))/min(cell2mat(BML8_PL.AvgWidth(:)));
AvgWidth_PLvar(12)=(max(cell2mat(BML18_PL.AvgWidth(:)))-
min(cell2mat(BML18_PL.AvgWidth(:))))/min(cell2mat(BML18_PL.AvgWidth(:)));
AvgWidth_PLvar(13)=(max(cell2mat(BML20_PL.AvgWidth(:)))-
min(cell2mat(BML20_PL.AvgWidth(:))))/min(cell2mat(BML20_PL.AvgWidth(:)));
AvgWidth_PLvar(14)=(max(cell2mat(BML21_PL.AvgWidth(:)))-
min(cell2mat(BML21_PL.AvgWidth(:))))/min(cell2mat(BML21_PL.AvgWidth(:)));
% AvgWidth_PLvar(15)=(max(cell2mat(BML16_PL.AvgWidth(:)))-
min(cell2mat(BML16_PL.AvgWidth(:))))/min(cell2mat(BML16_PL.AvgWidth(:))); %
N/A
```

```
AvgWidth_maxPLvar=max(AvgWidth_PLvar)
AvgWidth_minPLvar=min(AvgWidth_PLvar)

%%%%%%%%%%%%%%%%%%%%%%%%%%%%%%%%%%%%%%%%%%%%%%%%%%%%%%%%%%%%%%%%%%%%%%%%%%%%%%%%
%%% MAX AND MIN VALUES OF LOCAL WIDTHS %%%%%%%%%%%%%%%%%%%%%%%%%%%%%%%%%%%%%%%%%
%%%%%%%%%%%%%%%%%%%%%%%%%%%%%%%%%%%%%%%%%%%%%%%%%%%%%%%%%%%%%%%%%%%%%%%%%%%%%%%%

%%% Anterior Lambdoid
% 16 Week
Width_ALvar(1)=(max(cell2mat(BML3_AL_LHS.Width(:)))-
min(cell2mat(BML3_AL_LHS.Width(:))))/min(cell2mat(BML3_AL_LHS.Width(:)));
Width_ALvar(2)=(max(cell2mat(BML3_AL_RHS.Width(:)))-
min(cell2mat(BML3_AL_RHS.Width(:))))/min(cell2mat(BML3_AL_RHS.Width(:)));
Width_ALvar(3)=(max(cell2mat(BML11_AL_LHS.Width(:)))-
min(cell2mat(BML11_AL_LHS.Width(:))))/min(cell2mat(BML11_AL_LHS.Width(:)));
Width_ALvar(4)=(max(cell2mat(BML11_AL_RHS.Width(:)))-
min(cell2mat(BML11_AL_RHS.Width(:))))/min(cell2mat(BML11_AL_RHS.Width(:)));
Width_ALvar(5)=(max(cell2mat(BML12_AL_LHS.Width(:)))-
min(cell2mat(BML12_AL_LHS.Width(:))))/min(cell2mat(BML12_AL_LHS.Width(:)));
Width_ALvar(6)=(max(cell2mat(BML12_AL_RHS.Width(:)))-
min(cell2mat(BML12_AL_RHS.Width(:))))/min(cell2mat(BML12_AL_RHS.Width(:)));
Width_ALvar(7)=(max(cell2mat(BML35_AL_LHS.Width(:)))-
min(cell2mat(BML35_AL_LHS.Width(:))))/min(cell2mat(BML35_AL_LHS.Width(:)));
Width_ALvar(8)=(max(cell2mat(BML35_AL_RHS.Width(:)))-
min(cell2mat(BML35_AL_RHS.Width(:))))/min(cell2mat(BML35_AL_RHS.Width(:)));
Width_ALvar(9)=(max(cell2mat(BML36_AL_LHS.Width(:)))-
min(cell2mat(BML36_AL_LHS.Width(:))))/min(cell2mat(BML36_AL_LHS.Width(:)));
Width_ALvar(10)=(max(cell2mat(BML36_AL_RHS.Width(:)))-
min(cell2mat(BML36_AL_RHS.Width(:))))/min(cell2mat(BML36_AL_RHS.Width(:)));
% 20 Week
Width_ALvar(11)=(max(cell2mat(BML5_AL_LHS.Width(:)))-
min(cell2mat(BML5_AL_LHS.Width(:))))/min(cell2mat(BML5_AL_LHS.Width(:)));
Width_ALvar(12)=(max(cell2mat(BML5_AL_RHS.Width(:)))-
min(cell2mat(BML5_AL_RHS.Width(:))))/min(cell2mat(BML5_AL_RHS.Width(:)));
Width_ALvar(13)=(max(cell2mat(BML4A_AL_LHS.Width(:)))-
min(cell2mat(BML4A_AL_LHS.Width(:))))/min(cell2mat(BML4A_AL_LHS.Width(:)));
Width_ALvar(14)=(max(cell2mat(BML4A_AL_RHS.Width(:)))-
min(cell2mat(BML4A_AL_RHS.Width(:))))/min(cell2mat(BML4A_AL_RHS.Width(:)));
Width_ALvar(15)=(max(cell2mat(BML15_AL_LHS.Width(:)))-
min(cell2mat(BML15_AL_LHS.Width(:))))/min(cell2mat(BML15_AL_LHS.Width(:)));
Width_ALvar(16)=(max(cell2mat(BML15_AL_RHS.Width(:)))-
min(cell2mat(BML15_AL_RHS.Width(:))))/min(cell2mat(BML15_AL_RHS.Width(:)));
Width_ALvar(17)=(max(cell2mat(BML25_AL_LHS.Width(:)))-
min(cell2mat(BML25_AL_LHS.Width(:))))/min(cell2mat(BML25_AL_LHS.Width(:)));
Width_ALvar(18)=(max(cell2mat(BML25_AL_RHS.Width(:)))-
min(cell2mat(BML25_AL_RHS.Width(:))))/min(cell2mat(BML25_AL_RHS.Width(:)));
Width_ALvar(19)=(max(cell2mat(BML26_AL_LHS.Width(:)))-
min(cell2mat(BML26_AL_LHS.Width(:))))/min(cell2mat(BML26_AL_LHS.Width(:)));
Width_ALvar(20)=(max(cell2mat(BML26_AL_RHS.Width(:)))-
min(cell2mat(BML26_AL_RHS.Width(:))))/min(cell2mat(BML26_AL_RHS.Width(:)));
% 24 Week
Width_ALvar(21)=(max(cell2mat(BML8_AL_LHS.Width(:)))-
min(cell2mat(BML8_AL_LHS.Width(:))))/min(cell2mat(BML8_AL_LHS.Width(:)));
Width_ALvar(22)=(max(cell2mat(BML8_AL_RHS.Width(:)))-
min(cell2mat(BML8_AL_RHS.Width(:))))/min(cell2mat(BML8_AL_RHS.Width(:)));
```

```
Width_ALvar(23)=(max(cell2mat(BML18_AL_LHS.Width(:)))-
min(cell2mat(BML18_AL_LHS.Width(:))))/min(cell2mat(BML18_AL_LHS.Width(:)));
Width_ALvar(24)=(max(cell2mat(BML18_AL_RHS.Width(:)))-
min(cell2mat(BML18_AL_RHS.Width(:))))/min(cell2mat(BML18_AL_RHS.Width(:)));
Width_ALvar(25)=(max(cell2mat(BML20_AL_LHS.Width(:)))-
min(cell2mat(BML20_AL_LHS.Width(:))))/min(cell2mat(BML20_AL_LHS.Width(:)));
Width_ALvar(26)=(max(cell2mat(BML20_AL_RHS.Width(:)))-
min(cell2mat(BML20_AL_RHS.Width(:))))/min(cell2mat(BML20_AL_RHS.Width(:)));
Width_ALvar(27)=(max(cell2mat(BML21_AL_LHS.Width(:)))-
min(cell2mat(BML21_AL_LHS.Width(:))))/min(cell2mat(BML21_AL_LHS.Width(:)));
Width_ALvar(28)=(max(cell2mat(BML21_AL_RHS.Width(:)))-
min(cell2mat(BML21_AL_RHS.Width(:))))/min(cell2mat(BML21_AL_RHS.Width(:)));
Width_ALvar(29)=(max(cell2mat(BML16_AL_LHS.Width(:)))-
min(cell2mat(BML16_AL_LHS.Width(:))))/min(cell2mat(BML16_AL_LHS.Width(:)));
Width_ALvar(30)=(max(cell2mat(BML16_AL_RHS.Width(:)))-
min(cell2mat(BML16_AL_RHS.Width(:))))/min(cell2mat(BML16_AL_RHS.Width(:)));
Width_maxALvar=max(Width_ALvar)
Width_minALvar=min(Width_ALvar)

%%% Coronal
% 16 Week
Width_Corvar(1)=(max(cell2mat(BML3_Cor_LHS.Width(:)))-
min(cell2mat(BML3_Cor_LHS.Width(:))))/min(cell2mat(BML3_Cor_LHS.Width(:)));
Width_Corvar(2)=(max(cell2mat(BML3_Cor_RHS.Width(:)))-
min(cell2mat(BML3_Cor_RHS.Width(:))))/min(cell2mat(BML3_Cor_RHS.Width(:)));
Width_Corvar(3)=(max(cell2mat(BML11_Cor_LHS.Width(:)))-
min(cell2mat(BML11_Cor_LHS.Width(:))))/min(cell2mat(BML11_Cor_LHS.Width(:)));
Width_Corvar(4)=(max(cell2mat(BML11_Cor_RHS.Width(:)))-
min(cell2mat(BML11_Cor_RHS.Width(:))))/min(cell2mat(BML11_Cor_RHS.Width(:)));
Width_Corvar(5)=(max(cell2mat(BML12_Cor_LHS.Width(:)))-
min(cell2mat(BML12_Cor_LHS.Width(:))))/min(cell2mat(BML12_Cor_LHS.Width(:)));
Width_Corvar(6)=(max(cell2mat(BML12_Cor_RHS.Width(:)))-
min(cell2mat(BML12_Cor_RHS.Width(:))))/min(cell2mat(BML12_Cor_RHS.Width(:)));
Width_Corvar(7)=(max(cell2mat(BML35_Cor_LHS.Width(:)))-
min(cell2mat(BML35_Cor_LHS.Width(:))))/min(cell2mat(BML35_Cor_LHS.Width(:)));
Width_Corvar(8)=(max(cell2mat(BML35_Cor_RHS.Width(:)))-
min(cell2mat(BML35_Cor_RHS.Width(:))))/min(cell2mat(BML35_Cor_RHS.Width(:)));
Width_Corvar(9)=(max(cell2mat(BML36_Cor_LHS.Width(:)))-
min(cell2mat(BML36_Cor_LHS.Width(:))))/min(cell2mat(BML36_Cor_LHS.Width(:)));
Width_Corvar(10)=(max(cell2mat(BML36_Cor_RHS.Width(:)))-
min(cell2mat(BML36_Cor_RHS.Width(:))))/min(cell2mat(BML36_Cor_RHS.Width(:)));
% 20 Week
Width_Corvar(11)=(max(cell2mat(BML5_Cor_LHS.Width(:)))-
min(cell2mat(BML5_Cor_LHS.Width(:))))/min(cell2mat(BML5_Cor_LHS.Width(:)));
Width_Corvar(12)=(max(cell2mat(BML5_Cor_RHS.Width(:)))-
min(cell2mat(BML5_Cor_RHS.Width(:))))/min(cell2mat(BML5_Cor_RHS.Width(:)));
Width_Corvar(13)=(max(cell2mat(BML4A_Cor_LHS.Width(:)))-
min(cell2mat(BML4A_Cor_LHS.Width(:))))/min(cell2mat(BML4A_Cor_LHS.Width(:)));
Width_Corvar(14)=(max(cell2mat(BML4A_Cor_RHS.Width(:)))-
min(cell2mat(BML4A_Cor_RHS.Width(:))))/min(cell2mat(BML4A_Cor_RHS.Width(:)));
Width_Corvar(15)=(max(cell2mat(BML15_Cor_LHS.Width(:)))-
min(cell2mat(BML15_Cor_LHS.Width(:))))/min(cell2mat(BML15_Cor_LHS.Width(:)));
Width_Corvar(16)=(max(cell2mat(BML15_Cor_RHS.Width(:)))-
min(cell2mat(BML15_Cor_RHS.Width(:))))/min(cell2mat(BML15_Cor_RHS.Width(:)));
```

```
Width_Corvar(17)=(max(cell2mat(BML25_Cor_LHS.Width(:)))-
min(cell2mat(BML25_Cor_LHS.Width(:))))/min(cell2mat(BML25_Cor_LHS.Width(:)));
Width_Corvar(18)=(max(cell2mat(BML25_Cor_RHS.Width(:)))-
min(cell2mat(BML25_Cor_RHS.Width(:))))/min(cell2mat(BML25_Cor_RHS.Width(:)));
Width_Corvar(19)=(max(cell2mat(BML26_Cor_LHS.Width(:)))-
min(cell2mat(BML26_Cor_LHS.Width(:))))/min(cell2mat(BML26_Cor_LHS.Width(:)));
Width_Corvar(20)=(max(cell2mat(BML26_Cor_RHS.Width(:)))-
min(cell2mat(BML26_Cor_RHS.Width(:))))/min(cell2mat(BML26_Cor_RHS.Width(:)));
% 24 Week
Width_Corvar(21)=(max(cell2mat(BML8_Cor_LHS.Width(:)))-
min(cell2mat(BML8_Cor_LHS.Width(:))))/min(cell2mat(BML8_Cor_LHS.Width(:)));
Width_Corvar(22)=(max(cell2mat(BML8_Cor_RHS.Width(:)))-
min(cell2mat(BML8_Cor_RHS.Width(:))))/min(cell2mat(BML8_Cor_RHS.Width(:)));
Width_Corvar(23)=(max(cell2mat(BML18_Cor_LHS.Width(:)))-
min(cell2mat(BML18_Cor_LHS.Width(:))))/min(cell2mat(BML18_Cor_LHS.Width(:)));
Width_Corvar(24)=(max(cell2mat(BML18_Cor_RHS.Width(:)))-
min(cell2mat(BML18_Cor_RHS.Width(:))))/min(cell2mat(BML18_Cor_RHS.Width(:)));
Width_Corvar(25)=(max(cell2mat(BML20_Cor_LHS.Width(:)))-
min(cell2mat(BML20_Cor_LHS.Width(:))))/min(cell2mat(BML20_Cor_LHS.Width(:)));
Width_Corvar(26)=(max(cell2mat(BML20_Cor_RHS.Width(:)))-
min(cell2mat(BML20_Cor_RHS.Width(:))))/min(cell2mat(BML20_Cor_RHS.Width(:)));
Width_Corvar(27)=(max(cell2mat(BML21_Cor_LHS.Width(:)))-
min(cell2mat(BML21_Cor_LHS.Width(:))))/min(cell2mat(BML21_Cor_LHS.Width(:)));
Width_Corvar(28)=(max(cell2mat(BML21_Cor_RHS.Width(:)))-
min(cell2mat(BML21_Cor_RHS.Width(:))))/min(cell2mat(BML21_Cor_RHS.Width(:)));
Width_Corvar(29)=(max(cell2mat(BML16_Cor_LHS.Width(:)))-
min(cell2mat(BML16_Cor_LHS.Width(:))))/min(cell2mat(BML16_Cor_LHS.Width(:)));
Width_Corvar(30)=(max(cell2mat(BML16_Cor_RHS.Width(:)))-
min(cell2mat(BML16_Cor_RHS.Width(:))))/min(cell2mat(BML16_Cor_RHS.Width(:)));
Width_maxCorvar=max(Width_Corvar)
Width_minCorvar=min(Width_Corvar)

% Sagittal
% 16 Week
Width_Sagvar(1)=(max(cell2mat(BML3_Sag.Width(:)))-
min(cell2mat(BML3_Sag.Width(:))))/min(cell2mat(BML3_Sag.Width(:)));
Width_Sagvar(2)=(max(cell2mat(BML11_Sag.Width(:)))-
min(cell2mat(BML11_Sag.Width(:))))/min(cell2mat(BML11_Sag.Width(:)));
Width_Sagvar(3)=(max(cell2mat(BML12_Sag.Width(:)))-
min(cell2mat(BML12_Sag.Width(:))))/min(cell2mat(BML12_Sag.Width(:)));
Width_Sagvar(4)=(max(cell2mat(BML35_Sag.Width(:)))-
min(cell2mat(BML35_Sag.Width(:))))/min(cell2mat(BML35_Sag.Width(:)));
Width_Sagvar(5)=(max(cell2mat(BML36_Sag.Width(:)))-
min(cell2mat(BML36_Sag.Width(:))))/min(cell2mat(BML36_Sag.Width(:)));
% 20 Week
Width_Sagvar(6)=(max(cell2mat(BML5_Sag.Width(:)))-
min(cell2mat(BML5_Sag.Width(:))))/min(cell2mat(BML5_Sag.Width(:)));
Width_Sagvar(7)=(max(cell2mat(BML4A_Sag.Width(:)))-
min(cell2mat(BML4A_Sag.Width(:))))/min(cell2mat(BML4A_Sag.Width(:)));
Width_Sagvar(8)=(max(cell2mat(BML15_Sag.Width(:)))-
min(cell2mat(BML15_Sag.Width(:))))/min(cell2mat(BML15_Sag.Width(:)));
Width_Sagvar(9)=(max(cell2mat(BML25_Sag.Width(:)))-
min(cell2mat(BML25_Sag.Width(:))))/min(cell2mat(BML25_Sag.Width(:)));
Width_Sagvar(10)=(max(cell2mat(BML26_Sag.Width(:)))-
min(cell2mat(BML26_Sag.Width(:))))/min(cell2mat(BML26_Sag.Width(:)));
```

```
% 24 Week
Width_Sagvar(11)=(max(cell2mat(BML8_Sag.Width(:)))-
min(cell2mat(BML8_Sag.Width(:))))/min(cell2mat(BML8_Sag.Width(:)));
Width_Sagvar(12)=(max(cell2mat(BML18_Sag.Width(:)))-
min(cell2mat(BML18_Sag.Width(:))))/min(cell2mat(BML18_Sag.Width(:)));
Width_Sagvar(13)=(max(cell2mat(BML20_Sag.Width(:)))-
min(cell2mat(BML20_Sag.Width(:))))/min(cell2mat(BML20_Sag.Width(:)));
Width_Sagvar(14)=(max(cell2mat(BML21_Sag.Width(:)))-
min(cell2mat(BML21_Sag.Width(:))))/min(cell2mat(BML21_Sag.Width(:)));
Width_Sagvar(15)=(max(cell2mat(BML16_Sag.Width(:)))-
min(cell2mat(BML16_Sag.Width(:))))/min(cell2mat(BML16_Sag.Width(:)));
Width_maxSagvar=max(Width_Sagvar)
Width_minSagvar=min(Width_Sagvar)

% Posterior Lambdoid
% 16 Week
Width_PLvar(1)=(max(cell2mat(BML3_PL.Width(:)))-
min(cell2mat(BML3_PL.Width(:))))/min(cell2mat(BML3_PL.Width(:)));
Width_PLvar(2)=(max(cell2mat(BML11_PL.Width(:)))-
min(cell2mat(BML11_PL.Width(:))))/min(cell2mat(BML11_PL.Width(:)));
Width_PLvar(3)=(max(cell2mat(BML12_PL.Width(:)))-
min(cell2mat(BML12_PL.Width(:))))/min(cell2mat(BML12_PL.Width(:)));
Width_PLvar(4)=(max(cell2mat(BML35_PL.Width(:)))-
min(cell2mat(BML35_PL.Width(:))))/min(cell2mat(BML35_PL.Width(:)));
Width_PLvar(5)=(max(cell2mat(BML36_PL.Width(:)))-
min(cell2mat(BML36_PL.Width(:))))/min(cell2mat(BML36_PL.Width(:)));
% 20 Week
Width_PLvar(6)=(max(cell2mat(BML5_PL.Width(:)))-
min(cell2mat(BML5_PL.Width(:))))/min(cell2mat(BML5_PL.Width(:)));
Width_PLvar(7)=(max(cell2mat(BML4A_PL.Width(:)))-
min(cell2mat(BML4A_PL.Width(:))))/min(cell2mat(BML4A_PL.Width(:)));
Width_PLvar(8)=(max(cell2mat(BML15_PL.Width(:)))-
min(cell2mat(BML15_PL.Width(:))))/min(cell2mat(BML15_PL.Width(:)));
Width_PLvar(9)=(max(cell2mat(BML25_PL.Width(:)))-
min(cell2mat(BML25_PL.Width(:))))/min(cell2mat(BML25_PL.Width(:)));
Width_PLvar(10)=(max(cell2mat(BML26_PL.Width(:)))-
min(cell2mat(BML26_PL.Width(:))))/min(cell2mat(BML26_PL.Width(:)));
% 24 Week
Width_PLvar(11)=(max(cell2mat(BML8_PL.Width(:)))-
min(cell2mat(BML8_PL.Width(:))))/min(cell2mat(BML8_PL.Width(:)));
Width_PLvar(12)=(max(cell2mat(BML18_PL.Width(:)))-
min(cell2mat(BML18_PL.Width(:))))/min(cell2mat(BML18_PL.Width(:)));
Width_PLvar(13)=(max(cell2mat(BML20_PL.Width(:)))-
min(cell2mat(BML20_PL.Width(:))))/min(cell2mat(BML20_PL.Width(:)));
Width_PLvar(14)=(max(cell2mat(BML21_PL.Width(:)))-
min(cell2mat(BML21_PL.Width(:))))/min(cell2mat(BML21_PL.Width(:)));
% Width_PLvar(15)=(max(cell2mat(BML16_PL.Width(:)))-
min(cell2mat(BML16_PL.Width(:))))/min(cell2mat(BML16_PL.Width(:))); % N/A
Width_maxPLvar=max(Width_PLvar)
Width_minPLvar=min(Width_PLvar)
```

Appendix B: Finite Element Model Generation

B1 2DV Model Geometry Generation

The 2DV geometries used in the FE analysis discussed in Chapter 3 were generated by importing the select results of the image processing of Coronal_3351 (mentioned in Chapter 3 as Sample 1) to SolidWorks, where the 2DV models were created. Three 2DV solid bodies were generated using the endocranial-most plane (Coronal_1130), the midplane (Coronal_0980), and the ectocranial-most plane (Coronal_830) of the μCT dataset, the binarized images that were imported are shown in Figure 32.

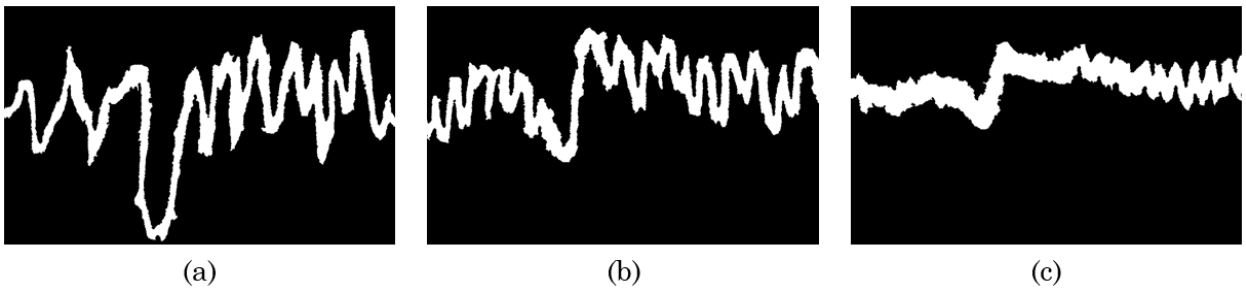

Figure 32 *Binarized images of isolated suture (shown in white); (a) ectocranial-most slice (Coronal_0830); (b) mid-plane slice (Coronal_0980); (c) endocranial-most slice (Coronal_1130)*

These images were exported from MATLAB in a .tif file, this was converted to a .dxg file to for compatibility with SolidWorks. The .dxg files were imported to SolidWorks where the suture bone interface was imported as a spline. Bone was drawn in SolidWorks to bound the bone. The suture and bone sketch were extruded 2.67 mm in order to maintain a consistent high with the 3DV model (301 planes generated from orthotropic voxels with 8.9 μm resolution; 300*8.9 μm = 2670 μm=2.67 mm) that was being simultaneously generated. The extrusion of the form ensured the structure represented the 2D assumption often taken when morphologically and mechanically analyzing sutures of only analyzing at a single 2D plane of a suture, as shown in Figure 33.

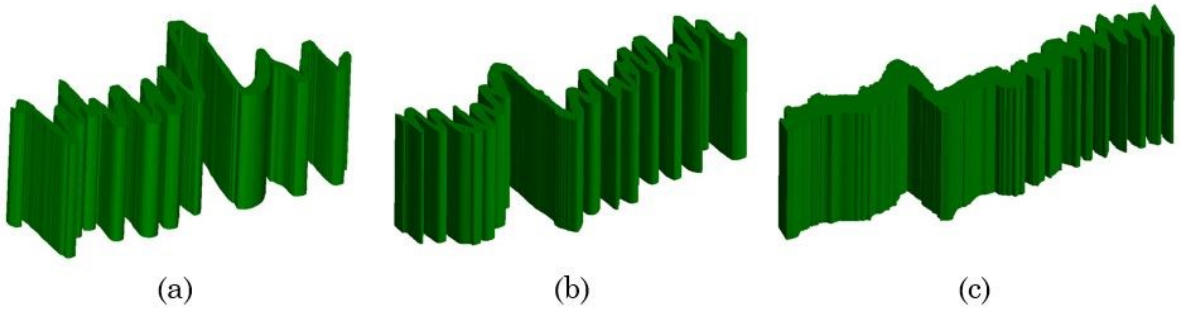

Figure 33 *2DV suture models with bone hidden; (a) ectocranial-most model (Coronal_0830); (b) mid-plane model (Coronal_0980); (c) endocranial-most model (Coronal_1130)*

B2 3DV Model Geometry Generation

The μCT dataset Coronal_3351 was imported to Mimics 23.0 where the same range (0830-1130) was chosen to generate the 3DV model. The initial importing interface with the extreme planes of the range, the endocranial and ectocranial-most is shown below in Figure 34.

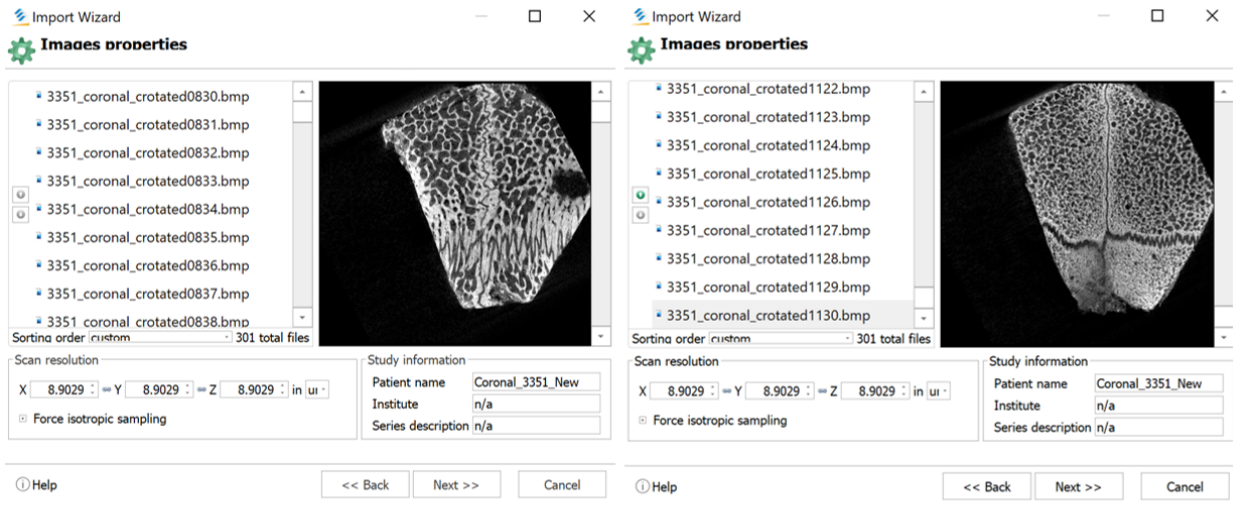

Figure 34 *Importing Coronal_3351 μCT data to Mimics 23.0; (a) ectocranial-most plane of range; (b) endocranial-most plane of range*

Once the data was imported to Mimics 23.0, the dataset was cropped in order to use the same region of interest as was in the image processing analysis and 2DV

models. The dataset was then thresholded in order to create a mask for the bone that bound the suture (Figure 35a). Once thresholded, each of the 301 slices that made up the dataset were manually cleaned in order to isolate the suture region from adjacent diploë, vasculature, and other soft tissues (Figure 35b). When the manual segmentation was completed, a mask was generated for the isolated suture region by cavity filling the mask of the bones in the empty suture region (Figure 35c).

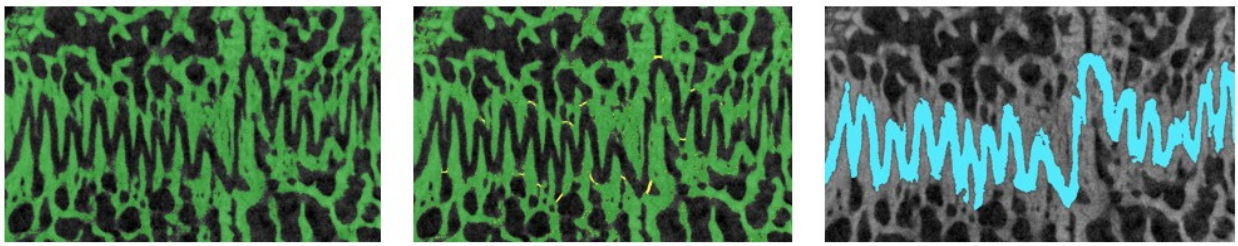

Figure 35 *Single plane of process to generate initial mask of suture for 3DV model*

Once a mask was generated for the suture at each of the 301 planes in consideration, a 3D object was created of using the mask, this allowed for problem regions to be easily identified, as shown in Figure 36.

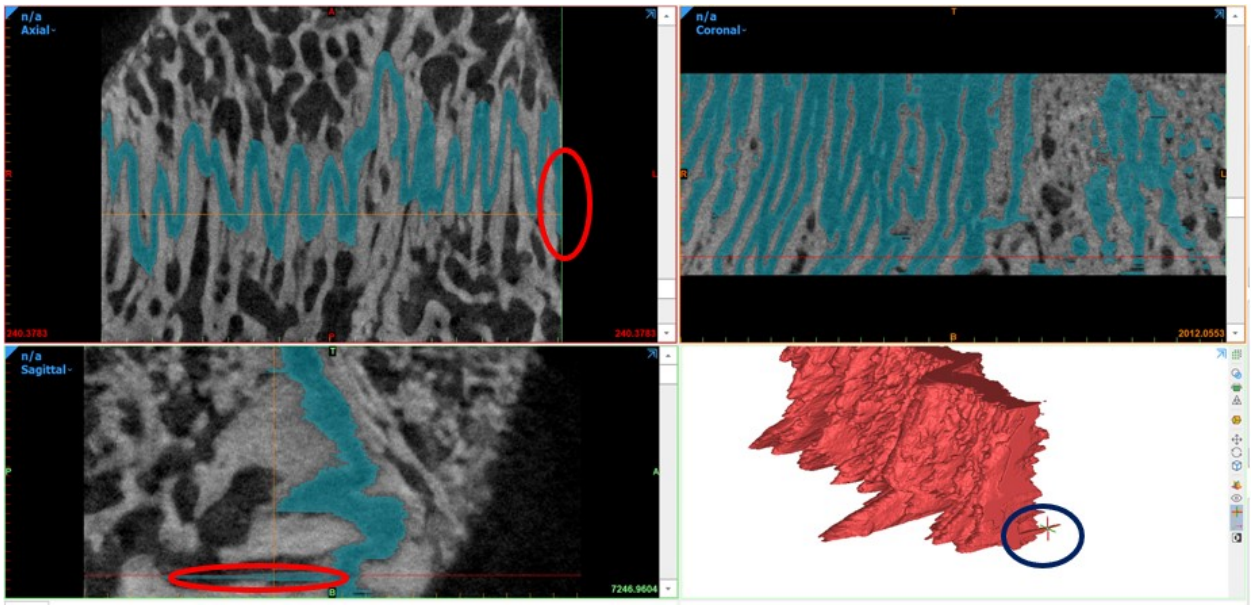

Figure 36 *Mimics 23.0 interface for identifying problem regions in the mask*

This process was iteratively performed until the large protrusions and problem regions were removed. Once all of the problem regions were cleaned, the morphological operations described in Section 3.2.1 were performed to the suture region and a 3D object was generated by interpolating the shape between each adjacent plane and smoothing the surface. The progress from the initial mask generated solid to the final solid used to generate the exported .stl file can be seen in Figure 37.

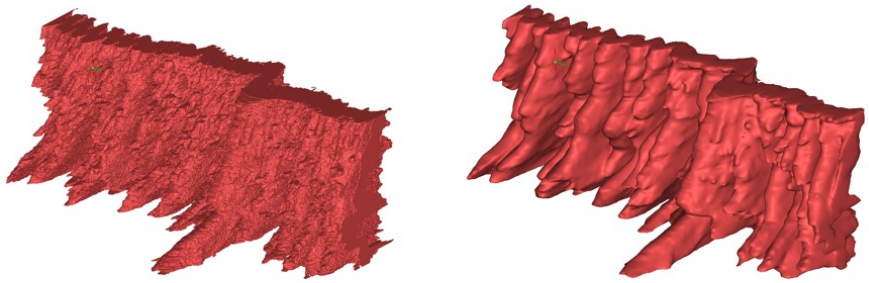

Figure 37 *Coronal suture objects generated in Mimics; (a) initial; (b) exported*

The .stl file was imported to SpaceClaim 2020 R2 where the surface mesh was automatically generated, the first step was to regularize the element sizes in order to generate a surface mesh compatible with the element size that would be used in the FE analysis. Once the surface mesh was regularized, the mesh was processed by first identifying and removing small floating facets. The surface mesh was then checked for sharp edges and vertices. All concave and convex regions were identified automatically to the specified sharp edge and vertices angle, 120° and 270° respectively. All sharp edges were manually fixed and rebuilt. Once the suture region was processed, a solid bone block was generated to bound the suture similar to the bone block in the 2DV models described in Appendix B1. The bone block was converted to a faceted body with the same element size as the suture, then the suture region was subtracted from the bone block, ensuring a face-to-face contact between the bone and the suture, this process is shown in Figure 38.

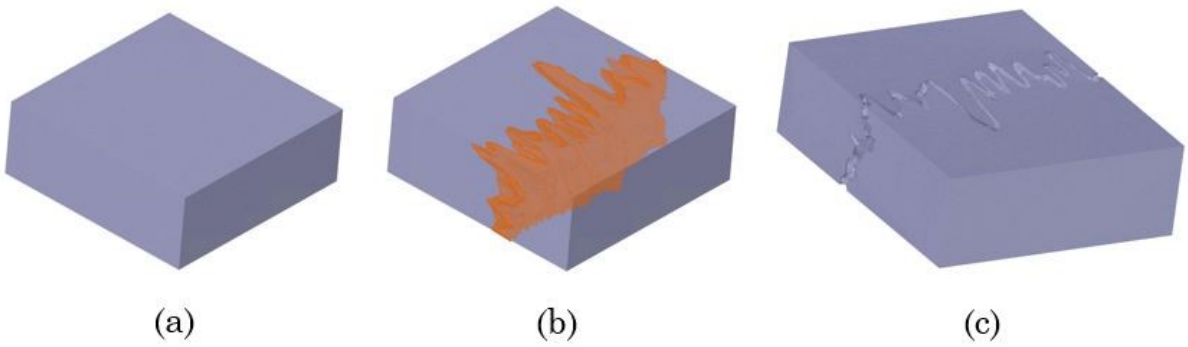

Figure 38 *Creating bone block for 3DV coronal suture model. (a) initial bone with suture hidden before facet subtraction was performed; (b) Bone with suture highlighted; (c) bone with suture hidden after facet subtraction*

The suture and bone were then both converted from faceted bodies to solid bodies, while preserving their surface meshes. Once this step was completed, the 3DV bone suture complex was ready to be imported to ANSYS Workbench 2020 R2 for mechanical analysis.

B3 Finite Element Model Mesh Sensitivity Analysis

The mesh sensitivity analysis was completed on the most complicated model, the 3DV suture model. The model was created using quadratic tetrahedron elements, and the sensitivity analysis was performed using element sizes of 50 μm, 60 μm, 75 μm, and 100 μm. The elements and nodes in each model can be seen below in Table 4 and Figure 39.

Table 4 *3DV solid model mesh refinement statistics*

Size of Elements [μm]	Elements	Nodes
100	265861	447516
75	499632	826350
60	839521	1359706
50	1361742	2173586

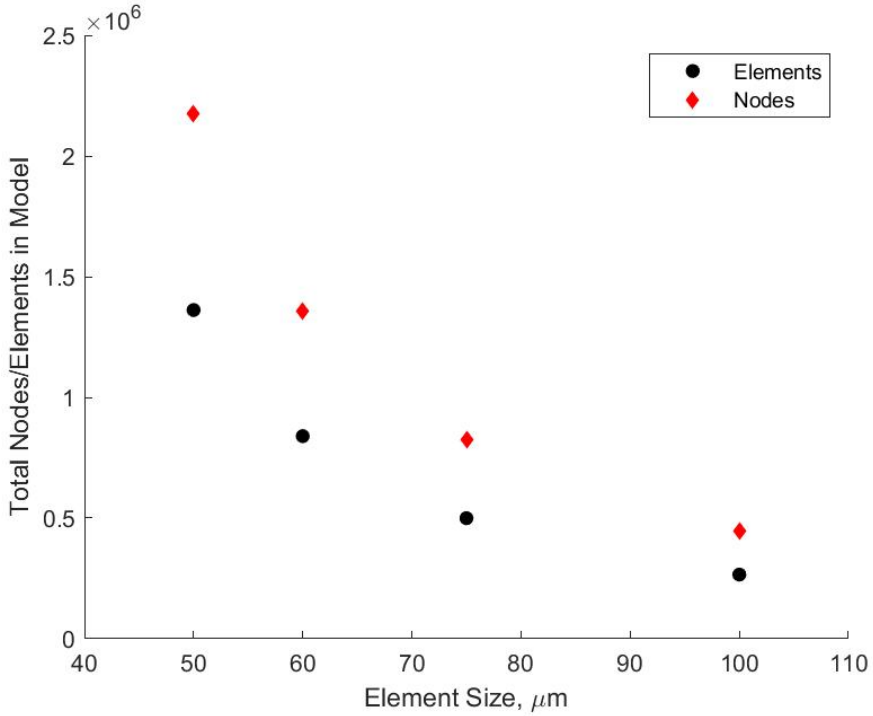

Figure 39 *Mesh statistics: Sensitivity analysis*

Five regions of interest were chosen to analyze the results of the different suture models, these regions can be seen in Figure 40.

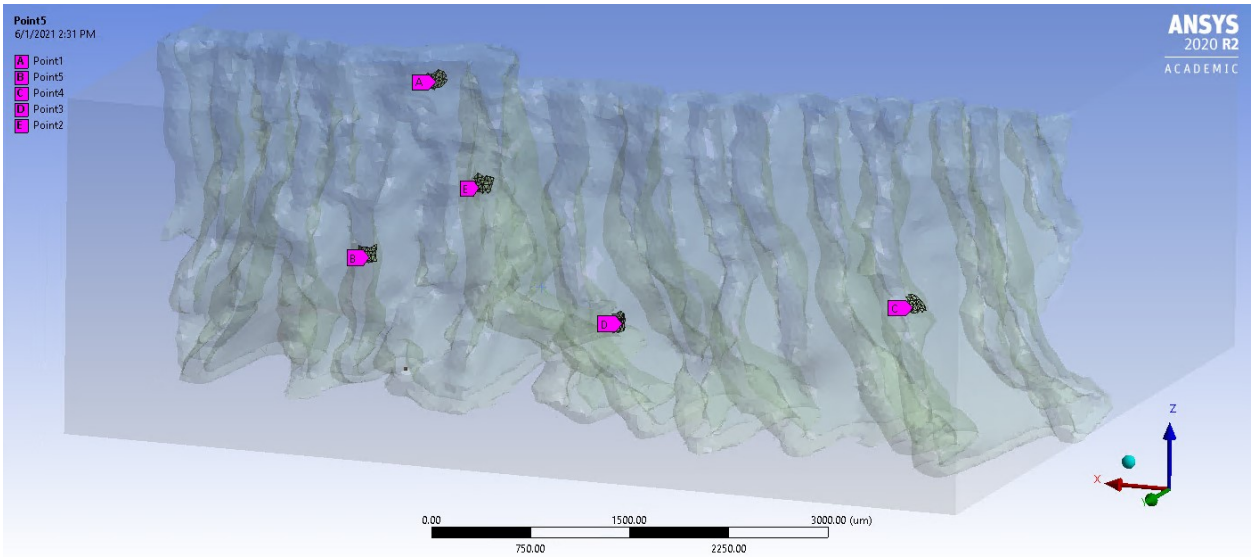

Figure 40 *Regions of interest for mesh sensitivity analysis of 3DV model*

The numerical results for each model used in the mesh sensitivity analysis at the regions of interests shown in Figure 40 above can be seen below in Table 5-Table 8.

Table 5 *100 µm mesh sensitivity results at regions of interest*

100 µm	Point	1	2	3	4	5
Equivalent Elastic Strain [µm/µm]	Min.	4.29E-03	1.41E-03	3.45E-03	1.34E-03	1.38E-03
	Max.	6.88E-03	2.10E-03	4.79E-03	3.46E-03	2.17E-03
	Avg.	5.08E-03	1.72E-03	4.12E-03	2.28E-03	1.68E-03
Maximum Principal Strain [µm/µm]	Min.	4.46E-03	1.92E-03	3.33E-03	1.68E-03	1.83E-03
	Max.	6.09E-03	2.65E-03	4.45E-03	3.84E-03	2.60E-03
	Avg.	4.93E-03	2.26E-03	3.92E-03	2.62E-03	2.18E-03
Minimum Principal Strain [µm/µm]	Min.	-5.29E-03	-5.22E-04	-3.26E-03	-1.54E-03	-7.13E-04
	Max.	-2.24E-03	-6.48E-05	-2.21E-03	-3.81E-04	-1.18E-04
	Avg.	-3.19E-03	-2.61E-04	-2.71E-03	-9.13E-04	-2.47E-04

Table 6 *75 µm mesh sensitivity results at regions of interest*

75 µm	Point	1	2	3	4	5
Equivalent Elastic Strain [µm/µm]	Min.	4.41E-03	1.35E-03	3.44E-03	1.57E-03	1.35E-03
	Max.	5.47E-03	2.28E-03	4.85E-03	3.03E-03	1.88E-03
	Avg.	4.95E-03	1.72E-03	4.14E-03	2.36E-03	1.57E-03
Maximum Principal Strain [µm/µm]	Min.	4.20E-03	1.82E-03	3.37E-03	1.94E-03	1.80E-03
	Max.	5.37E-03	2.83E-03	4.45E-03	3.39E-03	2.41E-03
	Avg.	4.82E-03	2.25E-03	3.93E-03	2.71E-03	2.06E-03
Minimum Principal Strain [µm/µm]	Min.	-3.68E-03	-6.29E-04	-3.37E-03	-1.36E-03	-4.12E-04
	Max.	-2.24E-03	-5.90E-05	-2.15E-03	-4.05E-04	-1.03E-04
	Avg.	-3.11E-03	-2.67E-04	-2.73E-03	-9.46E-04	-1.99E-04

Table 7 *60 µm mesh sensitivity results at regions of interest*

60 µm	Point	1	2	3	4	5
Equivalent Elastic Strain [µm/µm]	Min.	4.18E-03	1.39E-03	3.23E-03	1.48E-03	1.26E-03
	Max.	6.28E-03	2.32E-03	4.83E-03	3.08E-03	2.08E-03
	Avg.	4.87E-03	1.67E-03	4.12E-03	2.33E-03	1.60E-03
Maximum Principal Strain [µm/µm]	Min.	3.92E-03	1.86E-03	3.18E-03	1.79E-03	1.68E-03
	Max.	6.19E-03	2.82E-03	4.46E-03	3.36E-03	2.57E-03
	Avg.	4.83E-03	2.18E-03	3.91E-03	2.65E-03	2.09E-03
Minimum Principal Strain [µm/µm]	Min.	-3.92E-03	-7.34E-04	-3.28E-03	-1.47E-03	-5.62E-04
	Max.	-2.04E-03	-4.58E-05	-1.98E-03	-4.33E-04	-9.96E-05
	Avg.	-2.92E-03	-2.64E-04	-2.70E-03	-9.53E-04	-2.11E-04

Table 8 *50 µm mesh sensitivity results at regions of interest*

50 µm	Point	1	2	3	4	5
Equivalent Elastic Strain [µm/µm]	Min.	4.19E-03	1.32E-03	3.15E-03	1.30E-03	1.21E-03
	Max.	6.12E-03	2.24E-03	4.99E-03	3.20E-03	2.11E-03
	Avg.	4.79E-03	1.64E-03	4.15E-03	2.32E-03	1.61E-03
Maximum Principal Strain [µm/µm]	Min.	4.17E-03	1.81E-03	3.14E-03	1.68E-03	1.64E-03
	Max.	5.86E-03	2.71E-03	4.65E-03	3.56E-03	2.62E-03
	Avg.	4.74E-03	2.16E-03	3.93E-03	2.66E-03	2.11E-03
Minimum Principal Strain [µm/µm]	Min.	-3.98E-03	-7.21E-04	-3.38E-03	-1.54E-03	-5.76E-04
	Max.	-2.03E-03	-6.79E-05	-1.90E-03	-2.33E-04	-8.71E-05
	Avg.	-2.92E-03	-2.46E-04	-2.74E-03	-9.40E-04	-2.21E-04

The equivalent strain of each model was plotted, the results can be seen below in Figure 41.

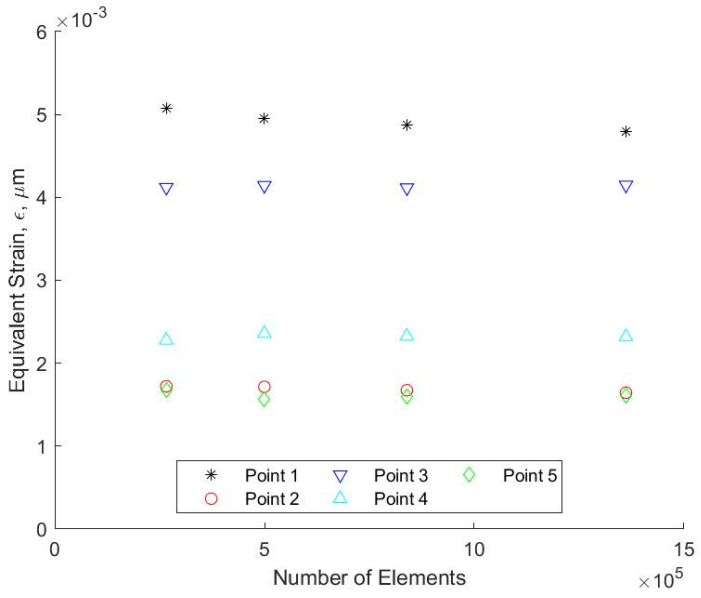

Figure 41 *Equivalent strain mesh sensitivity*

The maximum principal strain of each model was plotted, the results can be seen below in Figure 42.

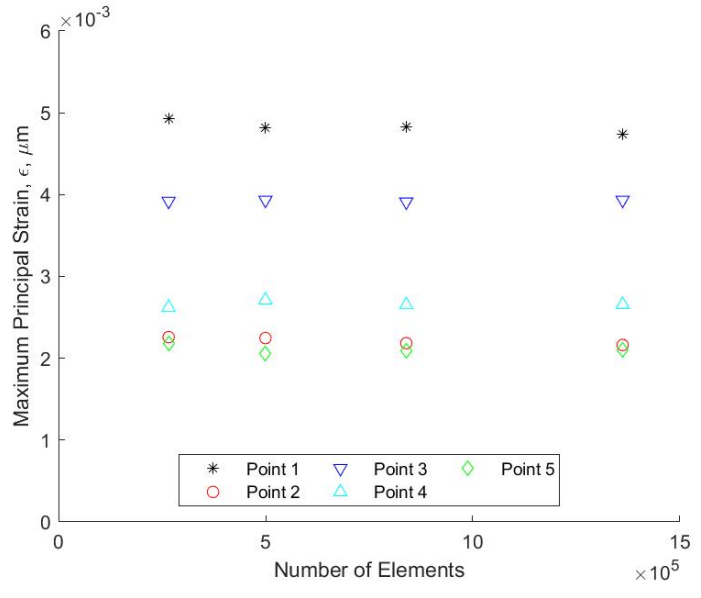

Figure 42 *Maximum principal strain mesh sensitivity*

The minimum principal strain of each model was plotted, the results can be seen below in Figure 43.

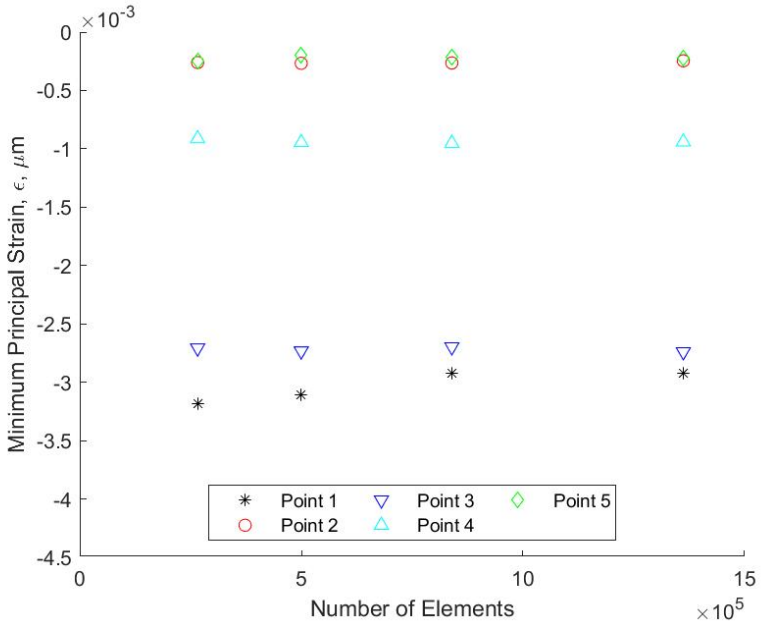

Figure 43 *Minimum principal strain mesh sensitivity*

Being that there were four element sizes analyzed in the mesh sensitivity analysis, there were a total of 3 refinements, shown below in Table 9.

Table 9 *Element sizes considered in mesh sensitivity refinements*

Refinement	Initial Element Size, E_i [μm]	Final Element Size, E_f [μm]
1	100	75
2	75	60
3	60	50

The strain values were averaged across the points in the suture and the relative difference in results were calculated by first determining the relative difference between the results at the 5 points as the mesh was refined from 100 μm to 50 μm. The relative differences were calculated using the equation (7).

$$R.D. = \frac{\varepsilon_{E_f} - \varepsilon_{E_i}}{\varepsilon_{E_i}} \cdot 100\% \qquad (7)$$

The relative differences between each point for the three mesh refinements can be found in Table 10-Table 12.

Table 10 *Refinement 1, relative differences at regions of interest (100 μm - 75 μm)*

Refinement 1	Point	1	2	3	4	5
Equivalent Elastic Strain R.D. [%]	Min.	2.6%	-4.4%	-0.2%	16.4%	-2.0%
	Max.	-20.5%	8.9%	1.3%	-12.4%	-13.2%
	Avg.	**-2.5%**	**-0.4%**	**0.6%**	**3.6%**	**-6.6%**
Maximum Principal Strain R.D. [%]	Min.	-5.7%	-5.2%	1.2%	15.4%	-1.4%
	Max.	-11.8%	6.7%	0.0%	-11.7%	-7.3%
	Avg.	**-2.3%**	**-0.5%**	**0.3%**	**3.4%**	**-5.5%**
Minimum Principal Strain R.D. [%]	Min.	-30.5%	20.4%	3.4%	-11.7%	-42.2%
	Max.	0.0%	-9.0%	-2.4%	6.5%	-12.8%
	Avg.	**-2.5%**	**2.4%**	**0.9%**	**3.6%**	**-19.6%**

Table 11 *Refinement 2, relative differences at regions of interest (75 μm - 60 μm)*

Refinement 2	Point	1	2	3	4	5
Equivalent Elastic Strain R.D. [%]	Min.	-5.1%	2.7%	-6.2%	-5.5%	-7.1%
	Max.	14.8%	1.6%	-0.5%	1.5%	10.2%
	Avg.	**-1.6%**	**-2.4%**	**-0.7%**	**-1.4%**	**2.1%**
Maximum Principal Strain R.D. [%]	Min.	-6.6%	2.4%	-5.4%	-8.1%	-6.7%
	Max.	15.3%	-0.5%	0.4%	-1.0%	6.8%
	Avg.	**0.2%**	**-2.8%**	**-0.5%**	**-2.2%**	**1.2%**
Minimum Principal Strain R.D. [%]	Min.	6.6%	16.6%	-2.5%	8.1%	36.5%
	Max.	-8.8%	-22.3%	-7.9%	6.9%	-3.1%
	Avg.	**-6.0%**	**-1.1%**	**-1.3%**	**0.7%**	**6.1%**

Table 12 *Refinement 3, relative differences at regions of interest (60 μm - 50 μm)*

Refinement 3	Point	1	2	3	4	5
Equivalent Elastic Strain R.D. [%]	Min.	0.2%	-4.5%	-2.3%	-12.4%	-3.8%
	Max.	-2.5%	-3.4%	3.3%	3.9%	1.7%
	Avg.	**-1.6%**	**-1.8%**	**0.8%**	**-0.3%**	**0.5%**
Maximum Principal Strain R.D. [%]	Min.	6.4%	-3.2%	-1.3%	-5.8%	-2.8%
	Max.	-5.3%	-3.8%	4.2%	6.0%	1.9%
	Avg.	**-1.9%**	**-1.0%**	**0.6%**	**0.2%**	**1.1%**
Minimum Principal Strain R.D. [%]	Min.	1.3%	-1.7%	2.9%	4.7%	2.6%
	Max.	-0.6%	48.3%	-4.0%	-46.2%	-12.5%
	Avg.	**0.1%**	**-6.9%**	**1.6%**	**-1.3%**	**4.8%**

The relative difference results shown above in Table 10-Table 12 were used to calculate the refinement averaged relative differences between the refinement models by using the bolded average relative differences and equation (8).

$$ARD = \frac{\sum_{i=1}^{5} |RD_{avg,i}|}{5} \tag{8}$$

The results of the average relative difference for the equivalent, maximum principal, and minimum principal strains for each refinement can be seen below in Table 13 and Figure 44. It was deemed acceptable when each of the averaged relative differences were below 3% for the refinement, therefore 50 μm element size was chosen for the analysis.

Table 13 *Average relative difference of mesh sensitivity refinements*

	Refinement		
Strain	**1**	**2**	**3**
Equivalent Elastic ARD [%]	2.7%	1.6%	1.0%
Maximum Principal ARD [%]	2.4%	1.4%	0.9%
Minimum Principal ARD [%]	5.8%	3.0%	2.9%

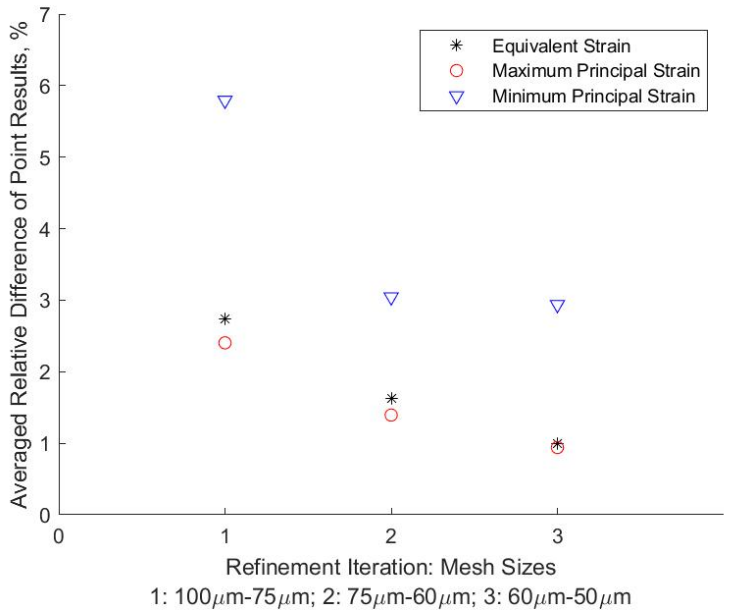

Figure 44 *Refinement averaged relative differences between refinement models*

B4 Finite Element Model Material Sensitivity Analysis

The material sensitivity analysis was performed in order to ensure that the results were not significantly dependent on the suture material properties that were used in the study. In order to show that, material properties that ranged the linear elastic models presented in literature were used, 1 – 600 MPa. The analysis was performed on all 3 of the 2DV models and the 3DV model to ensure that the relationship in results between models was similar despite the varying suture properties. Numerical results of the analysis can be seen below in Table 14.

Table 14 *Suture material refinement results*

Model		Suture Young's Modulus [MPa]				
		1	**6**	**15**	**100**	**600**
2DV Endocranial	Min.	9.05E-05	4.57E-05	3.54E-05	1.81E-05	2.03E-05
	Max.	7.18E-02	1.18E-02	4.53E-03	5.87E-04	9.18E-05
	Avg.	1.61E-02	2.68E-03	1.10E-03	1.79E-04	4.62E-05
2DV Midplane	Min.	1.36E-04	2.89E-05	5.60E-06	1.96E-05	1.95E-05
	Max.	9.05E-02	1.48E-02	5.78E-03	6.94E-04	1.01E-04
	Avg.	1.88E-02	3.18E-03	1.29E-03	2.05E-04	4.97E-05
2DV Ectocranial	Min.	1.82E-04	5.78E-05	3.84E-05	2.54E-05	2.37E-05
	Max.	1.56E-01	2.42E-02	8.87E-03	9.82E-04	1.02E-04
	Avg.	2.29E-02	3.83E-03	1.54E-03	2.47E-04	5.47E-05
3DV	Min.	2.14E-06	3.48E-07	3.37E-07	1.31E-07	5.04E-08
	Max.	2.24E-01	3.82E-02	1.50E-02	1.96E-03	2.60E-04
	Avg.	1.90E-02	3.18E-03	1.28E-03	2.03E-04	4.93E-05

Appendix C: Rat μCT Data Manipulation

C1 Rat Samples and Euler Rotations of Datasets

The individual specimens used in the rat suture morphometric analysis can be found below in Table 15.

Table 15 *Age of rats and corresponding datasets*

Age [Weeks]	Datasets				
16	BML-3	BML-11	BML-12	BML-35	BML-36
20	BML-5	BML-4A	BML-15	BML-25	BML-26
24	BML-8	BML-18	BML-20	BML-21	BML-16

The original scan datasets were imported to DataViewer and rotated in 3D until approximately normal to the suture of interest on the reoriented transaxial plane as shown in Figure 19. Table 16, Table 17, and Table 18 display the rotations performed on the 16, 20, and 24-week-old rats respectively in order to obtain a normal view of the suture of interest of each rat.

Table 16 *16-week-old rats: Euler rotations of original datasets [deg]*

Specimen	Rotation Direction	PL	AL RHS	AL LHS	Sagittal	C RHS	C LHS
BML-3	α	6.169	3.880	0.625	267.132	359.825	359.825
	ß	7.684	9.854	12.522	268.575	20.587	20.587
	γ	349.728	354.083	3.288	110.564	349.907	3.703
BML-11	α	229.57	253.784	132.205	84.73	174.271	192.636
	ß	3.283	23.462	3.820	266.767	13.148	13.776
	γ	307.201	274.084	50.284	98.204	352.538	345.435
BML-12	α	235.510	198.324	190.222	64.857	133.547	168.886
	ß	7.329	7.451	8.423	263.073	15.768	16.985
	γ	279.279	306.938	329.831	102.326	11.453	350.206
BML-35	α	159.468	123.626	209.683	266.247	243.554	102.645
	ß	338.057	335.131	340.971	278.590	350.178	339.612
	γ	16.646	44.935	335.928	278.506	284.150	81.329
BML-36	α	173.675	257.753	264.992	84.725	104.444	227.835
	ß	353.696	30.234	334.191	92.356	21.647	15.763
	γ	358.981	267.056	274.871	85.051	62.096	311.246

Table 17 *20-week-old rats: Euler rotations of original datasets [deg]*

Specimen	Rotation Direction	PL	AL RHS	AL LHS	Sagittal	C RHS	C LHS
BML-5	α	71.560	72.766	76.601	254.219	282.602	282.602
	β	342.090	342.741	342.530	104.695	21.946	21.946
	γ	272.049	261.702	273.976	81.454	53.803	70.333
BML-4A	α	58.955	58.955	58.955	247.936	301.767	301.767
	β	347.547	347.547	347.547	102.468	16.873	16.873
	γ	279.747	272.922	284.25	81.082	27.980	46.147
BML-15	α	0.0434	52.871	335.740	279.886	330.320	16.496
	β	13.751	22.610	19.648	90.904	32.654	28.819
	γ	8.553	318.215	34.787	66.82	28.500	357.454
BML-25	α	51.464	56.785	270.762	63.105	292.085	23.821
	β	11.691	30.111	18.04	277.599	18.475	26.429
	γ	282.662	267.148	68.61	259.121	28.810	316.688
BML-26	α	277.107	77.477	301.842	276.407	307.074	54.963
	β	358.053	29.276	19.923	86.878	23.273	24.617
	γ	90.000	281.941	68.759	76.597	47.412	316.155

Table 18 *24-week-old rats: Euler rotations of original datasets [deg]*

Specimen	Rotation Direction	PL	AL RHS	AL LHS	Sagittal	C RHS	C LHS
BML-8	α	303.163	307.678	278.034	273.834	29.345	29.345
	β	349.967	353.259	354.811	81.099	9.329	9.329
	γ	62.219	49.045	93.221	84.321	327.727	338.448
BML-18	α	318.959	85.179	326.467	133.252	4.047	55.913
	β	8.464	6.649	40.264	86.829	18.651	12.385
	γ	84.312	311.055	88.353	281.847	34.408	355.299
BML-20	α	286.194	3.580	2.647	275.088	8.806	8.806
	β	358.543	7.912	8.957	86.768	21.450	21.450
	γ	76.533	352.077	6.403	73.478	350.569	5.788
BML-21	α	307.128	75.511	13.813	216.478	311.707	311.707
	β	353.245	2.918	356.810	90.988	10.691	10.691
	γ	357.455	225.195	299.364	84.363	348.772	0.364
BML-16	α	-	58.813	44.807	233.121	68.355	45.121
	β	-	24.538	338.384	86.596	337.245	22.532
	γ	-	257.226	289.130	84.861	247.214	285.769

C2 Mean Suture LII and Width Results

The values of the mean suture LII and widths, as well as the associated standard deviations of the mean suture values can be found below for the 16-week-old rats in Table 19, the 20-week-old rats in Table 20, and the 24-week-old rats in Table 21.

Table 19 *16-week-old rats: Mean suture LII and widths*

Specimen	Mean Suture	PL	AL RHS	AL LHS	Sagittal	C RHS	C LHS
BML-3	LII	1.24	1.39	1.37	1.24	1.71	1.73
	W [μm]	157.9	199.1	199.5	162.0	187.0	172.0
BML-11	LII	1.68	1.87	1.75	1.34	2.12	1.99
	W [μm]	208.8	276.4	275.9	267.2	254.9	220.9
BML-12	LII	1.45	1.52	1.78	1.22	1.72	2.16
	W [μm]	203.3	246.9	274.6	247.3	243.0	208.4
BML-35	LII	1.67	1.56	1.68	1.28	1.99	1.86
	W [μm]	224.0	266.6	287.6	273.6	253.0	267.5
BML-36	LII	1.83	1.80	2.07	1.38	2.04	2.24
	W [μm]	225.8	264.2	249.4	254.7	216.8	208.1

Table 20 *20-week-old rats: Mean suture LII and widths*

Specimen	Mean Suture	PL	AL RHS	AL LHS	Sagittal	C RHS	C LHS
BML-5	LII	1.41	1.93	2.01	1.25	1.78	1.78
	W [μm]	165.0	190.4	175.8	169.3	181.3	181.1
BML-4A	LII	1.39	1.68	1.56	1.25	1.75	1.89
	W [μm]	159.8	216.5	227.1	189.2	166.2	178.5
BML-15	LII	1.53	1.96	1.91	1.32	2.23	1.75
	W [μm]	186.1	204.9	207.1	187.0	163.4	191.6
BML-25	LII	1.66	1.96	1.82	1.43	2.04	2.12
	W [μm]	154.1	201.1	187.9	169.3	232.2	192.5
BML-26	LII	1.55	1.78	1.91	1.32	2.16	1.92
	W [μm]	173.91	213.9	213.3	158.4	166.7	176.4

Table 21 *24-week-old rats: Mean suture LII and widths*

Specimen	Mean Suture	PL	AL RHS	AL LHS	Sagittal	C RHS	C LHS
BML-8	LII	1.40	1.62	1.62	1.19	1.92	1.78
	W [µm]	234.4	219.1	208.3	234.4	219.2	205.4
BML-18	LII	1.90	2.56	2.16	1.25	1.69	1.67
	W [µm]	212.3	266.2	276.1	314.8	310.4	322.0
BML-20	LII	1.80	2.52	2.28	1.97	1.97	1.77
	W [µm]	180.0	170.9	215.7	183.9	215.0	210.4
BML-21	LII	1.45	2.01	1.78	1.29	2.37	1.98
	W [µm]	142.6	165.7	200.8	201.6	168.6	190.4
BML-16	LII	-	2.51	2.64	1.47	2.28	2.29
	W [µm]	-	179.4	179.8	181.9	172.9	184.3